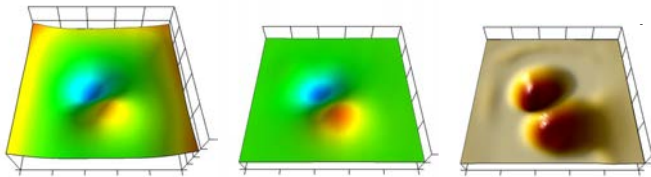


Scanning Hall probe microscopy of vortex matter in single- and two-gap superconductors



Bart Raes

Promotors:
Prof.Dr. Victor V. Moshchalkov
Prof.Dr. Jacques Tempère

Dissertation presented in partial
fulfillment of the requirements for the
PhD degree

July 2013

Scanning Hall probe microscopy of vortex matter in single-and two-gap superconductors

Bart RAES

Dissertation presented in partial fulfillment of the requirements for the PhD degree

Members of the Examination committee:

Prof. Dr. Victor V. Moshchalkov	KU Leuven	(Promotor)
Prof. Dr. Jacques Tempère	Universiteit Antwerpen	(Co-promotor)
Prof. Dr. J. Van de Vondel	KU Leuven	(Secretary)
Prof. Dr. L. Chibotaru	KU Leuven	(President)
Prof. Dr. J. Vanacken	KU Leuven	
Dr. J. Gutierrez Royo	KU Leuven	
Prof. Dr. A.V. Silhanek	Université de Liège	
Prof. Dr. S. Bending	University of Bath	
Prof. Dr. G. Borghs	KU Leuven, IMEC	



July 2013

© 2013 KU Leuven, Groep Wetenschap & Technologie,
Arenberg Doctoraatsschool, W. de Croylaan 6, 3001 Leuven, België

Alle rechten voorbehouden. Niets uit deze uitgave mag worden vermenigvuldigd en/of openbaar gemaakt worden door middel van druk, fotocopie, microfilm, elektronisch of op welke andere wijze ook zonder voorafgaande schriftelijke toestemming van de uitgever.

All rights reserved. No part of the publication may be reproduced in any form by print, photoprint, microfilm or any other means without written permission from the publisher.

ISBN 978-90-8649-638-9
D/2013/10.705/53

Dankwoord-Acknowledgements

Doctoreren is niet alleen het resultaat van bijna vier jaar wetenschappelijk onderzoek, het is een lange weg met veel hindernissen maar zeker ook enkele hoogtepunten. Het is door de inzet en het enthousiasme van heel wat mensen dat deze hindernissen overwonnen zijn en de hoogtepunten samen gevierd konden worden. Achter dit werk staat immers een sterk team van collega's die ondertussen vrienden geworden zijn. In wat volgt wil ik dan ook tot ieder een persoonlijk woordje van dank uiten.

In de eerste plaats gaat mijn dank uit naar mijn promotor, Prof.Dr. Victor V. Moshchalkov, die mij niet alleen de kans heeft geboden te doctoreren binnen zijn onderzoeksgroep, maar me ook wegwijs heeft gemaakt in de wetenschappelijke wereld als beginnend onderzoeker.

Vervolgens wil ik mijn co-promotor, Prof.Dr. Jacques Tempère, bedanken. Al heb ik niet echt de deur bij u plat gelopen, wanneer ik langskwam in Antwerpen was u altijd bereid te luisteren en advies te geven. Wat ik zeker wil vermelden, is dat uw fantastische manier van lesgeven een blijvende indruk heeft nagelaten op mij. Bijvoorbeeld, ik vergeet nooit de dag dat u met een gelatine taart de les binnenkwam bij de inleiding over Bose-Einstein condensaten. Dit niet alleen omdat de taart lekker was, maar vooral omdat u het onderwerp boeiend kon en kan vertellen.

I want to extend my thanks to the members of the jury for a thorough evaluation of my work and for valuable comments.

Wie ik ook zeker wil bedanken, is Prof.Dr. Joris van de Vondel. Een paar summiere zinnen gaan hier niet volstaan. Elke dag was ik welkom bij je en dat apprecieer ik ten zeerste. Ik ben er zeker van dat de onderzoeker in mij gevormd en gekneed is door het geluk te hebben gehad nauw met je te kunnen samenwerken. Het enthousiasme waarmee je werkt heeft mij aangestoken om er dag in dag uit 100 % voor te gaan. Zonder jou had ik dit doctoraat misschien nooit tot een goed einde gebracht en ik ben je hier ontzettend dankbaar voor! Wat ik steeds fantastisch vond, waren de urenlange discussies (al dan niet

wetenschappelijk) in de auto, tijdens de evenlang durende dagelijkse files. Door de jaren heen, vanaf mijn masterthesis tot nu, ben je dan ook meer een vriend geworden dan een collega.

Also, I want to specially thank Prof.Dr. Alejandro Silhanek. I still remember the first day I encountered you. I chose a masterproject about superconductivity, my first experience as a researcher. After a short and enthusiastic introduction about superconductivity in the (at that time) impressive room where the He⁴ cryostat is standing, my first impression was 'ooooe this project is going to be a difficult one'. However, because you have patience and the fantastic power to explain things in different and enlightening ways, this project and my thesis were a success. I am convinced that encountering you that first day at the He⁴ cryostat, is for sure the reason why I was able to reach my goals. Alejandro, I am very happy that you were there all these years, not only to help me out at work, but also to colour my days at the office. Concerning the latter, I will never forget the first years together with you and Werner in the office. The atmosphere was great and your complains when Werner created a less good 'atmosphere'(read:'smell') were hilarious.

Further, special thanks are necessary for Dr. Joffre Gutierrez. I think I can safely say that we both have struggled in the beginning with the setup for days and nights...This was for sure a frustrating process as we had a lot of headwind. However, somehow there was still the drive to continue until we had success. I am convinced this kind of teamwork wouldn't have been possible if you were not the funny guy you are, driving us both to go out there and do our best, 'break a leg' as they say. To prove this point you even literally broke you leg during football. To remember you left the trophy, the bandage, in the lab! In any case, I enjoyed all the days in our lab and at the office!

And then there are my colleagues, ex-colleagues and the technical and administrative staff. A fantastic collection, with some special cases in it, drinking strange cocktails, organizing crazy activities, designing experiments, of course helping me out with several small and bigger problems and last but not least creating a fantastic atmosphere at work.

Om op tijd en stond te ontspannen, heb ik altijd kunnen rekenen op mijn vrienden. Zowel de kameraden waarmee ik geregeld ga klimmen als mijn vrienden uit Puurs waar ik vele leuke avonden mee heb beleefd. Merci om er steeds te zijn wanneer ik mijn hoofd even wilde leegmaken. Zonder onze amusante avonturen, hadden de voorbije jaren veel saaier geweest.

Wie zeker niet mag ontbreken in dit dankwoord, zijn mijn ouders. Moeke en Vake, ik weet dat een paar korte zinnetjes hier niet volstaan, maar het is door jullie motivatie, steun en liefde dat ik mijn doelen kan waarmaken in het leven. In alles wat ik doe, staan jullie 100 % achter mij en dat gevoel geeft mij de kracht om uitdagingen aan te gaan. Verder is er mijn zus, Leen, die ik zeker wil bedanken om er elke keer te zijn en mijn avonden en weekends te kleuren wanneer ik thuis kwam. Ook Dianeke en Herman stonden steeds voor me klaar, net zoals José en Marcel. Een schoonfamilie waarop ik steeds kon en kan rekenen.

Een heel speciaal dankwoordje gaat uit naar mijn Moemoe. Moemoe, het is door jouw levensverhalen dat ik tegenslagen heb leren relativeren en heb geleerd dat alles altijd wel op zijn pootjes terecht komt. Een belangrijke troef om het hobbelige pad dat een doctoraat is, te bewandelen. Ik hoop dat je vandaag trots kan zijn, en ik weet dat onze Vava dat zeker ook zou geweest zijn.

Als laatste wil ik mijn liefje, Carole, in de bloemetjes zetten. Bedankt voor je liefde, voor je steun en om in mij te blijven geloven. Er zijn dagen geweest waarop ik met mijn hoofd zweefde tussen de 'wervelwinden' die ik bestudeerde, met als gevolg dat mijn hoofd soms zelf meer een wervelwind was. Tijdens de soms drukke en vermoeiende dagen was je mijn steun en toeverlaat, bij wie ik altijd liefdevol kon thuis komen. De afgelopen jaren met jou, waren de beste in mijn leven en ik kijk dan ook eens zo hard uit naar onze toekomst samen. Prottie ik zien u graag!

Preface

New insights in physics have been revealed each time a new research area became available. For example, better microscopes and particle accelerators allowed physicists to explore the nature of things on the smallest length scales, which resulted in Schrödinger's 'Quantum mechanical' description of the microscopic world. On top of that, the acquired accessibility to new domains allows to check experimentally different pioneering theoretical predictions. For example, new telescopes allowed researchers to explore physics on cosmic length scales, confirming Albert Einstein's 'Theory of relativity'. A new research area, low temperature physics, became available in 1911 when H. Kamerlingh Onnes successfully liquefied Helium in Leiden. Onnes wanted to test the validity of the Drude theory at the lowest temperature possible, a theory describing the resistive behavior of a metal. However, when he turned his attention to Mercury, he observed that all signs of resistance appeared to vanish suddenly below $\sim 4\text{K}$. A new remarkable state of condensed matter was found, superconductivity. Superconductivity, a macroscopic quantum effect, allows dissipationless transport of electrical current and envisions a way out in a world where energy dissipation has become a universal and top priority problem. The zero resistance, the hallmark of superconductors, makes them very attractive candidates for a variety of technological applications. These applications range from high power transmission lines, high speed 500 km/h levitating trains to the production of large volume, stable, high magnetic fields essential in human health monitoring and diagnosis such as MRI scanners.

Regretfully, it is a well established fact that all technologically useful superconductors (type-II superconductors), subjected to the flow of an electrical current, give rise to energy losses as a consequence of the motion of quantum units of flux and thus threatening their utility. This is why for decades scientists and engineers have strived to understand, improve and optimize the mechanisms to control and prevent the motion of these so called fluxons or vortices.

With the advent of modern lithographic techniques, it became possible to nano-pattern the superconductors at length-scales comparable to the size of

a fluxon ($<1\mu\text{m}$) and to systematically investigate the effect of different well characterized pinning centers (antidots, blind holes, etc.) and their distribution (periodic, quasiperiodic, random) on the vortex properties. These pinning centers provide a competing force for the repulsive vortex-vortex interaction favoring triangular order in conventional superconductors and the driving Lorentz force exerted by an induced or applied transport current. The control over the interplay between these different competing forces allows to tune, improve and optimize the critical currents and fields of a superconductor, which is of fundamental importance for applications.

A new different kind of competition is observed in high quality single crystals of MgB_2 . In this prototypical two-gap superconductor, the presence of two coupled coexisting condensates, having different characteristic length scales, has profound consequences for the superconducting properties. Due to these extra degrees of freedom, two-gap superconductors offer new possibilities interesting for both fundamental research and applications. In particular, the response to an applied magnetic field can result in completely new physics as compared to single-gap superconductors. In one extreme case, one condensate will promote the formation of normal metal-superconductor(NS) boundaries resulting in a vortex state, while the other component will try to minimize the NS surface favoring the Meissner state. This results in a non-monotonic vortex-vortex interaction and a vortex distribution having vortex clusters immersed in domains of the Meissner state.

Most of the research tools to investigate the vortex properties probe the response of the whole superconducting volume and include the reaction of millions of vortices (transport-and magnetization measurements, susceptibility measurements, etc.) upon changing external variables (current, magnetic field, temperature, etc.). Here the relation between the measured dependencies of the macroscopic response and the microscopic vortex properties is indirect and adequate theories have to be used to connect both worlds. As such a continuous drive exists within the superconductivity community to develop techniques which reveal directly the microscopic vortex properties. Different tools are used to reveal single fluxons by probing their normal metallic core (scanning tunneling microscopy) or the magnetic field attached to them (Bitter decoration, magnetic force microscopy, scanning Hall probe microscopy, etc.), each technique having its range of applicability.

In this thesis, under the idiom, ‘seeing is believing’, vortex matter is studied at the single ‘particle’ scale. The ‘camera’ to visualize a single fluxon makes use of a submicron ($<10^{-6}\text{m}$) Hall probe which is moved in close proximity over the sample surface and allows to

detect a single quantum unit of flux carried by a vortex. This technique, scanning Hall probe microscopy (SHPM) and a lock-in variant, are used in this thesis to study the competition between the pinning forces exerted by natural defects or nano-structuring, the vortex-vortex interaction and an external driving force in a variety of single-gap and two-gap superconductors. With these techniques the observation of the single fluxon world becomes accessible, in this way pioneering models used to explain the macroscopic response can be checked. In the end, a direct experimental observation provides irrefutable evidence. Moreover, just as K. Onnes discovered superconductivity by checking Drude's theory of resistivity at the lowest temperatures, it is hoped to find new and remarkable properties at this scale.

This dissertation comprises a series of chapters, each exemplifying a specific aspect of the above described interplay determining the extraordinary superconducting properties.

Chapter 1. In this chapter an introduction to some theoretical aspects of superconductivity is presented. These concepts are necessary to understand and interpret the results presented in other chapters. However, where needed, additional theoretical background is provided in each of the following chapters and references therein.

Chapter 2. Since the work in this thesis is mostly of experimental nature, this chapter gives a brief description of some selected experimental techniques. The focus is on the description of the technique central in this work, SHPM. The sample fabrication method is also described.

Chapter 3. In this chapter the pinning properties of flux lines in a quasi-periodically nano-structured superconductor are investigated at the single vortex scale by SHPM. The competition between the vortex-vortex interaction favoring triangular order and the extraordinary properties of the quasi-periodic modulated pinning landscape has profound consequences for the resulting vortex distributions and their dynamical properties. The obtained flux distributions not only show the anticipated vortex configurations for specific matching fields, as suggested from macroscopic transport measurements, but unveil new and so far unpredicted local vortex distributions.

Chapter 4. In general, a type-II superconductor is flooded with vortices above a critical entry field. The magnetic response of a type-II superconductor is radically different, depending on whether the superconductor is in the Meissner

state, characterized by a reversible magnetic response, or in the mixed state, where vortices appear. As such, the determination of this field is of fundamental importance, although it is never investigated at the single vortex level. In this chapter, we study in detail the microscopic process of the first vortex penetration in a carefully designed sample which captures the first entered vortex in close neighbourhood of the sample border, making the observation possible by scanning Hall probe microscopy.

Chapter 5. While in the two preceding chapters the visualisation of a static vortex distribution by SHPM is used to infer information about the vortex properties. In this chapter we present a novel local imaging technique with unprecedented resolution, termed scanning ac-susceptibility microscopy (SSM), which allows us, for the first time, to directly visualize the microscopic dynamics of a single flux quantum. This new tool permits to check different models describing the dynamical properties of vortex matter at the relevant length scale and provides new insights concerning their dissipative behavior.

Chapter 6. In this chapter, we focus on vortex patterns in clean MgB_2 single crystals by SHPM. Whereas, in previous chapters the competition between the vortex-vortex interaction, the pinning force and the driving Lorentz force were investigated, here due to the two-gap nature of MgB_2 an intrinsic competition arises, resulting in a non-monotonic vortex-vortex interaction accompanied by the appearance of unconventional vortex patterns. We have been able to observe the progressive formation of vortex stripes in MgB_2 and investigated their stability.

Finally, we will conclude and present an outlook for the future.

Contents

Dankwoord-Acknowledgements	i
Preface	v
Contents	ix
1 Theoretical introduction	1
1.1 Historical background	1
1.2 The Ginzburg-Landau theory	8
1.3 The characteristic length scales	13
1.4 Type-I and type-II superconductors	15
1.5 The London equations	18
1.6 The structure of a single vortex and the vortex lattice	19
1.7 Superconducting thin films in a perpendicular magnetic field. .	23
1.8 Non-equilibrium properties of superconductors	24
1.8.1 Electromagnetic properties of an Ohmic material	25
1.8.2 Ac magnetic field penetration in a superconductor	29
2 Experimental techniques	41
2.1 Introduction	41
2.2 Scanning Hall probe microscopy	41
2.3 Sample fabrication	48

3	Symmetry-induced giant vortex state in a superconducting Pb film with a fivefold Penrose array of magnetic pinning centers	51
3.1	Introduction	51
3.2	The quasiperiodic Penrose tiling	52
3.2.1	Commensurability effects in periodic nano-structured superconductors	55
3.2.2	Commensurability effects in quasiperiodic nano-structured superconductors	56
3.3	Results	57
3.3.1	Sample details	58
3.3.2	Transport measurements	60
3.3.3	Scanning Hall probe microscopy measurements	62
3.4	Conclusion	68
4	First vortex entry into a perpendicularly magnetized superconducting thin film	69
4.1	Introduction	69
4.2	Theoretical background	70
4.3	Sample details	74
4.4	Experimental results	79
4.5	Discussion	80
4.6	Conclusion	85
5	Local mapping of the response of a superconductor to a perpendicular alternating magnetic field	87
5.1	Introduction	87
5.2	The response of a superconductor to an ac magnetic field . . .	88
5.2.1	Introduction	88
5.2.2	A classical example, the driven damped harmonic oscillator	89

5.2.3	The response of a superconductor to an ac magnetic field	92
5.3	Results	99
5.3.1	Ac response of a superconducting Pb ribbon	99
5.3.2	Ac response of a nano-structured superconductor	109
5.4	Conclusions	116
6	Scanning Hall probe microscopy of unconventional vortex patterns in the two-gap MgB₂ superconductor	119
6.1	Introduction	119
6.2	Type-1.5 superconductivity	121
6.3	Experimental details	127
6.4	Unconventional vortex patterns in MgB ₂	127
6.5	Stripe pattern evolution in MgB ₂	131
6.6	Vortex pattern stability in MgB ₂	134
6.7	Conclusions	136
7	Conclusions and outlook	139
	List of symbols	145
	Bibliography	147
	Curriculum Vitae	163
	Publications	165

Theoretical introduction

This introductory chapter gives a brief overview limited to the scope of this PhD research of the most important physical concepts necessary to understand and interpret the main results of this work. It introduces the macroscopic quantum effect of superconductivity, being one of the most fascinating phenomena in condensed matter physics. A more detailed discussion of these concepts can be found in several excellent books, to list a few:

- Introduction to superconductivity, Tinkham, M. [1]
- Superconductivity of metals and alloys, De Gennes, P.G. [2]
- Superconductivity, superfluids and condensates, Annett, J.F. [3]

1.1 Historical background

Every journey begins with a first step. The first step in the long quest of superconductivity(SC) was set by H. Kamerlingh Onnes[4] in 1911 in Leiden. He was the first to liquefy Helium resulting in the birth of a new vigorous research area, low temperature physics. The phenomenon of superconductivity was a complete surprise when it was first observed by Onnes in 1911. He wanted to test the validity of the Drude theory by measuring the resistivity at the lowest temperature possible. But, when he turned his attention to Mercury, he observed that all signs of resistance appeared to vanish suddenly below 4K, see Fig.1.1(a). This first key characteristic, infinite conductivity below a critical temperature, T_c , introduced a new state of matter: superconductivity.

A second remarkable feature of superconductivity is the observation that in the superconducting state, an external magnetic field is completely expelled. This

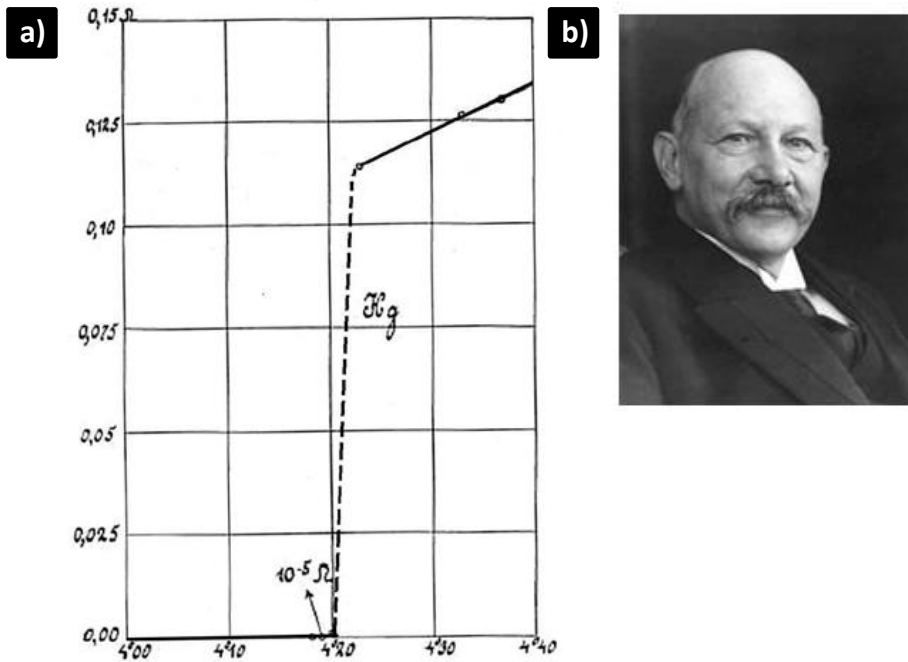


Figure 1.1: (a) Experimental observation by H. Kamerlingh Onnes of the superconducting transition, which shows the resistance (unit:Ohm) versus temperature (unit:Kelvin) for Mercury. This historical experiment reveals the superconducting transition at 4.2K, the resistance drops from 0.1 Ohm to zero ($< 10^{-6}\text{Ohm}$) within a narrow temperature range of 10mK[5]. (b) H. Kamerlingh Onnes (Groningen, 21 September 1853- Leiden, 21 February 1926)[Picture taken from Wikipedia]

effect, perfect diamagnetism, discovered in 1933 by Meissner and Ochsenfeld[6], 22 years later than the first key characteristic, is called the Meissner-Ochsenfeld effect. Combining perfect conductivity and Faraday's law of induction cannot explain this effect. Indeed, Meissner and Ochsenfeld not only observed that a magnetic field is excluded from entering a superconductor, as might be explained by perfect conductivity, but also that a field in an originally normal sample is expelled as it is cooled through the superconducting transition. The latter can certainly not be explained by perfect conductivity as it would trap the flux in.

These two key properties of a superconductor exist only within a certain thermodynamical phase space, meaning below a certain critical magnetic

field, temperature and current. If we exceed one of the critical values, the superconductor is in the normal phase.

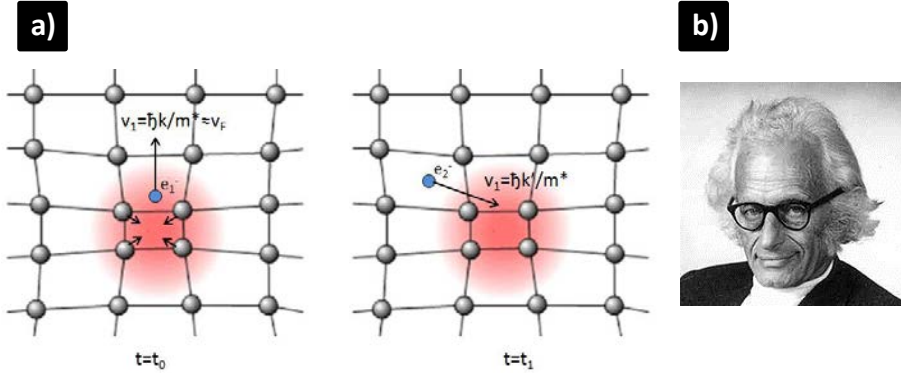


Figure 1.2: (a) Illustration of the effective interaction mechanism proposed by H. Fröhlich. At $t = t_0$, an electron is travelling through the ion lattice, with velocity $v_1 \approx v_F$ resulting in a positive polarization cloud behind it due to the retarded ionic response. At $t = t_1$ a second electron is attracted by the polarization left behind by the first electron which is long gone. (b) Herbert Fröhlich (Rexingen, 9 December 1905- Liverpool, 23 January 1991)[Picture taken from Wikipedia]

The microscopic mechanism of superconductivity was described by Bardeen, Cooper and Schrieffer (BCS) in 1957[7]. After some crucial experiments¹, one could argue that superconductivity arises when electrons couple into pairs which behave as bosons. Theoretically this was an interesting challenge, since this behavior demands the existence of an attractive interaction between electrons. However, in the simple electron gas model for a metal, the only interactions are repulsive Coulomb interactions which do not favor pairing. Fröhlich proposed in 1950, in accordance with the isotope-experiment, that the interaction between electrons and ionic lattice vibrations, or phonons, could lead to an effective attractive interaction between the electrons themselves. Fröhlich pictured an electron travelling through the lattice, typically moving at the Fermi velocity, $v_F = \hbar k_F / m^* = 10^6 \text{ m/s}$, with k_F the Fermi wave-vector and m^* an effective electron band mass[13]. During this trip, the electron will deform or polarize the lattice a bit as the ions are positively

¹(i) Ac conductivity[8] and specific heat capacity measurements[9] indicated the existence of a band gap, a kind of bonding energy which has to be delivered to make excitations. (ii) The critical temperature, T_c is isotope dependent[10, 11], $T_c M^a = \text{const}$ with M the mass of the isotope and $a = 0.5$ for the majority of superconductors, indicating an influence of phonons. (iii) Flux-quantization in units of $h/2e$, which indicates that electrons move in pairs[12].

charged, see Fig.1.2(a). Due to the retarded response of the much heavier ions ($v_I < 0.01v_F$), the electron is long gone by the time the ions polarize themselves. It will look like the electron drags a positively charged cloud behind itself like a comet. A second electron, feels a net attractive force due to the positively charged polarization left behind by the first electron resulting in a net effective attraction between both electrons at much larger distances than the lattice constant. The effective interaction, consisting of a (screened) repulsive Coulomb-interaction and the above described interaction due to coupling with the ionic lattice (electron-phonon coupling), turns out to be:

$$\begin{aligned} V_{eff}(\mathbf{k}, \mathbf{k}', \mathbf{q}) &= V_{Coulomb} + V_{phonon-exchange} \\ &= \frac{e^2}{\epsilon(q)\mathbf{q}^2} + \frac{|g(q)|^2 \hbar\omega_{\mathbf{q}}}{(\epsilon_{\mathbf{k}+\mathbf{q}} - \epsilon_{\mathbf{k}})^2 - (\hbar\omega_{\mathbf{q}})^2} \end{aligned} \quad (1.1)$$

which depends on the momenta of both electrons², $\hbar\mathbf{k}$ and $\hbar\mathbf{k}'$, corresponding with energies $\epsilon_{\mathbf{k}}$ and $\epsilon_{\mathbf{k}'}$, respectively and on the momentum of the exchanged phonon, $\hbar\mathbf{q} = \hbar(\mathbf{k} - \mathbf{k}')$, with corresponding energy $\hbar\omega_{\mathbf{q}}$. The coupling constant, $|g(q)|$, describes the interaction strength between the electrons and the phonons, while ϵ is the dielectric constant reducing the strength of the bare coulomb interaction due to screening by the other electrons[14]. The frequency dependence of the second term reflects the retarded nature of the phonon-exchange interaction. The important aspect of Eq.1.1 is that the interaction part describing phonon-exchange is negative, meaning attractive, when $|\epsilon_{\mathbf{k}+\mathbf{q}} - \epsilon_{\mathbf{k}}| < \hbar\omega_{\mathbf{q}}$. Superconductivity arises when the net force, the balance between the phonon-induced attraction and the Coulomb repulsion is overall attractive. Note, that a strong electron-phonon coupling favors superconductivity, this is why somehow counterintuitive, good conductors are poor superconductors.

The basic idea that even a weak effective attractive interaction can bind pairs of electrons in a bound state, a so called ‘Cooper pair’, was presented in 1956 by L. Cooper [15]. He showed that the Fermi sea of electrons is unstable against at least one bound pair, so long as there is an attractive interaction present. This was a first step towards a microscopic description of superconductivity. Having seen that the Fermi sea is unstable against the formation of a bound Cooper pair when the net interaction is attractive, then, clearly we must expect pairs to condense until an equilibrium point is reached and the ground state energy is lowered.

However, the main problem of Cooper’s calculation is that it singles out two particular electrons. In the theory of Bardeen, Cooper and Schrieffer (BCS) one treats all electrons on the same footing within a simplified model where only

²In this thesis we use boldface font to denote a vector.

those pairs of electrons which interact most strongly are taken into account³. This is why BCS proposed the following effective hamiltonian:

$$\begin{aligned}\hat{H}^{BCS} &= \sum_{\mathbf{k}, \sigma} \frac{(\hbar\mathbf{k})^2}{2m^*} \hat{c}_{\mathbf{k}\sigma}^\dagger \hat{c}_{\mathbf{k}\sigma} + \hat{H}_{int}^{BCS} \\ \hat{H}_{int}^{BCS} &= -\tilde{V} \sum_{\mathbf{k} \in D} \sum_{\mathbf{k}' \in D} \hat{c}_{-\mathbf{k}', \downarrow}^\dagger \hat{c}_{\mathbf{k}', \uparrow}^\dagger \hat{c}_{\mathbf{k}, \uparrow} \hat{c}_{-\mathbf{k}, \downarrow}\end{aligned}\tag{1.2}$$

Composed of a kinetic energy term and an interaction term, where $\hat{c}_{\mathbf{k}, \sigma}^\dagger$ and $\hat{c}_{\mathbf{k}, \sigma}$ are the creation and annihilation operators for an electron of momentum $\hbar\mathbf{k}$ and spin $\sigma = \uparrow, \downarrow$, respectively. The interaction term describes an interaction scattering the pair $(-\mathbf{k}, \downarrow), (\mathbf{k}, \uparrow)$ into the states $(\mathbf{k}', \uparrow), (-\mathbf{k}', \downarrow)$. The effective force between all pairs of electrons, is modeled by a constant attractive interaction of strength, \tilde{V} , between electrons with opposing spin and momentum within momentum space D. Where D is a set of states in a shell surrounding the Fermi-level of thickness, $\hbar\omega_D$, the Debye phonon energy. The proposed hamiltonian is treated with an elegant variational principle, with a smart choice for the variational wave-function:

$$|\psi_{BCS}\rangle = \prod_{\mathbf{k}} (u_{\mathbf{k}}^* + v_{\mathbf{k}} \hat{c}_{\mathbf{k}, \uparrow}^\dagger \hat{c}_{-\mathbf{k}, \downarrow}^\dagger) |0\rangle\tag{1.3}$$

In this wave-function, $|0\rangle$ is the electron-vacuum and $u_{\mathbf{k}}$ and $v_{\mathbf{k}}$ are some variational parameters. This choice of variational wave-function has a nice interpretation, it describes a state where a pair, $(\mathbf{k}, \uparrow)(-\mathbf{k}, \downarrow)$, is occupied with electrons ($v_{\mathbf{k}} = 1, u_{\mathbf{k}} = 0$) or unoccupied ($v_{\mathbf{k}} = 0, u_{\mathbf{k}} = 1$). A good choice of the variational parameters reproduces again the Fermi-sphere:

$$u_{\mathbf{k}} = 0 \quad \text{and} \quad v_{\mathbf{k}} = 1 \quad \text{for} \quad |\mathbf{k}| < k_F\tag{1.4}$$

$$u_{\mathbf{k}} = 1 \quad \text{and} \quad v_{\mathbf{k}} = 0 \quad \text{for} \quad |\mathbf{k}| > k_F\tag{1.5}$$

But BCS found that another choice of the variational parameters exist, describing the superconducting ground state, which results in a lower energy

³(i) The majority of the electrons cannot participate in SC because they sit too deep into the Fermi sphere ($\epsilon_F \approx 1\text{eV}$), as such they cannot exchange a typical phonon-energy ($\hbar\omega_D \approx 10^{-3}\epsilon_F$). Only electrons in a shell of thickness $\hbar\omega_D$ can participate. (ii) From Eq.1.1 we know $|\epsilon_k - \epsilon_{k'}| \ll \hbar\omega_D$ has to be small, and it is best to minimize the total impulse to have a total momentum of zero for the Cooper pair, this can be obtained by taking $\mathbf{k}' = -\mathbf{k}$. (iii) The exchange interaction will decrease the interaction strength between electrons with the same spin. Electrons with opposite spin will interact more strongly, they provide the strongest ‘glue’.

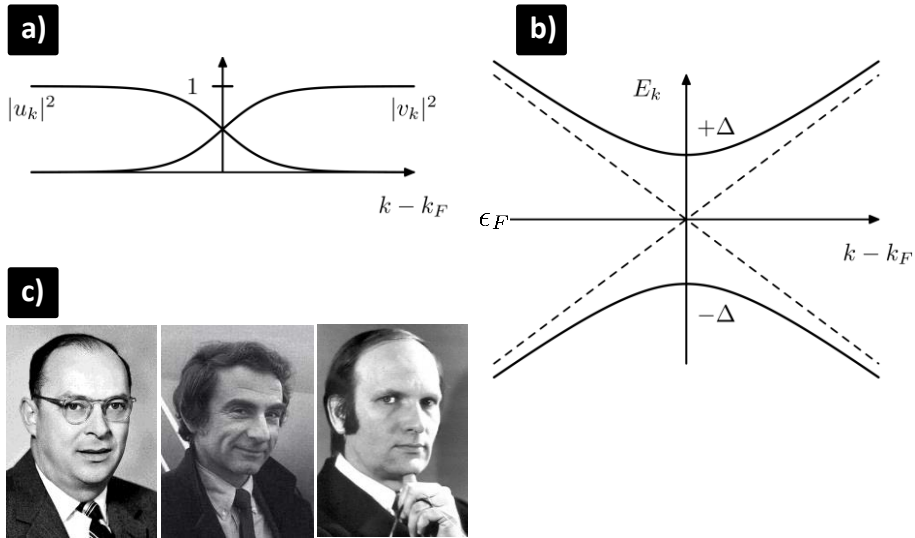


Figure 1.3: (a) The BCS wave-function parameters near the Fermi surface. Well below and above k_F they approach the parameters of the normal metallic state. Whereas near k_F pairing arises. (b) Dispersion relation of the elementary excitation spectrum, showing the energy eigenvalues around the Fermi wave-vector k_F . The dashed lines show the excitation spectrum of the normal metallic state relative to the Fermi-energy, ϵ_F , which are just the electron and-hole energy levels $\epsilon_k - \epsilon_F$ and $-\epsilon_k + \epsilon_F$, respectively. In the superconducting state they become hybridized, resulting in the BCS excitation spectrum $\pm E_k = \pm \sqrt{(\epsilon_k - \epsilon_F)^2 + \Delta^2}$. One can see that there are no single quasiparticle states with energy less than Δ near the Fermi energy. (c) From left to right the names behind the three-letter acronym BCS: John Bardeen Madison (Wisconsin, 23 May 1908 -Boston, 30 January 1991), Leon N Cooper (New York, 28 February 1930), John Robert Schrieffer (Illinois, 31 May 1931)[Pictures taken from Wikipedia]

than the filled Fermi sphere, see Fig.1.3(a). It is clear in Fig.1.3(a) that in the neighbourhood of the Fermi surface the values for $(v_{\mathbf{k}}, u_{\mathbf{k}})$ deviate from Eq.1.4 and are smeared out. In contrast to the Fermi sphere there is a region where $v_{\mathbf{k}}u_{\mathbf{k}} \neq 0$. The BCS ground-state at $T=0\text{K}$ is no longer the filled Fermi-sphere but contains electrons with an energy $E_F - \hbar\omega_D$, which do not participate in the conduction process and a set of Cooper pairs. The Cooper pairs behave as bosons, will Bose-condensate and participate in the conductivity process. At zero temperature the energy difference between the filled Fermi sphere and the BCS ground state is $E_{BCS} - E_N \approx -\frac{1}{2}N(0)\Delta^2$, where $N(0)$ is the density of

states at the Fermi-level and $\Delta = 2\hbar\omega_D e^{-1/\tilde{V}N(0)}$ plays the role of an energy gap or excitation energy⁴. By calculating the elementary excitation spectrum, as shown in Fig.1.3(b), BCS were able to show that 2Δ can be interpreted as the minimum excitation energy, or energy gap to create a broken pair state. In a normal metal an electron with energy $E > E_F$ will lose a small amount of energy during each collision. In a SC it is impossible to lose a small amount of energy in subsequent collisions. It will cost at least a finite amount of energy, $2\Delta = 3.52k_B T_c$ to create an excitation which corresponds with the energy necessary to break up a Cooper-pair. This explains the origin of the zero resistivity property⁵.

The BCS-theory is a very successful theory and was able to explain a whole set of experimental features. Before 1987, it was expected and accepted from BCS-theory that superconductivity was a phenomenon occurring in metals and alloys and that the critical temperature could not surpass 30K. However, in 1987, J.G. Bednorz and K.A Müller discovered a layered material which became superconducting around 40K[17] and later on Chu with co-authors found superconductivity in a Y-Ba-Cu-O compound with $T_c \approx 90K$ [18]. From that moment on, superconductivity could be investigated and commercially used at temperatures above the boiling temperature of liquid nitrogen (77K). However, the unique properties and the microscopic pairing mechanism of these so called high- T_c superconductors can not be explained within the BCS-theory. In 2001, the scientific community was taken by surprise again as MgB_2 showed a superconducting transition at 39K, much higher than any other binary compound[19]. This high critical temperature results from the existence of two coupled condensates in the electronic bands of MgB_2 . Moreover, the interplay between these two condensates results in exotic magnetic behavior such as Type-1.5 superconductivity[20], non-composite-and fractional vortices[21], etc. Even more recently, yet another new class of layer superconductors was discovered, the ferropnictides, with critical temperatures ranging up to 56K[22]. The observation of a superconducting transition in these compounds containing the element Iron was a big surprise as it was long thought that magnetic elements have disastrous effects on the nucleation of superconductivity. It is clear that even after more than 100 years since the discovery, superconductivity is still a very dynamic research area where the hunt for a microscopic theory, that

⁴We assumed for the expression of Δ that $N(0)\tilde{V} \ll 1$. From the expression for Δ one can see that the typical energy scale for superconductivity, $\Delta(0) \approx 1K$, is very much less than the Debye energy $\hbar\omega_D \approx 100 - 300K$. This is why the critical temperature is typically low for conventional superconductors which can be described within the BCS theory.

⁵The existence of a condensate is not a sufficient condition for superfluidity to occur. Whether a system having a condensate is also superfluid depends on the nature of the excited states. This particular point is summarized by an elegant criterium for superfluidity proposed by Landau in 1941[16].

explains the mechanism for SC in these unconventional superconductors and a first room-temperature superconductor, is still open.

In the next sections we will describe two phenomenological theories historically preceding the BCS theory of superconductivity, the Ginzburg-Landau theory (1950)[23] and the London theory (1935)[24]. Although these two theories do not explain the microscopic mechanism of superconductivity, they do have the ability, within restricted limits, to predict different superconducting equilibrium properties in a simpler framework than the BCS theory. The Ginzburg-Landau theory embodies the macroscopic quantum mechanical nature of the superconducting state, where the overall free energy is important instead of the detailed spectrum of excitations. It is crucial for understanding the unique electrodynamic properties of a superconductor and deals elegantly with any spatial inhomogeneity of the density of superconducting electrons, n_s , where the fully microscopic theory becomes difficult. The Ginzburg-Landau theory is reduced to the London theory when n_s equals the equilibrium constant value everywhere, which is an interesting limit in many cases. In a last section we will turn our attention to the non-equilibrium properties of superconductors.

1.2 The Ginzburg-Landau theory

The superconducting state and the normal metallic state are two separate thermodynamic phases of matter just the same way gas, liquid and solid are different phases. Similarly, the normal Bose gas and Bose-Einstein Condensate(BEC), or normal He^4 and superfluid He-II are separated by a thermodynamic phase transition. This suggests that the phenomenon of superconductivity can be examined from the point of view of the thermodynamics of phase transitions.

The theory of superconductivity introduced by Ginzburg and Landau in 1950 describes the superconducting phase transition from this thermodynamic point of view[23]. It was originally introduced as a phenomenological theory, but later Gor'kov showed that it can be derived from the microscopic BCS theory close to the critical temperature[25]. Landau had noticed that typically second-order phase transitions, involve some discontinuous change in the symmetry of the system at the transition, meaning it is a phase transition of the type 'disorder-order'[26]. The low-temperature phase is the one of reduced symmetry, i.e., more ordered. In Landau's theory such phase transitions are characterized by an order parameter which is zero in the disordered state above T_c , but becomes nonzero below T_c . For example, a magnet above the Curie temperature, T_c , has no magnetic moment. But below T_c neighbouring spins align and a spontaneous

magnetic moment develops. In the case of a magnet the magnetization vector, $\mathbf{M}(\mathbf{r})$, is a suitable order parameter.

For superconductivity Ginzburg and Landau (GL) postulated the existence of a complex spatially varying order parameter denoted by $\psi(\mathbf{r})$, thinking of it as a macroscopic wave function for the superconductor. In fact, we can even identify:

$$|\psi(\mathbf{r})|^2 = \frac{n_S(\mathbf{r})}{2}, \quad (1.6)$$

as the density of ‘Cooper pairs’ present in the sample, with n_s the density of electrons belonging to these Cooper pairs. This complex order parameter characterizes the superconducting state completely, in the same way as the magnetization vector does in a ferromagnetic material.

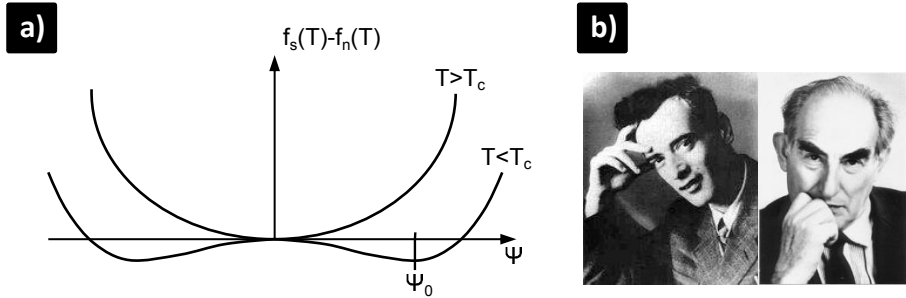


Figure 1.4: (a) Free energy difference between the normal and superconducting states (per unit volume) as a function of the order parameter. For $T < T_c$ the free energy has a minimum at $|\psi_0| \neq 0$, while for $T > T_c$ the only minimum is at $|\psi| = 0$. (b) (Left) Lev Davidovich Landau (Baku, January 22, 1908-Moscow, April 1, 1968 (Right) Vitali Lazarevitsj Ginzburg (Moscow, October 4, 1916 - Aldaar, November 8, 2009)[Pictures taken from Wikipedia]

Ginzburg and Landau derived two coupled partial differential equations which describe the macroscopic behavior of superconductors. These two GL equations are obtained by minimizing an expression for the total free energy, proposed by Ginzburg and Landau, with respect to the order parameter and the vector-potential. They argued that close to T_c and in absence of an external magnetic field or an applied current, the order parameter is small and the free energy can be expanded in powers of the order parameter as [1, 2]:

$$f_s(T) = f_n(T) + \alpha|\psi|^2 + \frac{\beta}{2}|\psi|^4 + \dots \quad (1.7)$$

$f_s(T)$ and $f_n(T)$ are the superconducting state and normal state free energy densities, respectively and $\alpha(T)$ and $\beta(T)$ are phenomenological parameters, characteristic for the material and in general smooth functions of temperature. We must assume that $\beta(T)$ is positive, otherwise the free energy would not have a minimum which is nonphysical. When we evaluate $f_s(T) - f_n(T)$ versus ψ , it is easy to see that there are two possible curves, depending on the sign of $\alpha(T)$, see Fig.1.4(a). Note that when $\alpha(T) > 0$, the curve has a minimum at $\psi = 0$ and we obtain the normal state free energy density $f_s = f_n$. However, when $\alpha(T) < 0$, there are minima wherever $|\psi|^2 = -\alpha(T)/\beta(T) \equiv |\psi_0|^2$, corresponding with the superconducting state and a lower free energy density compared to the normal state:

$$(f_s(T) - f_n(T))_{H=0} = -\frac{\alpha(T)^2}{2\beta(T)} = -\mu_0 \frac{H_c^2}{2} \quad (1.8)$$

This free energy difference (per unit volume) between the superconducting and normal phase at temperature T in zero external magnetic field, is equal to the so called condensation energy of the superconductor and defines the bulk thermodynamical critical field H_c . The bulk thermodynamical field, is the field where the gain in condensation energy per unit volume is equal to the loss in energy for expelling the magnetic field. Ginzburg assumed that above T_c , $\alpha(T)$ is positive, meaning we are in the normal state, and that $\alpha(T)$ changes sign at $T = T_c$ corresponding with the normal to superconducting state transition. Near T_c , one can Taylor expand the expansion coefficients $\alpha(T)$ and $\beta(T)$:

$$\begin{aligned} \alpha(T) &\approx \frac{d\alpha}{dT} \times (T - T_c) + \dots \\ \beta(T) &\approx b + \dots \end{aligned} \quad (1.9)$$

The complete GL theory also allows for spatial variations in the order parameter and takes into account the effect of an applied magnetic field. The new free energy functional reads:

$$\begin{aligned} F_s(T) = F_n(T) &+ \int \left(\frac{\hbar^2}{2m^*} |(\nabla_{\mathbf{r}} - \frac{iq}{\hbar} \mathbf{A}(\mathbf{r}))\psi(\mathbf{r})|^2 + \alpha |\psi(\mathbf{r})|^2 + \frac{\beta}{2} |\psi(\mathbf{r})|^4 \right) d^3r \\ &+ \int \frac{\mathbf{B}^2(\mathbf{r})}{2\mu_0} d^3r, \end{aligned} \quad (1.10)$$

The first integral is carried out over points \mathbf{r} inside the sample, while the second is performed over all space. Here $F_s(T)$ and $F_n(T)$ are the superconducting state and normal state free energies, respectively. Further, m^* and q are the effective mass and charge of the Cooper pairs, respectively. With $q = -2e$,

and $e > 0$ the charge of one electron, \hbar the reduced Planck's constant, μ_0 the magnetic permeability and \mathbf{A} the magnetic vector-potential. The first term in the first integral, represents a combination of the kinetic energy density of the superconducting electrons and an extra term depending on the gradient of $\psi(\mathbf{r})$ and is basically the same term showing up in the Schrödinger equation for a charged particle in a magnetic field. The last integral includes an additional term, corresponding to the energy of the magnetic field. We find after minimizing the free energy with respect to $\psi(\mathbf{r})$ and \mathbf{A} , the two GL equations:

$$-\frac{\hbar^2}{2m^*}(\nabla_{\mathbf{r}} - \frac{iq}{\hbar}\mathbf{A}(\mathbf{r}))^2\psi(\mathbf{r}) + \beta |\psi(\mathbf{r})|^2 \psi(\mathbf{r}) = -\alpha\psi(\mathbf{r}), \quad (1.11)$$

$$\mathbf{j}_s = \frac{q\hbar i}{2m^*}(\psi(\mathbf{r})^*\nabla_{\mathbf{r}}\psi(\mathbf{r}) - \psi(\mathbf{r})\nabla_{\mathbf{r}}\psi(\mathbf{r})^*) - \frac{q^2}{m^*}|\psi(\mathbf{r})|^2\mathbf{A}(\mathbf{r}), \quad (1.12)$$

Finally the vector potential must be obtained from the magnetic field arising from both the super-currents and any other currents, such as the external currents, \mathbf{j}_{ext} ,

$$\nabla_{\mathbf{r}} \times \mathbf{B} = \nabla_{\mathbf{r}} \times (\nabla_{\mathbf{r}} \times \mathbf{A}(\mathbf{r})) = \mu_0(\mathbf{j}_s + \mathbf{j}_{\text{ext}}), \quad (1.13)$$

as given by Maxwell's equations.

The first GL equation, Eq.1.11, has the form similar to that of a Schrödinger equation, for a particle with mass m^* , charge q and energy $-\alpha$, apart from the nonlinear term which acts as a repulsive potential of ψ on itself, favoring wave-functions which are spread out as uniformly as possible in space. As such α can be interpreted as the binding-energy of a Cooper-pair and the first GL equation represents an effective Schrödinger equation for the condensate wavefunction. We can rewrite the second GL equation, by introducing the phase $\vartheta(\mathbf{r})$ of the order parameter $\psi(\mathbf{r}) = |\psi(\mathbf{r})| \exp i\vartheta(\mathbf{r})$, as:

$$\mathbf{j}_s = -\frac{q\hbar}{m^*}|\psi(\mathbf{r})|^2\nabla_{\mathbf{r}}\vartheta(\mathbf{r}) - \frac{q^2}{m^*}|\psi(\mathbf{r})|^2\mathbf{A}(\mathbf{r}), \quad (1.14)$$

$$= -q|\psi(\mathbf{r})|^2\mathbf{v}_s, \quad (1.15)$$

with $\mathbf{v}_s = \frac{1}{m^*}(\hbar\nabla_{\mathbf{r}}\vartheta(\mathbf{r}) + q\mathbf{A}(\mathbf{r}))$. The superfluid velocity, \mathbf{v}_s , has two contributions. The first contribution is due to the gradient of the phase, if the order parameter has a 'twist', it corresponds to a supercurrent. The second contribution is due to electromagnetic expulsion, and shows a proportionality between the supercurrent density and the vectorpotential. This is the so called phenomenological London equation, which explains the Meissner effect and to which the GL equations reduce if one considers no spatial variations in the density of Cooper pairs and $|\psi|^2 = -\alpha(T)/\beta(T) \equiv |\psi_0|^2$.

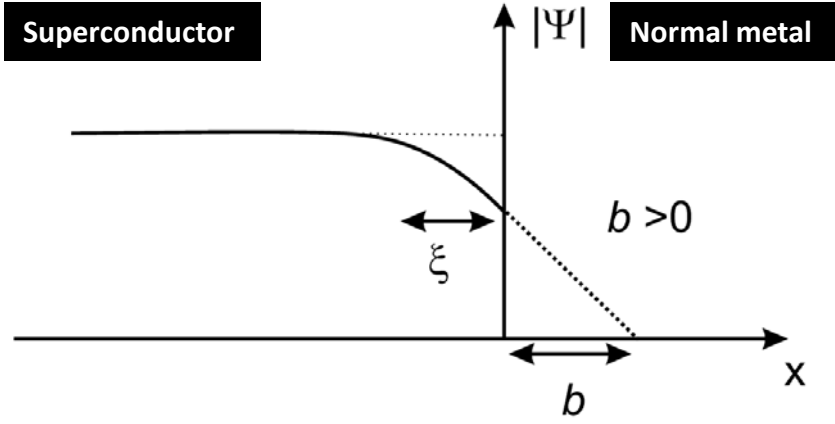


Figure 1.5: Illustration of the boundary condition proposed by de Gennes, showing the spatial variation of the order parameter at a superconducting interface. The value b is dependent on the nature of the material at $x > 0$ and equal to the distance between the boundary and the point where $\psi(\mathbf{r}) = 0$ if $\mathbf{A} \cdot \mathbf{n} = 0$, where \mathbf{n} is the unit vector normal to the surface of the superconductor. For magnetic materials, $b \rightarrow 0$ and for insulators, $b \rightarrow \infty$. For a superconductor-metal interface, b has an intermediate finite value.

As the GL equations are a set of coupled non-linear differential equations, one should provide them with the appropriate boundary conditions. In general, de Gennes derived from the microscopic theory that the appropriate boundary condition at the interface of a superconductor is given by[2]:

$$\mathbf{n} \cdot (-i\hbar\nabla_{\mathbf{r}} + q\mathbf{A}(\mathbf{r}))\psi(\mathbf{r}) = \frac{i\hbar}{b}\psi(\mathbf{r}), \quad (1.16)$$

where \mathbf{n} is the unit vector normal to the surface of the superconductor and the value b is material dependent and equal to the distance between the boundary and the point where $\psi(\mathbf{r}) = 0$ if $\mathbf{A} \cdot \mathbf{n} = 0$, as illustrated in Fig.1.5. For magnetic materials, $b \rightarrow 0$ and for insulators, $b \rightarrow \infty$. For a superconductor-metal interface, b has an intermediate finite value, accounting for the proximity effect⁶. For insulators this boundary condition expresses that no supercurrent crosses the superconductor-insulator interface.

⁶For a superconducting-normal metal interface, the Cooper pairs can penetrate from the superconductor into the metal and ‘live’ there for some time, however this penetration results

1.3 The characteristic length scales

The GL equations have to be solved in most cases numerically, but for certain easy cases, analytical solutions exist. We will consider an easy system of a superconductor occupying the $x > 0$ half space and a normal metal occupying the $x < 0$ half space and introduce in a natural way the fundamental length scales characterizing this superconducting-normal metal interface.

First consider the case where no external field is applied, in this case the GL equations decouple. On the normal side of the interface $x < 0$, the superconducting order parameter should be zero within a distance b from the interface, Eq.1.16. We assume the order parameter is continuous across the interface and the first GL equations, reduces to:

$$-\frac{\hbar^2}{2m^*} \frac{\partial^2 \psi(x)}{\partial x^2} + \alpha \psi(x) + \beta \psi^3(x) = 0, \quad (1.17)$$

which we have to solve in the region $x > 0$ with the boundary condition $\psi(0) = C < \psi_0$. It turns out one can solve this equation analytically:

$$\psi(x) = \psi_0 \tanh\left(\frac{x+x_0}{\sqrt{2}\xi(T)}\right), \quad \text{with } \xi(T) = \sqrt{\frac{\hbar^2}{2m^*|\alpha(T)|}}, \quad (1.18)$$

and x_0 is chosen so that,

$$\psi(0) = C = \psi_0 \tanh\left(\frac{x_0}{\sqrt{2}\xi(T)}\right) \quad (1.19)$$

The length scale $\xi(T)$, the coherence length or healing length of the condensate, represents the smallest distance over which we can bend the condensate. Or the length scale over which the condensate heals from a disturbance like an interface, see Fig.1.6(top). If we keep in mind that the GL parameter α corresponds with the binding-energy of the Cooper pairs, we see⁷ that the coherence length ξ at $T = 0$ is a typical length scale for the Cooper pairs. The temperature dependence of $\xi(T)$ is related to the microscopic BCS coherence

in a reduced Cooper pair density in the superconductor near the interface. This phenomenon is called the proximity effect.

⁷You can see this easily because Eq.1.18. is nothing else than an expression for the energy of a particle in a box of size ξ at $T = 0$.

length ξ_0 , as:

$$\begin{aligned}\xi(T) &= 0.74 \frac{\xi_0}{\sqrt{1 - T/T_{c0}}} & (\xi_0 \ll \ell, \text{ clean limit}), \\ \xi(T) &= 0.855 \sqrt{\frac{\xi_0 \ell}{1 - T/T_{c0}}}, & (\xi_0 \gg \ell, \text{ dirty limit})\end{aligned}\tag{1.20}$$

and depends on the degree of purity, determined by the ratio of the mean free path ℓ and the coherence length. In Eq.1.20, T_{c0} denotes the critical temperature at zero field. We see that only in the limit of $T \rightarrow 0$, the coherence length coincides more or less with the BCS coherence length which is a measure of the spatial extend of a Cooper pair. And that if $T \rightarrow T_{c0}$, the coherence length goes to infinity, which means we can bend the condensate over much larger distances if the temperature increases towards T_{c0} , or in other words the condensate will heal much slower.

Next, we consider the case where a homogeneous external magnetic field, B_0 , is present in the z-direction, parallel to the surface of a superconductor occupying the half-space $x > 0$. Let us assume the field is sufficiently small, meaning we neglect in the first approximation any depletion of the condensate due to a kinetic suppression of the density of states to calculate the field variation. As such, the second GL equation reduces to the so called London equation, where we assume the density of Cooper pairs is constant, and is equal to the bulk equilibrium value, $\psi = \sqrt{|\psi_0|^2} = -\alpha(T)/\beta(T)$. The second GL equations becomes, together with Ampère's law:

$$\nabla \times (\nabla \times \mathbf{B}) = -\frac{1}{\lambda_L^2} \mathbf{B}, \quad \text{with } \lambda_L(T) = \sqrt{\frac{m^*}{\mu_0 |\psi_0|^2 q^2}},\tag{1.21}$$

where λ_L denotes the so called London penetration depth. The meaning of λ_L becomes clear if we look at the solution of Eq.1.21,

$$B(x) = B_0 e^{-x/\lambda_L},\tag{1.22}$$

as illustrated in Fig.1.6(top). We see that the magnetic field can penetrate the SC only over a characteristic distance corresponding with the London penetration depth. This explains effectively the Meissner-Ochsenfeld effect. As we assumed to have no depletion of the condensate due to the induced screening currents, the value of λ_L for the characteristic decay of a magnetic field is an underestimate. The first GL equation which describes conservation of energy, takes into account this effect of current induced suppression of the

density of states resulting in a less efficient screening. As such within the GL theory the penetration depth is defined as,

$$\lambda(T) = \sqrt{\frac{m^*}{\mu_0 |\psi|^2 q^2}} \quad (1.23)$$

which exceeds the London penetration depth by the factor $(|\psi_0|^2/|\psi|^2)^{1/2}$. The penetration depth shows the same temperature dependence as the coherence length and again depends on the degree of purity, characterized by the mean free path. An expression for the temperature dependence of λ related to the microscopic BCS theory is:

$$\begin{aligned} \lambda(T) &= 0.71 \frac{\lambda_L(0)}{\sqrt{1 - T/T_{c0}}} & (\xi_0 \ll \ell, \text{ clean limit}), \\ \lambda(T) &= 0.64 \lambda_L(0) \sqrt{\frac{\xi_0}{\ell(1 - T/T_{c0})}} & (\xi_0 \gg \ell, \text{ dirty limit}), \end{aligned} \quad (1.24)$$

1.4 Type-I and type-II superconductors

Let's look now at a situation where the external field is equal to the thermodynamical critical field, defined as in Eq.1.8, and inquire how the field penetrates the SC?

To answer this question we have to calculate the energy cost to make a normal-superconducting(NS) interface. The total energy you have to invest to make an interface per unit area, is roughly⁸:

$$\gamma \approx (\xi - \lambda) \times \left(\frac{\mu H_c^2}{2} \right), \quad (1.25)$$

as illustrated in Fig.1.6. From this estimate we can make a distinction between two types of superconductors.

- When $\xi \gg \lambda$, the domain wall energy, γ , is positive and energy is furnished to make a NS interface. When we apply a small magnetic field

⁸The magnetic field will penetrate in a volume of λA , with A the surface area, resulting in a reduction in the energy to expel the magnetic field of roughly $\lambda A \times \frac{\mu_0 H_c^2}{2}$. The surface, however, destroys superconductivity in the volume ξA , as such you lose some condensation energy of roughly $\xi A \times (f_s - f_n) = \xi A \times \frac{\mu_0 H_c^2}{2}$.

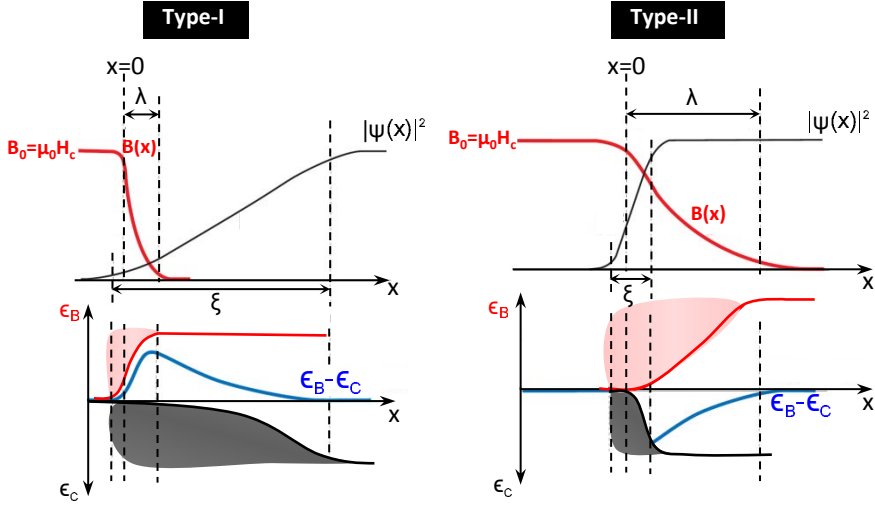


Figure 1.6: (Top) Schematic illustration of the spatial variation of the order parameter (black) and the magnetic field (red) at a normal metal($x < 0$)-superconductor($x > 0$) interface located at $x=0$ if an external field, $B_0 = \mu_0 H_c$, is applied. The variations are shown for a type-I (left) and a type-II (right) superconductor. (Bottom) The corresponding spatial variation of the magnetic field exclusion energy (red, light grey), ϵ_B and the condensation energy (dark grey), ϵ_C together with their difference (blue) in the neighbourhood of a superconducting-insulator interface for both types of superconductors. The red (light grey) shaded area indicates the gain in magnetic field energy at an interface, whereas the dark grey shaded area indicates the lost condensation energy at an interface.

in this case⁹, the SC doesn't favor magnetic flux penetration and the SC is in the Meissner state. When the field exceeds the thermodynamical critical field, H_c , the slab will become normal as a whole. This behavior characterizes a type-I superconductor.

- When $\xi \ll \lambda$, the domain wall energy is negative. The Meissner state will only be stable in this case for fields below the so called lower critical field, $H < H_{c1}$. When an external field is applied between the first and second critical field $H_{c1} < H < H_{c2}$, the superconductor favors the formation of NS interfaces, flux will penetrate in small areas and the SC will try to

⁹Remark: This is only valid for a infinite cylinder. As due to demagnetization effects a different geometry can result in local differences in field at the surface or a strong enhancement of the field at the surface. The first resulting in to the so called intermediate state, the latter can result in a vanishing small critical field value (e.g. thin film geometry).

maximize the surface of these interfaces. The smallest scale these areas can have is limited by the coherence length, because we cannot ‘bend’ the superconducting condensate over a smaller length scale. Flux will penetrate in the form of so called ‘flux tubes’ or ‘vortices’ as shown in Fig.1.9. This behavior is the hallmark of type-II superconductors in the mixed state.

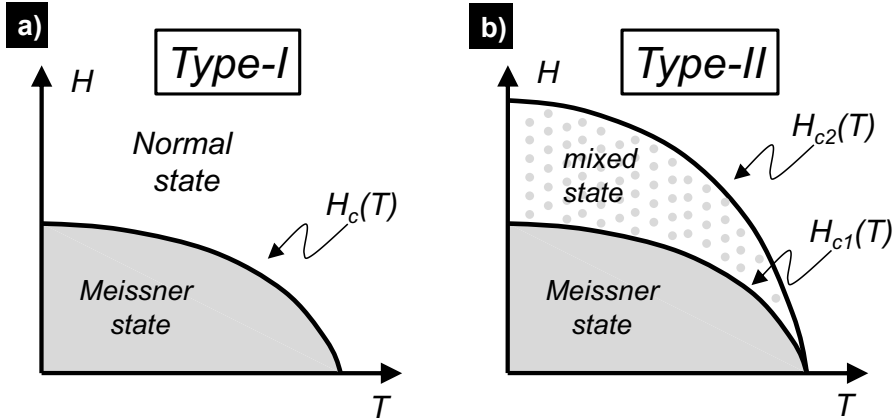


Figure 1.7: The H-T phase diagram for (a) a type-I, and (b) a type-II superconductor.

It is not surprising from the previous considerations, we can make a distinction between these two types of superconductors by using as a criterium the temperature independent ratio, $\kappa = \lambda(T)/\xi(T)$, defining the GL-parameter. It turns out that a material is type-I if $\kappa < 1/\sqrt{2}$ and type-II if $\kappa > 1/\sqrt{2}$. An overview is given in Fig.1.7.

The various critical fields of a type-I and type-II superconductor can be expressed in terms of the characteristic length scales discussed in Sec.1.3. For a bulk superconductor, the thermodynamical critical field is given by:

$$\mu_0 H_c(T) = \frac{\phi_0}{2\sqrt{2}\pi\mu_0\lambda(T)\xi(T)}, \quad (1.26)$$

whereas the first and second critical fields of a type-II bulk superconductor can be written as:

$$\mu_0 H_{c1}(T) = \frac{\ln(\kappa)\phi_0}{4\pi\lambda^2(T)} = \frac{\ln(\kappa)}{\sqrt{2}\kappa}\mu_0 H_c(T), \quad (1.27)$$

and

$$\mu_0 H_{c2}(T) = \frac{\phi_0}{2\pi\xi^2(T)} = \sqrt{2}\kappa\mu_0 H_c(T), \quad (1.28)$$

1.5 The London equations

In this section we consider an interesting limit of the GL equations, historically already proposed in 1935 by F. and H. London[24] as a first attempt to describe the electrodynamic properties of superconductors. The so called ‘London limit’ arises when we neglect any spatial variations of the density of condensed pairs and any possible kinetic induced reduction of the density of states as described by the first GL equation. This is a good approximation when the supercurrent density \mathbf{J}_s and the magnetic field \mathbf{B} are slow varying functions in space, $\kappa \gg 1$ and the currents are insufficient to cause depairing. For latter purposes, we derive the London equation, Eq.1.21, again by minimizing a free energy functional as in the GL theory. However, contrary to the quantum description used in the GL theory, we start here from a classical picture. If we assume that the supercurrent, $\mathbf{j}_s = n_s e \mathbf{v}_s$, flows without dissipation in a superconductor, where n_s is the density of superconducting electrons and \mathbf{v}_s is their velocity. One could argue that this current, being non-dissipative, contributes only to the kinetic energy of the superconducting electrons. The total free energy is given by:

$$F = \int F_s d^3r + \int \left[\frac{n_s m^* \mathbf{v}_s^2}{2} + \frac{\mathbf{B}^2}{2\mu_0} \right] d^3r = \int \left[\frac{m^* \mathbf{j}_s^2}{2n_s e^2} + \frac{\mathbf{B}^2}{2\mu_0} \right] d^3r, \quad (1.29)$$

Where the first term, F_s , is the energy of the electrons in the condensed state at rest and the second integrand contains the sum of both the kinetic energy density and the magnetic field energy density. The integrals being extended over the sample volume. Using Maxwell equations, the total free energy functional is given by:

$$F[\mathbf{B}] = \int F_s d^3r + \int \left[\frac{\lambda_L^2 (\nabla \times \mathbf{B})^2}{2\mu_0} + \frac{\mathbf{B}^2}{2\mu_0} \right] d^3r, \quad (1.30)$$

In equilibrium, the free energy is minimal with respect to the magnetic field distribution. This condition leads to the London equation which describes the spatial variation of the local magnetic induction:

$$\mathbf{B}(\mathbf{r}) + \lambda_L^2 \nabla \times (\nabla \times \mathbf{B}(\mathbf{r})) = 0, \quad (1.31)$$

and explains the Meissner-Ochsenfeld effect, see Sec.1.3.

1.6 The structure of a single vortex and the vortex lattice

The accent in this work lies on the study of the dynamic properties of the flux lines in the mixed state or vortex state of type-II superconductors. In this section and the next we will discuss the structure of these vortices, and their dynamic properties. A single vortex consists of a core region of diameter $\sim 2\xi(T)$, where the density of superconducting electrons is strongly suppressed and $|\psi|^2 = 0$ exactly in the center. Around this core a rotating condensate of paired electrons is flowing in an area of the order $\lambda(T) > \xi(T)$. The local magnetic field, $|\mathbf{B}(\mathbf{r})|$, is maximum at the center of the vortex and decays over the typical length scale $\lambda(T) > \xi(T)$. The radial distribution of the local field $\mathbf{B}(\mathbf{r})$, the absolute value of the supercurrent density $\mathbf{j}(\mathbf{r})$ and the density of Cooper pairs $|\psi(\mathbf{r})|^2$ are schematically shown in Fig.1.8 .

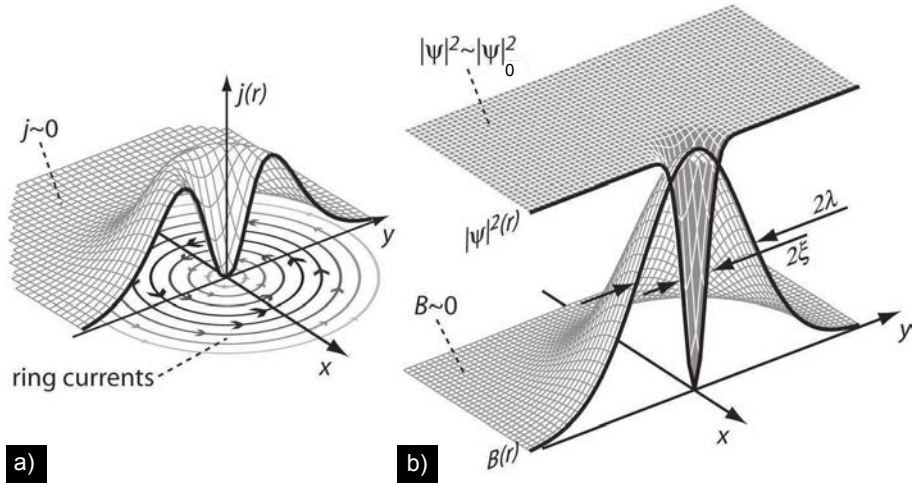


Figure 1.8: **The structure of a vortex.** (a) Schematics of the current distribution $\mathbf{j}(\mathbf{r})$ inside a vortex. (b) The distribution of the order parameter $|\psi(\mathbf{r})|^2$ and the local field $\mathbf{B}(\mathbf{r})$ inside a vortex.[27]

In the case of a strong type-II superconductor, $\kappa \gg 1/\sqrt{2}$, we can make a convenient approximation. Since the density of pairs quickly returns to its maximum value over a distance $\xi(T)$, we can treat all except the core region as if having a constant Cooper pair density. This is exactly the prerequisite to use the London theory, for describing the magnetic fields and currents in a superconductor. In order to deal with the normal core, one generalizes the

London equation to:

$$\mathbf{B}(\mathbf{r}) + \lambda_L^2 \nabla \times \nabla \times \mathbf{B}(\mathbf{r}) = \phi' \delta_2(\mathbf{r}) \mathbf{e}_v \quad (1.32)$$

with \mathbf{e}_v the unit vector along the direction of the applied field and the small core is represented by a two-dimensional delta-function. The spatial field distribution and the current distribution of a vortex can be found analytically by solving Eq.1.32 and combining it with Maxwell equations:

$$B_z(r) = \frac{\phi'}{2\pi\lambda^2} K_0\left(\frac{r}{\lambda}\right) \quad (1.33)$$

with $K_0(x)$ the zeroth-order second-kind modified Bessel function. Up to now ϕ' is introduced as a constant which signifies the singularity at the vortex center. Therefore, the origin of ϕ' has to be discussed. Integrating Eq.1.32 over the interior surface of a circle of radius r and using Stokes's theorem, we have

$$\oint \mathbf{B}(\mathbf{r}) \cdot d\mathbf{S} + \lambda_L^2 \oint \nabla \times \mathbf{B}(\mathbf{r}) \cdot d\mathbf{l} = \phi' \quad (1.34)$$

If we take a circle with $r \gg \lambda_L$, the second term can be neglected and it is clear ϕ' represents the total magnetic flux carried by the vortex. The fact that a superconducting state is a macroscopic quantum effect, characterized by a macroscopic complex wave-function $\psi(\mathbf{r})$, has some interesting consequences for the total flux carried by a vortex. As $\psi(\mathbf{r}) = |\psi(\mathbf{r})| \exp i\vartheta(\mathbf{r})$ has to be single-valued, the value of the phase has to return upon itself when encircling a closed contour. When we integrate the superfluid velocity, Eq.1.14, along a closed path,

$$\oint m^* \mathbf{v}_s \cdot d\mathbf{l} = \hbar \oint \nabla \vartheta(\mathbf{r}) \cdot d\mathbf{l} - q \oint \mathbf{A}(\mathbf{r}) \cdot d\mathbf{l} \quad (1.35)$$

we obtain, using $\Delta\vartheta = 2\pi n$, $n \in \mathbb{Z}$,

$$\frac{-nh}{q} = n\phi_0 = \phi - \frac{1}{q} \oint m^* \mathbf{v}_s \cdot d\mathbf{l} \quad (1.36)$$

with $q = -2e$, the elemental flux quantum is given by

$$\phi_0 = \frac{h}{2e} = 2.067 \text{mT}\mu\text{m}^2 \quad (1.37)$$

As such if a contour is chosen sufficiently far away from the vortex core, so $|\mathbf{v}_s| = 0$, the second term in Eq.1.36 vanishes and the total flux carried by the vortex is an integer multiple of the flux quantum, $\phi' = n\phi_0$.

Let us discuss further Eq.1.33, the divergence at $\mathbf{r} = 0$ is not physical, and is

cut off by the finite coherence length of the superconductor ξ . The asymptotic expressions are:

$$B_z(r) = \frac{\phi'}{2\pi\lambda^2} \ln\left(\frac{\lambda}{r}\right) \quad \xi < r \ll \lambda \quad (1.38)$$

$$B_z(r) = \frac{\phi'}{2\pi\lambda^2} \sqrt{\frac{\pi\lambda}{2r}} \exp\left(-\frac{r}{\lambda}\right) \quad r \gg \lambda \quad (1.39)$$

From this radial dependence of the local field one can calculate the current distribution of a single vortex:

$$j(r) = \frac{\phi'}{2\pi\mu_0\lambda^2} K_1\left(\frac{r}{\lambda}\right) \quad (1.40)$$

where $K_1(x)$ is the first-order modified Bessel function. The asymptotic expressions are:

$$j(r) = \frac{\phi'}{2\pi\mu_0\lambda^2} \quad \xi < r \ll \lambda \quad (1.41)$$

$$j(r) = \frac{\phi'}{2\pi\mu_0\lambda^2} \sqrt{\frac{\pi\lambda}{2r}} \exp\left(-\frac{r}{\lambda}\right) \quad r \gg \lambda \quad (1.42)$$

It is instructive to calculate the energy of a vortex per unit length, which is a combination of the magnetic field energy and the kinetic energy of the rotating super-currents. If one substitutes for the field distribution, Eq.1.33, in the London expression for the free energy, Eq.1.30, one obtains:

$$\varepsilon_v = \frac{\phi'^2}{4\pi\mu_0\lambda^2} \ln\left(\frac{\lambda}{\xi} + \epsilon\right) \quad (1.43)$$

where $\epsilon \approx 0.12$ is an extra numerical constant introduced to describe a small contribution due to the loss of condensation energy in the normal core. The line energy of a vortex ε_v is a quadratic function of ϕ' , therefore it is energetically unfavorable in homogeneous superconductors to form multi-quanta vortices carrying more than one flux quantum. However, we ignored in this consideration the vortex-vortex interaction. Although the total line energy of a lattice consisting of $n\phi_0$ -vortices is higher than a lattice of single ϕ_0 -vortices, $\varepsilon_v(n\phi_0) > n\varepsilon_v(\phi_0)$, the vortex-vortex (VV) interaction energy will be reduced if $n\phi_0$ vortices are formed since the distance between them increases. As such under the good conditions, for example in samples with antidots, multi-quanta vortex lattices can have a lower energy than a single quantum vortex lattice.

Now that we described the structure of an isolated vortex let's discuss their mutual interaction. The interaction energy per unit length between two parallel

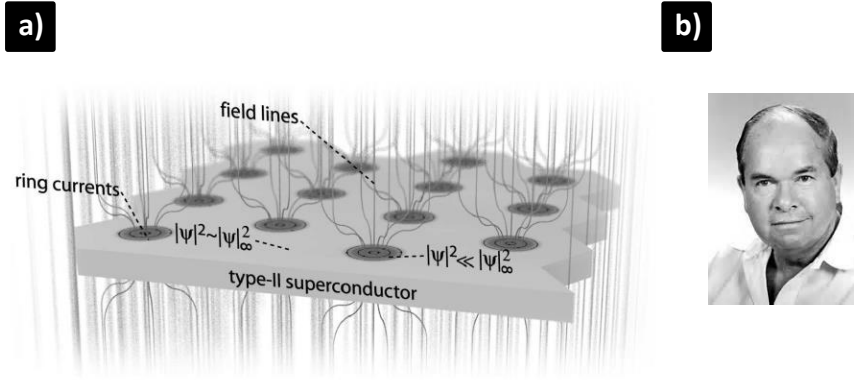


Figure 1.9: (a) Artwork of the mixed state or the Abrikosov vortex state in a type-II superconductor[27]. (b) Alexei Alexeyevich Abrikosov[Picture taken from Wikipedia]

single quantized vortices at position \mathbf{r}_i and \mathbf{r}_j , is given by:

$$U_{ij}(|\mathbf{r}_{ij}|) = \frac{\phi_0^2}{2\pi\mu_0\lambda^2} K_0\left(\frac{|\mathbf{r}_{ij}|}{\lambda}\right) \quad (1.44)$$

where $|\mathbf{r}_{ij}| = |\mathbf{r}_i - \mathbf{r}_j|$ is the mutual distance between vortex ‘i’ and ‘j’. The interaction energy per unit length in bulk is repulsive since it decreases with increasing VV-distance, $|\mathbf{r}_{ij}|$ and is very weak when the vortices are far apart. The forces between vortices in bulk are short-range with the penetration depth, a measure of the range. As such they must be sufficiently close together, compared to λ , for their interaction to be appreciable. The asymptotic expressions are:

$$U_{ij}(|\mathbf{r}_{ij}|) = \frac{\phi_0^2}{2\pi\mu_0\lambda^2} \ln\left(\frac{\lambda}{|\mathbf{r}_{ij}|}\right) \quad \xi < |\mathbf{r}_{ij}| \ll \lambda \quad (1.45)$$

$$U_{ij}(|\mathbf{r}_{ij}|) = \frac{\phi_0^2}{2\pi\mu_0\lambda^2} \sqrt{\frac{\pi\lambda}{2|\mathbf{r}_{ij}|}} \exp\left(-\frac{|\mathbf{r}_{ij}|}{\lambda}\right) \quad |\mathbf{r}_{ij}| \gg \lambda \quad (1.46)$$

This repulsive interaction between flux lines of the same polarity gives rise to a regular arrangement of vortices and the formation of a flux line lattice, the so called ‘Abrikosov vortex lattice’, see Fig.1.9(a). Taking into account the repulsion of the vortices, it is reasonable that the vortex configuration maximizing the nearest neighbour distance will be favored. It has indeed

been shown that a triangular array is the energetically most favorable vortex configuration, with the nearest neighbour distance, a_v given by:

$$a_v = \sqrt{\frac{2\phi_0}{\sqrt{3}B}} \quad (1.47)$$

However the energy difference with a square flux line lattice is small. We considered here the ideal case of a perfect homogeneous superconductor. As we will see in Sec.1.8 defects in the material, whether intrinsically present or deliberately introduced by nano-structuring, may introduce sufficient inhomogeneity to destroy the regular vortex arrangement entirely. Certainly at low vortex densities where the VV-interaction energy favoring triangular order is small, these defects or so called pinning centers can destroy or modify the lattice arrangement dramatically.

1.7 Superconducting thin films in a perpendicular magnetic field.

Thin superconducting film geometries, meaning $d \ll \lambda(T)$, play an important role in a variety of applications and are of fundamental interest. The ease to produce and structure high quality thin films with standard lithographic techniques at the nanometer scale and the behavior of the vortices as essentially 2D objects makes these films interesting systems to isolate and study superconducting properties. The small film thickness has important consequences on the superconducting properties[28, 29], to list a few:

- The screening current density is essentially uniform over the thickness of the film. Vortices can not bend and the vortex lattice can be considered as two dimensional.
- As the superconducting screening currents are limited by the thickness of the film. This results in a larger effective penetration depth,

$$\Lambda(T) \approx \lambda(T)^2/d, \quad (1.48)$$

In this work we deal mostly with type-II superconductors, as often a thin film geometry is used, resulting in a higher effective penetration depth, and part due to the high level of impurities.

- As such, the field around a single vortex in a thin film is less effectively screened at large distances. Instead of the exponential screening at large

distances for bulk vortices, the field falls off only as r^{-3} for a vortex in a thin film.

$$B_z(r) = \frac{\phi_0}{4\pi\Lambda(T)r} \quad \xi < r \ll \Lambda \quad (1.49)$$

$$B_z(r) = \frac{2\phi_0\Lambda(T)}{\pi r^3} \quad r \gg \Lambda \quad (1.50)$$

And the associated supercurrent distribution around the vortex core is given by:

$$j(r) = \frac{\phi_0}{2\pi\Lambda(T)r} \quad \xi < r \ll \Lambda \quad (1.51)$$

$$j(r) = \frac{\phi_0}{\pi r^2} \quad r \gg \Lambda \quad (1.52)$$

- Important is that due to the thin film geometry, the repulsive energy between two vortices decreases as r^{-1} , similar to a Coulomb repulsion between two electric charges. Vortices in a thin film interact primarily through their fields in the free space adjacent to the film, where no screening current can flow resulting in a long-range interaction.
- Due to demagnetizing effects the local magnetic field at the surface cannot be considered anymore to be uniform over the surface and equal to the applied magnetic field. This can have profound consequences for the superconducting properties, such as the appearance of the intermediate state in type-I superconductors, the drastic reduction of the critical fields in thin film geometries, etc.

1.8 Non-equilibrium properties of superconductors

Up till now, we only considered the equilibrium properties of superconductors. In this section, we focus on the non-equilibrium properties of type-II superconductors in the mixed state, in particular we describe the response to an electromagnetic field excitation. As we will see, just as the dynamical properties of electrons determine the electromagnetic properties of a metal. The dynamical properties of the vortices together with the response of the screening currents completely define the electromagnetic response of a type-II superconductor in the mixed state.

1.8.1 Electromagnetic properties of an Ohmic material

The penetration and propagation of electromagnetic waves in conducting media and the detailed response has been an intensive line of theoretical and experimental research. The interest extends from a classic topic such as the skin effect in normal conductors towards the ac response of superconductors and further towards the novel communities of plasmonics and meta-materials. In general an alternating electromagnetic field induces screening currents in a conductor (normal or superconducting), which will reduce the strength of the field inside the conductor (cf. Lenz' Law). The efficiency of screening is determined by the conductivity, $\sigma(\omega)$ and the rate of change of the electromagnetic field. To quantitatively describe screening phenomena, we consider propagation of an ac-magnetic field wave¹⁰ as described by the classical wave propagation equation in an Ohmic medium[30],

$$\nabla^2 \mathbf{B}(\mathbf{r}) = \mu\sigma \frac{\partial \mathbf{B}(\mathbf{r})}{\partial t} - \mu\varepsilon \frac{\partial^2 \mathbf{B}(\mathbf{r})}{\partial t^2} \quad (1.53)$$

Where $\mathbf{B}(\mathbf{r})$ denotes the magnetic field vector and μ, ε denote the material parameters the magnetic permeability and the electric permittivity, respectively. Both are connected with the speed of the electromagnetic wave in the medium as $v = \sqrt{1/\mu\varepsilon}$. We assume further that the medium can be considered to be linear and isotropic, no free charge is present in the conducting media and the conducting media's response can be described by Ohm's Law,

$$\mathbf{j}(\mathbf{r}, \omega) = \sigma(\omega) \mathbf{E}(\mathbf{r}, \omega), \quad (1.54)$$

Where $\mathbf{E}(\mathbf{r}, \omega)$ is the electric field vector, $\mathbf{j}(\mathbf{r}, \omega)$ the current density and this Ohmic relation effectively defines the conductivity of the media, $\sigma(\omega)$. This equation has plane wave solutions with a complex wave number, as can be checked by substitution,

$$\mathbf{B}(\mathbf{r}, t) = \mathbf{B}_0 \exp^{i(\mathbf{k} \cdot \mathbf{r} - \omega t)} \quad \text{with } \mathbf{k}^2 = \mu\omega^2(\varepsilon + \frac{\sigma i}{\omega}), \quad (1.55)$$

What is the meaning of the complex wave-number? As is clear from,

$$\mathbf{B}(z, t) = \mathbf{B}_0 \exp^{-\Im m(\mathbf{k}) \cdot \mathbf{r}} \exp^{i(\Re e(\mathbf{k}) \cdot \mathbf{r} - \omega t)}, \quad (1.56)$$

the complex part of the wave-number describes the decay of the amplitude of the magnetic wave into the volume of the conductor, the characteristic decay

¹⁰As in this work the main study probes the response to an ac-magnetic field, we will only consider the relevant equation for this case.

length is called the skin depth,

$$\delta = 1/\Im m(|\mathbf{k}|) \quad (1.57)$$

The real part of the wave-number describes the wavelength, $\lambda = 2\pi/\Re e(|\mathbf{k}|)$, the phase velocity, $v = \omega/\Re e(|\mathbf{k}|)$ and the index of refraction, $n = c\Re e(|\mathbf{k}|)/\omega$, in the usual way. Furthermore, the wave equation has to be supplemented with the appropriate boundary conditions, as in general $\mathbf{B}(\mathbf{r})$ is discontinuous at a surface that carries a surface current, these are provided by the Maxwell equations.

$$\varepsilon_1 E_1^\perp - \varepsilon_2 E_2^\perp = \sigma_f, \quad E_1^\parallel - E_2^\parallel = 0 \quad (1.58)$$

$$B_1^\perp - B_2^\perp = 0, \quad \frac{1}{\mu_1} B_1^\parallel - \frac{1}{\mu_2} B_2^\parallel = \vec{K}_f \times \mathbf{n} \quad (1.59)$$

where \mathbf{n} is a unit vector perpendicular to the surface.

Note that in the above description of ac magnetic-wave propagation in a conducting medium, we didn't make any assumption about the origin of the material property 'conductivity'. The considerations mentioned above describe the penetration and propagation in any conducting media which can be described by Ohm's Law. These conducting media satisfying Ohm's law include, under certain conditions, not only normal metals, but also superconductors and plasma's and in general linear response. The material property, 'conductivity', should be distinguished from the actual conductance of the body. The conductance requires also the knowledge of the spatial distribution of the electromagnetic field within the medium. In the following we will describe from the expression of the complex ac conductivity of a superconductor, as derived from microscopic arguments, the consequences for the macroscopic response to an ac-magnetic field. But let us first consider the ac magnetic field penetration in a normal metal.

In the standard Drude model for a normal metal, the material property 'conductivity' is derived from a classical equation of motion for the charge carriers[14], the electrons,

$$\frac{d\mathbf{p}}{dt} = -\frac{\mathbf{p}}{\tau} - e\mathbf{E} \quad (1.60)$$

Here $\mathbf{p} = m\mathbf{v}$ is the average impulse of electrons, \mathbf{v} is called the 'drift' velocity and τ describes a characteristic relaxation time¹¹ related to scattering processes,

¹¹The relaxation time, in principle, describes the average time in between electron scattering processes. The path the electron travels before it is scattered is termed the mean

typically of the order 10^{-14} s to 10^{-15} s at room temperature in normal metals. The competition between a dc driving force, $-e\mathbf{E}$ and the frictional scattering processes leads to a steady state average drift velocity $\mathbf{v} = -e\mathbf{E}\tau/m$. For n conduction electrons per unit volume a net current density results, given by: $\mathbf{J} = -ne\mathbf{v} = \sigma_0\mathbf{E}$, i.e. Ohm's law, where $\sigma_0 = (ne^2\tau/m)$ is the Drude result for the dc conductivity.

When the driving force is an external or induced ac electrical field, $\mathbf{E}(\omega, t) = \Re(\mathbf{E}_0(\omega)e^{i\omega t})$, we can describe the response of a normal metal by the ac-conductivity. This time, using the complex number representation, Ohm's law will look like:

$$\mathbf{J} \exp^{-i\omega t} = \sigma(\omega)\mathbf{E}_0 \exp^{-i\omega t}, \text{ with } \sigma(\omega) = \frac{\sigma_0}{1 - i\omega\tau} \quad (1.61)$$

where $\sigma(\omega)$ is the frequency dependent ac conductivity as derived from the equation of motion and which reduces to σ_0 , the dc Drude result, when $\omega = 0$. It's real part corresponds to currents which are in phase with the applied electrical field (resistive), while the imaginary part corresponds to out-of-phase currents (inductive and capacitive). In deriving the material property 'ac conductivity', using the Drude model, we made some important approximations. First point, in Eq.1.60 we didn't add the additional Lorentz force term $e\frac{\vec{p}}{m} \times \vec{B}$, which is expected as an electromagnetic wave is accompanied by a perpendicular magnetic field component. This term is a factor v/c smaller. As such for the slow drift velocities of electrons in a metal we can safely ignore this term. The second assumption is what we call 'locality'. As the fields in an electromagnetic wave vary in space and time, it is not that straightforward to assume a spatially uniform force in the equation of motion, Eq.1.60. This assumption is ok as long as the wavelength, characterizing the scale of the field variations, is large compared to the mean free path l or $\omega\tau \ll 1$. For typical metals at room temperature, this is still satisfied for visible light, whose wavelength is of the order of 10^3 to 10^4\AA , thousand times the typical electron mean free path and corresponding with frequencies $\omega < 800\text{Thz}$.¹²

In the limit $\omega\tau \gg 1$, the metal behaves as a plasma and the electron's inertia becomes the dominant factor. In this high frequency limit, where the metal behaves as a plasma, the ac conductivity can be rewritten in a first

free path, $l = v\tau$, typically of the order of $l = 10^{-10}\text{m}$ at room temperature, a length scale comparable with the interatomic spacing.

¹²The result of Eq.1.61, i.e. Ohm's law $\mathbf{j}(\mathbf{r}, \omega) = \sigma(\omega)\mathbf{E}(\mathbf{r}, \omega)$, incorporates that the current density at a point is related to the field at the same point, $\mathbf{E}(\mathbf{r}, \omega)$ under the assumption $\omega\tau < 1$. If this is not the case we have to use non-local theories c.f. Chambers's generalization of Ohm's law.

approximation, neglecting the locality assumption, as a pure complex number, $\sigma(\omega) = -\sigma_0/i\omega\tau$. The dispersion relation, Eq.1.55 , becomes:

$$\mathbf{k}^2 = \frac{\omega^2}{v^2} \left(1 - \frac{\omega_p^2}{\omega^2}\right), \text{ with } \omega_p = \frac{ne^2}{m\varepsilon} \quad (1.62)$$

where we introduced the so called plasma frequency ω_p . For frequencies below the plasma frequency, $\omega < \omega_p$, the wave-number is complex. In this case the solutions of the wave equation decay exponentially over a skin depth, δ , and the waves are totally reflected as they cannot penetrate in the plasma. For frequencies above the plasma frequency, $\omega > \omega_p$, the wave-number is real and the solutions become oscillatory, meaning the metal becomes transparent. Moreover, this indicates that a plasma can sustain charge density oscillations known as plasmons. For Pb, the material mainly used in this work, the plasma frequency is in the ultraviolet, $f_p = 1.8 \times 10^{15} \text{Hz}$.

In this work however, we are interested in what we call the low frequency regime, $\omega\tau \ll 1$. This first of all means we can apply Ohm's law, it is the assumption that 'locality' is ok and we assume a pure real resistivity, meaning we neglect the electrons inertia completely. On top of that, we can apply a second approximation, called the 'eddy current approximation', which can be used for a good conductor up till the microwave regime¹³: $\sigma \gg \omega\varepsilon$. We can understand this approximation by looking at the wave equation. The right hand side of Eq.1.53 are essentially the first two terms in an expansion of powers of the field frequency. Since we assume the frequency is 'low', it can be shown that this second term only contributes a small correction. However note that for poor conductors or semiconductors this term can become important at 'low' frequencies. This approximation transforms the wave equation for the magnetic field into a diffusion equation (c.f. heat equation):

$$\nabla^2 \mathbf{B} = \mu\sigma \frac{\partial \mathbf{B}}{\partial t} \quad (1.63)$$

This linear differential equation describes how a magnetic field wave penetrates or diffuses into a conductor for a given boundary condition, with diffusion constant $1/D = \mu\sigma$. The higher the conductivity the lower the diffusion constant, as it is more difficult for a field to penetrate. We obtain for the dispersion relation:

$$\mathbf{k}^2 = \mu\sigma\omega i \quad (1.64)$$

¹³For Pb, the material mainly used in this work, the conductivity is about 10^7S/m , and the condition $\sigma \gg \omega\varepsilon$ is satisfied up to the microwave regime ($< 100 \text{GHz}$).

As such, from Eq.1.57, the skin depth is:

$$\delta = \sqrt{\frac{2}{\mu\sigma\omega}} \quad (1.65)$$

If the skin depth is large compared to the dimensions of the sample, we can assume that the magnetic field distribution is identical to the steady state field. In the opposite limit, when the skin depth is much smaller than the dimensions of the conductor, the field only penetrates into a thin surface layer. In this sense a conductor in a high frequency magnetic field behaves as a superconductor in a constant field. For the frequencies used in this work, the normal skin depth in Pb is $\delta > 5\text{mm}$, much larger than the relevant sample dimensions. For an overview, see Fig.1.11.(a).

1.8.2 Ac magnetic field penetration in a superconductor

In type-II superconductors, the electrodynamic properties are completely determined by the vortex dynamics and the screening currents response. Both contribute to the bulk property, conductivity, of a type-II superconductor in the mixed state and consequently determine the penetration characteristics of an ac magnetic field into the sample volume. Similar to a normal metal, we can derive an expression for the material property ‘conductivity’ from microscopic arguments. Describing the response of the entities responding to the electromagnetic field excitation (the Cooper pairs and the vortices) in a superconductor will provide us with the screening currents and the vortex motion contributions to the ‘conductivity’.

Screening currents

Let’s start with describing the contribution of the screening currents to the conductivity. In a first approximation one can use the simplified model introduced by the London brothers. Inspired by the two fluid model of superfluid ^4He , they assumed that free electrons in a superconductor can be divided in two groups: superconducting electrons with density, n_s , which flow without losses, and normal ones with density, n_n , which continue to act as if they had finite resistivity. The relative amount of these two types of carriers depends on the temperature. With the total density of free electrons conserved, $n = n_s + n_n$, $n_s = 0$ and $n_n = n$ at $T > T_c$, while at $T = 0$, $n_s = n$ and $n_n = 0$. The ‘normal’ electrons still have a typical metallic damping time, τ_n , but the superfluid electrons would move without dissipation, corresponding to $\tau_s = \infty$. It can be shown, combining the solution for the equation of motion, Eq.1.60,

for both groups of carriers, that the total ac-conductivity is given by,

$$\Re(\sigma(\omega)) = \frac{\pi n_s e^2}{2m} \delta(\omega) + \frac{n_n e^2 \tau_n}{m} = \frac{1}{\mu_0 \lambda_L^2} \left[\frac{\pi}{2} \delta(\omega) + \frac{n_n}{n_s} \tau_n \right] \quad (1.66)$$

$$\Im m(\sigma(\omega)) = \frac{n_s e^2}{m\omega} = \frac{1}{\mu_0 \omega \lambda_L^2} \quad (1.67)$$

Here we assumed that the frequencies are low enough so that $\omega \tau_n \ll 1$, which is a good approximation as this derivation is only valid for frequencies below the SC energy gap. It is clear that the normal electron fluid always provides a finite dissipation for all non-zero frequencies. However, this contribution becomes only appreciable for frequencies approaching the SC gap $\sim 10\text{GHz}$, above which the ac-response of a superconductor equals the one of a normal metal. For the low frequencies used in this work, the screening current contribution can be considered purely inductive and as such dissipationless as the current is always out of phase with the applied or induced electric field. As expected, using this expression for the conductivity of a ideal superconductor, neglecting the vortex contribution, the dispersion-relation and the skin depth becomes,

$$\mathbf{k}^2 = \frac{-1}{\lambda_L^2}, \text{ with } \delta = 1/\Im m(|\mathbf{k}|) = \lambda_L, \quad (1.68)$$

thus reproducing the London type screening, where the skin depth, in contrast to a normal metal, equals the frequency independent London penetration depth and there is no propagating component as the wave-number has no real part. For an overview, see Fig.1.11.(b).

Vortex response

As anticipated, also the vortices contribute to the material property, ‘conductivity’ and it can be derived by describing the response of a vortex in a type-II superconductor to an induced or applied current. However, before we dig into the equation of motion for a vortex, let us ask the question why vortex motion contributes to the conductivity of a type-II superconductor? A pioneering experiment of Giaever[31], provided the first experimental evidence that a voltage drop arises along a type-II superconductor as a direct consequence of the motion of Abrikosov vortices. If a vortex moves with velocity \mathbf{v} , with a direction of motion perpendicular to a current drive, it induces essentially an electric field of magnitude

$$\mathbf{E} = \mathbf{B} \times \mathbf{v} \quad (1.69)$$

parallel to the current drive. As such, in the presence of moving vortices, the superconductor is no longer ‘superconducting’ in a practical sense, as a resistive voltage drop arises. This is why the study of vortex dynamics is an important topic in superconductivity and of fundamental importance for the applications

of superconducting materials. In the easiest approximation one can consider a vortex as a rigid entity and describe the dynamics using particle-like equation of motion[32],

$$\mathbf{F}_I = \mathbf{F}_{VV} + \mathbf{F}_L + \mathbf{F}_{\text{drag}} + \mathbf{F}_P + \mathbf{F}_M + \mathbf{F}_{Th} \quad (1.70)$$

Let us discuss the different terms appearing in this phenomenological force-balance equation.

The Inertial term is equal to $\mathbf{F}_I = m^* \ddot{\mathbf{u}}_i$, where m^* is the mass of a vortex per unit length, which is only effective in nature as a vortex cannot exist outside a superconductor. The displacement field of the vortex ‘i’ is denoted by \mathbf{u}_i . There are several mechanisms proposed to contribute to the effective vortex mass per unit length[33, 34], in general it is accepted to amount to several thousands of electron masses and represent only a small contribution which can be easily neglected for the frequencies used in this work.

The vortex-vortex interaction denoted by \mathbf{F}_{VV} , describes the interaction with neighbouring vortices. The repulsive force between two vortices can be calculated from the interaction-energy, Eq.1.44, as:

$$f_{ij}(|\mathbf{r}_{ij}|) = \frac{-\partial U_{ij}(|\mathbf{r}_{ij}|)}{\partial |\mathbf{r}_{ij}|} = \frac{\phi_0^2}{2\pi\mu_0\lambda^3} K_1\left(\frac{|\mathbf{r}_{ij}|}{\lambda}\right) \quad (1.71)$$

From the expression for the supercurrent density, one can write the force exerted by vortex ‘i’ on vortex ‘j’ as:

$$\mathbf{f}_{ij} = \mathbf{J}_i(\mathbf{r}_j) \times \phi_{0j} \quad (1.72)$$

where ϕ_{0j} is a vector of size the flux quantum and with a direction parallel to the flux density of the vortex ‘j’. This expression, resembles the structure of a ‘Lorentz’ force density and corresponds to a repulsive interaction in case that both vortices have the same polarity and an attractive one when they have an opposite polarity. The interaction energy of vortex ‘i’ with the rest of the vortices is additive and can be calculated as $\mathbf{F}_{VV}^i = -\sum_{j \neq i}^N \nabla U_{ij}$. Note that, as discussed before, for a thin film the interaction range is much longer as compared to a bulk sample.

The ‘Lorentz force’ We can obviously generalize the above result for the force on a vortex ‘i’ due to screening currents or transport currents as,

$$\mathbf{f}_i = \mathbf{J}(\mathbf{r}_i) \times \phi_{0i} \quad (1.73)$$

where \mathbf{J} is the total supercurrent density at the location of the core of the vortex under consideration. However, note that both forces, $\mathbf{F}_{\mathbf{L}}$ and $\mathbf{F}_{\mathbf{V}\mathbf{V}}$, are not a ‘Lorentz force’ in the usual sense, it is $q\mathbf{v} \times \mathbf{B}$, the force experienced by a moving charge q with velocity \mathbf{v} in a field \mathbf{B} and that the name is somewhat confusing¹⁴.

The viscous damping force The drag force, \mathbf{F}_{drag} , can be described as $\mathbf{F}_{\text{drag}} = -\eta\dot{\mathbf{u}}$, where η describes the viscosity experienced by the vortex when moving through the superconducting medium. The ultimate mechanism for the damping coefficient η is still a controversial issue. The most popular explanation is the model proposed by Bardeen and Stephen. They related η to ordinary resistive processes in the core of a vortex due to the electric field needed to maintain a cycloidal motion of electrons when a vortex moves [36]. Other mechanisms have been suggested even before the Bardeen-Stephen theory, Tinkham had shown that dissipation comparable to that observed in experiments could be explained if the GL wave-function could adjust to the time-varying field configurations induced by a moving vortex only in a finite relaxation time[37]. Another approach has been proposed by Clem and is associated with the local temperature gradients in the vicinity of the normal like regions produced due to a difference in entropy between the leading edge and the trailing edge when a vortex is moving[38]. It is not entirely clear to what extent all these various mechanisms are additive and to what extent they simply prove ways of looking at the same thing. As pointed out by Suhl[33], the ratio η/m^* , which in the case of free flux flow describes the initial time necessary to reach steady state motion is of the order of picoseconds. Therefore the dynamics of vortices at low enough frequencies can be described by ignoring the vortex mass.

The pinning force The motion of vortices can be reduced or eliminated by providing pinning centers which ‘pin’ the vortex by exerting a pinning force per unit length on the vortices, $\mathbf{F}_{\mathbf{P}}$. The pinning centers can be of two types.

Intrinsic pinning This type of pinning is caused by impurities, naturally occurring crystal defects such as lattice imperfections, grain- and twin boundaries which are typically distributed random and which strength is difficult to control.

Artificially manufactured pinning centers The technological revolution made it possible to introduce deliberately pinning centers

¹⁴Indeed if you would just translate $q\mathbf{v}$ and \mathbf{B} into \mathbf{J} and ϕ_0 , one will find that $\mathbf{J} \times \phi_0$ is the force acting on the current, and therefore, the driving force on the vortex should be $\phi_0 \times \mathbf{J}$, which has the opposite direction. A more detailed discussion can be found in Ref.[35], where the driving force is derived from kinetic energy considerations.

with required shape, size and distribution by means of lithographical techniques. These artificial pinning centers such as holes, blind holes or magnetic dots with magnetic moment in and out of plane acquired a lot of attention in the previous years as well theoretically as experimentally[27].

Mkrtchyan and Schmidt[39] considered a basic example of vortex pinning by calculating in the London limit the interaction energy between a vortex and an insulating cylindrical cavity, analogue to an anti-dot(AD). The vortex-antidot interaction depends upon the magnetic flux trapped in the antidot. The interaction between a vortex and an empty antidot is attractive for all V-AD distances. However once a flux is trapped, the competition between the attraction by the antidot and the repulsion of the present screening currents due to the trapped flux quantum will introduce a surface barrier at the edge of the antidot(see Chapter 4). The height of the barrier will increase with the number of trapped flux quanta. The saturation number, n_s is defined as the point where the interaction becomes repulsive and no additional flux can be trapped anymore by the antidot. The saturation number depends on the ratio between the size of the antidot and the size of the vortex, $\sim \xi$. For small antidots, $r_0 \ll \lambda$, the saturation number is approximately given by,

$$n_s \cong \frac{r_0}{2\xi(T)} \quad (1.74)$$

This indicates that the presence of an antidot or pinning center in general can stabilize multi-quanta vortices[40, 41] and can have profound consequences for the vortex lattice arrangements.

An important property of the superconductor is the maximum current that can flow before the onset of motion of vortices, i.e. the critical current, J_c , as it determines the lower limit to have dissipationless current transport. As such, research to optimize the vortex pinning in superconductors as to increase the critical current is of technological importance. The upper limit of current that can flow through a superconductor is given by,

$$j_d^{GL} = \frac{H_c}{\left[\frac{3\sqrt{6}}{4} \lambda(T) \right]}, \quad (1.75)$$

the so called Ginzburg-Landau depairing current, which is the theoretical upper limit for the critical current at which the superconducting Cooper pairs are destroyed.

The Magnus force Is a hydrodynamic force experienced by a vortex moving in a liquid, $F_M = \alpha \phi_0 \times \dot{\mathbf{u}}_i$, where α is the Magnus force coefficient. This force results in a component of the vortex velocity transversal to the drive current, which will lead to a Hall-voltage. In most cases and for small vortex velocities, this force can be ignored as most experimental data indicate that the Hall angle is very small.

Thermal fluctuations At high temperatures or low frequencies, due to Brownian motion induced by thermal fluctuations, a vortex may have time to diffuse out of its pinning potential well and wander some distance around. To model this effect one supplements the equation of motion with a random force which is assumed to be Gaussian white noise with zero mean, in analogy with an earlier work of Fulde[42].

Discussion

Analytical solutions for this equation of motion exist for certain limiting cases[43, 44, 45]. For example let us assume that the vortices are all driven by an identical weak periodic force due to an induced or applied ac current, $\mathbf{j}_{ac}(t) = \mathbf{j} \exp^{-i\omega t}$. The steady state solution to the equation of motion, Eq.1.70, within this single particle model is:

$$\mathbf{u}(t) = \mathbf{u}(\omega) \exp^{-i\omega t}, \text{ with } \mathbf{u}(\omega) = \frac{\mathbf{j} \times \phi_0}{-i\eta\omega + \langle \alpha_L \rangle}, \quad (1.76)$$

We considered only weak excitations, as then the local potential each vortex experiences, due to a combination of random disorder, neighbouring vortices or boundaries, can be approximated by a harmonic potential with spring constant $\langle \alpha_L(r) \rangle$, (meaning we consider only linear response)

$$\mathbf{F}_P + \mathbf{F}_{VV} = - \langle \alpha_L(r) \rangle \mathbf{u} \quad (1.77)$$

$\langle \alpha_L \rangle$ is called the Labusch constant, which is, in principle, within this single particle model, a statistical average over all restoring forces. We neglected further any thermal, inertial and Magnus effects. In the case of artificial pinning arrays, all restoring forces are supposed to be similar, so $\langle \alpha_L \rangle$ can be taken as a constant. However, in these artificial pinning arrays different types of vortices can coexist, each still experiencing a different $\langle \alpha_L \rangle$ (see Chap.5). For example, pinned vortices by an antidot lattice will experience a completely different restoring force than an interstitial vortices caged by the pinned ones[46].

For low frequencies, $\omega \ll \omega_L \equiv \langle \alpha_p \rangle / \eta$, the restoring force dominates the motion over the viscous drag force which can then be neglected. Here we introduced the pinning frequency ω_L , which is typically of the order of

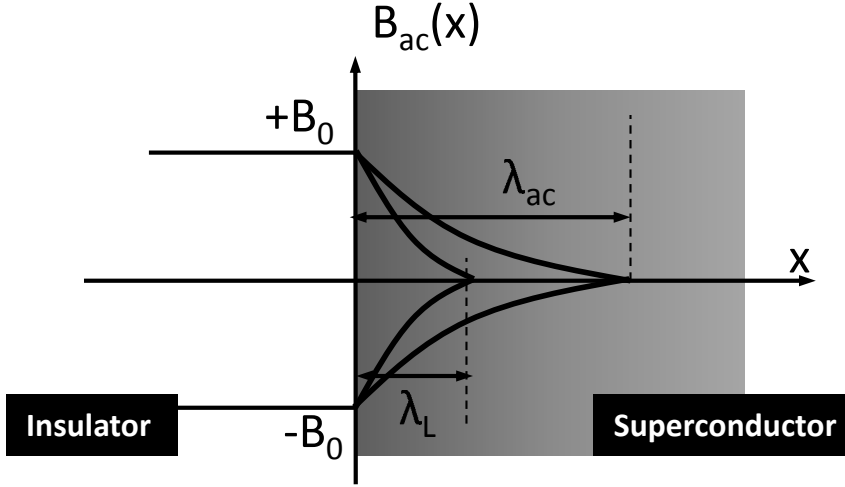


Figure 1.10: Schematic presentation of the ac penetration depth in the Campbell regime. For rigidly pinned vortices is $\lambda_{ac} \sim \lambda_L$, whereas for weak pinning $\lambda_{ac} \sim \lambda_C$.

10^7 Hz[47]. In this case, only the elastic interaction with the pins has to be considered and the motion consists of a pure reversible harmonic motion perfectly in phase with the driving force,

$$u(\omega) = \frac{\phi_0 J}{\eta} \frac{1}{\omega_L} \quad (1.78)$$

We call this regime the Campbell regime[48]. Using the relation $\mathbf{E} = \dot{\mathbf{u}}(t) \times \mathbf{B}$, where we use $B = n\phi$ to make the step from a single particle model to the whole sample' average response, this leads to a pure complex contribution to the ac-resistivity due to ac-vortex dynamics. Together with the screening current contribution, Eq.1.66, we obtain a pure complex conductivity,

$$\sigma_C(\omega) = (\omega\mu\lambda_L^2 + \omega\mu\lambda_C^2)^{-1}i, \text{ with } \lambda_C = \sqrt{\frac{\phi_0 B}{\langle \alpha_L \rangle_\mu}}, \quad (1.79)$$

where we defined the Campbell penetration depth, λ_C , which is real and frequency independent. As such in this low frequency regime, the ac-vortex dynamics alters effectively the inductive properties of the superconductor as compared to the ideal case where only the screening currents contribute. In general the ac vortex dynamics can also change the resistive properties of the superconductor, as we will see below. The dispersion relation and the total ac

penetration depth are given by:

$$k^2 = \mu\sigma_C\omega i = \frac{-1}{\lambda_{ac}}, \text{ with } \lambda_{ac}^2 = \lambda_L^2 + \lambda_C^2 \quad (1.80)$$

where λ_{ac} is the skin depth or effective ac-penetration depth, which is larger than the London penetration depth. The response is still a pure inductive response which resembles the ideal Meissner response, see Eq.1.68. For weak pinning and considering the applied ac and dc magnetic fields perpendicular to the sample surface, this Campbell penetration depth can be written as $\lambda_C = (c_{11}/<\alpha_L>)^{1/2}$, where c_{11} is the compressional modulus of the vortex lattice. By this it is clear that the ac-field penetration is carried by reversible vortex oscillations near the equilibrium positions. For very strong pinning, it is when $<\alpha_L>\rightarrow\infty$, the vortices are immobile under external field changes and the superconductor behaves as if it were in the Meissner state, in this case the ac penetration depth reduces to the London one, see Fig.1.10.

In the opposite limit, for high frequencies $\omega \gg \omega_L$, the viscous drag force dominates the response and we can neglect the restoring force all together. The motion is just like in a normal metal a motion damped by a viscous force

$$u(\omega) = \frac{\phi_0 J}{\eta} \frac{i}{\omega}, \quad (1.81)$$

This motion is completely out-of phase with the driving force. The resulting ac resistivity contribution due to the ac vortex dynamics is identical to the so called flux flow (FF) resistivity, independent on the frequency, but dependent on the field:

$$\rho_{ac}(\omega) = \frac{B\phi_0}{\eta} = \rho_{FF} = \sigma_{FF}^{-1}, \quad (1.82)$$

It is clear that in this regime the ac vortex dynamics alters the material property ‘conductivity’ of the superconductor by a pure resistive contribution. For the ac magnetic field penetration, the superconductor will behave identical to a normal metal with a field dependent and frequency dependent skin depth. The dispersion relation and the so called flux-flow penetration depth are given by,

$$k^2 = \mu\sigma_{FF}\omega i, \text{ and } \delta_{FF}^2 = \frac{2B\phi_0}{\mu\eta\omega} \quad (1.83)$$

A more complete description of the vortex’ linear response has been done by Coffey and Clem, who derived a complete expression for the ac-resistivity by solving the equation of motion, Eq.1.70, taking into account, in addition to

the previous dynamic modes, also vortex motion due to thermal fluctuations. Within linear response the motion due to thermal fluctuations is found to be accounted for by the following equation of motion,

$$\dot{u} \sim e^{(-U/k_B T)} \quad (1.84)$$

meaning the vortices move with a linear average vortex velocity proportional to a Boltzmann factor, where U describes an effective activation energy related to the strength of the intrinsic pinning landscape. Because of the activated nature of this type of flux motion, one speaks of ‘thermally assisted flux flow’(TAFF). The resulting ac resistivity contribution due to TAFF is similar to the case of FF, purely resistive,

$$\rho(\omega) = \rho_{TAFF} \sim \exp(-U/k_B T) = \sigma_{TAFF}^{-1} \quad (1.85)$$

and results likewise in a frequency dependent skin depth,

$$k^2 = \mu \sigma_{TAFF} \omega i \quad , \text{ and } \delta_{TAFF}^2 = \frac{2\rho_{TAFF}}{\mu \omega} \quad (1.86)$$

Rigourously, for the whole superconductor containing vortices and screening currents one has to add all the different contributions. A general form for the equation of motion taking into account all the above described contributions is given by[43, 44],

$$\mathbf{u}(t) = - \left[\frac{-\langle \alpha_L(r) \rangle}{1-i/\omega \tau_1} + i\omega \eta \right]^{-1} \mathbf{f}_L(t) \quad , \quad (1.87)$$

$$\text{with } \tau_1 = \left(\frac{\eta}{\langle \alpha_L(r) \rangle} \right) I_0^2 \left[\frac{U}{2k_B T} \right]$$

where $I_0(x)$ is the modified Bessel function, which closely resembles an exponential for large argument x and $I_0(0) = 1$. Further τ_1 is a characteristic relaxation time below which thermally activated hopping of vortices becomes important. For conventional superconductors this characteristic time is of the order of $1/\tau_1 < 10Hz$ and scales with the ratio between an effective activation energy characterizing the intrinsic pinning, U and the thermal energy, $k_B T$. For high- T_c superconductors the effect of TAFF can be much more pronounced. This equation of motion describing the linear response of a vortex to an ac-drive is a combination of in-phase(reversible motion) and out-of-phase(dissipative motion) components and will be probed directly in Chapter.5.

It is clear that when neglecting thermal fluctuations as can be done for low temperatures, meaning $U \gg k_B T$, τ_1 diverges exponentially and the equation of motion reduces to the previous discussed cases in both limits of high and low frequencies. Moreover for high temperatures and low frequencies, $f < 1/\tau_1$, the TAFF regime is recovered. This description of the vortex response, taking into account all the above mechanisms, results, in general, in a complex ac resistivity and a complex wave-vector. A schematic overview of the above described linear response taking into account only the response of the screening currents is given in Fig.1.11(b) and for the vortex contribution in a type-II superconductor in Fig.1.11(c).

A few last remarks. The simplified model used here to describe the ac-dynamics, considering a vortex as a particle-like object has of course its limitations, as it ignores the internal structure of the vortices and their elastic nature. It is expected to fail for high vortex velocities where more realistic approaches such as time-dependent GL theory become necessary. Moreover, in the above we considered only linear response, which is valid for small disturbances from equilibrium. Once the applied ac-field amplitude becomes sufficiently high, it is able to introduce vortex displacements much larger than the pinning site size (intrinsic defects, surface barriers, etc.), the system will be in a regime of strong nonlinear response. In this regime Ohm's law will not be valid anymore and, in general, the material property 'conductivity' will become a function of the induced or applied current. In this case the response can be described by critical state models not further discussed here[49].

Figure 1.11: This figure presents an overview of the above discussion regarding the penetration of an ac magnetic field in a conductive medium. Schematic presentations of the different dispersion relations for a normal metal (a) and a superconductor (b and c) are given. The left column shows the frequency dependence of the real part of the wave vector related to the wavelength by, $\lambda = 2\pi/\Re(|\mathbf{k}|)$. The right column shows the frequency dependence of the complex part of the wave-number related to the characteristic length scale over which the amplitude of the magnetic wave decays into the volume. This characteristic length scale, the skin depth, is given by $\delta = 1/\Im m(|\mathbf{k}|)$. For the normal metal (a) the skin effect regime ($\omega < 10^{11}\text{Hz}$) and the plasma regime are shown $\omega > 10^{15}\text{Hz}$. The light line indicates the propagation of an ac-magnetic field in the absence of any conductive medium, $\omega = ck$. For the superconductor, both contributions of the screening currents (b) and the vortices (c) are shown separately. In (b), the Meissner response is shown for frequencies below the gap frequency $\omega < \delta/\hbar = 10^{10}\text{Hz}$ and the normal skin effect is recovered for frequencies above the gap frequency. In (c) the different indicated frequency regimes are related to the corresponding dominant mechanism describing linear ac-vortex motion in this regime. for frequencies below 10 Hz, thermally activated flux flow (TAFF) contributes substantially to the ac-vortex motion. For $10\text{Hz} < \omega < 10^7\text{Hz}$, the ac-vortex motion is described within the Campbell model of reversible oscillations. For $10^7\text{Hz} < \omega < 10^{10}\text{Hz}$, the linear ac-vortex response will be of flux flow (FF) type.

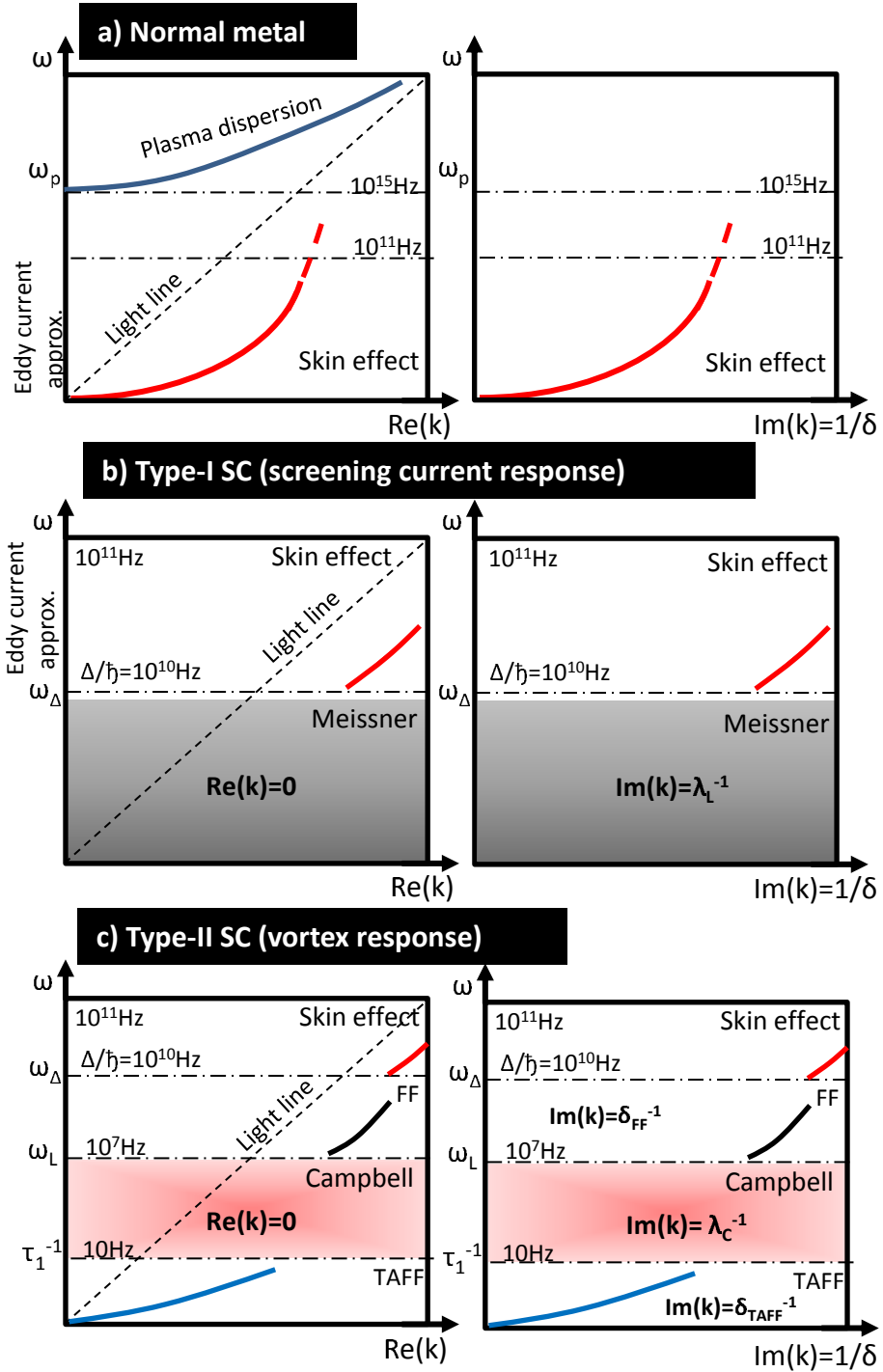


Figure 1.11

Experimental techniques

2.1 Introduction

This chapter will introduce the experimental technique central to this work, scanning Hall probe microscopy (SHPM). A brief review will be given describing the setup, the principle of operation and the general characteristics. Further, a general description is provided of the production process used to fabricate the nano-structured superconducting thin films studied in this work.

2.2 Scanning Hall probe microscopy

The operating principle of a typical scanning Hall probe microscope is schematically illustrated in Fig.2.1(a). In SHPM, a submicron-sized Hall probe is scanned in close proximity to the sample surface and measures at every pixel, within a certain scan area, the Hall voltage. The Hall voltage is in first approximation proportional to the perpendicular component of the local magnetic induction, and as such a SHPM acts as a high resolution ‘magnetic field plotter’. The first two dimensional SHPM images were made in 1972 by Goren and Tinkham[50]. They used micrometer-based scanning stages and Hall probes made of the semi-metal bismuth, which has a low carrier density. A spatial resolution as high as $4\mu\text{m}$ was obtained, with a magnetic field sensitivity of 0.01mT . In the following we will discuss the different components of the setup and the principle of operation.

The Hall effect

Hall probes are based on the Hall effect, a phenomenon discovered by Edwin Herbert Hall as Phd student in 1878[52]. In his experiment he noticed that

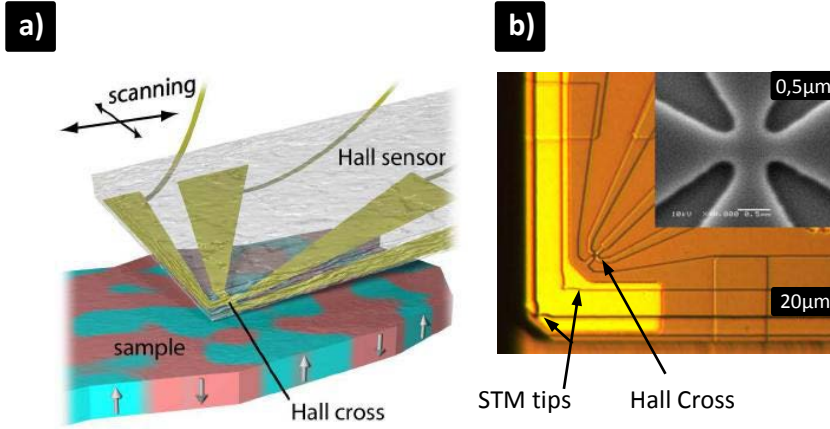


Figure 2.1: (a) Schematic illustration of the operating principle of SHPM, a Hall sensor scans over a magnetic sample and measures the induced Hall voltage at every pixel.[51] (b) Optical microscopy image of a typical Hall sensor integrated on a chip. The arrows indicate the position of the Au metallization for the STM tips and the position of the Hall cross. The inset shows a SEM image providing a closer view on the Hall cross itself.

when a current carrying conductor is placed in a perpendicular magnetic field, a transverse voltage appears, V_H , the so called Hall voltage. What Hall observed (the electron was still to be discovered) is nowadays ascribed to the deflecting Lorentz force on the carriers. For an ideal plate like Hall device in a uniform perpendicular magnetic field, B , the Hall voltage can be obtained in terms of the applied current bias, I_{bias} , through the plate as

$$V_H = R_H \frac{I_{\text{bias}} B}{t} \cong \frac{1}{nq} \frac{I_{\text{bias}} B}{t} = \frac{\mu}{\sigma} \frac{I_{\text{bias}} B}{t}, \quad (2.1)$$

here q denotes the charge of the carriers, n is the carrier concentration in the plate and t is the plate thickness. Further, R_H denotes the Hall coefficient characterizing the intensity and sign of the Hall effect. In the last equality we expressed¹ the Hall coefficient in terms of σ and μ denoting the conductivity and the mobility of the carriers, respectively. For a long rectangular bar, with small sense contacts, Eq.2.1 applies and can be derived from a semi-classical equation of motion for the carriers, Eq.1.60. When R_H and the thickness of

¹When an electric field E is applied across a piece of material, the electrons respond by moving with an average velocity called the drift velocity, v_d . Then the electron mobility μ is defined as $v_d = \mu E$. As the total current is given by $J = nq\mu E$, the relation between the conductivity and the mobility is $\sigma = nq\mu$.

the Hall device are known, a one-to-one relationship exists between the field through the device and the experimentally accessible Hall voltage. Conversely, the Hall effect can also be used to obtain some important material properties, e.g. type of carriers, mobility, etc[14]. Real Hall devices usually have different shapes and larger contacts and a detailed treatment is necessary taking into account the geometry, the type of carriers, their concentration and kinetic properties (eg. diffusive or ballistic transport). However, Eq.2.1 provides us with a first-order approximation, and indicates the main properties and the rules of thumb for the design of a good Hall sensor.

Magnetic field resolution

What are the necessary ingredients to assemble a high quality Hall probe? First of all, from Eq.2.1, the Hall voltage is inversely proportional with the carrier density, this is why the Hall effect is typically small in metals having high carrier densities (10^{22}cm^{-3}). From this point of view, the much lower carrier densities in semiconductors ($10^{14} - 10^{20}\text{cm}^{-3}$) result in Hall coefficients as much as 7 orders of magnitude larger than in metallic Hall devices, making them perfect candidate materials for magnetic field sensors. Secondly, note that the Hall effect is larger for thinner conductors. On top of that, thin Hall probes have the advantage of sampling the field at a well defined height. Thirdly, from Eq.2.1, we see that a good Hall sensor also exhibits a high carrier mobility, which additionally determines, for a fixed carrier concentration, bias current and probe size the signal-to-noise ratio (SNR). At low temperatures ($T < 100\text{K}$), the main noise component of the current state-of-the-art probes up to a certain critical dc bias current I_{max} is the Johnson (thermal) white noise of the Hall voltage contacts. For an ideal 2D Hall device at temperature T with carrier density n_{2D} , the SNR for a sensor is given by[53],

$$SNR = \sqrt{\frac{\mu}{n_{2D}}} \sqrt{\frac{w}{4k_B T q l \Delta f}} I_{\text{bias}} B, \quad (2.2)$$

where w and l are the width and length of the voltage leads, respectively. Further, Δf is the measurement bandwidth. It is clear that high carrier mobilities, low carrier concentrations, low temperatures and a small bandwidth (Lock-in techniques) for a certain Hall probe geometry provide the best SNR.

The invention of modulated doped² semiconductors in 1978 has subsequently revolutionized the field, as it became possible to fulfil the above considerations for having an optimum Hall probe. This advance to develop semiconductor heterostructures with well defined electronic properties, together with the

²In modulation doping, the doping elements are implemented in such a way that the resulting free electrons are spatially separated from the positive donor ions, as a result scattering of moving electrons on the dopant atoms is avoided.

development of lithographic techniques to produce sub-micron sized probes, paved the way to SHPM devices with very high field and spatial sensitivity. The prime candidate for high resolution Hall probes are heterostructures assembled of GaAs/Al_{0.3}Ga_{0.7}As, where the electrons are confined in a very narrow layer of thickness around 10nm typically located at 100 nm below the surface. This ‘electron sheet’ embedded in an insulating matrix, referred to as a two dimensional electron gas (2DEG) has very high carrier mobilities and low carrier concentrations at liquid Helium temperatures of 100m²V⁻¹s⁻¹ and 10¹¹cm⁻², respectively. This results in typical Hall coefficients of $R_H=3\Omega$ mT⁻¹. The 2DEG Hall probes used in this work are manufactured by Magcam, see Fig.2.1(b) and the detailed production process can be found in Ref.[54]. The probes have effective dimensions of 0.4μm×0.4μm, the Hall sensor asymmetry is +/−1% and it is integrated on a chip of size 3mm×3mm. The resistance at 300K is around 50kOhm, while at 4K the resistance is around 5kOhm. The specifications of the sensors, as provided by Magcam, are checked for the different Hall probes used in this work. For the optimum choice of the bias current through the Hall cross³, typically ~20μA, a practical detection limit(DL) of 5μT is obtained. A thorough characterization of the Hall probes can be found in Ref.[54].

Spatial resolution

The spatial resolution of the Hall probe scales roughly as $\sqrt{s^2 + h^2}$, where s is the size of the probe and h the height of the probe above the sample. From this, it is clear there is no reason to have a probe with size $s \ll h$, since having the smaller s in that limit does not improve the spatial resolution, but would decrease the sensitivity. To have optimum spatial and magnetic field resolution, while investigating a certain area of interest, one places the probe as close to the sample surface as possible using piezoelectric actuators and one determines the optimum probe size to have a good magnetic field resolution. To be able to approach the sensor within close proximity of the field source, the Hall sensor is processed on a chip, see Fig2.1(b) containing the above described sub micrometer sized Hall cross in close proximity to an STM tip⁴. This chip is mounted in a modified scanning probe setup of nano-magnetics which allows accurate positioning and scanning of the Hall probe over the surface.

An overview of the scan head is given in Fig.2.2(a) and Fig.2.2(b) This scan head contains two sets of piezo-actuators. The first set, indicated as Set I in

³In this work we mainly use dc bias current, the advantage of using dc bias currents is that it results in faster acquisition times for an image and it allows an easy implementation of an alternative technique, scanning ac susceptibility microscopy as described in Chap.5 However when using dc bias currents the detection limit is somewhat lower.

⁴The chip contains two STM tips as indicated in Fig.2.1(b), a distance of 15μm away from the actual Hall cross.

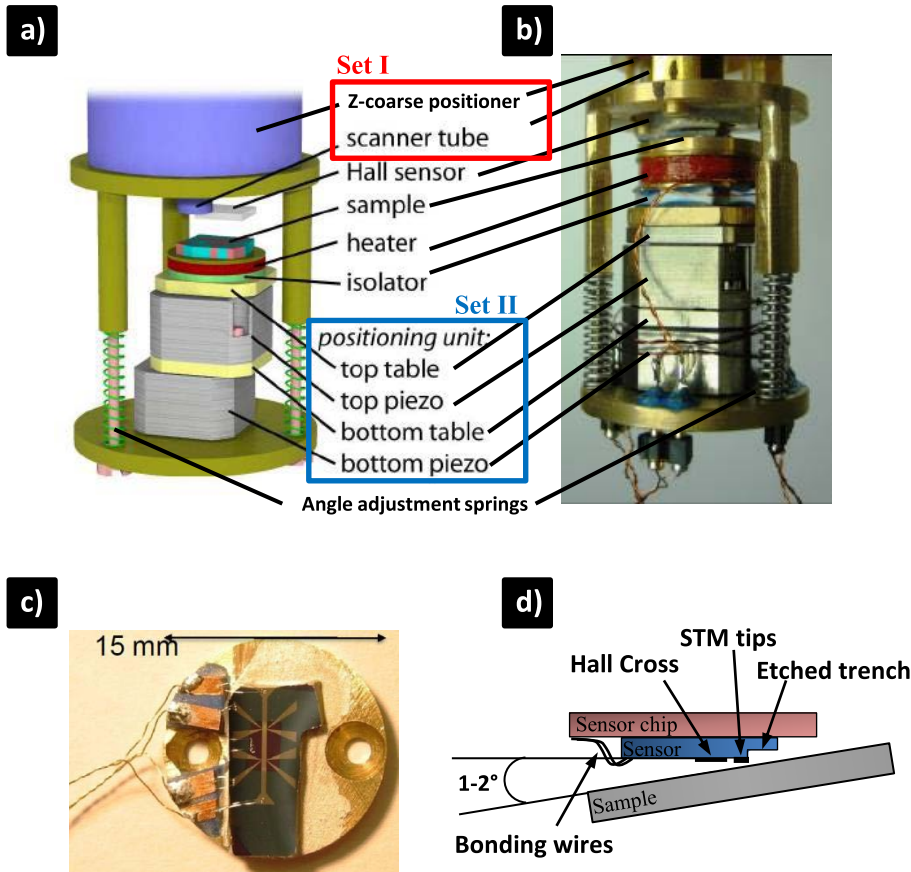


Figure 2.2: (a) Schematic overview and a photograph (b) of the modified SHPM-setup with incorporated coarse positioning unit and the heater in proximity to the sample.[51] (c) Photograph of the sample holder with contacts for transport measurements. (d) Schematic illustration of the sample-sensor chip orientation and position.

Fig.2.2, contains a coarse z-positioning system and a scan tube having the Hall chip at the end of it. This set allows to scan the Hall probe over the sample surface in a scan area of $16 \times 16 \mu\text{m}^2$ at 4.2K with nanometer scale resolution and to approach the surface until tunneling between the STM tip and the sample surface is reached. To allow STM approach, the sample is covered with a conductive Au layer and biased to a potential of -100mV. The approach process is as follows. First, the scan tube is elongated over a maximum distance

of $2.4\mu\text{m}$ while continuously monitoring the tunnel current. When no tunnel current is found during elongation, the coarse z-positioner⁵ approaches one step, where the approach distance corresponding with one step is less than the elongation of the scanner tube, to avoid crashing the probe during approach. However, when tunnel current is found a PID protocol stabilizes the tunnel current by continuously adjusting the elongation of the z-scanner. This process is repeated until a tunnel current of 0.5nA is obtained corresponding to a tunnel resistance of $200\text{M}\Omega$ and a tip-sample distance of $<1\text{nm}$. The second set of positioners, indicated as Set II in Fig.2.2, contains two x and y coarse piezoelectric stick-slip motors of Attocube, allowing for moving the sample plate up to 3mm in both lateral directions with nanometer-scale resolution. This second set of positioners makes it possible to explore different areas of the sample.

Once the tip is in ‘STM-contact’ with the sample, the ultimate lower limit for the height above the sample surface is determined by the depth of the 2DEG below the surface of the heterostructure, typically 100nm . However an additional limitation comes from the angle between the sample and probe chip $\sim 1\text{-}2^\circ$, put during the installation process to assure the STM tip is the closest point to the surface and to provide room for the current and voltage leads coming from the Hall probe chip, see Fig.2.2(d). Both the distance between the active area and the STM tip and the tilt angle contribute to the height of the probe. In principle it is possible to scan the sensor over the sample surface while keeping the tunneling current constant, using continuously the PID feedback on the z-piezo. As such we can obtain simultaneously the topography and the magnetic field distribution. However, in practice we always prefer to operate in ‘flying mode’. In this mode the probe is lifted a few 100nm after ‘STM-contact’ in the highest corner of the scan area, and the scan is performed at this fixed distance. The lift height is limited by the surface roughness within the scanarea and can be continuously adjusted during scanning in both lateral and transversal directions for compensating the tilt of the sample. This ‘flying mode’ allows for faster imaging, with less risk of crashing the probe. Eventually, the typical scan height is around $\sim 1\mu\text{m}$.

Is it possible to obtain quantitative and qualitative data with the SHPM? In the end, the spatial resolution of the Hall probe is comparable with the length scale of magnetic field variations in Type-II superconductors, it is the penetration depth (cf. Sec.1.4) and as such one expects appreciable convolution effects. In a first approximation one could argue that the Hall probe measures an average

⁵The z-coarse positioner consists of a glass tube glued to a piezo-actuator. The whole copper part carrying the first set of piezo’s and the sample moves over the glass tube by a stick-slip inertial principle. The scanner tube is located inside the glass tube.

of the local field distribution over the whole square cross junction. However, at low temperatures the electron mobility reaches such high values that the mean free path exceeds the Hall cross size. In this ballistic regime, carriers can be imagined to fly in long straight lines over the cross junction. A local magnetic field in the junction can then be considered as a scattering center strongly affecting the electron transport. As such, when a spatially inhomogeneous field is present, the Hall voltage will depend on the exact position of the inhomogeneities within the Hall probe. In general, one describes the response of the Hall cross by a response function $\Gamma(x, y)$, which modifies the simple relation between the measured Hall voltage and the applied field, Eq.2.1, as,

$$V_{Hall} = \frac{I_{bias}}{n_{2D}e} \frac{\int \int dx dy B_z(x, y) \Gamma(x, y)}{\int \int dx dy \Gamma(x, y)}, \quad (2.3)$$

The integral in the denominator normalizes the introduced response function, so that it is simplified to Eq.2.1 in the case of an homogeneous field. Several references can be found that calculate this response function depending on the kinetics of the electrons (diffusive regime[55, 56], ballistic regime[57, 58]) and the size of the Hall probe. It is shown that when the Hall sensor operates in the ballistic regime and at low field, i.e. $\mu b_z \ll 1$, the response function can be considered as a constant within the main junction area, with rapid decaying tails in the contact paths and independent of the shape and position of the field inhomogeneity profile in the junction.

Operation environment

The scanning head operates in a ^4He variable temperature (4.2K-300K) flow cryostat from Cryogenic Limited. In this cryostat liquid helium is pumped from a 52 liter liquid helium reservoir via a needle valve into variable temperature insert space (VTI), where the temperature is controlled using a temperature sensor and a heater (50W) connected to a Lake Shore 340 temperature controller. The helium gas flows around the sample space containing some static He exchange gas (1bar) and the SHPM head. The static gas suppresses vibrations which would have been caused by a helium flow. A second temperature sensor and small heater (500mW) are mounted on the SHPM head itself which can be controlled by a second PID loop of the Lake Shore 340 temperature controller. Temperature stabilities up to 1mK are reached at liquid helium temperatures. Further, a superconducting magnet is available and installed in the helium reservoir, capable of generating fields up to 5T. To prevent vibrational noise, the whole cryostat is suspended on a two-stage vibration-isolation stage. Further the scanhead contains the sample table on which the sample holder is screwed, see Fig.2.2(c). As the sample holder contains copper contact pads, it is possible to do standard transport measurements even while measuring. The whole scan head is surrounded by a

small copper coil which allows to apply small dc and ac fields in a range of $|\leq 5\text{mT}|$. A small IR LED is present to activate the 2DEG after the cooling process from room temperature to He^4 temperatures. The electrical connections between the scan head and the control electronics run through the center of the microscope insert and subsequential through three lemo connectors. The Hall voltage is amplified by a factor of 1000 and the tunnel current is converted using a 100mV/nA current-to-voltage converter in a shielded box at the top of the cryostat. As current source for delivering the bias current a Keithley 220 programmable current source is used and the Hall voltage is digitized by an ADC card of Nanomagnetix having 16 bit resolution at a maximum speed of 200ks/s .

Some important properties of SHPM, as compared to other magnetic imaging techniques (e.g. The bitter decoration technique, Magnetic force microscopy, scanning SQUID, magneto-optical imaging, etc.), are listed in Ref.[59, 53]. In summary, SHPM is a direct non-invasive magnetic field sensor, having self fields of only $<10^{-3}\text{mT}$ at typical operating currents ($20\mu\text{A}$) and sample-probe distances. The magnetic field detection limit is around $5\mu\text{T}$ and as the probe size can be made much smaller than typical standard scanning SQUID probes⁶, a good spatial resolution below $1\mu\text{m}$ can be obtained. These properties, together with the possibility of measuring over broad temperature ranges and field ranges, without strict sample preparation requirements, make SHPM a powerful tool for the investigation of magnetic flux structures in a variety of materials.

2.3 Sample fabrication

All samples are fabricated by a standard e-beam lithography process and subsequent deposition of a variety of materials using standard e-beam evaporation or dc-sputtering techniques. An overview of the different steps in the production process are schematically shown in Fig.2.3. In a first step, a substrate [Fig.2.3(a)] consisting of single crystalline Si, covered with a thermally grown amorphous SiO_2 layer of 2000\AA is coated [Fig.2.3(b)] with a single or double ‘positive’ resist layer(s) by a spinning process. The resist layer(s) consists of the polymers, typically Co-PMMA/PPMA, and has a total thickness of about 150nm . Next, a desired mask is imprinted by means of a scanning electron beam [Fig.2.3(c)]. By exposing the polymer to a focused electron-

⁶Currently, nano-meter sized SQUIDs are fabricated on the apex of a sharp quartz tip and integrated into a scanning SQUID microscope. The diameter of these nanoSQUIDs ranges down to 100 nm , having a flux sensitivity as high as $1.8 \times 10^{-6}\Phi_0/H\text{z}^{1/2}$ and they are operational in fields as high as 0.6T [60].

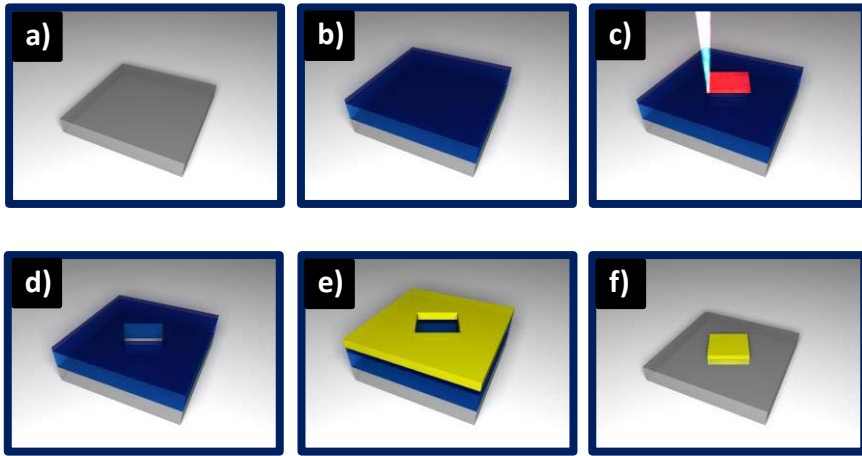


Figure 2.3: Schematic overview of the sequential steps describing the sample production process by e-beam lithography.

beam, which serves as ‘pen’, a computer generated pattern can be transferred to the polymer film by locally destroying or breaking up the polymer chains (positive resist). The electron beam used to write the pattern can be focussed to a spot of typically around 2nm diameter. However, the resolution of the resulting structures exceeds the focus size due to proximity effects; the resist is exposed not only by electrons from the beam, but also by secondary and backscattered electrons. As such, the typical line widths are limited around 10nm. In the next step, the so called ‘development’ step [Fig.2.3(d)], the e-beam exposed regions, consisting of broken up polymers, are removed by immersing the substrate into a development solution (typically, 4 methyl-2 pentanone:1-pentanol(1:1) for 1m45sec) followed by rinsing in 1-pentanol to stop the development process and flushing with nitrogen gas. Now that a resist mask is established, the desired metal is evaporated onto the substrate [Fig.2.3(e)]. The resist pattern will function as a protective mask, it must ‘resist’ or protect the underlying substrate while bared areas are being exposed to the evaporated materials. The materials Pb and Ge used mainly in this work are deposited using a Varian ultra high vacuum system. It can reach a base pressure of 10^{-9} mbar, by using an ion pump and assisted cooling with liquid nitrogen. Two electron guns of 6KW and 10KW are used to evaporate Pb and Ge, respectively. The materials are grown in a pressure range of $(3-8) \times 10^{-8}$ mbar with a typical rate of $1-3 \text{ \AA/s}$ depending on the material. For uniform Pb film growth the sample is cooled during the deposition with liquid nitrogen to a temperature of 77K, as at elevated temperatures Pb tends to form

clusters. The Microscience dc-magnetron sputtering system is used to deposit Ti and Au films, where the latter is used frequently in this work as a conductive top layer for STM approach of the Hall probe, see Sec.2.2. The base pressure of the system is 5×10^{-8} mbar and the deposition itself is done at Ar-pressures of 5×10^{-3} mbar. The typical deposition rate is 16nm/min. As Au films do not ‘stick’ well to the SiO₂, typically a thin Ti adhesion layer has to be deposited to prevent the release of the Au film during the final step. This final step, the so called ‘lift-off’, involves the removal of the resist layers, including the metal deposited on top, using hot acetone, so that only the metal deposited on top of the patterned area remains on the substrate(Fig.2.3[f]). A successful lift-off usually requires applying ultrasonic agitation. For more details concerning the e-beam lithography process an excellent and detailed description can be found in Ref.[61].

In this work, the first four steps in the above described e-beam lithography process are preformed at the Interuniversity Micro-electronics Centre (IMEC), whereas the last two steps are preformed in our group. Further, structural characterization of the nano-structured thin films is done using room temperature atomic force microscopy (AFM) and scanning electron microscopy (SEM). The electrical transport properties were investigated by standard transport measurements using a standard four-probe configuration in cryogenic set-ups.

Symmetry-induced giant vortex state in a superconducting Pb film with a fivefold Penrose array of magnetic pinning centers

3.1 Introduction

Crystals are classified according to their translational and rotational symmetry (cf. 14 three dimensional Bravais lattices and the related 7 point symmetry groups)[14]. Until mid 80's, the lack of crystalline structures having a five fold rotation symmetry axis was generally accepted. However, the revolutionary discovery in 1984 of crystals with "forbidden" symmetry [62], introduced a new family of crystallographic structures, known as quasicrystals. These new structures are like crystals in that they have long-range translational order and long-range orientational order, however the translational order is not periodic¹ and the structures have no rotational point symmetry group². Instead, the quasicrystals are quasiperiodic, a well-defined but more subtle kind of translational order and although they have no rotational point symmetry group, they exhibit long-range orientational order. Experimentally, this quasiperiodicity was observed by Shechtman in the diffraction patterns produced by certain Aluminium-Manganese alloys, for which he was awarded

¹In case of periodic translational order, a translational operation exists carrying the lattice in itself. This means that there exists a Bravais lattice.

²The point group of a crystal is the collection of symmetry operations (rotations, inversions, reflections) applied about a lattice point carrying the lattice into itself.

the Nobel price in chemistry in 2011. Quasiperiodic tilings in two dimensions with similar properties as the quasicrystals discovered by Shechtman, were already earlier introduced by Penrose [63] in a mathematical context. These famous two dimensional Penrose tilings, combine two different unit cells or tiles to fully cover a two-dimensional plane. The resulting tilings possess likewise quasiperiodic translational order and long-range orientational order.

The interest to the unique properties of quasi crystals has nowadays surpassed the boundaries of the crystallographic community and reached most research fields in condensed matter physics [64, 65, 66, 67, 68]. Particular attention has been recently devoted to the pinning properties of flux lines in superconducting thin films with aperiodic, fractal or quasiperiodic arrays of pinning sites [69, 70, 71, 72, 73, 74].

In this Chapter we will first introduce the extraordinary properties of a quasiperiodic tiling. Next, the pinning properties of flux lines in periodically nano-structured superconductors are discussed and compared with the theoretical predictions (Molecular dynamics) [69, 70] and experimentally measured (indirect transport measurements) [72, 73] commensurability effects in quasiperiodic nano-structured superconductors. We used scanning Hall probe microscopy as introduced in Chap.2, to directly visualize the flux distribution in a specific two-dimensional quasiperiodic nano-structured superconductor, containing a five-fold Penrose array of Co dots underneath a Pb film. The obtained flux distributions not only show the theoretically and experimentally anticipated vortex configurations for specific matching fields but unveil new and so far unpredicted vortex patterns. The most fascinating result is the collective and synchronized arrangement of both, pinned and interstitial vortices, forming ring-like structures which stabilize a giant vortex at the center of this "vortex corral". To the best of our knowledge, this finding represents the first direct evidence of symmetry induced giant vortices, a long standing subject of theoretical investigation which remained experimentally elusive up to now.

3.2 The quasiperiodic Penrose tiling

In this work we will use the famous two-dimensional rhombus Penrose tiling as a quasi periodic modulation of the trapping potential for flux lines. However, before discussing the resulting effects on the vortex distribution, let us discuss first the properties of this specific quasiperiodic tiling[75]. An ideal quasiperiodic tiling is constructed by the infinite repetition of two or more distinct "cells" or "tiles", packed in a lattice that has long-range quasiperiodic translational order and long-range orientational order. We illustrate the

latter two terms "long-range quasiperiodic translational order" and "long-range orientational order" within the rhombus Penrose tiling, after discussing the construction of this tiling.

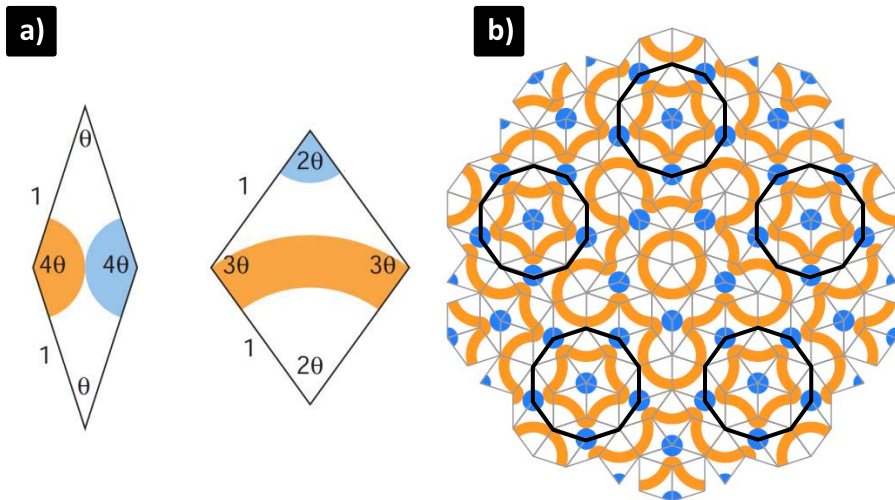


Figure 3.1: (a) The geometry of the Penrose rhombs, the basic building blocks of the two-dimensional Penrose Patterns. The matching rule restricting the juxtapositions is illustrated by the coloured circular arcs and $\theta = 36^\circ$. (b) Two-dimensional Penrose tiling, illustrating how the rhombuses fit together using the matching rule. Five decagons are shown in boldface, illustrating the ten-fold, long-range orientational order[76].

Construction

The two-dimensional rhombus Penrose tiling is constructed from a basis set of two rhombuses. These basic building blocks, the so-called thick and thin rhombs, are depicted in Figure 3.1(a). Both rhombs have identical edge lengths and all interior angles are multiples of 36° . To assure that the tiles form a non-periodic tiling, restrictions have to be made on the assembly of the tiling. For example, no two tiles can form a parallelogram, as this would allow a periodic tiling, however this is not a sufficient constraint for aperiodicity of the tiling. The so called matching rules to obtain aperiodicity, restrict the juxtapositions between tiles and can be described in several ways. One way is illustrated in Figure 3.1(b), here tiles must be assembled such that the curves on the faces match in colour and position crossing an edge. The golden ratio, $\tau = (\sqrt{5} + 1)/2 = 1.618$, satisfying $\tau^2 = \tau + 1$, shows up in several properties of the rhombus Penrose tiling. In an infinite Penrose tiling, the two rhombuses

occur in the ratio of the golden mean, with the larger tile being more prevalent. Moreover, the ratio of the areas of the thick to the thin rhombus is equal to the golden mean.

Properties

A Penrose tiling has several interesting properties. First of all, as the interior angles of the tiles are multiples of one-tenth of a complete rotation, a Penrose lattice has ten-fold, **long-range orientational order**. This is illustrated by the boldface decagons with identical orientations in Fig.3.1(b).

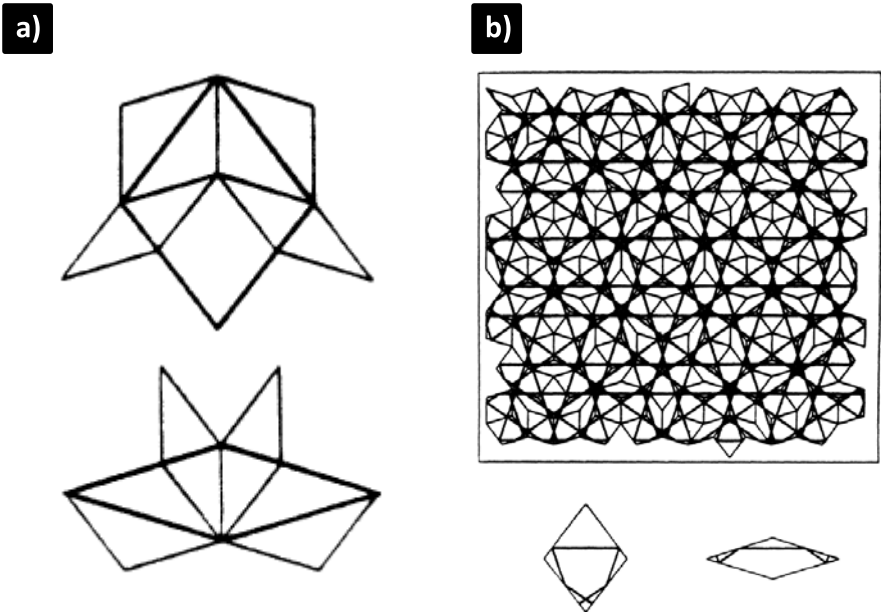


Figure 3.2: (a) The deflation rules for the two cells. (b) Each tile in Fig.3.1 has been decorated with line segments as shown. These segments join to form five sets of quasiperiodically spaced parallel lines[75].

On top, they possess the more subtle, **quasiperiodic ‘translational’ symmetry**. The definition of a quasiperiodic function is that it can be expressed as a sum of periodic functions, where at least some of the periods are incommensurate (i.e. have an irrational ratio.). There are several ways to demonstrate this for the rhombic Penrose lattice. The nicest way is pointed out by Ammann[75], who showed that by decorating each tile with a line segment as according to Fig.3.2(b), the line segments join to form sets of continuous lines running parallel to each of the symmetry axes of a pentagon. The position of

the Nth line of a parallel set is given by:

$$x_N = N + \alpha + \frac{1}{\tau} \left[\frac{N}{\tau} + \beta \right], \quad (3.1)$$

here τ is the golden ratio; α, β are arbitrary real numbers and $\lfloor \cdot \rfloor$ represents the greatest integer function. The alpha parameter alone will result in a periodic spacing, while the second term increases by τ^{-1} every time N is increased by τ . As τ and 1 are irrational, this satisfies indeed a quasiperiodic function. The spacing between two consecutive parallel lines ($x_N - x_{N-1}$) is given by L or S where $L/S = 1 + 1/\tau$. This quasiperiodicity will result in sharp Bragg spots in a diffraction pattern.

The Penrose tiling is also **self-similar**³, meaning it is exactly or approximately similar to a part of itself. As such, a so called deflation rule or self-similarity transformation exists to form a new tiling with all unit cells scaled down by a constant factor. This deflation rule is illustrated in Fig.3.2(a) and is closely connected with the appearance of the golden ratio in Eq.3.1. The self-similarity results in many built-in periods within the Penrose lattice.

3.2.1 Commensurability effects in periodic nano-structured superconductors

With the advent of modern lithographic techniques it is possible to structure superconductors at the micro-and nano-meter scale. By nano-structuring, it is possible to create an artificial potential in which the superconducting condensate or flux lines are confined. Confinement of the condensate itself at it's characteristic length scales, the coherence length and the penetration depth, can result in mesoscopic effects where the boundary conditions and the confinement geometry predominantly determine the superconducting properties [77, 40, 41, 78]. In this work, however, we focus on the effect of a spatial modulation of the trapping (pinning) potential on the properties of the flux line lattice. Resonant or commensurability effects are expected when the scale of the modulation matches the field dependent lattice constant of the vortex lattice, c.f. Eq.1.47.

When arranging the pinning centers in a regular (translational-invariant) periodic lattice, so called matching effects are observed as a consequence of commensurability between the vortex lattice and the periodic pinning potential. In particular the first matching field,

$$H_1 = \Phi_0/S, \quad (3.2)$$

³Many objects in the real world do posses this property, eg. fern leaves, fractals,etc.

is defined as the field where the density of vortices equals the density of pinning centers forming the lattice with a unit cell area S . Similarly, matching features are expected to appear at integer or rational multiples of H_1 , due to commensurability between the vortex lattice and the pinning array. In general these matching fields are denoted as,

$$H_n = n \times H_1 \quad \{n\} \in \mathbb{N}, \quad (3.3)$$

$$H_{p/q} = \frac{p}{q} \times H_1 \quad \{p, q\} \in \mathbb{N}, \quad (3.4)$$

respectively. These commensurability effects result in a strong overall enhancement of j_c compared to a film without a regular pinning array. On top, when the matching conditions between the vortex lattice and the regular pinning potential are fulfilled, sharp local maxima in $j_c(B)$ appear close to T_c . This enhancement is a consequence of the perfect compensation of the vortex-vortex interaction at every matching field, resulting in a more stable vortex configuration.

However, the highly symmetric configuration resulting in a local enhancement of j_c at the matching conditions, can promote at the same time channeling or guidance of vortices for particular current directions. This results in a strong suppression of the critical current for these particular current directions [79, 80]. To prevent this channeling effect, random pinning centers can be introduced at the expense of suppressing the matching features [81]. An alternative way is presented below, where the extraordinary properties of quasiperiodic arrays (cf. Sec.3.2) of pinning centers have been used.

3.2.2 Commensurability effects in quasiperiodic nano-structured superconductors

The effect of quasiperiodic and fractal pinning arrays is more recently investigated in Ref.[69, 70, 72, 73]. Quasiperiodic pinning arrays have, from technological point of view, several advantages as compared to periodic pinning arrays. In this case, the lack of perfect periodic translational order of the pinning landscape prevents the formation of one-dimensional channels for easy vortex flow. Moreover, whereas in regular pinning arrays the enhancement of $j_c(B)$ occurs only for applied fields close to the matching conditions, the convolution of many build-in periods (self-similarity) present in a quasi crystal favors the proliferation of many matching features or an extremely broad peak in $j_c(B)$. In principle, both properties tend to improve the maximum current attainable without dissipation, i.e. the superconducting critical current.

Indeed, it is shown that a quasi-periodic tiling can result in a dramatic increase of j_c even compared to triangular or random pinning arrays. It is worth noticing that, unlike a regular periodic pinning array, the vortex-vortex interaction is never perfectly compensated in a quasiperiodic lattice.

Molecular dynamic simulations of driven vortices interacting with a rhombic two dimensional Penrose array of pinning sites predicted local enhancements of the critical current at external fields $H = 0.757H_1$, H_1 , and $1.482H_1$, where H_1 is the field at which the density of singly quantized vortices coincides with the density of pinning centers [69, 70]. The non trivial matching features below and above H_1 , should correspond to the occupancy of three out of four pinning sites in the vertices of the thin tiles and the presence of an interstitial vortex in each thick tile, respectively. Indirect evidence of these stable vortex configurations has been obtained by transport measurements for a Penrose array of holes in a Nb film [72] and magnetic dots in Al and Pb films [73]. In both experimental investigations additional unforeseen features were also reported. Unfortunately, the lack of direct visualization of the vortex patterns in this sort of systems have concealed the real space vortex arrangement associated with the observed matching features in the transport properties.

3.3 Results

In this section we establish a clear correlation between the theoretical predictions and the transport measurements by mapping the local field distribution in a Pb film covering a Penrose array of Co dots via scanning Hall probe microscopy (SHPM). The vortex patterns, directly visualized at $H = 0.765H_1$ and $H = H_1$, are in agreements with the theoretical expectations. Additional matching features below H_1 are investigated at $H = 0.25H_1$ and $H = (1/\tau)H_1$. However for these low field features the limited scan area cannot provide us with a complete picture of the corresponding vortex distribution. For $H > H_1$, interstitial vortices are placed inside the thick tiles, as anticipated by molecular dynamic simulations [69, 70]. However, as we will see below these interstitial vortices lie at a bistable position rather than in the geometrical center of the tile. Due to the long range vortex-vortex interaction, this degeneracy is lifted by the lack of reflection symmetry of the surrounding tiles. As a result, at certain magnetic fields the interstitial vortices accommodate themselves in order to achieve an ordered ring-like structure involving several tiles. Strikingly, this highly symmetric ring like structure is similar to that obtained in disk-shaped mesoscopic structures and results from the local field pressure exerted by the surrounding vortices. Complementary transport measurements show that this behavior leads to the appearance of a

clear matching feature at $H \approx \tau H_1$. Additional unforeseen commensurability effects above H_1 are also found at $H = 3.8H_1$ and $H = 6.0H_1$. However, the accompanying vortex distributions can not be probed by SHPM, as at these high fields, individual vortices can not be resolved anymore.

3.3.1 Sample details

In this work we will use the famous two-dimensional rhombus Penrose tiling, introduced in Sec.3.2, as a quasi periodic modulation of the trapping potential for flux lines.

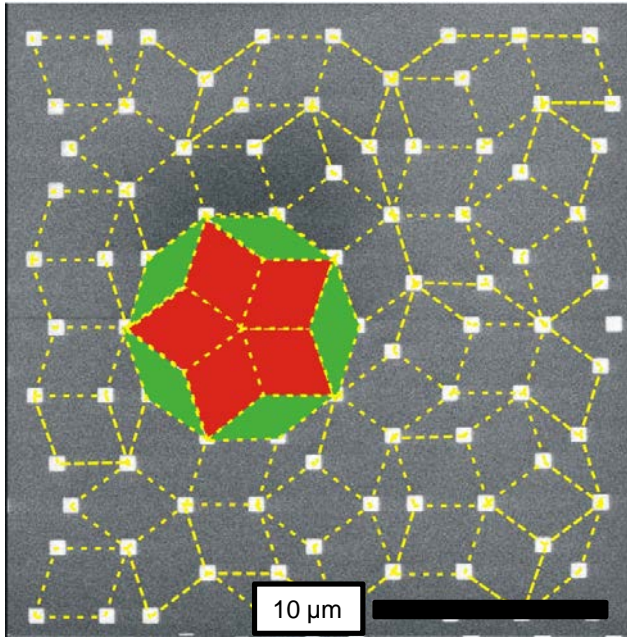


Figure 3.3: Scanning electron microscopy image of the square dots distributed in a five-fold Penrose array. For clarity, the dots are connected with dotted (yellow) lines. Five thin and thick tiles are painted with green and red color, respectively. The black bar indicates a distance of $10 \mu\text{m}$. [82]

The investigated samples consist of a 50 nm thick Pb film evaporated directly on top of a five-fold Penrose array of square Co dots made by electron beam lithography and subsequent lift-off. The experimental procedure used for the sample preparation can be found in Sec.2.3. Fig. 3.3 shows a scanning electron

microscopy image of the dot array. For clarity the magnetic particles have been connected by dotted lines to indicate the distribution of the thin and thick tiles, which represent the building blocks of the five-fold Penrose lattice. The size of the Co dots is $0.7 \mu\text{m}$ and the length of the connecting lines is $3.1 \mu\text{m}$. The pinning potential is created predominantly by a local depletion of superconductivity above the Co dots due to the proximity effect at the Co/Pb interface. Experiments performed before and after magnetizing the dots, show no differences, thus confirming that the electromagnetic coupling does not play a relevant role. For transport measurements the samples were patterned in a bridge shape, $102 \mu\text{m}$ wide with a voltage contacts' separation of $392 \mu\text{m}$.

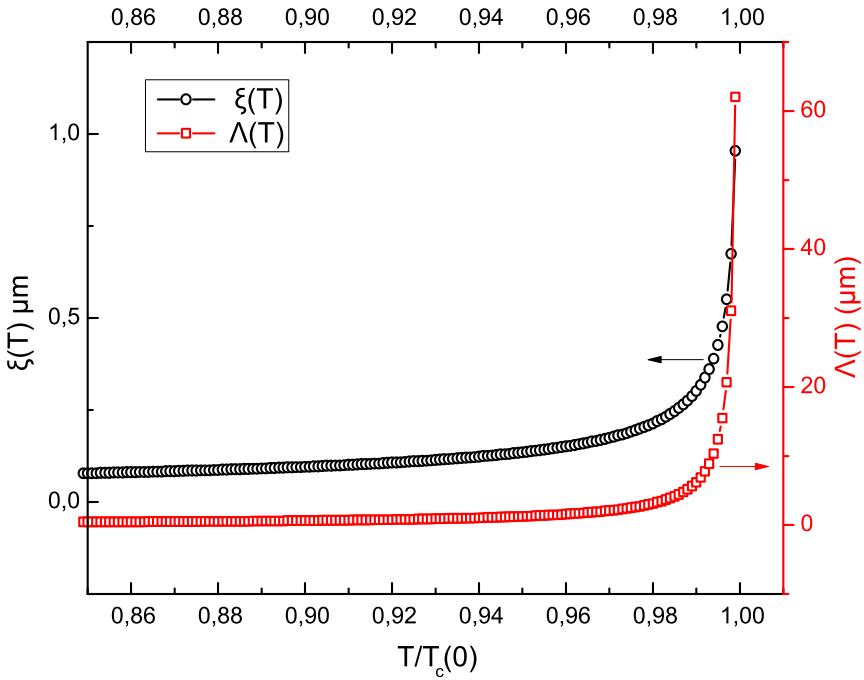


Figure 3.4: Temperature dependence of the coherence length and the effective penetration depth versus reduced temperature for a typical 50 nm Pb film, as derived from Eq.1.20 and Eq.1.48 using the dirty limit expressions for $\xi(T)$ and $\Lambda(T)$ (Eq.1.48) .

As in this chapter and the next, thin Pb films will be used to investigate vortex physics, we give here an overview of the characteristic superconducting length scales. The Pb film has a critical temperature $T_{c0}=7.24\text{K}$ as determined by 50% of the normal state resistance. The intrinsic BCS coherence length for pure Pb is $\xi_0=0.083\mu\text{m}$ and the London penetration depth is $\lambda_L=0.037\mu\text{m}$ (Values taken

from Ref.[2] p.24). From measurements of the temperature dependence of the perpendicular upper critical field $H_{c2}(T)$ of a reference film, Eq.1.28, we obtain from the $H_{c2}(T)$ slope, the superconducting coherence length $\xi(0)=0.033\mu\text{m}$. Using the dirty limit expression for the coherence length, Eq.1.20, the electron mean free path $\ell=0.015\mu\text{m}$ is found. As such, using similarly the dirty limit expression for the penetration depth, Eq.1.24, we obtain $\lambda(0)=0.06\mu\text{m}$. As we are dealing with a thin film restricting the screening-currents to the thickness of the film, t , the field is less efficiently screened resulting in an even larger penetration depth as suggested by Pearl, see Sec.1.7. This effective penetration depth, Λ , is given by, Eq.1.48. The temperature dependence of the effective penetration depth $\Lambda(T)$ and coherence length $\xi(T)$ for the 50 nm thick Pb film used in this work, are shown in Fig.3.4. For the experimental temperatures used in this work, $T>4.2\text{K}$, we obtain the following lower limits, $\kappa>3.3$, $\xi>0.046\mu\text{m}$ and $\Lambda>0.15\mu\text{m}$. Due to the dirty limit constraint and the fact that the increase of Λ with increasing temperatures is stronger than the increase of ξ , $\kappa_{\text{eff}}=\Lambda/\xi$ exceeds $\kappa(0)$ at the experimental temperatures and the film behaves as a type-II superconductor.

3.3.2 Transport measurements

We first investigated the vortex dynamics of the prepared sample by measuring a series of current-voltage characteristics as a function of field H at temperatures very close to T_{c0} . A detailed measurement of the voltage V vs H at constant current $I = 300\mu\text{A}$ and $T = 7.21\text{ K}$ is shown in the upper panel of Figure 3.5.

The first matching field $H_1 \sim 0.28\text{ mT}$ can be clearly identified as a pronounced dip in the dissipation, indicating that each pinning site can trap a maximum of one flux quantum⁴. The value of the first matching field, where we assume there is one flux quantum per tile, can also be derived from the geometric details of the Penrose lattice. Knowing that the thick(fat) tiles, having an area of $S_F=a^2 \sin \pi/5$, outnumber the narrow(small) ones by a factor corresponding to the golden mean, τ , we find with $a=3.1\mu\text{m}$,

$$< H_1 > = \frac{n_F H_{1F} + n_s H_{1s}}{n_F + n_s} = \frac{2\Phi_0}{(1 + \tau)a^2 \sin \pi/5} = 0.279\text{mT}, \quad (3.5)$$

We made use of several relations of the Penrose lattice. First of all in an infinite lattice, $n_F/n_s = \tau$, where n_F and n_s denote the number of fat and small tiles,

⁴This sharp decrease in the critical current typically indicates the appearance of interstitial vortices which drastically reduce the critical current as compared to double quantized ones.[77]

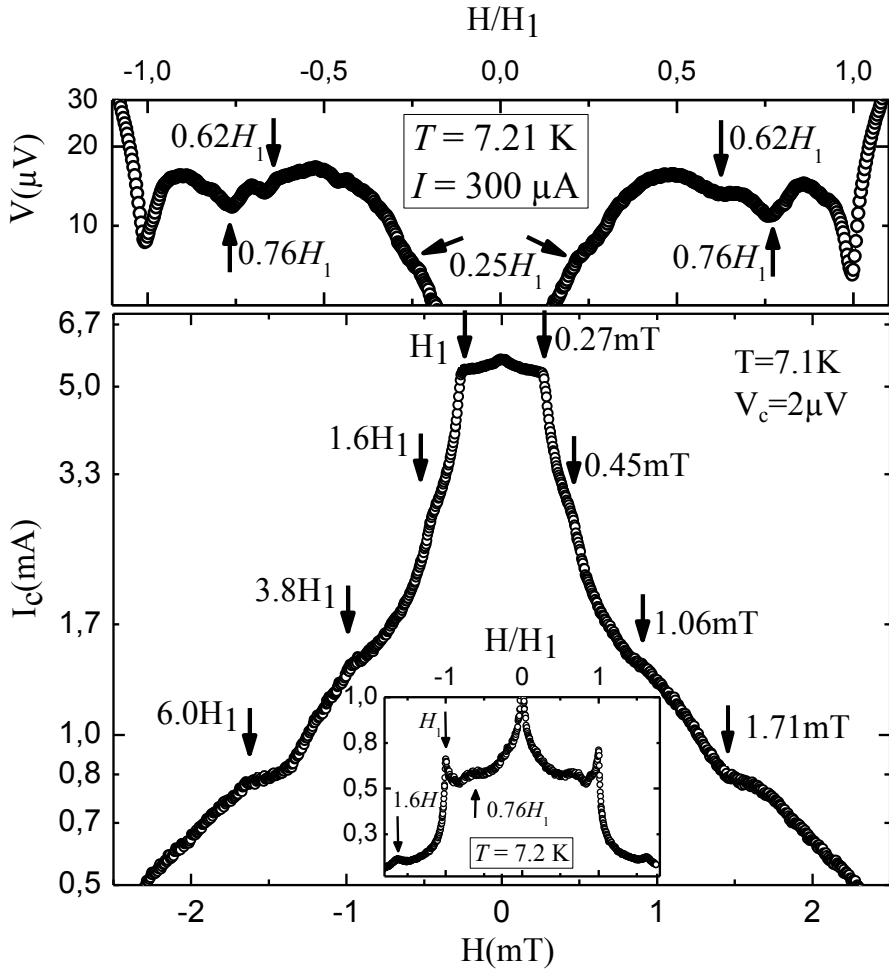


Figure 3.5: The upper panel shows the voltage for a fixed bias current of $300\text{ }\mu\text{A}$ as a function of the external field at $T = 7.21\text{ K}$. The lower panel and the inset shows the superconducting critical current, estimated with a voltage criterion of $2\text{ }\mu\text{V}$, as a function of the external field for $T = 7.1\text{ K}$ and $T = 7.2\text{ K}$, respectively. Matching features are indicated with black arrows.[82]

respectively. Further, the surface ratio between the fat and small tiles is given by, $S_F = \tau S_s$ and we defined $H_{1s} \equiv \phi_0/S_s$ and $H_{1F} \equiv \phi_0/S_F$, related by $H_{1s} = \tau H_{1F}$. This value agrees well with the experimentally obtained value, $H_1 = 0.28mT$, estimated from the sharp reduction of I_c .

Additional matching features are present at $H \sim 0.25H_1$, $H \sim 0.62H_1 \sim (1/\tau)H_1$ and $H \sim 0.76H_1 \sim \nu H_1 \sim (2/\tau^2)H_1$. These matching features were found in previous magnetoresistance measurements [73] and in molecular dynamic simulations [69, 73]. It is clear that the latter two can be related to the golden mean as derived from geometric considerations within the Penrose tiling and an assumption for the corresponding vortex distribution. The feature at $\mathbf{H} \sim 0.25\mathbf{H}_1$ is attributed to a situation where every flux line is surrounded by a corral of vacant pinning centers[73]. The dip at $\mathbf{H} \sim 0.76\mathbf{H}_1$ corresponds to a vortex distribution leaving one vacancy in one of the vertices of the thin tiles[70]. The feature at $\mathbf{H} \sim 0.62\mathbf{H}_1$ can be ascribed to the presence of one vortex line per thick tile[73].

To demonstrate the presence of stable vortex configurations at higher densities we plot the depinning current I_c , using a dissipation criterion of $2 \mu V$, for $T = 7.1$ K (Fig.3.5, lower panel). **Higher matching features** can be seen for $H \sim 1.6 \sim \tau H_1$, $3.8 H_1$, and $6.0 H_1$. It is worth stressing that typically commensurability effects in periodic pinning arrays are attributed to the perfect compensation of vortex currents, a condition which seems to be never satisfied in a quasiperiodic array.

3.3.3 Scanning Hall probe microscopy measurements

In order to clearly identify the microscopic vortex distribution associated with the different features observed in the $I_c(H)$ and $V(H)$ curves, we acquired scanning Hall probe microscopy images at different fields. The SHPM images presented in this work were recorded at $4.2K$ with a scanning area of $S_A = 14 \times 14 \mu m^2$ after field cooling the sample. Measurements performed at higher temperatures (up to $7.0K$) show no difference with those obtained at $4.2K$, thus indicating that the vortex distribution is frozen at high temperatures close to the onset of the superconducting state. The images were recorded in lift-off mode with the Hall sensor at about $1 \mu m$ above the surface of the sample. Xy positioners allow us to explore different regions of the same sample in order to avoid unwanted effects arising from the sample borders, imperfections, or small particles. A series of pictures obtained at 4.2 K after field cooling procedure with fields ranging from -1 mT to $+1$ mT ($-3.5H_1$ to $3.5H_1$) in steps of 0.005 mT allowed us to determine the remanent field with high accuracy. Indeed, notice

that steps of $0.010 \text{ mT} (\sim \phi_0/S_A)$ correspond to one extra vortex per scanning area between two consecutive images. Fig 3.6 summarizes the obtained images for a selected set of fields⁵ (different columns) and at three different locations on the Penrose pattern (different rows). In this figure we indicate the Penrose tiles with white lines for clarity. The determination of the dots' position was achieved by performing a scan in presence of a large external field ($\sim 400 \text{ mT}$) which produces a clear contrast of the Co microparticles as their magnetic moments are strongly aligned by the perpendicular field.

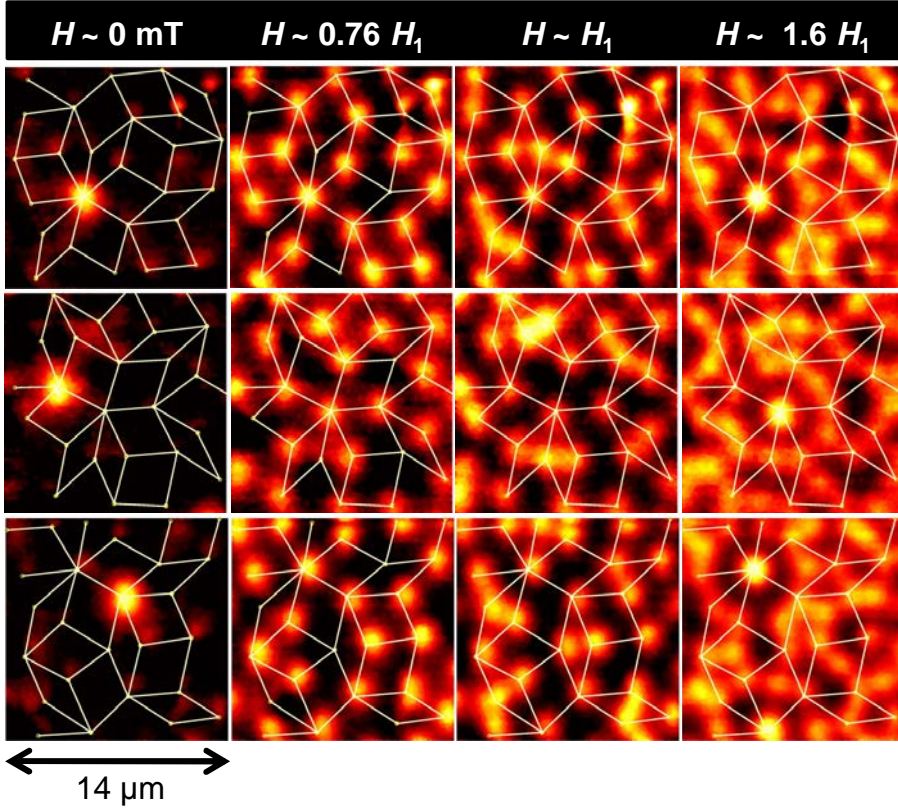


Figure 3.6: Scanning Hall probe microscopy images obtained after field cooling the sample down to 4.2 K . Each row corresponds to a different location of the array. The first, second, third and fourth columns corresponds to $H \sim 0 \text{ mT}$, $H \sim 0.220 \text{ mT} \sim 0.76 H_1$, $H \sim 0.275 \text{ mT} \sim H_1$, and $H \sim 0.455 \text{ mT} \sim 1.6 H_1$, respectively.[82]

⁵It is worth emphasizing that more than 600 images were acquired at each of the three different spots.

The first column in Fig. 3.6 shows the local field profile obtained at $\mathbf{H} \sim \mathbf{0}$. On this column, all panels show a single isolated vortex. The second column in Fig. 3.6 shows the vortex arrangement corresponding to the matching condition $\mathbf{H} \sim 0.76\mathbf{H}_1$ (see also Fig. 3.5). It is clear from this image that unoccupied pinning sites are located at one of the vertices of the thin tiles. This vortex distribution was anticipated by Misko *et al.* [70] based on the rapid increase of the vortex repulsion as the vortex separation decreases. The third column in Fig. 3.6 corresponds to the exact commensurability of the vortex lattice with the pinning landscape, $\mathbf{H} \sim \mathbf{H}_1$, i.e. every vortex sits on top of a Co dot. The last column illustrates the vortex pattern obtained at $\mathbf{H} \sim 1.6\mathbf{H}_1$. Here, due to the repulsive interaction between vortices, interstitial vortices are only inside the thick tiles. It is clear that these interstitial vortices tend to avoid the geometrical center of the tile. This is further supported by differential images, obtained by subtracting two consecutive field cooling around this matching feature[Fig. 3.7(c)]. This finding indicates that an interstitial bistable configuration exists inside each thick tile.

To indicate the stable energy positions within the thick tile, we calculated the spatial dependence of the interaction energy between a single interstitial vortex and the pinned vortices sitting at the corners of a thick tile, as such considering, in a first approximation, only the nearest neighbour interactions. The interaction energy is calculated as a superposition of the interaction energy between a Pearl vortex ‘i’ at position $\mathbf{r}_i = (x_i, y_i)$ within the thick tile and the pinned Pearl vortices ‘j’ sitting at the corners. For this an excellent fit for the interaction energy between two Pearl vortices is used as derived in Ref.[83],

$$V_{\text{int}}(r_i) = \frac{\phi_0^2}{2\pi\Lambda\mu_0} \sum_j \left[\ln\left(\frac{2.27\Lambda}{|\mathbf{r}_i - \mathbf{r}_j|} - \frac{0.27\Lambda}{9\lambda + |\mathbf{r}_i - \mathbf{r}_j|} + 1 \right) \right], \quad (3.6)$$

Further the dimensions of the thick tile are taken as $a = 3.1\mu\text{m}$ and $\Lambda = 0.15\mu\text{m}$ as discussed in Sec.3.3.1. The index ‘j’ in Eq.3.6 runs over the pinned vortices. Two local minima with equal energy are obtained. They are not in the center of the thick tile but along the long diagonal and offcenter by an amount $1.61\mu\text{m}$ or 54% .

The formation of ring-like structures or vortex corrals clearly seen in the last column of Fig. 3.6, demonstrates that a long range interaction eventually lifts this two-fold degeneracy of the interstitial positions. One of the discussed bistable states will become more favorable for vortex occupancy. This long range interaction is expected as we deal with a thin film and the vortices behave as Pearl vortices (cf. Sec.1.7.). More importantly, a detailed analysis of the field intensity at the core of the ring-shaped vortex structures indicates that the central vortex carries **two flux quanta**[see Fig. 3.7(f)]. These multiquanta

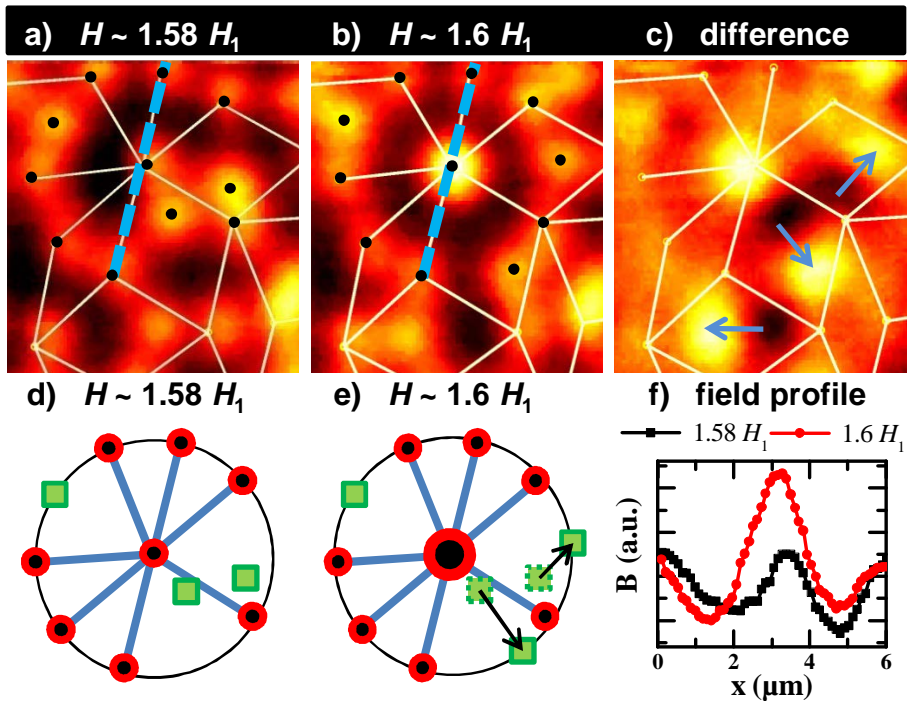


Figure 3.7: (Color) Scanning Hall probe microscopy images obtained at two consecutive field values, $H \sim 0.445 \text{ mT} \sim 1.58 H_1$ (a) and $H \sim 0.45 \text{ mT} \sim 1.6 H_1$ (b) together with the differential image (c) taken at a specific location where the vortex corral appears. Black dots in (a) and (b) mark the vortices illustrated in (d) and (e). Black and white spots in panel (c) indicate the change of position of individual vortices. In panels (d) and (e) a schematic representation of the vortex distribution is given for the two consecutive field values. Red circles represent pinned vortices and green squares represent the interstitial vortices. Panel (f) shows the magnetic field profile obtained along the dotted line drawn in panel (a) and (b) for both magnetic field values. Integrated field for $1.6 H_1$ clearly corresponds to the giant $2\phi_0$ -vortex.[82]

vortices are not a mere consequence of a stochastic distribution of pinning strength since they appear at well defined locations on the pinning landscape corresponding to multinodal agglomeration of Penrose tiles.

To obtain a better insight into the mechanism responsible for the creation of these multiquanta vortices we show the field profile corresponding to two consecutive images and their difference [Fig. 3.7 panel (a), (b) and (c)]

exactly at the creation of a vortex corral ($H \sim 1.6H_1$). A reconfiguration of the interstitial vortices creates a highly symmetrical vortex structure around specific multinodal points of the Penrose lattice. This process is schematically presented in Fig. 3.7 [panel (d) and (e)], which shows the distribution of pinned (red circles) and interstitial (green squares) vortices for both consecutive magnetic fields. At $H \sim 1.6H_1$ the mobile interstitial vortices rearrange themselves in a structure with high rotational order. The exact locations, where the vortex corral appears, are surrounded by ten vortices, seven pinned at the Penrose lattice and three interstitial vortices. As a result, a ten-fold rotational symmetry is obtained [Fig. 3.7(b) and (e)]. At the center of this highly symmetric vortex structure a multiquanta vortex is favored.

This unexpected result resembles the symmetry-induced giant vortex states in mesoscopic or microstructured superconductors close to the superconducting/normal phase boundary [84, 85, 86, 87, 88]. In that case, the boundary conditions impose the sample symmetry on the order parameter which manifest itself in the formation of unconventional vortex patterns as giant vortices or vortex-antivortex pairs. Here, the combination of the applied magnetic pressure, induced by the surrounding vortices, and the high local symmetry leads to the generation of a multiquanta vortex at the center of the vortex corral. This is in agreement with previous experimental [84, 89] and theoretical [90] reports showing that the number of vortices trapped by a single pinning site increases with increasing external field. In our particular case, it is the highly inhomogeneous *local field* which drives the system to the multiquanta vortex state.

It is important to emphasize that the theoretical investigations of the vortex matter in a five-fold Penrose array performed so far [69, 70], assumed a short range interaction between vortices. Since the present work has been done on a thin Pb film with thickness smaller than the temperature dependent penetration depth, a more suitable comparison should be done with long range repulsive Pearl vortices in the presence of a quasiperiodic array of pinning sites [28]. The combination of this long range vortex-vortex interaction with the large penetration depth expected by freezing the flux lattice at high temperatures are most likely necessary ingredients for the formation of a giant vortex state at $H \sim 1.6H_1$.

Now we discuss the two additional weak matching features observed in the transport measurements around $H \sim 0.62H_1$ and $H \sim 0.25H_1$ (see Fig.3.5). In Fig.3.8 we show scanning Hall probe images at two consecutive field values and their difference image to investigate the vortex pattern associated with the feature around $H \sim 0.62H_1$. We see that three out of four pinning sites in the vertices of the thin tiles are occupied with one or two defects,

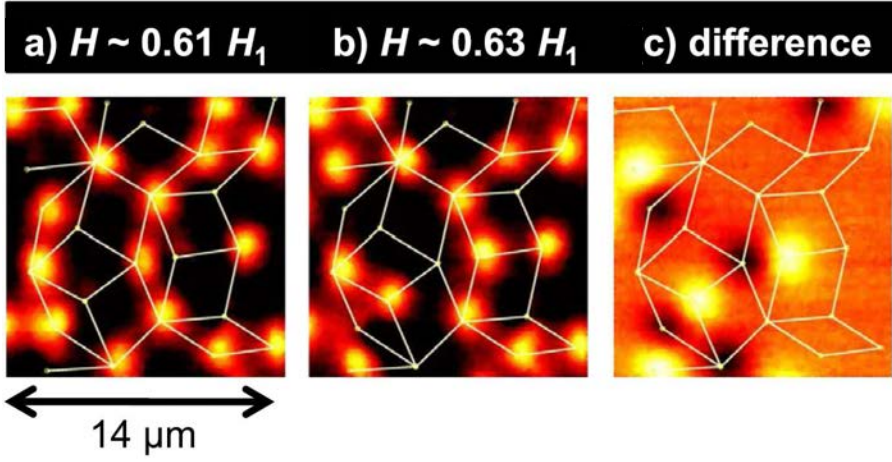


Figure 3.8: Scanning Hall probe microscopy images obtained at two consecutive field values, $H \sim 0.61H_1$ (a) and $H \sim 0.63H_1$ (b) together with the differential image (c) after field cooling the sample down to 4.2 K.[82]

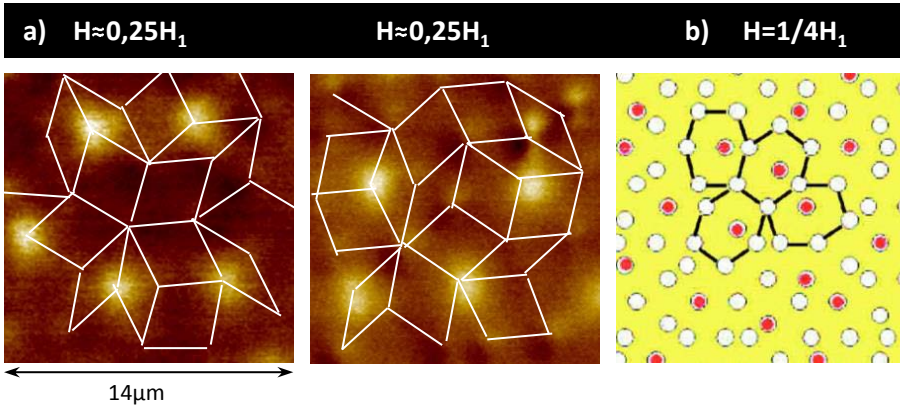


Figure 3.9: (a) Scanning Hall probe microscopy images obtained at two different location on the tiling after field cooling the sample down to 4.2 K in a field around $H \sim 0.25H_1$ (b) Possible vortex configuration at $H \sim 0.25H_1$ as determined by molecular dynamics simulations. Red dots indicate flux lines whereas open circles correspond to pinning sites.[73]

i.e., vortices not following this rule, per scanning area. We also notice that vortices arrange in ring-like structures and form vortex chains. Fig.3.9 shows scanning Hall probe images obtained around the matching feature $H \sim 0.25H_1$

and the corresponding result obtained from MD simulations[73]. As is clear from the MD simulations, every flux line is surrounded by a corral of vacant pinning centers as indicated by black lines. This distribution establishes a degree of correlation giving rise to the observed matching feature. A similar behavior is seen in the corresponding SHPM images obtained around this feature. Unfortunately, in both cases, $H \sim 0.62H_1$ and $H \sim 0.25H_1$ a larger scanning area is needed to discern the differences in the vortex distribution compared to the situation at $H \sim 0.76H_1$ and to extract a building rule for the vortex pattern at this matching field from the Hall probe images. Likely, the same argument as for the feature $H \sim 1.6H_1$ justifies the lack of the feature at $H \sim 0.62H_1$ and $H \sim 0.25H_1$ in the early molecular dynamics simulations which do not account for a long range interaction as expected for the Pearl vortices in this thin film geometry.

3.4 Conclusion

In conclusion, we have investigated the vortex distribution in a superconducting film with a Penrose lattice of Co dots by scanning Hall probe microscopy. The images not only show the theoretically anticipated vortex configurations for specific matching fields but unveil new and so far unpredicted vortex distributions. The most fascinating result is the collective and synchronized arrangement of both, pinned and interstitial vortices, forming ring-like structures which stabilize a giant vortex at the center of this "vortex corral". This arrangement indicates the importance of the interplay between the long range vortex interaction and the defining properties of the underlying quasiperiodic pinning potential. This chapter evidences the power of SHPM to discern and connect vortex properties measured before as a macroscopic response, involving millions of vortices, with the real microscopic vortex distributions.

First vortex entry into a perpendicularly magnetized superconducting thin film

4.1 Introduction

The magnetic response of a type-II superconductor is radically different depending on whether the superconductor is in the Meissner state, characterized by a reversible magnetic response, or in the mixed state, where vortices appear. The free motion of these vortices gives rise to energy dissipation and to an irreversible response. The transition between the Meissner and the vortex state is very crucial from a fundamental point of view as well as for applications, although it is never investigated at the single vortex level. In general, vortices do not simply enter the sample at the lower critical field H_{c1} , as discussed in Sec.1.4, but several contributions alter the entry field. These contributions include surface effects, the nucleation process of vortices at the edge, demagnetizing effects, etc. In this chapter, we study in detail the process of first vortex penetration in superconducting thin films. Superconducting thin films have a remarkable importance because the vast majority of applications for superconductivity involve this geometry. We first introduce some theoretical concepts, and then present experimental results from a carefully designed experiment. This experiment visualizes the first vortex penetration in a thin superconducting sample with a periodic array of antidots. Our results confirm that the mechanism for the first vortex penetration arises when the screening Meissner currents reach values of the depairing current (cf. Eq.1.75), breaking down locally superconductivity and thus leading to vortex nucleation.

4.2 Theoretical background

At which field vortices first appear in a zero-field cooled type-II superconductor?

The lower critical field

Vortex entry is thermodynamically allowed as soon as the applied field H becomes larger than the lower critical field H_{c1} [2]. The lower critical field, H_{c1} , is defined as the field at which the Gibbs free energy of the superconducting volume, \mathfrak{G}_s has the same value whether the first vortex is in or out of the sample. Thus at $H = H_{c1}$,

$$\Delta\mathfrak{G} = \mathfrak{G}_s|_{Meissner} - \mathfrak{G}_s|_{vortex} = 0 \quad (4.1)$$

For an Abrikosov vortex in a bulk sample the extra energy cost per unit length, ε_v is given in the London-vortex limit by Eq.1.43.

$$\varepsilon_v = \frac{\phi_0^2}{4\pi\mu_0\lambda^2} \ln\left(\frac{\lambda}{\xi} + 0.12\right) \quad (4.2)$$

Therefore in a superconductor with $n_v = N/A$ flux lines per unit area, the total energy cost due to vortices is, $\varepsilon_v n_v$ per unit volume. We assume that vortices are far enough from each other to neglect the vortex-vortex interaction energy. Each vortex carries a flux ϕ_0 , and so the change in the average induction in the sample, as compared to the Meissner state, is $dB = \phi_0 n_v$ ¹. The magnetic work per unit volume gained by the presence of vortices is $\mu_0 H dM = H dB$. The energy balance condition, Eq.4.1, takes the form

$$\Delta\mathfrak{G} = \varepsilon_v n_v - H \phi_0 n_v \quad (4.3)$$

Thus it becomes energetically favorable for vortices to enter a bulk sample when $H > H_{c1}$, where

$$H_{c1} = \varepsilon_v / \phi_0 = \frac{\phi_0}{4\pi\mu_0\lambda^2} \ln\left(\frac{\lambda}{\xi} + 0.12\right) = \frac{H_c}{\sqrt{2}\kappa} \ln(\kappa + 0.12) \quad (4.4)$$

where H_c is the thermodynamical critical field, defined as the condensation energy at zero external field and $\lambda(T)$ and $\xi(T)$ are the temperature dependent Ginzburg-Landau penetration depth and coherence length, respectively.

However, it is known that the Meissner state can remain thermodynamically metastable [91, 92, 93, 94] at higher magnetic fields, $H > H_{c1}$, up to the so

¹Here we consider a perfect infinite cylinder. As such we do not have to consider any demagnetizing effects.

called **superheating field**, H_{sh} , at which the first vortex penetrates. The determination of the field H_{sh} and the underlying criteria for first vortex entry has a long history.

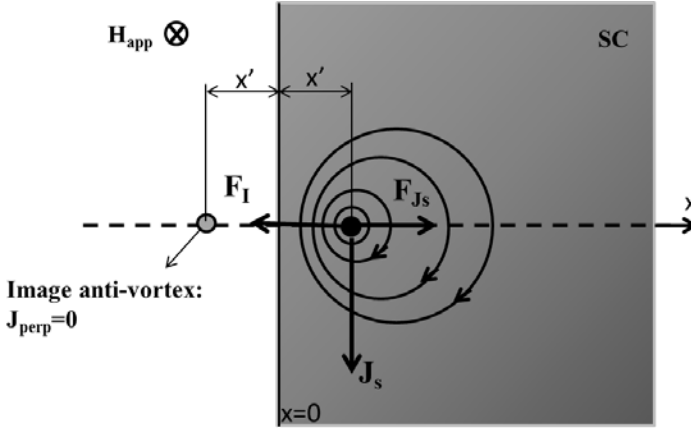


Figure 4.1: Top view of a superconducting half space occupying $x > 0$ containing a vortex at position x' . The external magnetic field, H_{app} , is applied as indicated and induces screening currents, J_s , in the superconducting half space. These decaying screening currents interact with the vortex located at position x' and produce a Lorentz force, F_L , towards the center of the sample. The vortex supercurrent distribution is distorted near the surface. This can be described conceptually by placing an image anti-vortex at position $-x'$ which acts attractively, F_I , on the vortex at position x' . As such, the distortion of the vortex supercurrent distribution results in an attractive force towards the surface.

The Bean and Livingston surface barrier field

A pioneering work [91] of Bean and Livingston (BL) describes, within the London limit, the effect of a surface on vortex penetration. They considered a vortex inside a type-II superconducting half-space parallel to a smooth surface as depicted in Fig.4.1. Close to the surface, the vortex' supercurrent distribution is distorted, as described by an image anti-vortex. The concept of an image anti-vortex to describe the distortion of the vortex' supercurrent distribution assures no current can flow perpendicular to the surface. Since currents with opposite senses attract, this results in an attractive force between the vortex and the surface. Work has to be done against this attractive force for a vortex to escape the attractive surface potential and to move into the bulk of the sample. The amount of work required per unit length equals the

interaction energy between two vortices, given by Eq.1.44. The energy per unit length of a vortex at a distance x' from the surface is given by,

$$\varepsilon_1(x') = \varepsilon_v - \frac{\phi_0^2}{2\pi\mu_0\lambda^2} K_0\left(\frac{2x'}{\lambda}\right) \quad (4.5)$$

where ε_v is the energy per unit length of a vortex far from the surface. Closer to the surface it is clear the interaction between the vortex and the image antivortex results in a lower energy. On the other hand, the vortex experiences a repulsive Lorentz force at the surface arising from the screening currents induced by the external magnetic field. This results in an energy per unit length of:

$$\varepsilon_2(x') = \phi_0 H_{surf} e^{-x'/\lambda} \quad (4.6)$$

Where H_{surf} , denotes the local field at the surface of the superconducting half space. As such the total potential energy per unit length of a vortex at a distance x' from the surface is given by:

$$\varepsilon_T(x') = \varepsilon_1(x') + \varepsilon_2(x') = \varepsilon_v - \frac{\phi_0^2}{2\pi\mu_0\lambda^2} K_0\left(\frac{2x'}{\lambda}\right) + \phi_0 H_{surf} e^{-x'/\lambda} \quad (4.7)$$

The dependence of ε_T is shown in Fig.4.2 as a function of position. For low fields a vortex parallel to the surface is impeded to penetrate, even though a vortex solution is thermodynamically allowed in the bulk for fields above H_{c1} . At higher fields, the repulsion from the surface due to the Meissner screening currents begins to dominate, resulting in a lower vortex energy in the center of the sample as compared to the edge. It is clear that the competition between both forces, results in the so called BL surface barrier for vortex entry. It was shown in Ref.[91] that this barrier disappears when, $H > H_{BL}$

$$H_{BL} = \frac{H_c}{\sqrt{2}} = \frac{\Phi_0}{4\pi\mu_0\lambda(T)\xi(T)}, \quad (4.8)$$

where H_{BL} is the BL surface barrier field. This estimate of H_{BL} assumes that the maximum of ε_T is within a coherence length of the surface. At finite temperatures, one has to take into account the thermal energy of a vortex, which allows in principle thermally activated penetration of a vortex for fields below H_{BL} . It is shown in Ref.[95, 96], that this process becomes ineffective for low temperature superconductors and $T \ll T_c$ as the energy scale of the BL barrier exceeds $k_B T$ substantially. To probe the BL surface barrier field, the observation time of the experiment has to be much less than the minimum time required for vortex energy fluctuations resulting in thermally activated penetration.

The Nucleation field

Furthermore, H_{BL} does not represent yet the field determining first flux

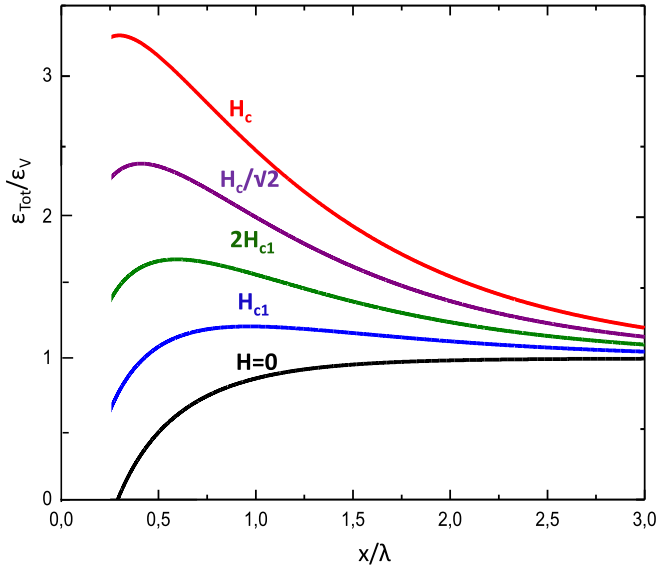


Figure 4.2: The distance dependence of total potential energy per unit length of a vortex at a distance x from the interface is illustrated for several applied magnetic field. The curves are calculated using Eq.4.7, with $\kappa = 5$ and $\lambda = 0.6\mu\text{m}$.

penetration, because it ignores the nucleation of the vortex at the border[97]. It was shown in Ref.[92, 93, 94, 98, 99], by investigating the onset of instability of the Meissner solution within the Ginzburg-Landau theory, that the necessary condition for vortex entry into a superconductor is fulfilled when the Meissner screening current density at an ideal defect-free surface approaches the depairing current density j_d of a one dimensional superconducting channel.

$$j_{\text{edge}} = j_d = \frac{H_c}{\left[\frac{3\sqrt{6}}{4} \lambda(T) \right]}, \quad (4.9)$$

We denote with \mathbf{H}_{j_d} , the external applied field where this criterium for the superheating field is met. The difference between Eq.4.9 and the London expression for the depairing current[1] is given by the factor $3\sqrt{6}/4=1.84$. This factor results from the decrease of the density of states with increasing current. It is described within the first Ginzburg-Landau equation, which expresses conservation of energy and effectively couples the Cooper pair-density with the pair velocity. This necessary condition and it's consequences for vortex entry

will be discussed further on in this chapter.

Demagnetizing effects

The sample geometry can play a crucial role for the vortex penetration, as it determines the current distribution within and at the edges of the sample. For example, for samples with a large demagnetization factor, such as thin films (width \gg thickness) in a perpendicular field, the strong curvature of the field lines at the edges can introduce a broad current distribution across the entire top and bottom surfaces and across the strip width. When the sample is thicker than the penetration depth, a competition between the line tension of a vortex cutting through the upper and lower ridges at the sample edge and the Lorentz force induced by the Meissner currents results in a so called geometrical barrier[100, 101]. When the sample thickness is smaller than the penetration depth, vortices are unable to tilt. However the hybrid effect of the distortion of the supercurrent flow caused by the strip geometry itself and the vortex' supercurrent deformation near the edges results in a so called edge barrier[102].

Indirect experimental verification of the superheating field and the correlation with the above described models was based on detecting the onset of nonlinearity of the initial magnetization in bulk superconductors[103, 104, 105]. We propose here a more direct and reliable way to determine the superheating field by imaging, with single vortex resolution, the first entered vortex in a thin superconductor. In order to achieve this goal, a careful sample design and fabrication has to be complied. Firstly, the presence of surface defects may create spots for premature entry of vortices [106, 93, 107], thus hindering the study of the intrinsic mechanisms. Secondly, in thin film geometry, vortices will move to the center of the sample as soon as they nucleate [108] making it impossible to experimentally observe their entry. The former problem can be solved by using a superconductor with well defined edges, whereas creating an array of antidots, acting as pinning centers, allows one to keep the entered vortices relatively close to the sample's edge, where they can be directly visualized by SHPM.

4.3 Sample details

In this work we study two high-quality Pb superconducting strips of widths $2a = 300\mu\text{m}$ (Sample A) and $2a = 600\mu\text{m}$ (Sample B), and thicknesses $t = 50$ nm, see Fig.4.3.

Sample A contains a triangular array of antidots with an antidot void area of

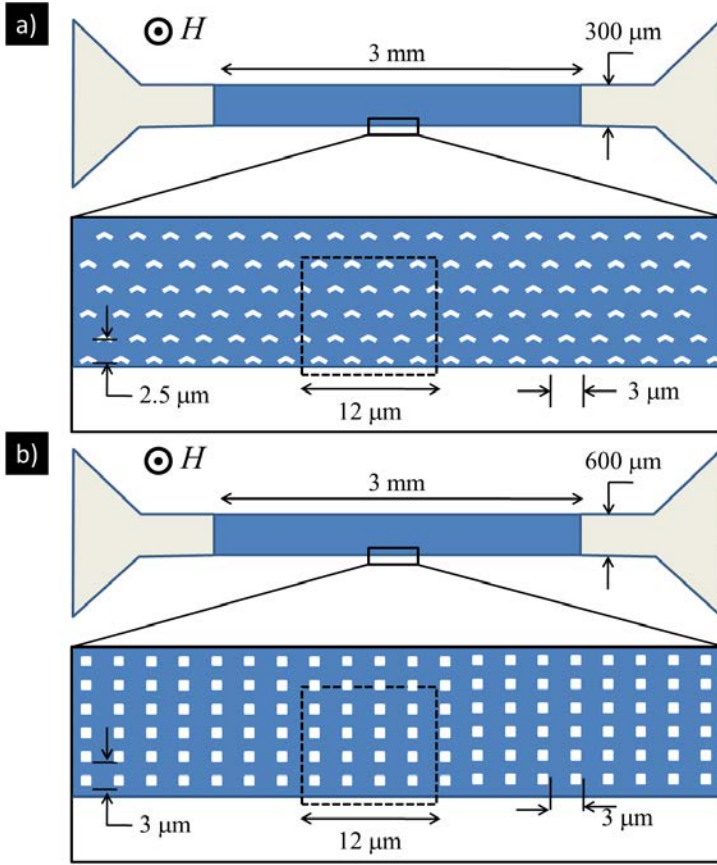


Figure 4.3: (a) Schematic layout of the investigated sample A. The upper panel shows the transport bridge with a 3 mm long patterned area. The lower panel shows a zoom-in close to the sample's border. The box indicated by the dashed line shows the area where most of the scanning Hall microscopy images were obtained. (b) Similar schematic layout of the investigated sample B.

$0.28\mu\text{m}^2$ obtained by electron beam evaporation and subsequent lift-off. The sample was deposited on top of a SiO_2 insulating substrate. The antidots have a V-shape with each leg of the V being $0.8\mu\text{m}$ long and $0.2\mu\text{m}$ wide and forming an angle of 120° . The period of the pattern is $w = 3\mu\text{m}$ which corresponds to a commensurability field $H_1 = (2\phi_0)/(\sqrt{3}w) = 0.27\text{mT}$ at which the density of vortices and antidots coincide, as described in Sec.3.2.1.

Sample B contains a square array of square antidots with an antidot void

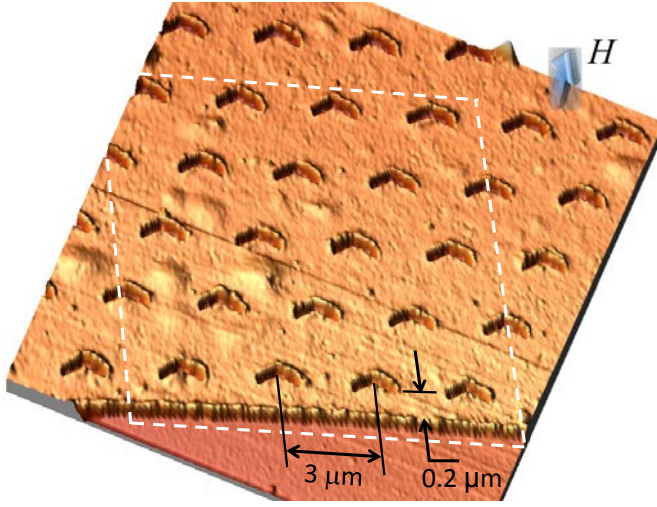


Figure 4.4: Atomic force microscopy image of Sample A. The box indicated by the dashed line of $12\text{ }\mu\text{m}$ side, shows the area where most of the scanning Hall microscopy images were obtained. Notice that the first row of boomerang shaped antidots is only $0.2\text{ }\mu\text{m}$ away from the edge of the film. The arrow indicates the direction of the applied field perpendicular to the plane of the film.

area of $0.36\text{ }\mu\text{m}^2$, obtained by an identical production process. The periodicity of the antidot lattice is likewise $3\text{ }\mu\text{m}$, resulting in a commensurability field $H_1 = (\phi_0)/(w^2) = 0.23\text{mT}$. The superconductor to normal transition at zero field occurs at $T_c = 7.2\text{K}$. Typical values of the superconducting coherence length and penetration depth at zero temperature estimated in similar samples are $\xi(0) \approx 33\text{ nm}$ and $\lambda(0) \approx 50\text{ nm}$, respectively. More details about the characteristic length scales can be found in Sec.3.3.1. Fig.4.4 and Fig.4.5 show representative atomic force microscopy images of the Sample A and Sample B surface, respectively. Notice that the antidots are close to the border but not at the border in order to avoid the creation of spots of premature flux entry. Further details about sample preparation can be found in Sec.2.3. In all cases the magnetic field is applied perpendicularly to the plane of the film. Local magnetic field measurements were carried out via scanning Hall probe microscopy (SHPM) near the sample's border. It is important to note that although previous works have shown spatial resolved flux penetration in bulk and thin films [109], the power of SHPM allows us to determine unambiguously the flux penetration with unprecedented resolution of a single vortex.

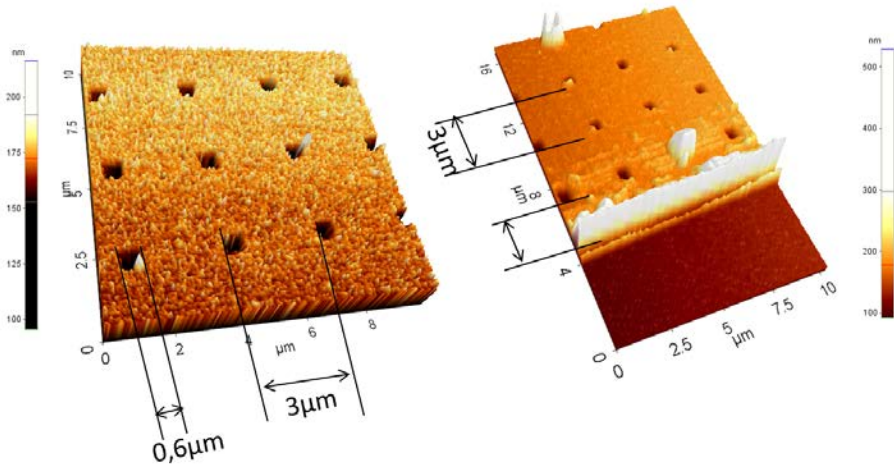


Figure 4.5: Atomic force microscopy image of Sample B. The left picture shows a representative image in the center of the sample, while the right AFM picture surveys a representative area at the edge of the sample. The large peak appearing at the edge and the peaks in some of the antidots are due to resist residues.

In samples with periodic arrays of antidots, stable vortex arrangements are expected for every value of field at which the vortex lattice commensurates with the antidot lattice, as theoretically studied via molecular dynamics simulations in [111, 110]. A way to quantify the quality of the samples consists of imaging low matching features where the vortex-vortex interaction is weak and therefore small imperfections on the pattern have a sizeable impact on the vortex distribution. Experimentally we can obtain near-to-equilibrium vortex distributions by performing field cooling experiments. Some examples of the resulting flux patterns for sample A directly visualized via SHPM at $T = 6.9$ K, and for different applied fields are shown in the upper row of Fig. 4.6. The observed sub-matching vortex patterns at $H = 0.33H_1$, $H = 0.52H_1$ and $H = 0.63H_1$, where H_1 is the first matching field, are in agreement with previous theoretical predictions [110] schematically depicted in the second row of Fig. 4.6. It is important to emphasize that the mere existence of regular patterns in the above field-cooling (FC) experiments is indicative of a low dispersion in pinning energy among different pinning sites and the fingerprint of a highly homogeneous sample [40, 77, 112, 113, 114, 115]. Vortex distributions above first matching, e.g. at $H = 1.3H_1$ [Fig. 4.6], show the appearance of double quantized vortices. Similarly, the near-to-equilibrium vortex distributions

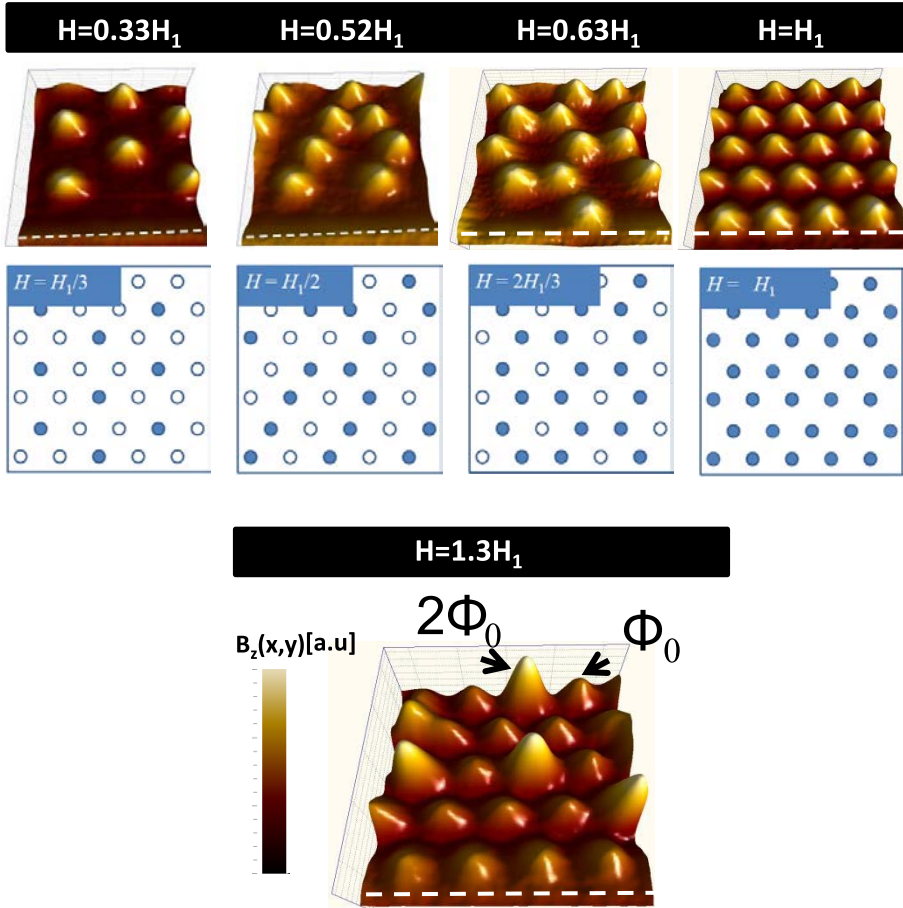


Figure 4.6: Upper row: scanning Hall probe microscopy images obtained for sample A at the sample's edge as indicated by the dashed box in Fig. 4.4 after cooling down to $T = 6.9$ K in presence of a field $H = 0.33H_1$, $H = 0.52H_1$, $H = 0.63H_1$ and $H = H_1$. The dashed line indicates the sample's edge. Second row: schematic representation of the expected vortex patterns according to Ref.[110]. Here the open (filled) circles represent empty (occupied) pinning sites. Lower row: scanning Hall probe microscopy images obtained for sample A at the sample's edge after cooling down to $T = 6.9$ K in presence of a field $H = 1.3H_1$.

obtained by FC in sample B show high quality commensurability effects, as will be further discussed in Chap.5.

4.4 Experimental results

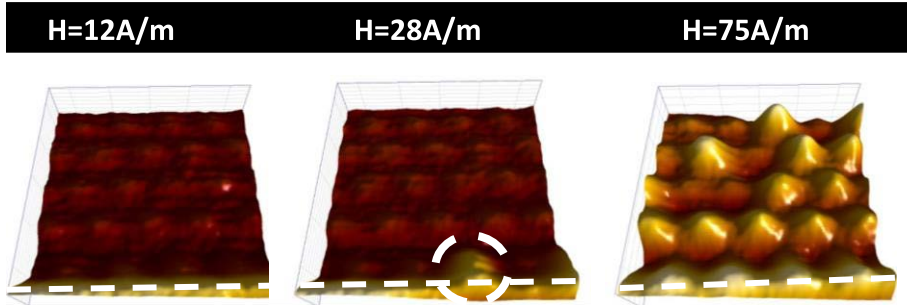


Figure 4.7: Scanning Hall probe microscopy images obtained at the sample's edge upon increasing external field, after preparing the sample in a zero-field cooled state at $T = 7$ K; for a field $H = 12$ A/m the sample is in the Meissner phase, at $H = 28$ A/m the first vortex enters as indicated by the white circle and at $H = 75$ A/m a more complex vortex state is observed. The dashed lines indicate the sample's edge.

We now focus on the vortex entry under zero-field-cooling condition. Fig.4.7 shows SHPM images for sample A at the same spot as in Fig.4.6, next to the sample's edge, at $T = 7$ K and after a progressive increase of the external field. At low fields, $H = 12$ A/m, the superconductor is in the Meissner state and no vortices are observed inside the sample. The strong screening currents give rise to the well known magnification of the local magnetic field close to the sample's edge. By increasing the field stepwise in intervals of 4 A/m it is possible to determine experimentally the field H_{en} at which the first vortex enters the scanned area, as shown in Fig.4.7, for $T = 7$ K this happens at $H = 28$ A/m. Because of the restricted scanning area, H_{en} is an overestimation of the first vortex entry field. For fields slightly above H_{en} the first row (i.e. the row closest to the sample's edge) of antidots is completely occupied by vortices before a vortex appears in the second row. Further increasing the external field leads to a completion of the second row of antidots. This process ends when the second row is completely occupied, beyond which a far more complex penetration is observed, see Fig.4.7 at $H = 75$ A/m. Indeed, (i) vortices can move further inside the sample skipping empty rows of antidots, (ii) double quantized vortices appear although they never nucleate at the sample's edge. This penetration process was associated with the terraced critical state proposed theoretically by Cooley and Grishin [116], as studied experimentally in [117]. A similar process is observed in Sample B. The temperature dependence of H_{en} for sample A (black square symbols) and sample B (red circular and triangular

symbols) are shown in Fig.4.8. The different symbols for sample B reflect two distinct locations at the sample border used to obtain H_{en} . The fact that the experimentally obtained values for H_{en} are independent on the measurement location, demonstrates that the nucleation field is homogeneous along the sample border, validating our determination of the overall superheating field as a reliable and accurate estimation.

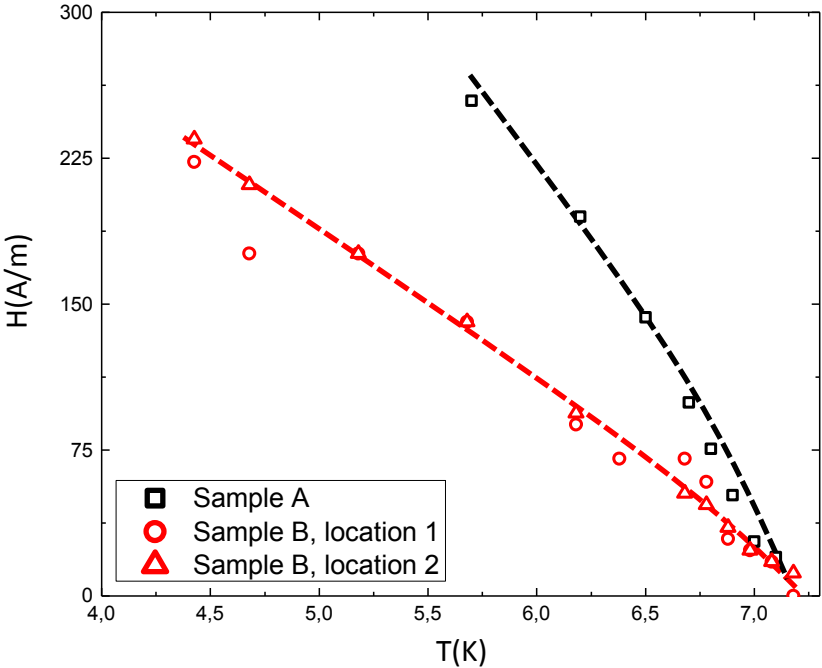


Figure 4.8: Temperature dependence of the field H_{en} at which the first vortex is visualized in the scanning area; Square symbols are experimental data obtained for sample A, whereas triangular and circular symbols present data obtained at two different locations for sample B. The dashed lines are a guide for the eye.

4.5 Discussion

Let's now compare these experimentally obtained values with the theoretical models for vortex entry. As explained above, the necessary criterium for vortex

entry is the requirement that the induced screening current density by an external magnetic field, H , at the edge matches the Ginzburg-Landau depairing current density, j_d , of a one-dimensional superconducting channel as given by Eq.4.9. The field where this condition is met, we denote with H_{j_d} . We need to extend the derivation for H_{j_d} , to the case of a perpendicularly magnetized thin superconducting strip.

To determine when the current density at the edge reaches this critical value, j_d , an expression for the current density at the edge has to be found. For an infinitely long thin strip of width $|y| < a$ and thickness, $|z| < t/2$, the complete current density distribution, $J(y)$, for a perpendicular applied external magnetic field field, $H\hat{z}$, was obtained as in Ref.[102] by solving numerically the Maxwell-London equations:

$$\frac{J(y)t}{H} = \frac{y}{\sqrt{\frac{1}{4}[a^2 - y^2] + \frac{\Lambda a}{\pi}}} \quad (4.10)$$

Where Λ denotes the effective screening length of the superconducting bridge. In the thin film limit (i.e. $\lambda \ll d$) the Ginzburg-Landau penetration length, λ , is replaced by the effective penetration depth[28], $\Lambda = \lambda(T)^2/t$. The reason for this is the reduced screening capacity of a very thin superconducting film (cf.Sec.??). It is shown in Ref.[118, 99, 119] that this expression derived from the Maxwell-London equations, fits over a broad range of parameters with the Ginzburg-Landau solutions for the screening-current distribution as long as $H < H_{\text{en}}$. Moreover, measurements of the magnetic field profile crossing the sample border when the sample is prepared in the Meissner state, can be well fitted using the current distribution in Eq.4.10 and Ampère's law. The agreement between the London limit approximation and the full Ginzburg-Landau solutions for the screening-current distribution in the regime $H < H_{\text{en}}$ can be interpreted as follows. First of all, our samples have a small κ at zero temperature, and therefore one could argue that the London limit approximation is not valid. However, due to the reduced screening efficiency in the thin film geometry, it is appropriate to use the effective penetration depth Λ . The increase of Λ with increasing temperatures is stronger than the increase of ξ . As a result, $\kappa_{\text{eff}} = \Lambda/\xi$ exceeds $\kappa(0)$ at the experimental temperatures (cf. Sec.3.3.1). Secondly, the condition $H < H_{\text{en}}$, means that there is a limited kinetic reduction of the density of states at the edge due to current induced depairing. Moreover, the periodic lattice of antidots forces the pair density to be nearly constant in the space between antidots, due to the boundary conditions at the superconductor-insulator interface[2].

However, we are interested in the condition that the induced screening current

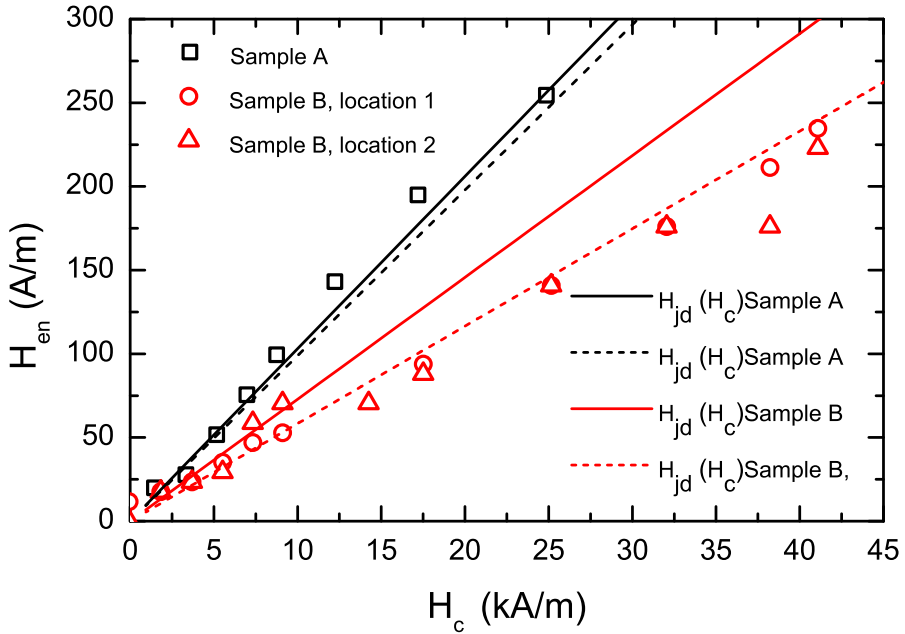


Figure 4.9: The obtained experimental data for the first vortex entry field versus $H_c(T)$ obtained by Dekker et al. is shown for sample A (square symbols) and for two locations at the border for sample B (circular and triangular symbols). The theoretical curves obtained from Eq.4.12 for sample A and B with $C=\frac{3\sqrt{6}}{4}$ are shown by the full black and red lines, respectively. The black and red dashed lines take into account the effect of the pattern induced enhancement of the screening current density for sample A and B, respectively.

at the edge of the sample approaches j_d . It is expected then that Eq.4.10 fails to describe the correct relation between the induced screening current density and the applied magnetic field particularly in the neighbourhood of the edge, as current-induced depairing will locally alter the density of states dramatically. However, at distances larger than the effective penetration depth away from the sample edge, the current density decreases quickly below the critical value for depairing and the London limit is restored. Since the global response of the superconducting strip to an applied magnetic field is determined by the whole current distribution, it is expected that in the limit $2a \gg \Lambda$, the London limit gives a very good description of the demagnetizing effects as it is valid in the majority of the sample volume. However, the condition for vortex entry is a local one and we have to take into account the effect of current induced

depairing at the edge. In first approximation, we will introduce this effect by using a new effective Ginzburg-Landau penetration length $\lambda' = C\lambda$ in Eq.4.10, as a cutoff factor at the edge. Here, C is a constant bigger than unity, since due to current induced depairing the screening-currents are weakened and the magnetic field is less effectively screened. Therefore, using Eq.4.10, the current at the edge ($y = a$) of the sample, is given by:

$$j_{edge} = \left[\frac{1}{C\lambda(T)} \right] \left[\sqrt{\frac{a\pi}{t}} \right] H \quad (4.11)$$

As such, rewriting j_{edge} and H as J_d and H_{jd} and using Eq.4.9 we obtain an expression for H_{jd} ,

$$H_{jd} = \left[\frac{C}{\frac{3\sqrt{6}}{4}} \right] \left[\sqrt{\frac{t}{a\pi}} \right] H_c(T) \quad (4.12)$$

As a result H_{jd} is determined by the temperature dependence of $H_c(T)$, a geometric demagnetizing factor and a constant related to the depletion of the condensate of our superconducting film.

The temperature dependence of H_c for bulk Pb samples was accurately measured by Decker *et al.*, leading to an extrapolated value of $H_c(0) = 63.87$ kA/m at $T = 0$ K [120]. This value is remarkably close to $H_c(0) = 64.06$ kA/m given in [121] for an amorphous Pb film. In Fig.4.9, the experimentally obtained values for $H_{en}(T)$ are plotted versus $H_c(T)$ obtained by Decker *et al.*[120]. According to Eq.4.12 and a linear fit of the data $H_{en}(T)$ for sample A (square symbols) versus $H_c(T)$, a slope of $(10, 6 \pm 0, 4) \times 10^{-3}$ is obtained. Taking into account the width, $2a=300\mu m$ and thickness, $t=50nm$ of the sample, we obtain for $C=1.03 \times \frac{3\sqrt{6}}{4}$. This means that if we enhance the Ginzburg-Landau penetration depth by this factor C to take into account the effect of current induced pairing within the London model expression for the screening-current density at the edge, a nice match is found between the experimental results, $H_{en}(T)$ and the theoretically estimated superheating field, $H_{jd}(T)$, as indicated by the full black line in Fig.4.9. The enhancement factor of the effective penetration depth, C , is in good agreement with the factor appearing in the Ginzburg-Landau expression for J_d due to current induced depairing. This is not a surprise, since in a bulk sample, in first approximation the field penetration at the edge can be assumed as an exponential decrease of the magnetic field, $B = B_0 e^{-y/\Lambda_{edge}}$. Where, Λ_{edge} is the locally increased penetration depth compared to the bulk value due to current induced depairing.

In the case of a thick superconductor, using an exponential penetration of magnetic field, the physical meaning of Λ_{edge} is nicely shown by applying Ampères Law:

$$|\nabla \times B| = \frac{B_0}{\Lambda_{edge}} = \mu_0 J_{edge}, \quad (4.13)$$

As the current density at the edge can be maximum the Ginzburg-Landau depairing current density, which is lower than the London depairing current density by a factor $(3\sqrt{6}/4)$, the field will be screened over a larger distance. It is clear from Eq.4.13 and Eq.4.9 that the new length scale on which the field varies at the edge is given by:

$$\Lambda_{edge} = (3\sqrt{6}/4)\lambda(T) \quad (4.14)$$

In order to corroborate these results we performed similar measurements on sample B. The obtained experimental data for the first vortex entry field versus $H_c(T)$ obtained by Dekker *et al.* is plotted in Fig.4.9 (triangular and circular symbols). As expected, a clear reduction of H_{en} is observed, see also Fig.4.8, related to the larger width of sample B (i.e. increased demagnetization field). However, the value we obtain for $C=0.74 \times \frac{3\sqrt{6}}{4}$ from a linear fit of the experimental data obtained for the first vortex entry field in sample B, deviates significantly from the value we obtained for C in sample A. Ascribing this factor C to the current induced depairing effect alone, one does not expect any difference in this factor for both samples.

It is worth discussing at this point some relevant differences between a plain amorphous Pb film (like the ones present in [121]) and an amorphous Pb film perforated with antidots (as it is in the present case), and how these differences may affect our results. It is known that in the presence of cylindrical antidots with a radius $R > \xi$, if a vortex is captured by the antidot there is no loss of superconducting condensation energy. Then, not only is the vortex core energy changed but the energy of the superconducting current will also be effected. In particular, in the vortex energy expression the cut-off is at R rather than at ξ , which, for $R \gg \xi$, leads to an essential decrease of the lower critical field and surface barrier [122]. This effect can be taken into account by a renormalization of the value of λ with respect to that of the plain film [123]. The renormalization depends entirely on the antidots / film surface ratio (S_a/S_t). For a dense antidot lattice the renormalization will be strong, λ will increase and hence H_s will decrease. Our antidot lattice is not cylindrical, but we estimate an effective radius of $R_{eff} = 0.3 \mu\text{m}$ and $0.33 \mu\text{m}$ for the

boomerang and the square antidot sample, respectively. Nonetheless, both antidot lattices are quite dilute, with first matching fields H_1 of only 0.27 mT and 0.23 mT, respectively. This incurs in a $S_a/S_t \leq 0.07$, which, consequently, yields to a renormalization of λ of only 7%. Therefore, in a first approximation, we will exclude from our current discussion the effect that the antidot lattice has on the H_s value. Finally, it is worth mentioning that previous reports show that the effect that a diluted antidot lattice (antidot separation $\geq 2\mu\text{m}$) have in ξ and λ in a Pb film is indistinguishable to those of the plain film [124]. Nevertheless, if Λ is comparable to the distance between the edge of the sample and the first antidot a local modification of the screening currents is expected. In this case, the presence of holes has a pronounced effect on H_{jd} . In first approximation, compared to an unpatterned film the current density is increased by a factor equal to the ratio between the period perpendicular to the current direction and the lattice period perpendicular to the current direction reduced by the cross section of the holes. Due to different sample antidot array geometry and effective antidot width, a more pronounced effect is expected in sample B compared to sample A. The periodicity of antidots perpendicular to current circulation is $5\mu\text{m}$ and $3\mu\text{m}$ for sample A (triangular array) and sample B (square array), respectively. For sample A the enhancement factor of the edge screening-current density is, $5\mu\text{m}/4.77\mu\text{m} = 1.05$, while for sample B this factor is, $3\mu\text{m}/2.4\mu\text{m} = 1.25$. In Fig. 4.9 the dashed curves incorporate this effect for both samples, while in the full lines this effect is neglected. It is clear that by taking this effect into account, a nice fit is recovered. The importance of these local enhancements of the current density at the edge due to the presence of the antidots is evidenced by observed modulations of the edge field in the vortex free state.

4.6 Conclusion

In conclusion, we have visualized the first penetration of vortices in superconducting films with antidots by Scanning Hall probe microscopy. The studied thin film geometry and the presence of antidots have allowed us to confirm at the single vortex scale, using the London approximation that the first vortex penetration occurs when the condition $j_{\text{edge}}=j_d$ is met. From the presented results, we can construct a picture for the observed vortex entry process as follows. At low values of the applied field, the superconductor is in the Meissner state, where supercurrents circulate in the whole sample with a decreasing density toward the center. When the applied field reaches H_{jd} and the edge current density approaches its depairing value (more accurately it should be the current density averaged over a ξ distance), there is a local breakdown of superconductivity and a first vortex nucleation at the edge near an antidot,

where the Meissner current density has a local maximum due to the reduced current path width. The nucleated vortex is immediately depinned from the edge and is caught by the nearest antidot, where it is observed by SHPM. Since the vortex current has its sense opposite to the Meissner current, the involved edge current density decreases back to below its depairing value, and the nucleation of the second vortex occurs in another place, and so on. The SHPM technique is used here to investigate a fundamental property of a superconductor, it is the first vortex entry field. Through the static imaging of the vortex distribution near the edge and the careful sample design, a one-to-one relationship exists between the observed vortex distribution and the dynamical entry of vortices. However, no observations are made during the motion itself. In the next chapters an alternative SHPM technique will be introduced allowing to probe and to infer information during vortex motion.

Local mapping of the response of a superconductor to a perpendicular alternating magnetic field

5.1 Introduction

The hallmark of type-II superconductors is the formation of quantized magnetic flux lines encircled by a rotating condensate of paired electrons when a sufficiently strong magnetic field is applied. A free motion of these fluxons leads to dissipation thus destroying the perfect conductivity of the system. Consequently, in a world where energy dissipation has become a top priority problem, the motion of fluxons restricts the technological desirable properties of superconductors. Understanding, improving and optimizing the mechanisms to prevent the motion of fluxons has become a top priority. This can be done by introducing a rich diversity of pinning centers and new methods to evaluate the efficiency of these pinning centers.

Among the most powerful experimental methods used to determine the efficiency of pinning sites is the ac-susceptibility technique which consists of shaking the flux line lattice with a small alternating magnetic field while recording the superconductor's in-phase and out-of-phase magnetic response. However, such experimental technique is focused on a macroscopic response where the recorded signal represents an average over millions of flux lines each of which trapped in different pinning potentials and subjected to different

environments. Hence, this technique gives little information about the local pinning potential that each flux line experiences. Moreover to derive more information about the dynamic properties of the vortices at the microscopic scale, pioneering theoretical works have been invoked to make the link between the experimentally measured integrated ac magnetic field response and the induced microscopic vortex dynamics.

These limitations of the conventional ac-susceptibility technique, it is the inability to resolve the ac-response of a single vortex and the indirect relation between the vortex dynamics and the integrated response, provides a drive to find alternative methods to directly probe the ac-properties of a superconductor with single vortex resolution. In this chapter these limitations are circumvented by using a recently introduced scanning probe technique, scanning ac-susceptibility (SSM), which reveals, with unprecedented resolution, the motion and dissipation of individual units of flux quanta driven by an applied ac magnetic field or current. In a similar fashion as in a driven damped harmonic oscillator, the visualization of the dissipation is directly inferred from the phase lag between the vortex motion and the driving force induced by an oscillatory magnetic field, whereas the amplitude of the oscillatory vortex motion provides us with information about the shape of the local potential each fluxon is experiencing. This method has permitted us to separate damping-driven (viscous) motion from pinning-driven (thermally activated) motion, to demonstrate the non dissipative (dissipative) nature of the Meissner(vortex) state at microscopic scale and to obtain a detailed cartography of the intensity of the pinning landscape. These results shed new light on unraveling the basic mechanisms of vortex dissipation with unmatched single vortex resolution and provide for the first time direct evidence for the previously introduced models to explain the measured integrated ac-vortex responses in ac-susceptibility experiments.

5.2 The response of a superconductor to an ac magnetic field

5.2.1 Introduction

In general, whenever a dissipative system is subjected to a periodic excitation, e.g. a crystal to electromagnetic radiation or a driven damped harmonic oscillator, the periodic force will perform work to drive the system through subsequent dissipative cycles. The dissipative or frictional component of the system, related to a non-conservative force, will induce a phase shift

between the response and the external drive, giving rise to hysteresis. For example, the imaginary part of the relative permittivity is closely related to the absorption coefficient of a material[125] or a phase-lag appears in the motion of a damped harmonic oscillator[126]. This close connection between dissipation of energy and the out-of-phase component of the system's response is used in spectroscopic measurements to gain information concerning the nature and efficiency of the dissipation processes. Likewise, we will use this spectroscopic approach to investigate the response of a superconductor to an applied ac magnetic field.

In this section we start with the description of the linear response of a classical system, a driven damped harmonic oscillator, to illustrate the above mentioned connection between dissipation and the appearance of a phase-lag between the drive and the response. Moreover, we will see that this simple classical system has it's merit of introduction as it has not only an instructive value, it can also be mapped to describe the linear response of the vortices and the screening currents in a type-II superconductor to an ac magnetic field as described in Sec.1.8

5.2.2 A classical example, the driven damped harmonic oscillator

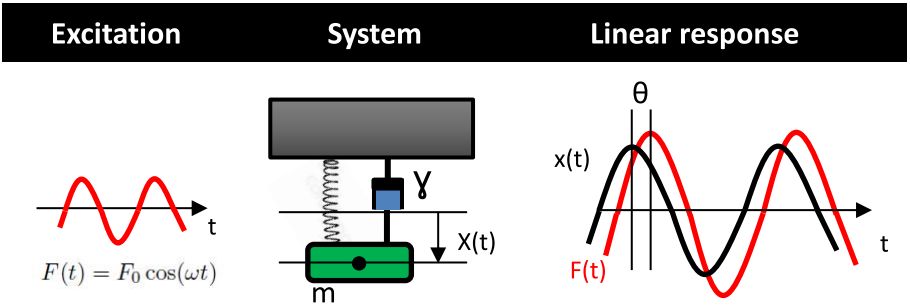


Figure 5.1: Schematic presentation describing the linear response of a driven damped harmonic oscillator. The (small) periodic driving force, $F(t)$, provides the excitation mechanism of a system consisting of a mass-spring system and a damping pot with friction coefficient, γ . The response (the displacement), $x(t)$, is also a periodic function in time. In general a phase lag, θ exists between the drive and the response.

A lot of physical systems in nature, driven out of equilibrium, can be modeled, when the drive is small, by a forced damped harmonic oscillator, e.g. we can

model absorption of light by the interaction of the electromagnetic field with an oscillating dipole, different dynamic modes in condensed matter resemble harmonic oscillator modes such as phonons in solids, spin waves in magnets, etc. Using Newton's equation for a forced damped harmonic oscillator, Fig.5.1, we obtain the general force balance equation of motion:

$$\ddot{x}(t) + \omega_0^2 x(t) + \gamma \dot{x}(t) = f(t)/m \quad (5.1)$$

here $x(t)$ is the displacement of the oscillator from equilibrium and $\omega_0 = \sqrt{k/m}$ is the natural frequency of the oscillator, with spring constant k and mass m . For a sphere of radius R moving in a fluid with shear viscosity η , $m\gamma$ is given by Stokes's law $m\gamma = 6\pi\eta R$. For a monochromatic oscillating driving source:

$$F(t) = F_0 \cos(\omega t) \quad (5.2)$$

Within linear response, Eq.5.1 has the steady state solution¹:

$$x(t) = F_0 \chi(\omega) \cos(\omega t) \text{ with } \chi(\omega) = \frac{1}{m(\omega_0^2 - \omega^2 + i\gamma\omega)}, \quad (5.3)$$

where the complex frequency dependent number $\chi(\omega) = \chi' + i\chi''$ describes the response of the system. This solution can be parameterized either by the amplitude and the phase of $\chi(\omega)$, or by the real and imaginary part. In the former case:

$$x(t) = F_0 |\chi(\omega)| \cos(\omega t + \theta(\omega)) \text{ with,} \quad (5.4)$$

$$|\chi(\omega)| = \frac{1}{m\sqrt{(\omega_0^2 - \omega^2)^2 + \gamma^2\omega^2}} \text{ and } \tan \theta(\omega) = \frac{\chi''}{\chi'} = \frac{-\gamma\omega}{(\omega_0^2 - \omega^2)}, \quad (5.5)$$

This equation of motion shows that the driven oscillator has an oscillation period dictated by the driving frequency ω . The phase and amplitude relative to the drive are determined by the detuning from the natural resonance frequency, $(\omega - \omega_0)$. The different lineshapes are plotted in Fig.5.2(a). It is clear the amplitude of $x(t)$ reaches a maximum for driving frequencies in the vicinity of the natural frequency ω_0 of the oscillator. Furthermore, the phase shift θ between $x(t)$ and the drive is always negative, meaning $x(t)$ lags behind the drive and passes through $-\pi/2$ at precisely ω_0 . For later purpose we rewrite the solution in yet another way, as having an in-phase component and an out-of

¹In principle, the general solution of the differential Eq.5.1, consists of the sum of the homogeneous solution and a particular solution. However, the homogeneous solution is transient, whereas the particular one describes the steady state solution.

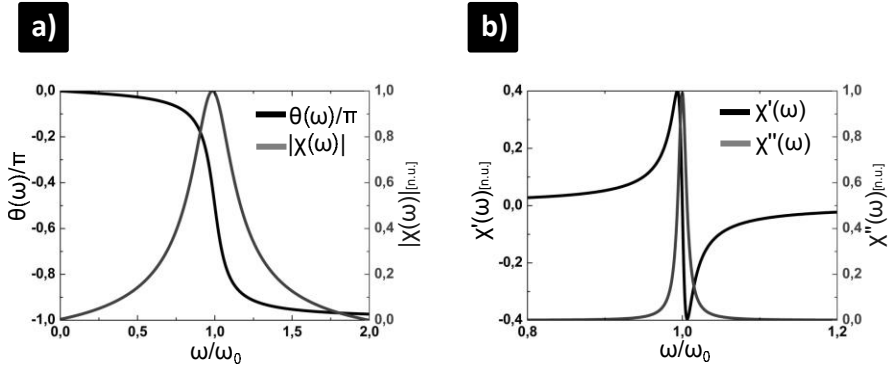


Figure 5.2: Lineshapes of a driven damped harmonic oscillator for the case $\omega_0/2\gamma = 8$. (a) The frequency dependence of the normalized modulus and the phase (b) The frequency dependence of the normalized in-phase and out-of-phase components.

phase component, in this form the solution resembles the first term in a Fourier series expansion,

$$x(t) = F_0(\chi'(\omega)\cos(\omega t) + \chi''(\omega)\sin(\omega t)) \text{ with,} \quad (5.6)$$

$$\chi' = \frac{(\omega_0^2 - \omega^2)}{m((\omega_0^2 - \omega^2)^2 + \gamma^2\omega^2)} \quad \text{and} \quad \chi'' = \frac{-\gamma\omega}{m((\omega_0^2 - \omega^2)^2 + \gamma^2\omega^2)}, \quad (5.7)$$

where the Fourier components are proportional to χ' and χ'' . What is the meaning of these Fourier components? To answer this question, let us consider the Q-factor of the system, which is defined as 2π times the mean energy stored in the system, divided by the work done per cycle[126],

$$Q = 2\pi \frac{\text{Energy stored}}{\text{Energy dissipated}} = \left[-\frac{(\omega_0^2 + \omega^2)}{2(\omega_0^2 - \omega^2)} \right] \frac{\chi'}{\chi''} \quad (5.8)$$

Apart from the frequency dependent prefactor between square brackets, it is clear the rate of energy dissipation is proportional to the out-of-phase component $\chi''(\omega)$, whereas the stored energy in the system is proportional to the in-phase component $\chi'(\omega)$. To see this explicitly, the rate at which the external drive performs work (the power) on the oscillator that is eventually dissipated as heat in the viscous fluid, is given by:

$$\frac{dW}{dt} = f(t)\dot{x}(t) \quad (5.9)$$

Since in steady state, both the drive $f(t)$ and the velocity $\dot{x}(t)$ are periodic functions of time with the same period, it is convenient to define the average power dissipated in one period,

$$W_q = \int_0^T dt f(t) \dot{x}(t) = \pi F_0^2 \chi''(\omega) \quad (5.10)$$

And a clear connection is made between the rate of energy dissipation and the out-of-phase component $\chi''(\omega)$. The in-phase response is related to the mean stored energy in the system, which is given by the sum of the average kinetic and potential energy in the system,

$$\langle E \rangle = \frac{1}{2} m \langle (dx/dt)^2 \rangle + \frac{1}{2} m \omega^2 \langle x^2 \rangle = \left[\frac{(\omega_0^2 + \omega^2)}{2(\omega_0^2 - \omega^2)} \right] \frac{F_0^2}{2} \chi'(\omega) \quad (5.11)$$

confirming the relation between the in-phase response and the stored energy. Moreover, it is clear that both response functions, $\chi'(\omega)$ and $\chi''(\omega)$ are related (cf. Kramers-Kronig Relations). In the following we will see that the above results, describing the linear response of a driven damped harmonic oscillator, can be mapped to a superconducting system driven by a weak ac magnetic field.

5.2.3 The response of a superconductor to an ac magnetic field

Macroscopic response

The integrated response of the superconductor upon the application of an external alternating magnetic field

$$h_{ac}(t) = h_{ac} \cos(\omega t), \quad (5.12)$$

with amplitude, h_{ac} and angular frequency $\omega = 2\pi f$, is standardly recorded in global ac-susceptibility measurements[127]. These measurements contain important information about the dynamics and the pinning properties of the vortex lattice in the mixed state, of fundamental importance for applications. In the following we will discuss the principle of this measurement technique.

Consider a type-II superconductor excited by an alternating external magnetic field, $h_{ac}(t)$. In general, it is then expected that the average sample response²,

²In principle, the response of the sample alone is the magnetization, $\langle M \rangle(t)$, related to the magnetic induction, $\langle B \rangle(t)$, and the applied field, $\langle h_a \rangle(t)$ as, $\langle M \rangle(t) = \frac{\langle B \rangle(t)}{\mu_0} - \langle h_a \rangle(t)$. As such, the magnetization does not include the contribution of the drive, $\langle h_a \rangle(t)$. As in our experiments we probe directly the local induction rather than the magnetization, we will describe the response in these terms.

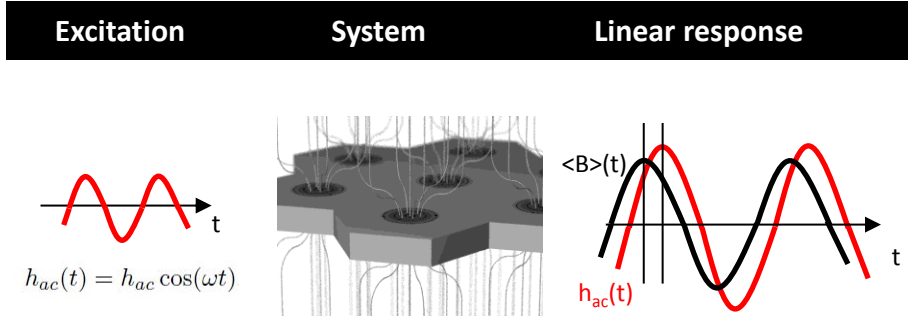


Figure 5.3: Schematic presentation of a superconductor excited by a small monochromatic oscillatory magnetic field, $h_{ac}(t)$. The periodic drive, $h_{ac}(t)$, provides the excitation mechanism of a type-II superconductor. The sample response, $\langle B \rangle(t)$, will also vary periodically in time, however a phase lag, θ may exists between the drive and the response.

the magnetic induction averaged over the sample volume, $\langle B \rangle(t)$, is also periodic, with the same period as the applied magnetic field $T = (2\pi)/\omega$, see Fig.5.3. Here the average denoted by, $\langle \rangle$, is taken over the whole sample volume. The distorted periodic wave form can be expressed as a Fourier series expansion.

$$\langle B \rangle(\omega, t) = \mu_0 h_{ac} \sum_{n=1}^{\infty} [\langle \mu'_n \rangle \cos(n\omega t) + \langle \mu''_n \rangle \sin(n\omega t)] \quad (5.13)$$

here $\langle \mu'_n \rangle$ and $\langle \mu''_n \rangle$ are the real and imaginary part of the n th Fourier component and μ_0 is the permeability of vacuum. In the first approximation, if one considers the ac drive to be sufficiently small, one can consider only the linear response.

$$\langle B \rangle \approx \mu_0 h_{ac} [\langle \mu'_1 \rangle \cos(\omega t) + \langle \mu''_1 \rangle \sin(\omega t)] \quad (5.14)$$

As such, the linear response is completely determined by a measurement of the Fourier components $\langle \mu'_1 \rangle$ and $\langle \mu''_1 \rangle$ which can be considered as the real and imaginary part of the so called complex relative permeability³, $\langle \mu_1 \rangle = \langle \mu'_1 \rangle + i \langle \mu''_1 \rangle$. What is the meaning of the two Fourier components

³As $\langle M \rangle(t) = \frac{\langle B \rangle(t)}{\mu_0} - h_{ac}(t)$, the first term in a Fourier series expansion of $\langle M \rangle(t)$, will have Fourier component $\langle \chi'_1 \rangle = \langle \mu'_1 \rangle - 1$ and $\langle \chi''_1 \rangle = \langle \mu''_1 \rangle$, which can be considered as the real and imaginary part of the complex ac susceptibility $\langle \chi \rangle = \langle \chi'_1 \rangle + i \langle \chi''_1 \rangle$, respectively. In terms of the magnetization, $\langle M \rangle(t)$, the response of the sample alone is considered.

appearing in Eq.5.14? The real part describes the in-phase response of the magnetic induction to the external magnetic ac field and is related to the macroscopic shielding abilities or the inductive properties. To see this, we calculate the time average of the magnetic energy supplied by an alternating field per unit volume into the sample[128],

$$W_a = \frac{1}{T} \int_0^T (h_{ac}(t) \langle B \rangle (\omega, t)) dt = \frac{\langle \mu'_1 \rangle B_a^2}{2\mu_0} \quad (5.15)$$

where $B_a = \mu_0 h_{ac}$. When no sample is present, the magnetic field energy stored is equal to $W_0 = \frac{B_a^2}{2\mu_0}$. The difference,

$$\delta W = W_a - W_0 = (\langle \mu'_1 \rangle - 1) \frac{B_a^2}{2\mu_0} \quad (5.16)$$

reflects the ac response of the sample. As such, $\langle \mu'_1 \rangle$ describes whether the material increases or decreases the amount of stored energy per unit volume. Diamagnetic behavior of the investigated sample, $0 < \langle \mu'_1 \rangle < 1$, leads to a reduction of the magnetic energy stored per unit volume as compared to a situation when no sample is present, this is reflected in a negative value of δW . Thus in case of a ideal superconductor in the Meissner state, we expect $\langle \mu'_1 \rangle = 0$. A paramagnetic response, $\langle \mu'_1 \rangle > 1$, leads to an increase of the magnetic field energy as compared to a situation when no sample is present.

The imaginary part describes the out-of-phase response of the magnetic induction, arising, as in the case of a driven damped harmonic oscillator, necessarily from dissipative ac-losses within the superconductor. To see this connection, we calculate the energy converted into heat during one cycle of the applied ac magnetic field[128]:

$$\begin{aligned} W_q &= \frac{1}{\mu_0} \int_0^T (h_{ac}(t) \frac{d \langle B \rangle (\omega, t)}{dt}) dt \\ &= \int_0^T (h_{ac}(t) d \langle M \rangle (\omega, t)) = \pi \frac{1}{\mu_0^2} B_a^2 \langle \mu''_1 \rangle, \end{aligned} \quad (5.17)$$

and a direct relation exists between the dissipated energy and the complex part of the permeability $\langle \mu''_1 \rangle$. Notice that the second equality in Eq.5.17, is just the the area of a magnetization hysteresis loop. As W_q is always positive, $\langle \mu''_1 \rangle > 0$. In general terms one can say that $\langle \mu'_1 \rangle$ measures magnetic irreversibility or the resistive reaction to ac fields, whereas $\langle \mu'_1 \rangle$ is related to the inductive properties of the sample. Note, that all of the above considerations are in one-to-one correspondence with the case of an harmonic oscillator, where the displacement plays the role of the magnetization and the

driving force plays the role of the applied ac magnetic field.

In standard ac-susceptibility measurements, one excites the sample with an ac magnetic field, h_{ac} , and detects the macroscopic response, $\langle B \rangle(t)$, inductively by a pick-up coil. Using a lock-in technique one can obtain directly $\langle \mu'_1 \rangle$ and $\langle \mu''_1 \rangle$ or higher Fourier components[127]. The dependencies of these two response functions upon changing the thermodynamical variables or the ac-excitation parameters, provide very valuable information concerning the pinning efficiency and reveal the fingerprints of the particular ac-dynamic phases the vortex lattice exhibits[129, 130, 131]. Since the recorded signal represents an average over all present flux lines and screening currents in the sample, the link with the microscopic ac-reponse is indirect. Pioneering theoretical works[48, 44, 45] contributed substantially to link this global response to the microscopic vortex dynamics and/or the ac-field penetration.

In these theoretical works, as discussed in Sec.1.8, the macroscopic response of a superconductor, or a conductive medium in general, to an ac magnetic field is described by introducing a complex frequency dependent conductivity or impedance. This complex conductivity, $\sigma(\omega)$, completely determines the ac magnetic field penetration through the dispersion relation, Eq.1.55. As such it determines the time evolution of the induction averaged over the sample volume, which is completely characterized by it's Fourier components. As the complex conductivity was determined by the equation of motion for the entities which respond to the ac excitation, the electrons for a normal metal and both, the screening currents and the vortices for a superconductor, it is possible to relate indirectly the measured dependencies of the Fourier components to the microscopic response. In the following we will introduce a technique which allows to probe directly, at the level of the screening currents and the vortices, the response of a superconductor to an ac-magnetic field.

Microscopic response

The above described variation of the average response, $\langle B \rangle(t)$, of a type-II superconductor is produced at the microscopic level by the vortices, the induced screening currents or the external field itself. In Fig.5.4 the reaction at the end of a long(0.5mm) superconducting Pb ribbon to a magnetic field variation is probed by making snapshots of the z-component of the local induction, $B_z(x,y)$, as measured at every pixel (x,y) by SHPM. The Pb ribbon is $9\mu\text{m}$ wide and 50 nm thick and is prepared by a field cooling procedure in a field of $h_{dc} = 0.13\text{mT}$ to $T = 7\text{K}$, see Fig.5.4(b) The prepared state contains two vortices whose positions are indicated by red dots, further a clear enhancement of the local field is observed at the border of the Pb ribbon due to demagnetizing effects. Two

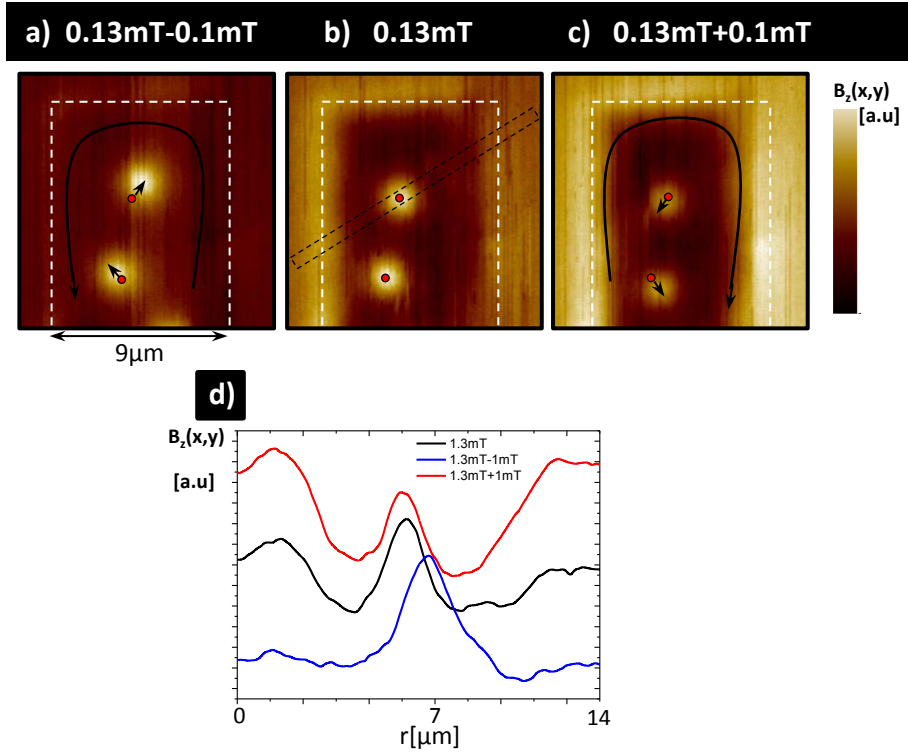


Figure 5.4: The reaction at the end of a $9\mu\text{m}$ wide superconducting Pb ribbon to a magnetic field variation is shown by making snapshots of the z-component of the local induction, $B_z(x,y)$, as measured by SHPM. The borders of the Pb ribbon are indicated by the dashed white line. The Pb ribbon is prepared by a field cooling procedure in a field of $h_{dc} = 0.13\text{mT}$ to $T = 7\text{K}$ (b). Two snapshots of $B_z(x,y)$ are shown at $h_{dc} = 0.23\text{mT}$ (c) and $h_{dc} = 0.03\text{mT}$ (a) obtained upon increasing and decreasing the field with 0.1mT after preparing the ribbon as described. In (d), the average cross section is shown for the different field configurations, as obtained by averaging the cross sections in the rectangular area indicated by the black dashed line in (b).

snapshots of $B_z(x,y)$ are shown at $h_{dc} = 0.23\text{mT}$ (Fig.5.4(c)) and $h_{dc} = 0.03\text{mT}$ (Fig.5.4(a)), obtained upon increasing and decreasing the field with 0.1mT after preparing the ribbon as described. The following observations can be made when the Pb ribbon undergoes a field variation of 0.1mT :

- When we increase or decrease the field by 0.1mT , additional screening

currents will be induced in the superconducting Pb ribbon as indicated by the long black arrows in Fig.5.4(a) and Fig.5.4(c). The magnetic field they generate will contribute to the local induction, $B_z(x,y)$, at the edge of the ribbon. This explains the observed field enhancement and reduction at the edge of the Pb ribbon, respectively. This field enhancement is also observed in the prepared state, Fig.5.4(b) and is determined by a geometrical demagnetizing factor, identical for every magnetic field amplitude as long as the induced current is insufficient to induce depairing.

- The induced screening currents will produce a Lorentz force on the vortices, that will displace them from their initial equilibrium position in the prepared state. The initial vortex position at $h_{dc} = 0.13\text{mT}$ is indicated by the red dots in every snapshot. The short black arrows in Fig.5.4(a) and Fig.5.4(c) show the displacement of the vortices as compared to the positions of the vortices in the prepared state. Both observations are clearly visible in the derived average cross sections for every field amplitude, shown in Fig.5.4(d).

The crucial point we want to make clear with the above ‘snapshot movie’, is that the variation of the magnetic induction, $B_z(x,y,t)$, at the microscopic scale or at every pixel of our scan area, is again a periodic function with the same period as the applied magnetic field, whether one looks at the variation of the field due to vortices deep in the sample volume or due to the screening currents at the edge. This is not surprising as the average response, $\langle B \rangle(t)$, is just a superposition of the individual microscopic contributions. Once again, $B_z(x,y,t)$ can be expressed as a Fourier series expansion and if we consider only linear response we obtain,

$$B_z(x, y, t) \approx \mu_0 h_{ac} [\mu'_1(x, y) \cos(\omega t) + \mu''_1(x, y) \sin(\omega t)] \quad (5.18)$$

Similar as in the macroscopic case, the observation and the study of these response functions or Fourier components and their dependencies upon variations of temperature, driving parameters, etc. will provide us with information concerning the vortex dynamics. Whereas up till now, one was able to track only the integrated response over the whole sample volume by macroscopic ac-susceptibility experiments. Where the connection between the measured response, $\langle \mu'_1 \rangle$ and $\langle \mu''_1 \rangle$ and the microscopic models is indirect. A measurement of $\mu'_1(x, y)$ and $\mu''_1(x, y)$, completely characterizing the linear variation of the local induction, will provide us with direct information about the microscopic response, without the need to invoke theoretical models to explain the measured responses.

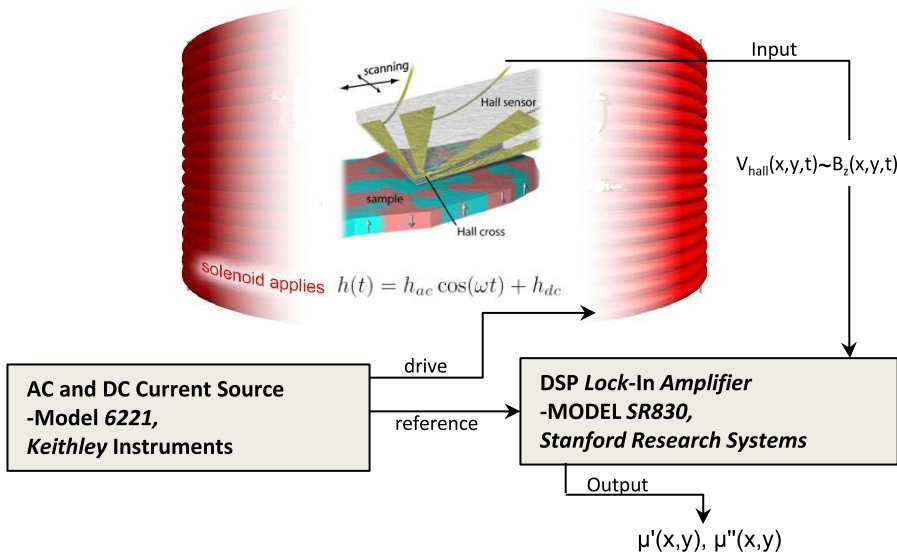


Figure 5.5: Schematic illustration of the experimental implementation of the scanning ac-susceptibility technique.

Scanning ac-susceptibility microscopy

Using a recently developed experimental technique, scanning ac-susceptibility microscopy (SSM), a lock-in variant of the SHPM technique it is possible to measure directly, with single vortex resolution, the two Fourier components, $\mu'_1(x,y)$ and $\mu''_1(x,y)$ and, in principle, all higher harmonics, see Fig.5.5. In SSM, we continuously excite the sample with an external ac magnetic field, $h_{ac}(t) = h_{ac} \cos(\omega t)$, applied perpendicular to the sample surface by a small copper coil. The Hall voltage, $V_H(x,y,t)$, measured locally by a Hall microprobe is picked up by a lock-in amplifier. The excitation signal for the external applied ac field, feeds a phase-locked loop which extracts the in-phase, $V'_1(x,y)$, and out-of-phase components, $V''_1(x,y)$, of $V_H(x,y,t)$. In the first approximation these are, respectively, proportional to the in-phase, $B'_z(x,y)$ and out-of-phase, $B''_z(x,y)$, ac-components of the local magnetic induction, $B_z(x,y,t)$, coarse grained by the size of the cross, which are directly related to the real and imaginary part of the local relative permeability,

$\mu_1(x, y) = \mu'_1(x, y) - i\mu''_1(x, y)$, through the definition[132]:

$$\begin{aligned}\mu'_1(x, y) &= \frac{B'_z(x, y)}{\mu_0 h_{ac}}, \\ \mu''_1(x, y) &= \frac{B''_z(x, y)}{\mu_0 h_{ac}}\end{aligned}\tag{5.19}$$

SSM provides a tool to spatially map these two Fourier components. The mapping of $B_z(x, y, t)$ was obtained using a modified low-temperature SHPM from Nanomagnetism Instruments as described in Chap.2. As the SHPM technique used to map $B_z(x, y, t)$ has single vortex resolution, SSM allows likewise to probe the ac-response of a superconductor at this scale. In all the experiments, the collinear DC and AC external magnetic fields are always applied perpendicular to the sample surface. Just as in the global ac-susceptibility technique, one can again relate, by making a similar analysis, the in-phase component, $\mu'_1(x, y)$, to the local inductive response, while the out-of-phase component, $\mu''_1(x, y)$, is related to microscopic ac-losses.

In the following sections, we will use this tool to analyse the ac-response of two superconducting systems. In the first system the ac-response of a Pb ribbon is investigated. Whereas in a second case the response of a periodically nano-structured superconductor is investigated. The interpretation of the measured local response functions $\mu'_1(x, y)$ and $\mu''_1(x, y)$ and the analysis of their dependencies upon varying thermodynamical variables (temperature, dc magnetic field) or the drive amplitude will be discussed for both case-studies.

5.3 Results

5.3.1 Ac response of a superconducting Pb ribbon

Sample layout

In this section we investigate the response of a superconducting Pb ribbon to an ac magnetic field. The Pb ribbon is 0.5 mm long, 50 nm thick and 9 μm wide. The characteristic superconducting properties of the Pb ribbons are similar to the ones discussed in Sec.3.3.1. As the signal picked up by the Hall probe contains different contributions, arising from the screening currents, the vortex signals and the external field itself, the measured local linear ac-response is also determined by all contributing factors. This particular sample design allows us to map the spatial dependence of the linear response to $h_{ac}(t)$, covering the

whole width of the sample in a single scanning area, including the Meissner response at the sample border and the vortex motion deeper into the ribbon volume.

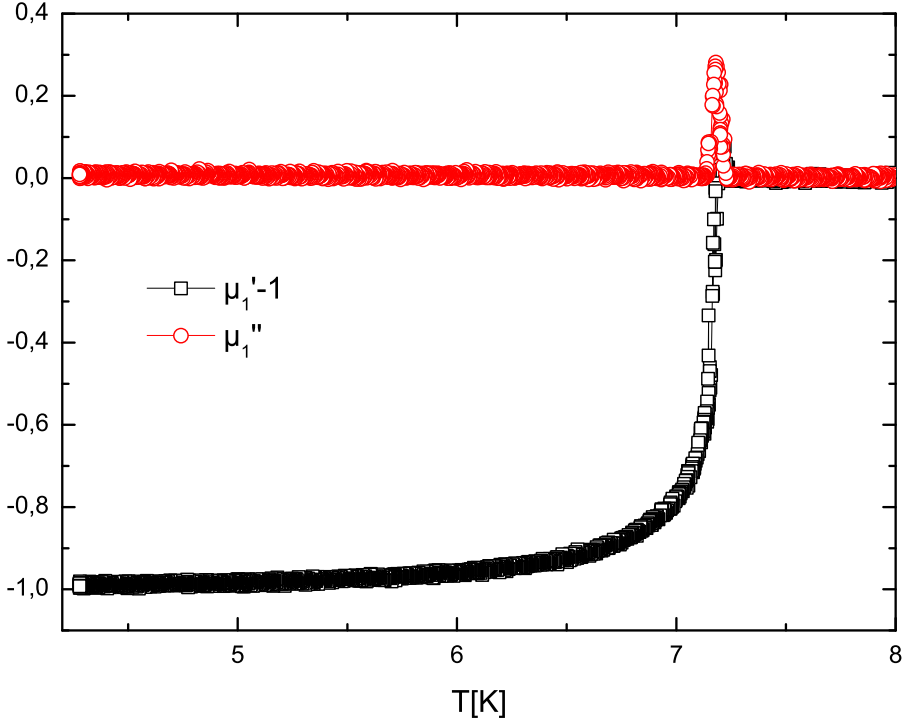


Figure 5.6: In-phase (χ') and out-of-phase (χ'') ac-signal picked up by the Hall cross located at the center of a 7 μm stripe, using an ac-amplitude of 0.1 mT and a frequency of $f = 77.5$ Hz.

Temperature dependence of the ac response

Before we discuss in detail the response in the whole scan area, let us first discuss the temperature variation of $\mu_1'(x, y)$ and $\mu_1''(x, y)$ picked up by the Hall cross located $\sim 1 \mu\text{m}$ above the center of a ZFC 7 μm wide Pb ribbon, see Fig. 5.6. An ac-amplitude of 0.1 mT and a frequency of $f = 77.123 \text{ Hz}$ are used for this measurement. This dependence is identical to the temperature dependence observed in macroscopic ac-susceptibility experiments. It is clear that the Pb ribbon exhibits a superconducting transition at $T_c = 7.20 \text{ K}$. For temperatures

below T_c a diamagnetic response is observed, $0 < \mu'_1(x, y) < 1$, meaning the ribbon screens out the applied field. Above T_c , $\mu'_1(x, y) \approx 1$, meaning the ac-magnetic field penetrates completely as expected for this low frequency for a normal metal, see sec.1.8. $\mu''_1(x, y)$ is initially zero, goes through a maximum, and reduces to a zero value near T_c . The maximum marks the coincidence of the magnetic penetration depth with the relevant sample dimensions (the film thickness)[127].

Fig.5.7(a) shows a SHPM image of a vortex distribution prepared by performing a field cool (FC) in $H=0.13\text{mT}$ to $T=6.7\text{K}$. After preparing the state, a SHPM image is obtained while an external field with $h_{ac}=0.1\text{mT}$ and $f=77.123\text{Hz}$, is continuously applied. The scan speed is chosen properly, $1\mu\text{m/s}$, to assure that the integration time at every pixel (125ms) is much larger than the period of the applied ac field (13ms). As one image has 128 by 128 pixels, the time for a single scan takes 1.13hr. The resulting vortex distribution obtained by performing a FC experiment, corresponds to a frozen vortex structure nucleated close to T_c [133]. The FC process forces vortices to nucleate at the strongest pinning sites and results in a non-symmetrical vortex distribution. The external ac-field shows up as an additional monochromatic noise in the SHPM images getting more pronounced for temperatures close to T_c . However, for all investigated temperatures the average vortex positions do not change, indicating that for $h_{ac}=0.1\text{mT}$ the resulting average vortex response is limited to displacements below the experimental spatial resolution.

Fig.5.7(b) shows a representative set of simultaneously acquired SSM images of $\mu'_1(x, y)$ (top row) and $\mu''_1(x, y)$ (bottom row), respectively describing the inductive and dissipative response, when the temperature is decreased progressively from $T=7\text{K}$ to $T=6.7\text{K}$. A first straightforward observation is that at the edges of the scan area, meaning relatively far away from the Pb ribbon, the local induction is equal to the applied ac magnetic field $h_{ac}(t)$ as $\mu''_1(x, y) = 0$ and $\mu'_1(x, y) = 1$. A clear paramagnetic response, $\mu'_1(x, y) > 1$, is visible at the edge of the Pb ribbon, where the response is dominated by the induced screening currents. This enhancement of the external ac-field is caused by a strong demagnetizing effect resulting from the thin film sample geometry[134]. Upon entering the volume of the ribbon, we observe an increasing diamagnetic response as $h_{ac}(t)$ gets shielded by the screening currents. At the center of the Pb ribbon, a maximum diamagnetic response due to the screening current of $\mu'_1(x, y)=0.27$ at $T=6.7\text{K}$ is reached, indicating an incomplete field expulsion. An important observation in Fig.5.7b is that the shielding currents do not show any contributing signal in $\mu''_1(x, y)$ for all temperatures, indicating that they are, within our experimental resolution, perfectly in-phase with the ac-excitation and as such are non-dissipative.

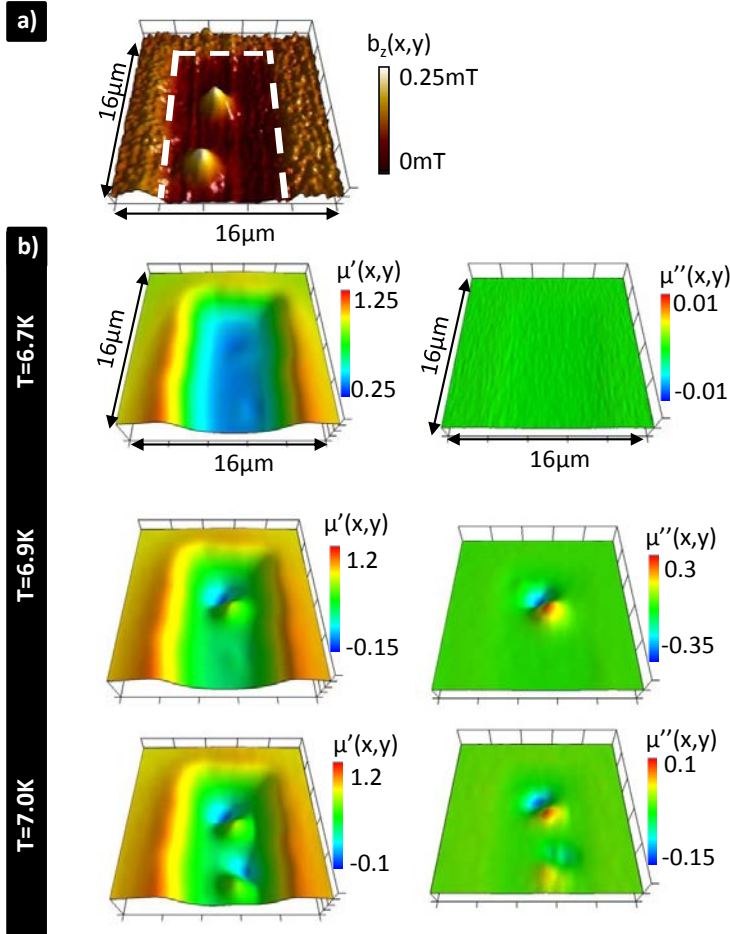


Figure 5.7: (a) Scanning Hall Probe Microscopy image of the local induction, $B_z(x,y)$, acquired during shaking with an external applied ac field of amplitude, $h_{ac}=0.1\text{mT}$, and with frequency, $f=77.123\text{Hz}$ at a temperature of $T=6.7\text{K}$. The initial vortex distribution is obtained by performing a field cool in an external applied dc magnetic field, $H=0.13\text{mT}$. The white dashed line indicates the border of the Pb ribbon. (b) Simultaneously acquired maps of the real part of the relative permeability, μ'_1 (left column) and the imaginary part of the relative permeability, μ''_1 (right column), for different temperatures: (top to bottom) $T=6.7\text{K}$, 6.9K and 7.0K .

Within the ribbon volume the induced screening currents, $\mathbf{j}(t)$, will periodically shake the vortices, with a force: $\mathbf{f}_L(t) = \mathbf{j}(t) \times \phi_0$. The ac-dynamics of the

vortices will crucially depend on the thermodynamical parameters of the SC system and the properties of the drive. As shown in Fig.5.7(b), the fingerprint of their motion in the SSM images, consists of two distinct unidirectional spots of opposite polarity surrounding the equilibrium vortex position. The inductive response can be easily interpreted. An area with a response exceeding the ac-response of the screening currents, $\mu'_1(x,y) > \mu'_1(x,y)_s$, corresponds with a vortex, carrying an intrinsic positive local induction, moving in-phase with $h_{ac}(t)$ within this area. A region with a response lower than the ac-response of the screening currents, $\mu'_1(x,y) < \mu'_1(x,y)_s$, in some cases resulting even in a local negative permeability, $\mu'_1(x,y) < 0$, indicates that $b_z(x,y,t)$ increases (decreases) upon decreasing (increasing) instantaneous $h_{ac}(t)$, corresponding with a vortex moving in anti-phase with $h_{ac}(t)$ within this area. A similar unique local negative $\mu'_1(x,y)$ response, but on a substantially larger spatial scale, has already been observed in the ac-dynamics of flux droplets in the presence of a geometrical barrier[132].

From thermodynamical considerations, neglecting the demagnetizing field, an overall integrated response between zero and one is expected for $\langle \mu'_1 \rangle$. Note however, that the meaning of the complex permeability as a macroscopic thermodynamical variable is lost in this local limit. Upon integrating the local signal over the whole scan area the expected non-negative response for $\langle \mu'_1 \rangle$ and $\langle \mu''_1 \rangle$ is recovered. This connection between $\langle \mu_1 \rangle$ as the integrand of the 'local' permeability, $\mu_1(x,y)$, which is directly related to the microscopic vortex dynamics, is used in theoretical models to explain the fingerprints of different dynamical VL regimes in measurements of the global ac-susceptibility and can be studied now directly by SSM. Furthermore it is clear, the particular depth and shape of the local pinning potential each vortex experiences has a profound effect on the ac-dynamics, i.e. at $T=6.9K$ only one of the two vortices present in our scan area is shaken by h_{ac} .

In sharp contrast to the screening currents' response, the vortices do leave a fingerprint in $\mu''_1(x,y)$ for sufficiently high temperatures. As such, the oscillating magnetic stray field produced by an harmonic motion of the vortices exhibits an out-of-phase component. The out-of-phase response disappears below $T < 6.8K$, here the ac-response of the vortices is weak and, within the experimental resolution, perfectly in-phase. The nature of the microscopic processes influencing vortex motion, each having a characteristic time, is a question of interest[135, 136, 37]. In the following we will start from an equation of motion for a vortex to explain the observed temperature dependence of the vortex response.

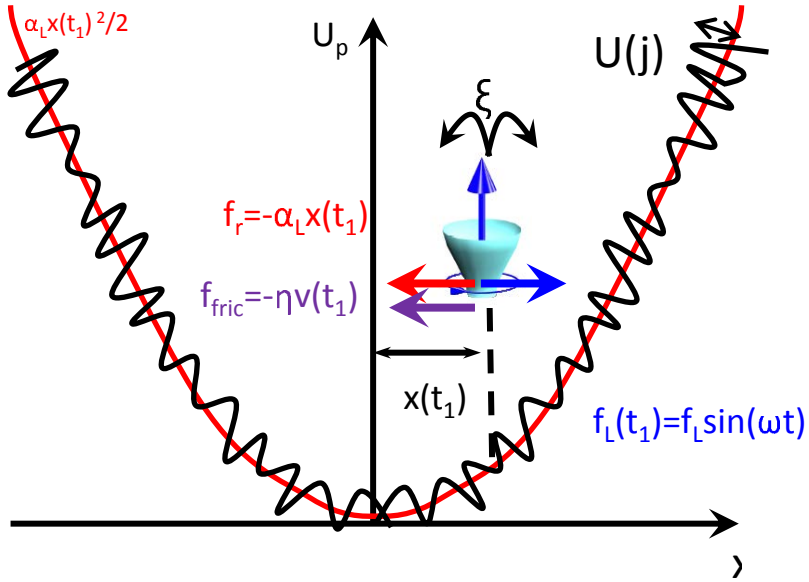


Figure 5.8: This figure illustrates schematically the forces working on a vortex in a harmonic well at time t_1 as described by Eq.5.20.

In general, as described in Sec.1.8, vortex-dynamics can be described by a phenomenological force balance equation of the form[47]:

$$m\ddot{\mathbf{x}}(t) - \mathbf{f}_L(t) + \nabla U = -\eta\dot{\mathbf{x}}(t) + \boldsymbol{\xi}(t) \quad (5.20)$$

Where $\mathbf{x}(t)$ is the vortex position. Here the left hand side describes the conservative part of the dynamics, including a combination of an inertial term, the periodic Lorentz drive, $\mathbf{f}_L(t)$ and the local potential, U , the vortex experiences due to a combination of interactions with other vortices, the surface and the local quenched disorder. For small excitations the local potential in the equation of motion can be approximated by an harmonic potential with spring constant α_L , called the Labusch constant[137]. The inertial term is accepted to be very small[33, 138] so that there is a short initial period of acceleration needed to reach the steady state motion we consider. The right hand side of Eq.5.20, describes the effects of the non-conservative environment presenting energy dissipation and modeled as a combination of a viscous friction, η , and a random thermal force, $\boldsymbol{\xi}(t)$ [42]. It is this right hand side of the equation of motion which describes the coupling to the environment. The linear approximation to the steady state solution of Eq.5.20, has the following

general form[44, 43]:

$$\mathbf{x}(\mathbf{t}) = -\left(\frac{-\alpha_L}{1 - i/\omega\tau_1} + i\omega\eta\right)^{-1}\mathbf{f}_L(t) \quad (5.21)$$

Here $\tau_1 = (\eta/\alpha_L)I_0^2(U(j)/2k_B T)$ is a characteristic relaxation time related to thermally activated hopping of the vortex, $I_0(\mathbf{x})$ is the modified Bessel function and $U(j)$ describes an effective activation energy which is a combination of the intrinsic pinning potential energy, $U(j=0)$ and the Lorentz force energy resulting from the induced super currents, $\mathbf{j}(t)$.

The solution, given by Eq.5.21, directly shows the out-of-phase component in the linear response induced by the aforementioned dissipative mechanisms. The term $i\omega\eta$ represents the viscous damping mechanism. It is connected by an elementary model developed by Bardeen and Stephen[136] with resistive processes in the normal core and by a more rigorous analysis with a finite intrinsic relaxation time of the SC order parameter[37]. This dissipative process has a typical short characteristic time of the order of, $\tau_p = \eta/\alpha_L \leq 0.1\mu s$ [47, 139]. For the applied low driving frequency, $f=77.123$ Hz, the restoring force dominates over the viscous drag force, as $\omega < 1/\tau_p$ and this term can be neglected. The term $i/\omega\tau_1$ is related to thermally activated vortex hopping across an effective activation barrier, following the classic ideas of Anderson and Kim[140] and results from $\xi(t)$ in Eq.5.20. This activated hopping process is typically associated with longer characteristic time scales[141]. Under certain conditions it is expected to contribute substantially in our low frequency SSM experiment.

It is interesting here to make a small intermezzo to compare the vortex system and the observed response with the driven damped harmonic oscillator(HO) discussed in Sec.5.2.2. If we consider the vortex-system in the limits of the experiment. Meaning we neglect the viscous damping force as for the applied low driving frequency, $f=77.123$ Hz, the restoring force dominates over the viscous drag force, $\omega < 1/\tau_p$. In this case we can rewrite Eq.5.21 in the following way, using the same structure as the driven damped harmonic oscillator. If we rewrite Eq.5.21 as,

$$\mathbf{x}(\mathbf{t}) = \chi(\omega)\mathbf{f}_L(t) \text{ with } \chi(\omega) = \left(\frac{1}{\alpha_L} - \frac{i}{\omega\tau_1\alpha_L}\right) \quad (5.22)$$

Here $x(t)$ is the vortex position and the complex number $\chi(\omega)$ describes the response of the vortex system. As in Sec.5.2.2, we can parameterized the solution by the amplitude and the phase of $\chi(\omega)$ as:

$$|\chi(\omega)| = \frac{1}{\alpha_L} \sqrt{1 + \frac{1}{(\omega\tau_1)^2}} \text{ and } \tan \theta(\omega) = \frac{1}{\omega\tau_1}, \quad (5.23)$$

In both expressions for the amplitude and the phase-lag, the term $\omega\tau_1$ shows up. For a fixed characteristic time τ_1 the deviation from pure reversible motion arises when $\omega\tau_1$ approaches 1. It implies that the driving frequency approaches the characteristic time for thermally activated motion and the vortex motion will be dominated by this process. It is clear that when the vortex motion is thermally activated a phase lag appears between drive and vortex displacement. When the driving frequency is much larger than $\omega\tau_1 \gg 1$, but still small enough to neglect viscous damping, $\omega \ll 1/\tau_p$, the motion reduces to Campbell's reversible vortex motion. In this frequency regime thermally activated motion will contribute negligible to the motion properties of a vortex. The situation where $\omega\tau_1 < 1$ can not be described within linear response, as in this case the response is strongly non-linear[44] and the above equations do not apply. In the reversible Campbell regime a one-to-one correspondence exists between a vortex and a driven damped harmonic oscillator as discussed in Sec.5.2.2, within the limits $\omega \ll \omega_0$ and $\omega \ll (k/\eta)$.

Before we continue with the interpretation of the measured temperature dependence of the vortex response, we show explicitly that the measured phase with SSM corresponds with the phase-lag in Eq.5.23. We denote with $B_z^v(x_i, y_i, t)$ the magnetic induction carried by a single vortex, shaking back and forth around its equilibrium position, r_{i0} . If we assume the vortex is driven by a small ac excitation in a way that $r_i = (x_i, y_i)$ oscillates about r_{i0} . In this situation, we can expand $B_z^v(x_i, y_i, t)$ in a Taylor series around r_{i0} . Without loss of generality, we can choose the x axis parallel to the applied drive. We further assume that the vortex displacement is parallel to the drive, which is valid for linear response. In this case, vortex motion is restricted to the x direction and the expansion can be performed in powers of $\delta x_i = x_i - x_{i0}$:

$$B_z^v(x - x_i(t), y) = \sum_{p=0}^{\infty} \frac{1}{p!} \frac{\partial^p B_z^v}{\partial x_i^p} \Big|_{x_{i0}} \delta x_i^p \quad (5.24)$$

$$= B_z^{v-dc}(x, y) - \frac{\partial B_z^{v-dc}}{\partial x} \delta x_i + \frac{1}{2} \frac{\partial^2 B_z^{v-dc}}{\partial x^2} \delta x_i^2 + \mathcal{O}(\delta x_i^3) \quad (5.25)$$

Notice the change of sign of the odd terms of the expansion due to changing x_i by x in the derivatives. If we assume the vortex displacement can be expressed as $\delta x_i = |\chi(\omega)| \cos(\omega t + \theta(\omega))$, as in Eq.5.23. We obtain for the in-phase and out-of-phase response,

$$B_z'^v = \frac{1}{T} \int dt \cos(\omega t) B_z(x, y, t) = -|\chi(\omega)| \frac{\partial B_z^{v-dc}}{\partial x} \cos(\theta(\omega)) \quad (5.26)$$

$$B_z''^v = \frac{1}{T} \int dt \sin(\omega t) B_z(x, y, t) = |\chi(\omega)| \frac{\partial B_z^{v-dc}}{\partial x} \sin(\theta(\omega)) \quad (5.27)$$

Notice that the length scale in the case of a diluted vortex distribution for B_z^{v-dc} , is the penetration depth, see Sec.1.6 for an Abrikosov vortex and Sec.1.7. for a Pearl vortex. This scale exceeds, in the linear regime, typical vortex displacements and hence one can safely keep the leading order terms. These results, leads to the conclusion that the measured modulus by SSM, $\sqrt{(B_z^{v})^2 + (B_z^{v})^2}$, is directly related with the amplitude of vortex motion, with a proportionality constant given by the gradient of B_z^{v-dc} in the direction of shaking. Further, the measured phase angle corresponds directly with the phase lag between the vortex motion and the Lorentz drive.

$$|\chi(\omega)| = \left(\frac{\partial B_z^{v-dc}}{\partial x}\right)^{-1} \sqrt{(B_z^{v})^2 + (B_z^{v})^2} \quad (5.28)$$

$$\tan(\theta(\omega)) = -\frac{B_z^{v}}{B_z^{v}} \quad (5.29)$$

In these parameters the dependence on the probe position cancel out and should be homogeneous, apart from the places where $\partial B_z^{v-dc}/\partial x = 0$.

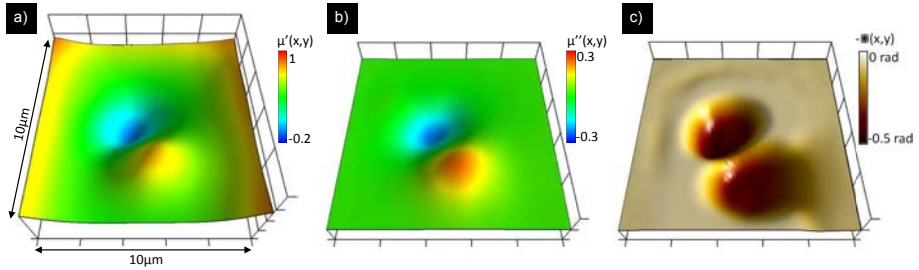


Figure 5.9: (a) Scanning Susceptibility Microscopy image of the real part of the relative permeability, μ'_r for a single vortex upon shaking with an external ac magnetic field of amplitude, $h_{ac}=0.1\text{mT}$, and frequency $f=77.123\text{Hz}$ at a temperature of $T= 6.9\text{K}$. The initial vortex distribution is obtained by performing a field cool in an external applied dc magnetic field, $H= 0.13 \text{ mT}$. (b) Simultaneously acquired map of the imaginary part of the relative permeability, μ''_r . (c) Calculated spatial dependence of minus the phase angle.

Let us use the above considerations to interpret the temperature dependence of out-of-phase component of the vortex response. At low temperatures, when $U(j) \gg k_B T$ and thermally activated flux motion can be neglected, τ_1 diverges exponentially and the character of the ac-response, $\mathbf{x}(t) = \alpha_L \mathbf{f}_L(t)$, is a pure

reversible harmonic motion as described by Campbell and Evetts[48]. This behaviour explains the absence of a response in the SSM images of $\mu_r''(x, y)$ for $T < 6.8\text{K}$, while a response is still visible in $\mu_r'(x, y)$. As the temperature rises, the thermal activation energy decreases and $1/\omega\tau_1$ becomes appreciable, meaning thermally activated vortex jumps between metastable states come into play and contribute substantially to the vortex motion. This explains the observed out-of-phase component for $T > 6.8\text{K}$. Fig.5.9 shows a zoom on the ac-response of a single vortex for $T = 6.9\text{K}$ and the corresponding spatial dependence of the calculated phase, where we use a cutoff for $|\mu_r'(x, y)| < 0.15$ to limit the divergence of arctan and we subtracted the contribution of the screening currents in $\mu_r'(x, y)$. As shown in Fig.2(c), the obtained phase shift is $\theta = -0.5\text{rad}$. From Eq.5.23, the phase shift between the response and the drive is given by $\theta = -\arctan(1/\tau_1\omega)$. As $\tau_p \leq 0.1\mu\text{s}$, we obtain a lower limit for the effective activation barrier height of $U(j) \geq 8.50 \times 10^{-3}\text{eV} \sim 14.3\text{ k}_B T$, similar to typical average effective barrier heights found in the literature by macroscopic measurements[142].

The temperature dependence of the phase shift shows a maximum at $T = 6.85\text{K}$. Optimal energy dissipation is expected when the driving frequency matches the characteristic frequency of our vortex system, it is, when the resonant absorption condition, $\omega\tau_1 = 1$, is fulfilled. As the driving frequency is fixed, we approach or de-tune from the resonant absorption condition by changing τ_1 with temperature. The non-monotonic temperature dependence of the phase shift reflects the non-trivial temperature dependencies of the different factors contributing in τ_1 .

Amplitude and field dependence

In the previous case we considered both the in-phase and out-of-phase response of a Pb ribbon to an ac magnetic field. The power of this technique is illustrated further for the same sample in Ref.[143], wherein the response to an ac magnetic field is probed upon changing the vortex distribution within the Pb ribbon. A clear correlation is found in this work between the position of the vortices within the Pb ribbon and the corresponding SSM images. For example, a vortex in a very symmetrical position in the center of the bar does not show up in the SSM image as the driving Lorentz force is zero in the center. However, vortices in off-center position clearly show a response in the SSM images. As such, SSM can be used as a tool to probe the vortex mobility. Further, the response is investigated for a fixed vortex distribution and temperature, upon increasing driving amplitude. A transition from intra-valley to inter-valley vortex motion is observed upon increasing amplitude. The low amplitude phase retains the original vortex configuration and vortices shake in their own potential well, whereas beyond a certain oscillation amplitude, vortices can escape from their

local potential well and the initial vortex distribution is altered. This transition was already pointed out by Campbell in 1969 and this model can now be checked directly by SSM with single vortex resolution[48].

5.3.2 Ac response of a nano-structured superconductor

Sample layout

In this section we study the ac-response to an applied ac magnetic field of a nano-structured high-quality Pb superconducting strip of width $2a = 600\mu\text{m}$, and thickness $t = 50\text{ nm}$, as described in Sec.4.3 (see Fig.4.3 and Fig.4.5). The sample contains a square array of square antidots ($b = 600\text{nm}$) with an antidot void area of $b^2 = 0.36\mu\text{m}^2$, as obtained by standard electron beam lithography technique, electron beam depositing techniques and subsequent lift-off as described in Sec.2.3. The sample was deposited on top of a SiO_2 insulating substrate and covered by a Ge layer of 60 nm to prevent it against oxidation processes. An additional gold layer of 50 nm covers the whole strip to allow an STM approach of the sample surface. The periodicity of the antidot lattice is $w = 3\mu\text{m}$, resulting in a commensurability field,

$$H_1 = \frac{\phi_0}{w^2} = 0.2298\text{mT}, \quad (5.30)$$

at which the density of holes coincides with the density of vortices. In all cases the magnetic field (ac and dc) is applied perpendicularly to the plane of the film. The superconductor to normal transition at zero field occurs at $T_c = 7.2\text{K}$ as measured by monitoring the in-phase and out-of-phase response to an applied ac magnetic field with the Hall probe while sweeping the temperature through the metal-superconductor transition. For the experimental temperatures used in this work, $T > 4.2\text{K}$, the film behaves as a Type-II superconductor as described in Sec.3.3.1. Before starting with the ac response, we investigate the dc response of the nano-structured superconducting film to an applied magnetic field.

Dc response of a nano-structured superconducting film

Some selected results of obtained dc vortex distributions at $T = 4.2\text{K}$ after performing field cooling procedures in different applied dc magnetic field H_{dc} , are shown in Fig.5.10 and Fig.5.11. The color scale is adjusted for every image to maximise the contrast. The detailed procedure follows respectively the next steps: we heat the sample up to $T > T_c = 7.2\text{K}$, subsequently we cool down to

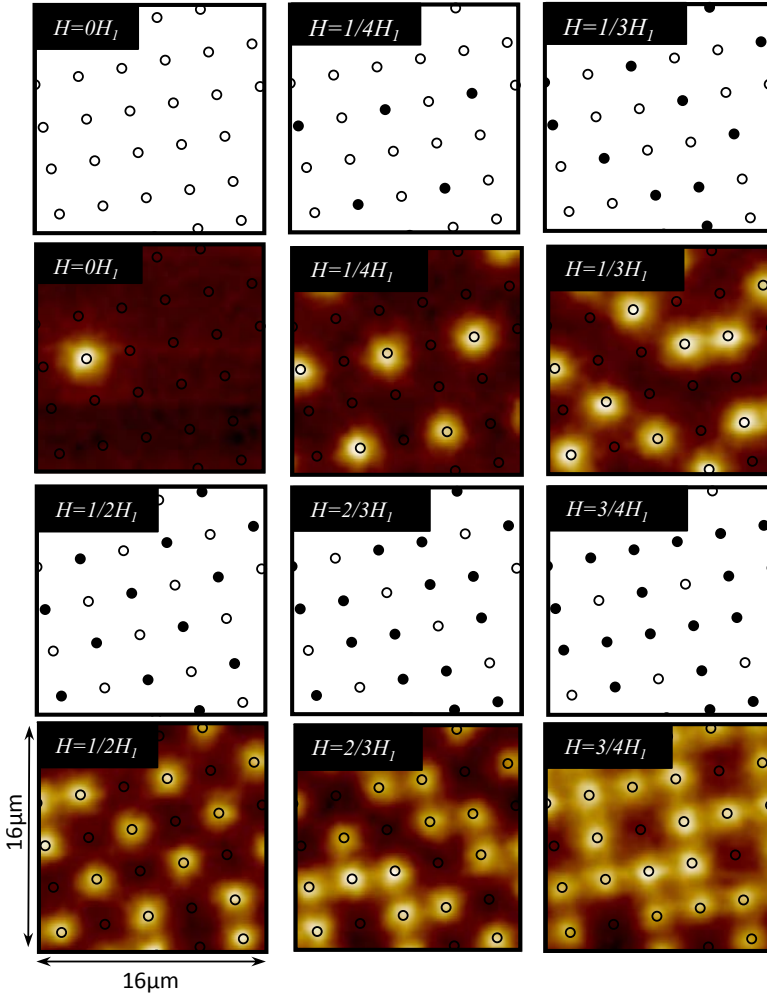


Figure 5.10: (Top rows) Schematic representation of the obtained equilibrium vortex distributions by MD simulations in a square array of antidots. Open circles indicate the unoccupied pinning centers, whereas filled circles indicate pinning centers occupied by a single vortex. (Bottom rows) Scanning Hall probe microscopy images obtained after cooling down to $T = 4.2$ K in presence of a field $H \sim 0H_1$, $H \sim 1/4H_1$, $H \sim 1/3H_1$, $H \sim 1/2H_1$, $H \sim 2/3H_1$ and $H \sim 3/4H_1$

$T=4.2\text{K}$, while a dc magnetic field H_{dc} is continuously applied (Field cooling process (FC)). When the temperature 4.2K is reached an image is captured

of the vortex distribution by measuring the local induction in a scan-range of $16 \times 16 \mu\text{m}^2$ with a micro-sized Hall probe ($0.5 \times 0.5 \mu\text{m}^2$), approximately $1.2 \mu\text{m}$ above the sample surface. This procedure explores near to equilibrium vortex distributions as the obtained nucleated vortex distribution is frozen in close to T_c [133]. The scan-speed for the images is $40 \mu\text{m}/\text{s}$ and the cross is biased by a dc current of $I = 20 \mu\text{A}$. The field steps are $h_{dc} = +0.004 \text{mT}$, which is less than the field necessary to have one additional vortex per scanarea $\phi_0/(16 \times 16 \mu\text{m}^2) = 0.008 \text{mT}$. The field is applied perpendicular to the sample surface.

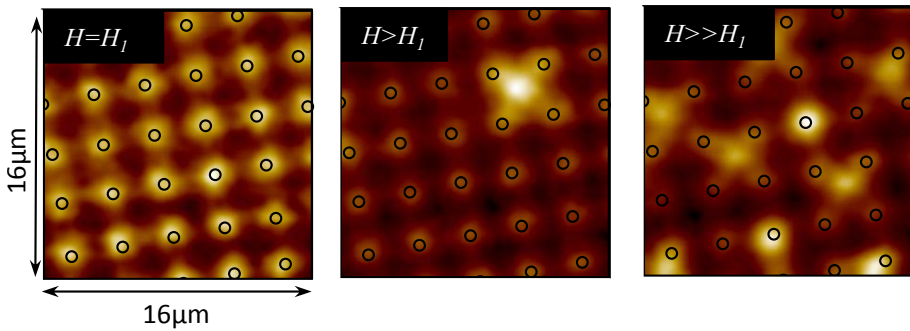


Figure 5.11: Scanning Hall probe microscopy images obtained after cooling down to $T = 4.2 \text{ K}$ in a scan area of $16 \times 16 \mu\text{m}^2$; for $H = H_1$ (Left), showing perfect commensurability; (Middle) for $H > H_1$, showing the presence of an interstitial vortex; (Right) for $H \gg H_1$, showing the presence of interstitial and double quantized vortices.

It is clear the sample shows nice commensurability effects. Not only first matching is nicely present, also fractional matching features can be identified in accordance with Ref.[111]. However, it is clear that the commensurate vortex distributions at fractional matching fields possess defects. These defective states can be attributed to the possible degeneracy of the fractional matching states under symmetry operations as compared to integer ones. This particular feature of fractional matching states can result in the domain formation as observed in Ref.[114, 115]. Nonetheless, the observation of these quasi sub-matching features, where the vortex-vortex interaction is weak and therefore small imperfections on the pattern have a sizeable impact on the vortex distribution, assure good sample quality and is indicative of a low dispersion in pinning energy among different pinning sites. Above the first matching field, first interstitial vortices appear while upon further increasing the dc field a combination of interstitial and double quantized vortices (at the pinning sites) is established. Detailed analysis shows that a clear difference in the field

profile is observed between interstitial, pinned and double quantized vortices. Whether a pinning center can sustain a multi quanta vortex, depends for an antidot upon the ratio between the dimensions of the antidot and the coherence length, see Sec.1.8. For a cylindrical cavity with radius $R = b/2$, the maximum number n_s of vortices trapped was theoretically estimated by Mkrtchyan and Schmidt[39], within the London approximation (high κ). According to this calculation, depending on the radius R_p of the defect, more than one flux can be trapped, up to a certain saturation number, n_s , given by Eq.1.74. In our particular case, with $R_p = 300\text{nm}$ and using an estimate for $\xi(T_f) \sim 0.18\mu\text{m}$ at the freezing temperature, $T_f > 7\text{K}$. We obtain $n_s \sim 0.85$. However, it is clear from the SHPM image at $H \gg H_1$ in Fig.5.11, that the antidots can stabilize in some cases double quantized vortices. This indicates clearly that the interaction with neighbouring vortices plays a role in the determination of the energy of a pinned n-quanta vortex.

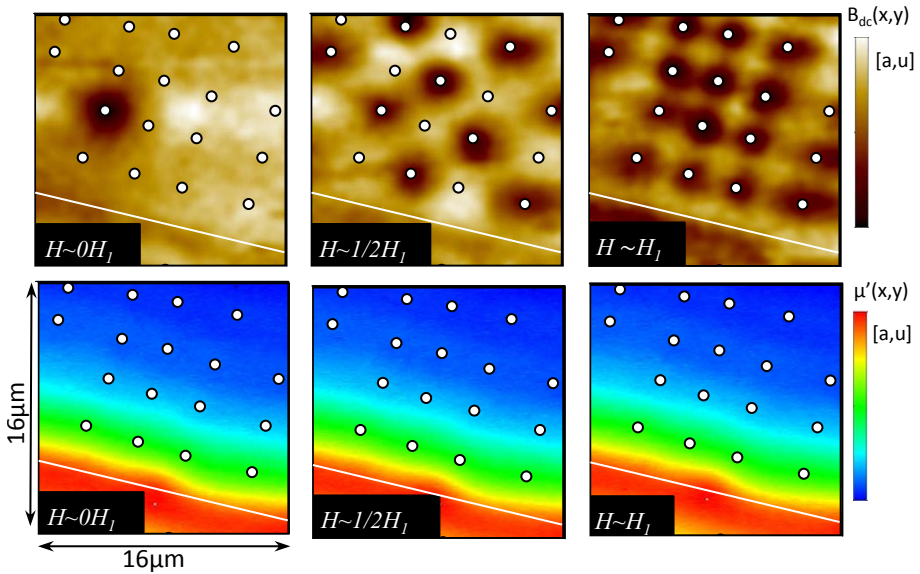


Figure 5.12: (Top row) Regular dc SHPM image at 4.2 K in a scan area of $16 \times 16 \mu\text{m}^2$, showing $B_z(x,y)$ after freezing in the motion for three different indicated field configurations, $H = 0, -1/2, -1H_1$. (Bottom row) Picked up in-phase response $\mu'(x,y)$ at 6.7K when an ac magnetic field is applied of $h_{ac} = 0.015\text{mT}$ and frequency $f = 77.123\text{Hz}$. The dots indicate the positions of the square antidots, while the white line indicates the physical edge of the sample.

Ac response of a nano-structured superconducting film

The SSM technique is applied to investigate the ac-response of the nano-structured superconductor. The response upon changing the vortex configurations, as obtained by a FC process, is investigated. The measurement procedure is the following: First, we preform a FC in h_{dc} to obtain a near-to equilibrium vortex distribution. Subsequently, we switch on an additional co-linear ac magnetic field, h_{ac} and measure simultaneously $\mu'(x, y)$, $\mu''(x, y)$ and the time averaged local magnetic induction $\langle B_z(x, y, t) \rangle_t$. As such, we obtain in linear approximation information about the ac-response of the prepared vortex distribution obtained by a FC process. Subsequently we cool down further to freeze in the vortex motion to obtain a snapshot during ac shaking.

A selected subset of data following the described measurement procedure is shown in Fig.5.12 and Fig.5.13, for $h_{ac} = 0.015\text{mT}$ and frequency $f = 77.123\text{Hz}$, sweeping the dc field over a broad interval. The ac dynamics is probed at $T = 6.7\text{K}$ and the snapshot of the motion is obtained by freezing to $T = 4.2\text{K}$. The white dots and the white line in Fig.5.12 and Fig.5.13 show schematically the position of the square anti-dots and the sample edge, respectively. The first row shows a SHPM image at 4.2 K, showing $B_z(x, y)$ after freezing in the motion. The second row is the picked up in-phase response $\mu'(x, y)$ at 6.7K. All images have optimized colour contrast to show the ac-dynamics in the optimum conditions. Below the first matching field, $H \leq -H_1$, the response is a pure Meissner response, the vortices are strongly pinned at this temperature and do not show up in $\mu'(x, y)$. As described before, within linear response, the equation of motion for a vortex at low temperatures and frequencies is given by, Eq.5.21, which reduces in these limits to:

$$\mathbf{x}(\mathbf{t}) = \chi(\omega) \mathbf{f}_L(t) \text{ with } \chi(\omega) = \left(\frac{1}{\alpha_L} \right) \quad (5.31)$$

In this case the motion is a pure reversible oscillatory motion in a potential well characterized by the Labush constant α_L . In this field range, it is expected each pinned vortex experiences a similar large restoring force. This can be argument from the observation of the fractional matching features indicating good sample quality and a uniform pinning strength of the antidots. From similar measurements in the field range $H \leq -H_1$ and for the same ac excitation, no response from single quanta vortices in $\mu'(x, y)$ is observed below 6.95K. Similar as for the Pb ribbon, a paramagnetic field enhancement is observed at the border due to demagnetization effects and upon penetrating deeper in the sample volume the field is diamagnetically screened. Above first matching, $H > -H_1$, the interstitial vortices show an in-phase response, which is even more clear in the images where the SSM image at $H = 0\text{mT}$ is subtracted,

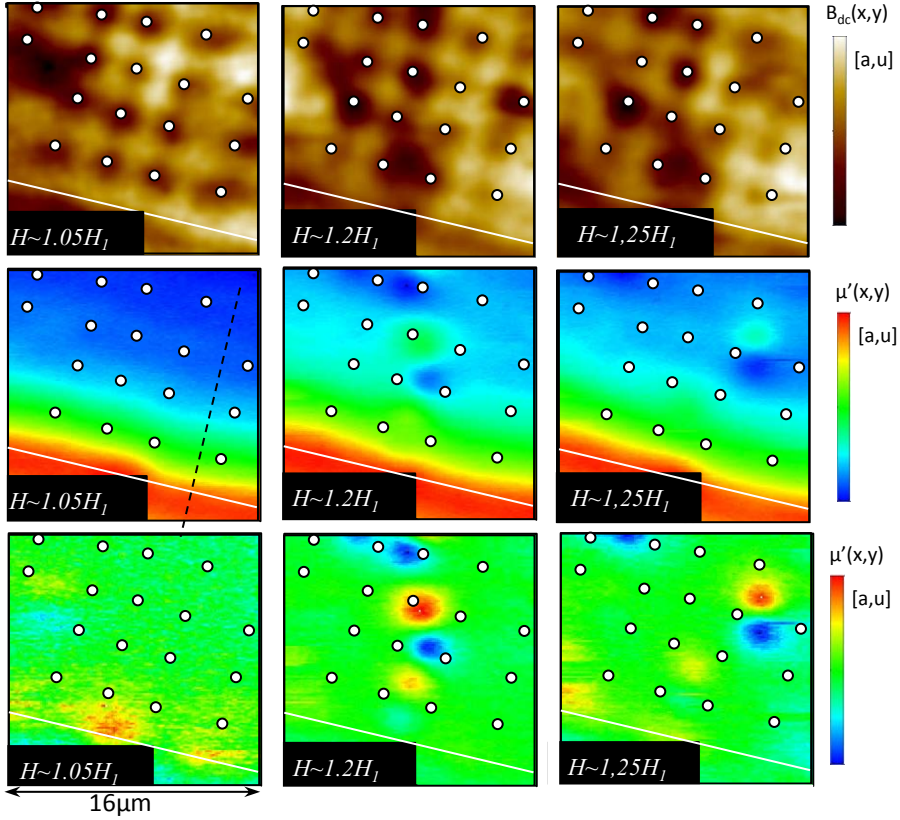


Figure 5.13: (Top row) Regular dc SHPM image at 4.2 K in a scan area of $16 \times 16 \mu m^2$, showing $B_z(x,y)$ after freezing in the motion for different indicated field configurations above first matching, $H > -H_1$. (Second row) Picked up in-phase response $\mu'(x,y)$ at 6.7K when an ac magnetic field is applied of $h_{ac} = 0.015\text{mT}$ and frequency $f = 77.123\text{Hz}$. (Third row) Similar images as in the second row, $\mu'(x,y)$, only here we tried to isolate the vortex response by subtracting $\mu'(x,y)(h_{dc} = 0)$. The dots indicate the positions of the square antidots, while the white line indicates the physical edge of the sample.

see Fig.5.13(third row). However, the vortices at the site locations stay perfectly pinned. The interstitial vortices are highly mobile as they are pinned by a cage formed by the surrounding repulsive pinned vortices, as discussed in Ref.[46]. The means the Labusch constant in Eq.5.31, characterizing the potential well each vortex experiences, is very different for pinned ($\alpha_L = \alpha_p$) vortices and interstitial ($\alpha_L = \alpha_v$) vortices, with $\alpha_p \gg \alpha_v$. This proves that the

SSM technique is able to probe the local pinning potential with single vortex resolution. Moreover, for the interstitial vortices the inductive response is not a sharply peaked distribution and it is clear in this regime the displacement at the edge diffuses into the sample due to elastic coupling. This results in the observation of chains which resemble a set of coupled harmonic oscillators.

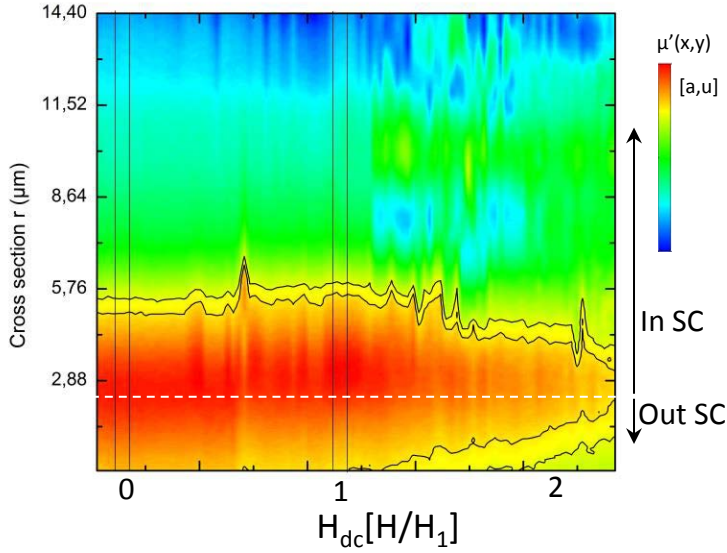


Figure 5.14: Field dependence of the average cross-sections as obtained from the SSM images. The average cross-section at a certain field amplitude, h_{dc} , is obtained by averaging over 80 cross-sectional lines parallel to the black dashed line indicated in Fig.5.13. The white dashed line indicates the sample border.

As the vortex dynamics alters the impedance of the superconductor, it determines completely the penetration of the ac magnetic field into the sample volume, as described in Sec.1.8. For the case of harmonic vortex motion (Campbell regime) as considered above, it is expected that for a fixed temperature, the penetration depth varies with the applied dc field, as derived in Eq.1.79. The ac-penetration depth is given in this particular case of a periodic pinning array having a composite vortex lattice, composed of strongly pinned vortices and weakly caged interstitial vortices by[46]:

$$\lambda_{ac}^2 = \lambda_L^2 + \lambda_C^2, \text{ with } \lambda_C^2 = [N_A \lambda_{C(A)}^2 + N_B \lambda_{C(B)}^2]/N, \quad (5.32)$$

where λ_L is the London penetration depth, $\lambda_{C(A)}^2 = (\phi_0 B^2)/B_1 \mu_0 \alpha_p$ the Campbell penetration depth for the pinned species of vortices and $\lambda_{C(B)}^2 = (\phi_0 B)/\mu_0 \alpha_v$, which describes likewise the contribution to the penetration depth of the interstitial vortices. In these expressions, α_p and α_v denote the Labusch constant for the pinned vortices and the interstitial vortices, respectively and B_1 denotes the first matching field. Further, we assumed in accordance with the observations that $\alpha_p \gg \alpha_v$. From Eq.5.32, it is clear that the screening currents at the edge will vary with the applied dc magnetic field. Moreover, it is expected that the introduction of interstitial vortices will result in a much larger field dependence of the ac penetration depth as compared to pinned vortices. In Fig.5.14 we show the field dependence of the average cross-section as obtained from the SSM images. The average cross-section at a certain field amplitude, h_{dc} , is obtained by averaging over 80 cross-sectional lines parallel to the black dashed line indicated in Fig.5.13. It is clear that above first matching, where interstitial vortices appear, the amplitude of the local induction at the edge, induced by the screening currents, decreases with field. This indicates that the field is less effectively screened and penetrates deeper inside the superconductor for $H > H_1$. Below first matching, as expected for very strongly pinned vortices, the screening current distribution and strength does not change.

These results provide for the first time direct evidence that the vortex dynamics inside the sample, changes the ac-penetration of the field. In macroscopic measurements, it is exactly this vortex dynamics induced change of the penetration depth that determines the measured inductive response. As the macroscopic measurements allow no direct measurement of individual vortices shaking back and forth. SSM allows to make a clear correlation between the observed dynamics of a single fluxon and the induced changes of the screening currents.

5.4 Conclusions

In summary, we explored and described the microscopic linear response of a SC to an applied alternating magnetic field. It should be noted that up till now the ac-response of individual vortices remained concealed, despite the enormous amount of theoretical works. In this work we combine the strength of phase sensitive detection used in global ac-susceptibility measurements and the power of individual vortex visualization, accessible with Scanning Hall probe microscopy (SHPM), to reveal the microscopic linear response of a type-II superconductor to an external applied ac-magnetic field. The local character of this scanning ac-susceptibility microscopy(SSM) technique and

the argument “Seeing is believing” allow us to bridge the gap between the global ac-susceptibility measurements and the associated microscopic theories of vortex motion and ac-field penetration and the real microscopic ac-response. In a first case study, the response of a SC ribbon to an external applied alternating magnetic field upon decreasing temperature is investigated. A clear dichotomy between the ac-response of the vortices and the screening currents was observed using the phase sensitive character of the SSM technique. The observed out-of-phase response of the vortices, which was absent for the reversible screening currents, directly shows the local dissipation of the vortex motion. As viscous losses can only account for a small fraction of the measured large phase-lag at the used experimental excitation frequency, the observed large phase-lag, $\theta = -0.5\text{rad}$, is explained by thermally activated vortex hopping over pinning centers. As such, a new and powerful tool is introduced and employed allowing to investigate for the first time vortex dynamics with single vortex resolution as has been done for example in Ref.[143]. This opens new and exciting possibilities to study locally loss mechanisms in a variety of not only superconducting systems but also magnetic systems, including magnetic domain walls, etc [144].

In a second case-study, a superconductor having a square lattice of antidots, the response to an external applied alternating magnetic field upon changing the vortex distribution is investigated. A clear difference in mobility is observed between pinned and interstitial vortices. This difference arises due to the different pinning potential each vortex species experiences. Whereas, vortices pinned by an antidot are strongly anchored, the interstitial vortices are very mobile as they are weakly caged due to surrounding pinned vortices. Moreover, we made a direct observation of the correlation between the ac-penetration depth and the vortex dynamics used in theoretical models[44, 45, 43] to explain macroscopic ac-susceptibility measurements.

Scanning Hall probe microscopy of unconventional vortex patterns in the two-gap MgB_2 superconductor

6.1 Introduction

Single-gap superconductors are usually categorized as being either type-I or type-II, depending on their behavior under a magnetic field (cf. Sec.1.4). For $\kappa < 1/\sqrt{2}$, the superconductor-normal state (SN) wall energy is positive and the magnetic field is expelled from the bulk. For $\kappa > 1/\sqrt{2}$, the SN wall energy is negative, and the superconductor gets rapidly flooded above a certain critical field, H_{c1} , with tiny tubes of magnetic field carrying one unit of flux quantum. These so called vortices repel each other and form in absence of pinning, the famous Abrikosov lattice as described in Sec.1.6. However, this classification of superconductors has been challenged by Babaev and Speight when considering a multigap superconductor, consisting of two coupled condensates[145]. In that paper, the authors propose that, in these materials within a broad range of material parameters, the flux distributes unevenly, combining bundles of vortices, as in Type-II materials, separated by vortex-free regions, like in Type-I superconductors. This vortex distribution arises due to a competition between a vortex-vortex long-range attraction and a short-range repulsion. Since this peculiar vortex clustering shared reminiscence with both Type-I(Meissner-state) and Type-II superconductors(Vortex-state), it was coined as the ‘semi-Meissner state’[145] or ‘type-1.5 superconductivity’[20]. Two-gap

superconductors, have many more remarkable new possibilities interesting for both fundamental research and applications. For example, upon confinement, it was shown, within the non-linear Ginzburg-Landau (GL) theory, that mesoscopic size effects stabilize fractional flux vortices in the thermodynamical ground state of s-wave two-gap superconductors. The value of these fluxes can be an arbitrary fraction of the flux quantum[146]. Further, in the mesoscopic regime novel vortex phases with non-composite vortices and with different vorticity in the two condensates have been found[147].

Vortex states similar to those predicted theoretically were first experimentally observed in 2009 by Moshchalkov et al.[20] in clean prototypical two-band superconductor MgB_2 . In these experiments, inhomogeneous vortex patterns, such as stripes and clusters, were found at low fields by the Bitter decoration technique.

With Bitter decoration, small magnetic particles ($\sim 10\text{nm}$) vaporized from a ferromagnetic filament are dispersed over a magnetic surface. The fine magnetic powder adheres to the sample surface via van der Waals forces. When an inhomogeneous magnetic field exists at the surface, the approaching ferromagnetic particles, having dipole moment \mathbf{m} , are attracted to regions having a high field gradient ($F_{\text{dip}} = -\nabla(\mathbf{m} \cdot \mathbf{B})$). The resulting decoration can be visualized with scanning electron microscopy and mimics the distribution of the magnetic induction at the time of decorating. The first successful decoration experiment revealing the Abrikosov flux line lattice was done by Essmann and Träuble in 1967[148].

However, the Bitter decoration technique suffers from certain drawbacks, such as the ex situ determination of the vortex patterns and the fact that only poor temperature control at the actual moment of decorating the vortex lattice is typically achieved. Moreover, as it is not a scanning technique it is not possible to investigate a certain area while changing continuously some thermodynamical parameters. Later on, scanning SQUID microscopy experiments performed on similar clean MgB_2 crystals revealed alike unusual vortex patterns typical of a type-1.5 superconductor[149]. However, due to the low spatial resolution only a few low field distributions could be investigated at $10\mu\text{T}$, $20\mu\text{T}$ and $50\mu\text{T}$. Moreover 2D multifits have to be used to identify the position of the vortices from the measured field distributions.

In this chapter, we investigate vortex patterns in clean MgB_2 single crystals by using scanning Hall probe microscopy (SHPM) having single-vortex resolution in a broader field range than the measurements described in Ref.[149]. On top, SHPM offers in contrast to the Bitter decoration technique the possibility to change the thermodynamic variables, magnetic field and temperature, while

simultaneously visualizing the vortex patterns in the same scanarea. We have been able to observe the progressive formation of stripes, in agreement with previous studies, and to investigate the reproducibility and stability of different vortex patterns. In addition, we have carried out a back-to-back comparison with the conventional type-II superconductor NbSe₂. These studies provide direct information about the vortex pattern formation and evolution of the vortex stripe phase observed in high quality single crystals of MgB₂[150].

6.2 Type-1.5 superconductivity

In this section we will first discuss the Vortex-Vortex(VV) interaction in single component and two-component superconductors within the GL theory. Next, the profound consequences of the particular VV-interaction potential for the vortex distribution are discussed.

The Vortex-Vortex interaction

The interaction energy per unit length between well-separated vortices in a **single-gap superconductor** is calculated within the GL theory in Ref.[151, 152]. The detailed interaction energy is given by,

$$U_{ij}(|\mathbf{r}_{ij}|) = \varepsilon_1 + \varepsilon_2 = d_1(\kappa)K_0\left(\frac{r}{\lambda}\right) - d_2(\kappa)K_0\left(\frac{\sqrt{2}r}{\xi}\right) \quad (6.1)$$

where ε_1 , is the repulsive contribution due to the interacting screening currents, whereas ε_2 represents an attractive term arising from the gain in condensation energy as vortices overlap. Here $d_1(\kappa)$ and $d_2(\kappa)$ are constants depending on the GL-parameter κ and $K_0(x)$ denotes the modified bessel function with the asymptotic limits, $\ln(x)$ for $x \ll 1$ and $(\pi/2x)^{1/2} \exp(-x)$ for $x \gg 1$. It is clear that the repulsive interaction of the screening currents acts on a scale of λ , while the attractive interaction has a range of $\xi/\sqrt{2}$. As discussed in Sec.1.4, we can make a distinction between two types of superconductors by using as a single criterium the temperature independent ratio, $\kappa = \lambda(T)/\xi(T)$, defining the GL-parameter. Kramer discusses in Ref.[152] the dependence of the VV-interaction on the GL-parameter. First of all, in the limit of high $\kappa \gg 1$, $d_1(\kappa)$ approaches $\phi_0^2/(2\pi\mu_0\lambda^2)$ whereas the term corresponding to ε_2 becomes negligible at low fields. As such Eq.6.5 reduces to the London limit expression for the interaction energy, Eq.1.44. As discussed in Sec.1.6, within the London model, the vortex core is taken into account by a delta-function arising in Eq.1.44. The London limit approximation does not consider the condensation energy gained by the overlap of the normal cores and is purely repulsive. Further, it is shown that for $\kappa = 1/\sqrt{2}$, $d_1 = d_2$ and the vortices do

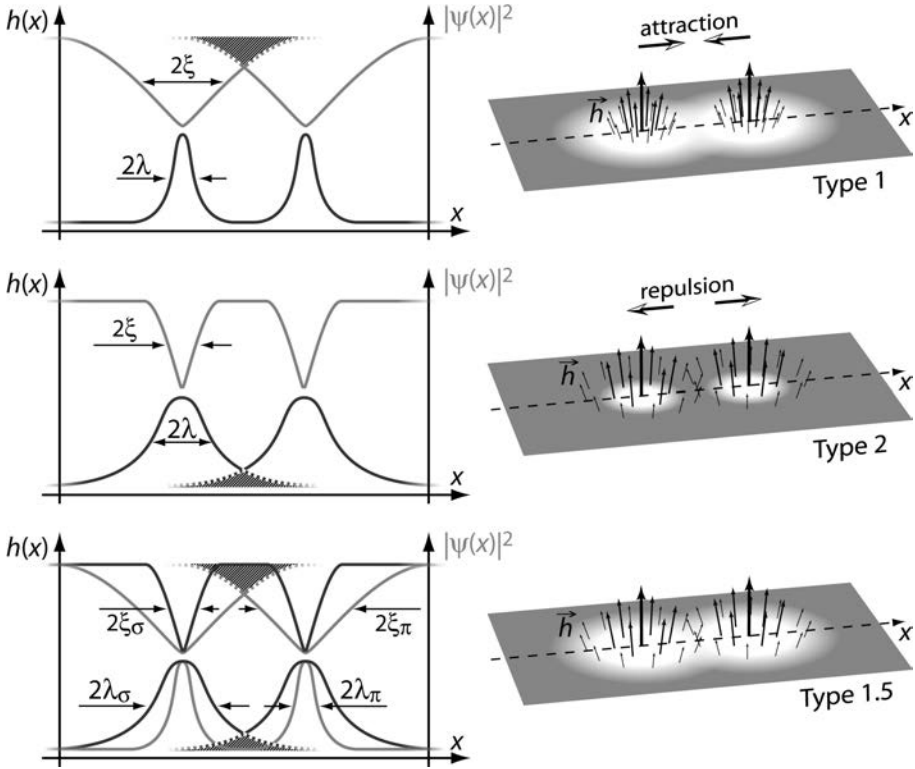


Figure 6.1: Schematics of the VV-interactions: in type-I superconductors, vortex cores are overlapping first, thus causing an attraction between vortices (top). In type-II materials, the first to overlap are the local field $h(x)$, which leads to a VV-repulsion (middle). Type-1.5 superconductors combine both the VV-attraction and repulsion, since type-I and type-II conditions are formally fulfilled for the two subcomponents of the order parameter simultaneously (bottom). Remark that this is only a didactic illustration as in principle the two-components will generate a common λ , characterizing the field penetration.[27]

not interact at all distances. Whereas, in the limits, $\kappa \lesssim 1/\sqrt{2}$, the following relations hold:

$$\varepsilon_1 + \varepsilon_2 \lesssim 0 \text{ for } \kappa \lesssim 1/\sqrt{2} \quad (6.2)$$

In case of a type-I superconductor vortices attract each other at all distances, since due to the larger ξ their cores overlap first and the gain in condensation energy dominates U_{ij} . For a type-II superconductor there is VV-repulsion at all

distances, as due to the larger λ their screening currents interact first. Moreover, in contrast to the type-I case, the vortex solution is thermodynamically stable in the regime $\kappa > 1/\sqrt{2}$. In Fig.6.1 both cases, type-I(a) and type-II(b) are illustrated.

The vortex-vortex interaction potential has been studied for **two-gap superconductors** within the two-component GL theory, by minimizing the free energy of two vortices with a variational procedure[145, 153]. The two-component GL theory starts as in the single component case, Eq.1.10, from a free energy functional which can be derived from the microscopic theory in the appropriate limits[154, 155]. For two-band superconductors with s-wave symmetry, characterized by two order parameters ψ_n , one for each band, the free energy functional is given by,

$$F_{GL} = F_1 + F_2 - \gamma(\psi_1^* \psi_2 + \psi_1 \psi_2^*) + \frac{\nabla \times \mathbf{A}^2(\mathbf{r})}{2\mu_0}, \quad (6.3)$$

where the contributions from each band

$$F_n(T) = \left(\frac{\hbar^2}{2m_n^*} |(\nabla_{\mathbf{r}} - \frac{iq}{\hbar} \mathbf{A}(\mathbf{r}))\psi_n(\mathbf{r})|^2 + \alpha_n |\psi_n(\mathbf{r})|^2 + \frac{\beta_n}{2} |\psi_n(\mathbf{r})|^4 \right) d^3r \quad (6.4)$$

are supplemented by a Josephson-type coupling term and the magnetic energy. The Josephson type coupling describes Cooper pair tunneling between the two bands. In principle it is possible that other mixing terms appear coupling both bands, however for the case of clean single crystals of MgB_2 we can neglect them[156]. Although α_1 and α_2 can change sign at different temperatures, a finite Josephson coupling γ forces both ψ_n to vanish at a single critical temperature T_c [157].

In contrast to single-component superconductors, where the VV-interaction is characterized by a single parameter which describes the ratio between the two characteristic length scales, the GL-parameter κ . In two-gap superconductors the situation is much more complex[153, 158] as three length scales are present with an additional Josephson coupling parameter. These three length scales characterizing the superconductor are: the two partial coherence lengths, ξ_n describing the smallest distance over which we can bend each component and a single penetration depth λ , which describes how deep a magnetic field penetrates the superconductor. When no coupling is considered, $\gamma = 0$, depending on the ξ_n and λ relative values, several different regimes can be realized. If $\xi_1 \approx \xi_2 \leq \lambda$, the two-component superconductor just shows typical type-II(\gg) and type-I(\ll) behavior. An interesting case is discussed in Ref.[145] for two uncoupled components having $\xi_2 < \sqrt{2}\lambda < \xi_1$. In this case

where one component is of type-I, while the other is of type-II, it is found that the VV-interaction varies non-monotonic. The origin of this non-monotonic VV-interaction when the two-components are in different regimes, it is one condensate is in the Type-I regime, while the other acts as being type-II is conceptually illustrated in in Fig.6.1. One can expect that the resulting VV-interaction results from a competition between the dominant attractive VV-interaction present in the type-I component favoring the overlap of vortex cores and a dominant repulsive VV-interaction in the type-II component due to the overlap of screening currents.

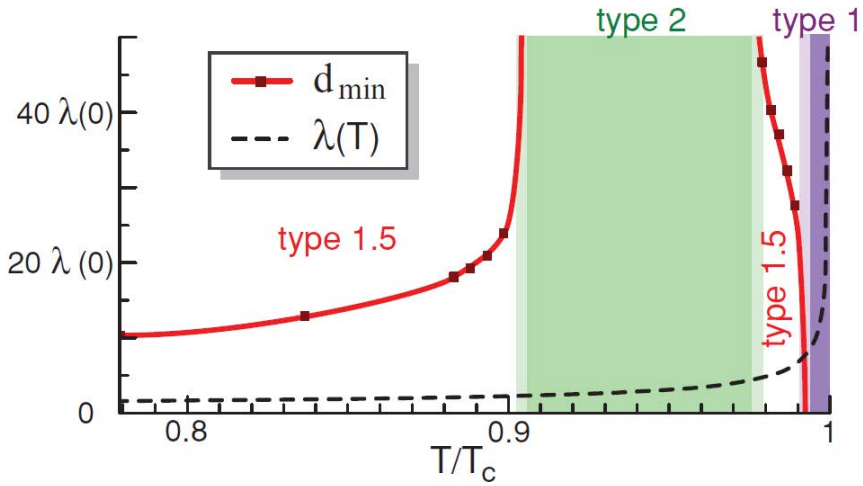


Figure 6.2: Temperature evolution of the separation d_{\min} at U_{vv} minimum and of the magnetic penetration depth λ for the material parameters corresponding with MgB_2 [153] in units of $\lambda(0)$.

A universal criterium to a priori determine the type of vortex interaction in a two-band system is discussed in analogy with the derivation of Kramer[152] in Ref.[158]. It is shown therein that the character of the short-range VV-interaction is determined by the sign of the NS surface energy, in analogy with the conventional differentiation between type-I and type-II superconductors. However, the long-range interaction is determined by a modified temperature dependent GL-parameter. As such a non-monotonic temperature dependent VV-interaction can result, characterized by a minimum (d_{vv}) in the VV-interaction potential. For MgB_2 , the evolution of the minimum in the VV-interaction potential, d_{vv} , is shown as a function of temperature in Fig.6.2. It is clear that upon cooling down, the VV-interaction crosses a sequence of transitions behaving as Type I($d_{vv} \rightarrow 0$) \rightarrow Type-1.5 \rightarrow Type-II($d_{vv} \rightarrow$

$\infty)) \rightarrow \text{Type-1.5}$. For a more detailed description of the possible VV-interaction potentials in two-component superconductors we refer to Ref.[153, 158, 145].

The Vortex distribution

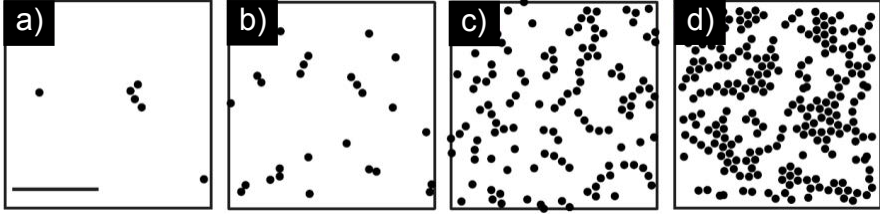


Figure 6.3: Molecular dynamics simulations of systems consisting of (a) 6, (b) 27, (c) 122, and (d) 500 vortices which have the interaction energy calculated from a two-gap GL theory for the type-1.5 condition. A scale bar corresponds to $10 \mu \text{ m}$. [149]

The particular interaction potential between two single-quantized vortices has profound consequences for the vortex distribution. Type-I superconductors in an applied magnetic field below the thermodynamical critical field, H_c , should exhibit an ideal Meissner effect. However, in samples of finite size the demagnetizing factor $N > 0$, allows for the observation of an ‘intermediate’ state containing superconducting and normal domains. Depending on the sample geometry, the amount of pinning, different topologies are observed such as tubular or laminar domains [159, 160]. For type-II superconductors the pure repulsive interaction between vortices results in the formation of the triangular Abrikosov lattice in the field range between $H_{c1} < H < H_{c2}$ when no pinning is present, as discussed in Sec.1.6. Also here pinning, sample geometry, crystal anisotropy can have profound consequences for the vortex-lattice structure. In the case of single component superconductors where $\kappa \sim 1/\sqrt{2}$, one does not expect to have any interaction between vortices within the GL model. However in a realistic system even in this limit, there will be always leftover inter-vortex interactions (appearing beyond the GL description) from underlying microscopic physics which can result in a non-monotonic VV-interaction [161]. The non-monotonic V-V interaction results in this case in unconventional vortex distributions, having a coexistence of Meissner regions and regions having a regular vortex lattice [162].

Within the two-component GL model, as discussed a non-monotonic VV-

interaction having a long-range attraction and short range repulsion can exist as a consequence of several superconducting components with different coherence lengths. This particular type of interaction results at low fields in a vortex distribution having vortex clusters wherein vortices sit a preferential distance, d_0 , from each other, immersed in domains of Meissner state[145, 163]. This is evidenced by molecular dynamic (MD) simulations modelling a system of overdamped vortices under influence of this specific interaction potential. The resulting vortex distribution upon changing the density is shown in Fig.6.3. The corresponding distribution of the first neighbour distance, P_a , for a vortex distribution obtained in a type-II and a type-1.5 superconductor by MD simulations is shown in Fig.6.4(a). It is clear that where the distribution function for the type-II case is single peaked, the distribution function for the type-1.5 case shows a bimodal behavior corresponding with both inter (green arrow)-and intra (red arrow) vortex cluster separations.

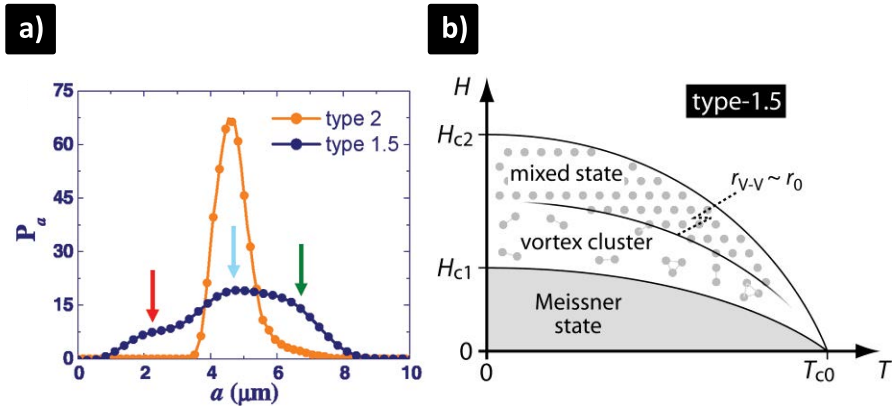


Figure 6.4: (a) The distribution of first neighbor distance, P_a , of the theoretical vortex structures obtained in a Type-II (orange) and a Type-1.5 (blue) superconductor by MD simulations. In the case of Type-1.5, P_a shows additional peaks at distances shorter (red arrow) and longer (green arrow) than the most probable separation (blue arrow). (b) A tentative schematic H-T phase diagram of a Type-1.5 two-gap superconductor. [20, 27].

At higher fields, when $d_0 > d_{vv}$ it is expected that a regular Abrikosov lattice is recovered. A schematic phase diagram characterizing the vortex distribution for a type-1.5 superconductor is given in Fig.6.4(b) and should be compared with the phase diagram for a single-component superconductor, Fig.1.7. An excellent review about type-1.5 superconductivity can be found in Ref.[164].

6.3 Experimental details

As discussed in Ref.[20, 27], the two-gap character and the details of every subband, make MgB_2 a prime candidate to observe type-1.5 superconductivity. The MgB_2 single crystals have been grown by a high temperature and high pressure cubic anvil technique, using a precursor containing Mg, B, and BN as described in Ref.[165]. The quality of similar crystals has been already confirmed by crystallographic studies and magnetization measurements showing low pinning and clean limit behavior. Additionally, 2H-NbSe_2 crystals grown by the standard iodine vapor transport method[166] have been used in this work as a reference well-understood type-II superconductor.

The SHPM images in this chapter are obtained by using a modified low temperature scanning Hall microscope from Nanomagnetism Instruments as described in Chap.2. By locating the Hall cross just above the surface of the crystals, we are able to determine the normal-to-superconducting phase transition temperature as the temperature at which the out-of-phase component χ'' of the ac response has a maximum. Using a magnetic field amplitude of 1 Oe and an excitation frequency of 77 Hz, we obtain a critical temperature $T_c \approx 38.2$ K with a transition width $\delta T_c \approx 90$ mK for the MgB_2 crystal, whereas for the NbSe_2 crystal, we found a $T_c \approx 7$ K with a transition width $\delta T_c \approx 100$ mK.

6.4 Unconventional vortex patterns in MgB_2

In order to corroborate the presence of unconventional vortex arrays in MgB_2 , we have investigated SHPM images under field-cooling (FC) conditions, i.e. the sample is cooled down from $T > T_c$, to a chosen temperature in presence of an external field. It is well known that following this protocol guarantees a nucleated vortex state closer to the equilibrium configuration in comparison to that taken under zero-field-cooling conditions, where surface barriers and pinning give rise to a more pronounced irreversible behavior. Fig.6.5 present a direct comparison of the flux distribution in the NbSe_2 single crystal [Fig.6.5 (a) at 1 Oe and Fig.6.5 (c) at 2 Oe] with those obtained in the MgB_2 crystal [Fig.6.5 (b) at 1 Oe and Fig.6.5 (d) at 2 Oe] after field-cooling down to 4.2 K.

Although NbSe_2 exhibits a nearly perfect triangular vortex lattice with long-range order in agreement with a scenario where pinning is weak, the MgB_2 crystal shows a highly inhomogeneous vortex distribution with coexistence of vortex chains and extensive vortex-free regions. These results confirm

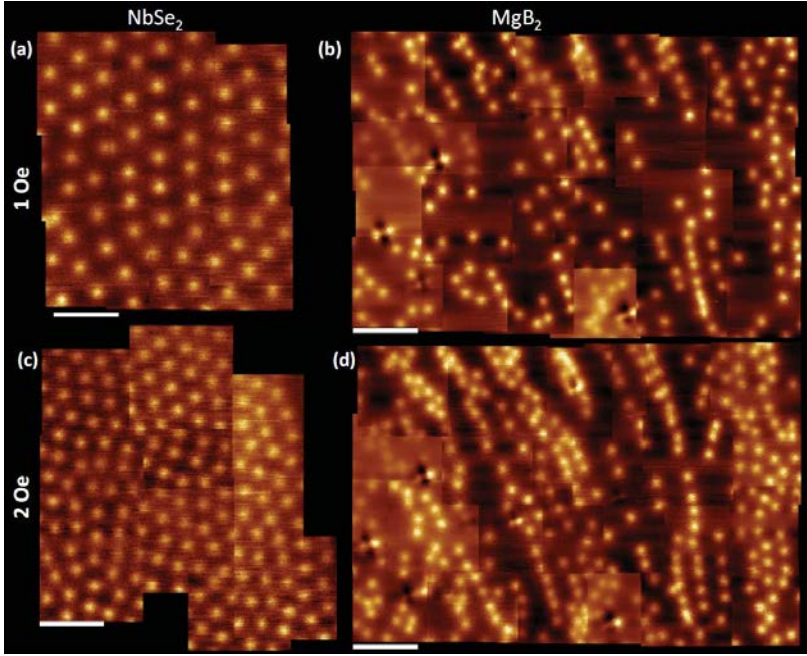


Figure 6.5: Scanning Hall probe microscopy images after performing a FC at 1 Oe for the (a) NbSe_2 and (b) MgB_2 single crystals; and after doing a FC at 2 Oe for (c) NbSe_2 and (d) MgB_2 single crystals. Images are taken at 4.2 K. The white bar on each picture corresponds to a length of $10 \mu\text{m}$. [150]

previous studies by Bitter decoration [20] and scanning SQUID microscopy [149] in similar MgB_2 single crystals from different sources. The question naturally arises whether the anomalous vortex patterns seen in MgB_2 result from unconventional vortex interactions [20, 161] or simply reproduce an accidental peculiar inhomogeneous pinning landscape strong enough to prevent the formation of a regular Abrikosov lattice. Before addressing this point, let us first consider whether a triangular lattice as seen in NbSe_2 necessarily implies negligible pinning. For the NbSe_2 single crystal, the average distance between first neighbors (d_{vv}) nicely follows the relation for a triangular lattice

$$a_v = \sqrt{\frac{2\phi_0}{\sqrt{3}B}}, \quad (6.5)$$

with B (the average internal field) being replaced by H (the applied external field), Fig. 6.6. Considering the penetration of the magnetic field in our sample $H_p(4.2 \text{ K}) > H_{c1}(4.2 \text{ K})\sqrt{d/W} \approx 36 \text{ Oe}$ (here, H_{c1} is the lower critical field,

W the sample half width, and d its thickness), it is surprising that the above relation for $d_{vv}(B)$, with $B=H$, works perfectly well all the way down to $1 \text{ Oe} \ll H_p$. This indicates that, in NbSe_2 , the vortex lattice is retained in a metastable state (i.e. frozen) by surface barriers or pinning sites at high temperatures, where H_{c1} is negligible and $B \approx H$. In other words, the temperature at which the vortex pattern is formed T_q seems to be substantially higher than the actual temperature of the experiment[133, 143]. We can obtain a lower limit for this freezing temperature as the temperature above which the vortex motion prevents a clear identification of vortices by SHPM and the image loses all contrast. Following this criterion, we have found that, for NbSe_2 , $T_q \geq 0.978 T_c$, in agreement with previous experiments[133], while for the MgB_2 , $T_q \geq 0.967 T_c$.

Figures 6.5.(c) and 6.5.(d) show the evolution of the flux patterns for both materials exactly at the same spots as in panels (a) and (b), respectively, but at higher magnetic field, $H = 2 \text{ Oe}$. For the NbSe_2 crystal, a vortex lattice containing some defects is observed[167]. As it has been pointed out by Larkin and Ovchinnikov, any disorder in a superconductor, no matter how weak, could destroy the long-range positional order in the vortex lattice due to collective pinning[168]. The increase in the magnetic field reveals that (i) the vortex stripes in MgB_2 have a range of preferential directions, and (ii) they are not straight but rather curved, i.e. they cannot be related to crystallographic orientations of the atomic lattice. It is also worth noticing that some vortex-free regions at 1 Oe become occupied at 2 Oe , indicating that the voids in the vortex lattice do not appear due to repulsive pinning potentials. Furthermore, at 2 Oe , it is possible to find stripes containing two rows of vortex chains forming a zigzag structure similar to that seen in narrow superconducting ribbons with weak pinning[143, 169]. In the case of broader stripes, containing three or more vortex chains, vortices with sixfold coordination, as in an Abrikosov lattice, are also observed. These features strongly suggest that the vortex clustering is not a consequence of an inhomogeneous vortex pinning.

Interestingly, vortices in MgB_2 not only depart dramatically from a triangular array, but they also violate locally the relation, Eq.6.5, found for the NbSe_2 single crystal. The existence of vortex clusters and stripes separated by vortex-free regions leads to a unique bimodal vortex distribution which has no counterpart in type-2 superconductors. This bimodal behavior can be split into an intragroup and an intergroup vortex distribution[20, 149]. We have found that the average first vortex neighbor distance in the intragroup distribution has changed only slightly, from $2.5 \mu\text{m}$ at 1 Oe to $2 \mu\text{m}$ at 5 Oe .

One possible explanation of this unique behavior can be found through the combination of the long-range attractive and short-range repulsive VV-interactions characteristic of the type-1.5 regime, where the VV-interaction

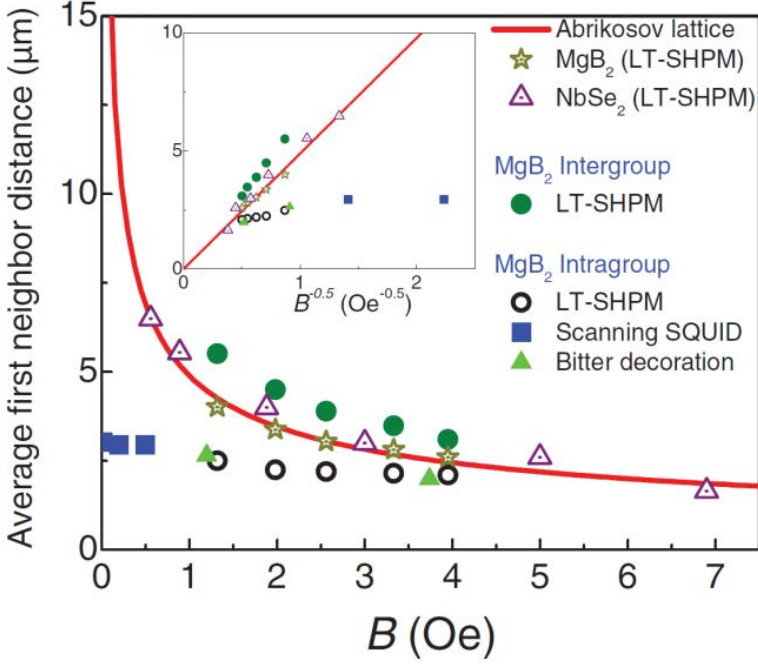


Figure 6.6: Average first neighbors distance as a function of B for an NbSe_2 single crystal (open triangles), an MgB_2 single crystal (open stars), and for a perfect Abrikosov lattice (solid line). Additionally, there is represented the intergroup first neighbor distances for an MgB_2 single crystal (full circles) and the intragroup first neighbor distances for different MgB_2 single crystals; squares, triangles, and open circles correspond to scanning Squid microscopy, Bitter decoration, and to our SHPM results, respectively. The inset shows the same data as a function of $1/\sqrt{B}$. [150]

potential, which is magnetic field independent, presents a minimum at a vortex separation d_{\min} [153]. Dao et al. predicted $d_{\min} \approx 2 \mu\text{m}$ in MgB_2 for the vortex lattice freezing at $T_q/T_c = t_q = 0.97$, see Fig.6.2. This estimate is in very good agreement with our experimentally determined intragroup average first neighbor distance, giving support for the two-gap origin of non-monotonic V-V interaction in clean MgB_2 crystals.

In Fig.6.6, we summarize the obtained average first neighbor vortex distances for NbSe_2 and MgB_2 single crystals as a function of the local induction B . The local induction has been calculated as the number of vortices divided

by the total area of the image. It is shown that both the NbSe_2 and the MgB_2 follow very well the expected behavior, Eq.6.5 (shown in the graph as the solid red/dark gray line). Nonetheless, it is worth noticing that, in the MgB_2 single crystal, the average first neighbor vortex distances in the intergroup distribution show strong magnetic field dependence while the intragroup distribution $d_{\min}(\text{B})$ data demonstrate only, as already mentioned, a weak dependence on the magnetic field. We observe that the average V-V intracluster distance changes only from $2.5 \mu\text{m}$ at 1 Oe to $2 \mu\text{m}$ at 5 Oe, in a good agreement with the equilibrium distance d_{\min} proposed by the theory. Since the theory predicts that d_{\min} is field independent, in our FC experiments, d_{\min} should vary with the magnetic field through $t_q(\text{B}) = T_q/T_c(\text{B})$, which explains why a weak dependence on the magnetic field is seen. Moreover, this is in accordance with the dependence shown in Fig.6.2. This striking feature has no counterpart in a type-II superconductor, irrespective of the details of the pinning landscape.

6.5 Stripe pattern evolution in MgB_2

Since in the absence of surface barriers or no pinning at all, one could expect strong degeneracy in the stripe ground state orientation each time a FC is performed[170], data shown in Fig.6.5(d) point out the possibility that pinning still might play a certain role in their stabilization. In order to address this point, we have performed successive FC experiments down to 4.2 K, under identical conditions and in the same area for both investigated materials. In Fig.6.7(a), we show four successive FC's at 0.9 Oe for NbSe_2 ; and in Fig.6.7(b), we repeat the same experiment for MgB_2 . The NbSe_2 shows a weakly distorted triangular lattice, which at every FC nucleates somewhat at a different position and with the principal axes of the triangular array slightly rotated. The same experiment performed for the MgB_2 crystal reveals a behavior similar to that for the NbSe_2 , but with very unusual inhomogeneous vortex patterns. Individual vortices nucleate in the successive FC's at positions that differ by more than $1 \mu\text{m}$, a distance which is larger than the typical range of the elementary pinning interaction ($r_p \approx \xi$ for fields $B \leq 0.25B_{c2}$)[168]. This behavior rules out the possibility of the existence of isolated strong pinning centers. Indeed, it has been demonstrated that, in the presence of such strong pinning sites, the positions of the vortices are not random, and they nucleate preferentially at these sites[171]. Clearly, our experiments reveal that, in both systems, the existing pinning centers must be quite diluted and weak, in agreement with the high quality of the crystals. Since the explored area in Fig.6.7(b) (about $16 \times 16 \mu\text{m}^2$) is rather small compared with the total crystal surface ($300 \times 200 \mu\text{m}^2$), we have performed other field-cooling experiments on the MgB_2

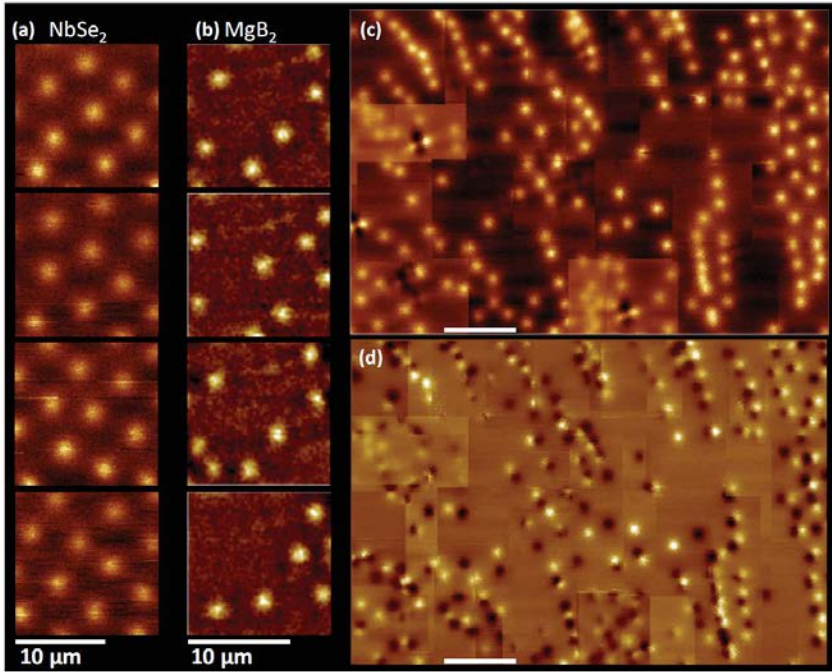


Figure 6.7: Four successive FCs at 0.9 Oe for (a) NbSe_2 and (b) MgB_2 single crystals. Panel (c) shows an FC at 1 Oe for the MgB_2 crystal. Panel (d) shows the difference in vortex position from two consecutive FCs. Images are taken at 4.2 K. The white bar on each picture corresponds to a length of 10 μm . [150]

crystal at 1 Oe, covering nearly the same extended area as in Fig.6.5(b) ($68 \times 45 \mu\text{m}^2$). The results are given in Fig.6.7(c). By comparing the two images, it is found that, even though generally individual vortices do not nucleate at the same position, there is a tendency for stripes and vortex-free regions to maintain their position and orientation. To better show this; in Fig.6.7(d), we present the difference between two consecutive FC's [those shown in Figs.6.5(b) and 6.7(c)]. Where a bright spot is observed, a vortex nucleated during the first FC [Fig.6.5(b)], but not during the second FC [Fig.6.7(c)]. Contrary to that, where a dark spot appears, a vortex nucleated during the second FC in vortex-free position seen at the first FC. It is important to mention that there exists an unavoidable error in our spatial distribution that comes mainly from the composition and alignment of the two images. We estimate this error to be certainly less than 0.5 μm , which in the image equals to approximately 1/3 of the size of a vortex. Therefore, all bright and dark spots in Fig.6.7(d) which

fall below this size can actually represent vortices nucleating at the same spot.

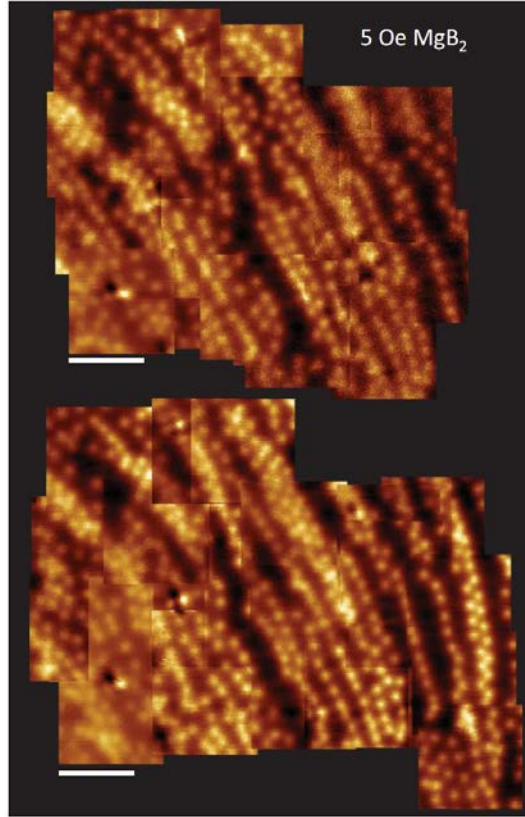


Figure 6.8: (a) Two successive field cools at 5 Oe for the MgB_2 . The images are taken at 4.2 K. The white bar on each picture corresponds to a length of $10 \mu\text{m}$. [150]

In Fig.6.8, we show two successive nucleations at 5 Oe in a partial area of the images shown in Fig.6.7. At 5 Oe, the vortex-free regions have greatly shrunk in size, while vortex clusters have grown and merged with some of the stripes appearing at lower fields. It is relevant to highlight that, at the right part of both images, extended vortex-free regions still coexist with long curved stripes where vortices with sixfold symmetry can be observed. A relevant question is why the stripes align for subsequent field cools in a single preferential direction? It is expected that the presence of any type of bias produced by the boundaries,

a substrate, a small in-plane component of the magnetic field, or an external drive, such as a shear, breaks the symmetry of the stripe ground state and causes the stripes to align in a single direction[170, 172]. Which particular bias mechanism resulting in stabilizing this preferential direction is still a question for further study.

6.6 Vortex pattern stability in MgB_2

Thus far, we have shown that the MgB_2 crystal exhibits a very weak pinning behavior, very much like NbSe_2 , although the vortex patterns are still very different. It is particularly relevant to find out which mechanism defines the preferential orientation of vortex stripes. In the absence of extended vortex pinning centers, this feature can be hardly described by only taking into account a weak diluted pinning landscape. Furthermore, MgB_2 is usually considered as a two-band material having an isotropic s-wave pairing potential with uniaxial symmetry[173], which rules out the possibility that in-plane modulations of the order parameters could cause some preferential vortex stripe orientations. We can also rule out the pinning produced by omnipresent surface defects, such as terraces, since the Bitter decoration experiment[20] already demonstrated that the vortex stripes actually run across terraces without being aligned by them. It is worth mentioning that, using the magneto-optical technique, Soibel et al.[174] observed inhomogeneous flux distributions in $\text{Bi}_2\text{Sr}_2\text{CaCu}_2\text{O}_8$ single crystals grown by the floating-zone method. These unusual flux patterns persisted up to magnetic fields as high as 100 Oe, and they were related to compositional inhomogeneities of the crystal and to structural defects. We can certainly rule out this effect in our MgB_2 single crystals, where the unusual patterns are observed only up to fields as high as 7-10Oe. At such fields, the first neighbor distance d_{vv} for a regular type-II system is of the order of $1.83\text{-}1.54\mu\text{m}$, and when $d_{min} > d_{vv}$, we find the whole surface covered by a vortex lattice in correspondence with the expectations from MD simulations for vortices having a Type-1.5 interaction potential.

In order to investigate whether the orientation of the vortex stripes responds to a particular sample boundary effect, we took SHPM images at the sample's border. Figure6.9(a) shows FC's at +3 Oe taken close to the sample's edge (indicated by a red/dark gray line) at $T/T_c = t = 0.78$. The picture shows a vortex-free region close to the edge of a length ranging between $\sim 10\text{-}20\mu\text{m}$. Similar vortex-free regions close to the edge have been observed in NbSe_2 and were attributed to geometrical barrier effects[175]. Behind the vortex-free region, vortices nucleate and form clusters with a tendency to be aligned parallel to the sample's edge. However, Fig.6.9(b), corresponding to a FC at -3

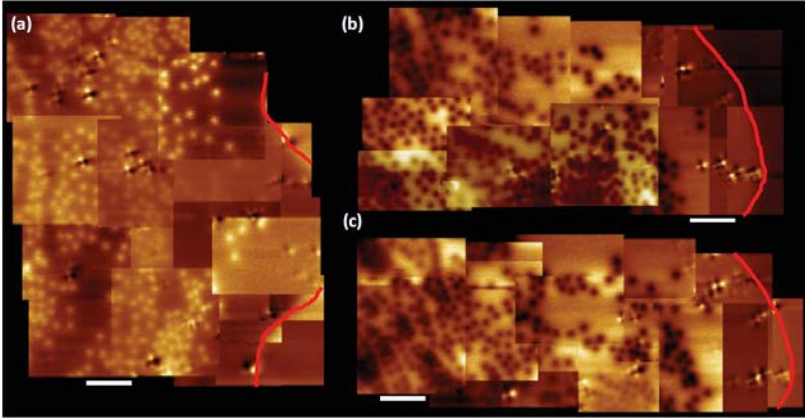


Figure 6.9: (a) Field cooling at +3 Oe for the MgB_2 crystals close to the sample's border (highlighted in red/dark gray). (b) Field cooling at -3 Oe for the MgB_2 crystal, and (c) image of the same region after shaking the vortex lattice at $t = 0.9$ and with $H_{ac} = 10$ Oe, $f = 77.1$ Hz. The images are taken at 30 K. Pictures are at the same scale, the white bar below each picture indicates $10 \mu\text{m}$. [150]

Oe and in a different spot close to the sample's border, shows that the stripes form a certain angle with respect to the sample border. This behavior suggests that there is no straightforward correlation between the border of the sample and the orientation of the observed vortex stripes.

The stability of the vortex stripes in MgB_2 can be investigated by applying an ac shaking. It is well known that, in the presence of a weak disorder (i.e. weakly distorted vortex lattices), vortices can be reordered by a symmetric shaking of the magnetic field [172]. In that sense, one may wonder if a similar disorder-to-order transition can be induced in MgB_2 . Starting from an FC at -3 Oe of the MgB_2 crystal taken at $t = 0.78$ as shown in Fig. 6.9(b), we then shake the lattice at $t \sim 0.9$ by applying an ac magnetic field of 10 Oe oscillating at a frequency of 77.1 Hz. The result (after switching off the ac field and cooling down back to $t = 0.78$) is shown in Fig. 6.9(c). Due to the strong shaking, vortices as far as $95 \mu\text{m}$ away from the edge (left-most vortices) have been displaced from their initial positions, but contrary to what has been observed in low pinning type-II superconductors, no disorder-to-order transition is observed. Moreover, vortex clusters and stripes persist, and they have realigned themselves following a different orientation. Additionally, after the shaking at $t \sim 0.9$ [Fig. 6.9(c)], vortices inside stripes show the tendency to have moved closer together, as revealed by the clear darkening and difficulty to further distinguish individual

vortices at some spots. This reveals that the equilibrium VV- distance, d_{\min} , is lower at $t \sim 0.9$ as compared to the freezing temperature t_q . The variation of d_{\min} with temperature is in agreement with Fig.6.2 showing the dependence of $d_{vv}(t)$ proposed by the theory of 1.5 superconductivity, where $d_{\min} \sim 1.25 \mu\text{m}$ in MgB_2 for the vortex lattice freezing at $t_q = 0.9$. Once more, this clearly demonstrates that pinning cannot account for the observed inhomogeneous vortex patterns, like vortex stripes, chains, and clusters, and more likely they are the result of competing VV- interactions.

6.7 Conclusions

By directly visualizing the vortex patterns via scanning Hall probe microscopy, we have provided convincing direct experimental evidence that the anomalous vortex distributions observed in MgB_2 are not caused by inhomogeneous pinning landscapes, even though pinning or/and surface barriers are playing an important role in trapping the vortices at fields much lower than the lower critical field. These results support the existence of a non-conventional VV- interaction in clean crystals of the two-gap MgB_2 superconductor. One possible explanation for this particular type of interaction reproducing the observed vortex distributions is the type-1.5 superconductivity scenario proposed within the GL-theory in Ref.[20, 21]. The measured intragroup VV-distance corresponds with the predictions made within this model. Future experiments, certainly in the mesoscopic regime, where the behavior of a two-gap superconductor differs significantly from the single-gap case (cf. fractional vortices[146], non-composite vortices[147], etc.), could provide a conclusive evidence of type-1.5 superconductivity.

In addition, we have tracked the evolution of the different patterns as a function of the vortex density (B) and interaction strength (T); as the density increases, the system progresses from a low-density clump phase to an intermediate-density stripe phase and then to a higher-density stripe phase, where vortex voids appear in the system. This extends the observations of the data taken by scanning SQUID[149] to a broader field regime and this further supports the previous data obtained by Bitter decoration[20] in the same field regime. Moreover, the SHPM technique allows, in contrast to Bitter decoration, an observation of the same scan area while continuously varying the controllable thermodynamical variables. For example, we were able to investigate the stability of the stripe patterns having a preferential direction when obtained in a FC process at the border. No direct correlation is found between the preferential direction of the stripe and the sample boundary. By shaking the distribution with an external ac magnetic field, the orientation of the stripes

changes, supporting further that pinning cannot account for the observed inhomogeneous vortex patterns and the existence of a non-conventional VV-interaction is responsible for this behavior. However, the driving mechanism resulting in the preferential nucleation direction of the vortex stripes still remains unsolved.

Conclusions and outlook

Conclusions

In the framework of this thesis the main pursued objective was to explore the superconducting properties at the single fluxon level. As the flux dynamics determines the electromagnetic properties of a superconductor, this study is of fundamental importance. The behavior of fluxons is determined by an interplay between different competing forces: the pinning force, the vortex-vortex interaction and an applied or induced driving force. Whereas, most of the research done up till now, probes the average response of millions of vortices in for example transport measurements or magnetization measurements. The observation of a single vortex allows to check the theoretical models introduced to explain these macroscopic measurements. Moreover, it was hoped to find extraordinary and unexplored behavior at this single vortex scale in similar manner as K. Onnes bumped onto the phenomenon of superconductivity, while checking Drudes theory of resistivity at the lowest temperature possible. These objectives, which are described more in detail in the preface, are pursued by using scanning Hall probe microscopy, a technique which scans a sub-micron sized Hall probe over the sample surface to reveal the flux carried by a single vortex. Further this dissertation strived to contribute to the continuous drive to push further the techniques which allow access to investigate the superconducting properties at the single fluxon scale.

In a first part of this dissertation these objectives are addressed using well defined playgrounds to check the described interplay between the repulsive vortex-vortex interaction in conventional superconductors and the tunable force field created by the pinning potential. These playgrounds are provided by the production of nano-structured superconductors. With the advent of nanolithography it is possible to structure superconductors at the characteristic length scales, ξ and λ and to create well defined pinning centers. The shape and

distribution of these pinning centers has profound consequences for the vortex properties. A particular interesting case is discussed in Chapter 3, where the influence of a quasiperiodic Penrose tiling of pinning centers upon the vortex lattice properties is investigated. The competition between the vortex-vortex interaction favoring triangular order and the extraordinary properties of the quasi-periodic modulated pinning landscape has profound consequences for the resulting vortex distributions and their dynamical properties.

Regular (translational-invariant) periodic lattices of pinning centers are well studied, here so called matching effects are observed as a consequence of commensurability between the vortex lattice and the periodic pinning potential. When the matching conditions between the vortex lattice and the regular pinning potential are fulfilled, sharp local maxima in $j_c(B)$ appear close to T_c . This enhancement is a consequence of the perfect compensation of the vortex-vortex interaction at every matching field, resulting in a more stable vortex configuration. However, the highly symmetric configuration resulting in a local enhancement of j_c at the matching conditions, can promote at the same time channeling or guidance of vortices for particular current directions, resulting in a strong suppression of the critical current for these particular current directions [79, 80].

From technological point of view, quasiperiodic pinning arrays provide several advantages as compared to periodic pinning arrays. In this case, the lack of perfect periodic translational order of the pinning landscape prevents the formation of one-dimensional channels for easy vortex flow. Moreover, whereas in regular pinning arrays the enhancement of $j_c(B)$ occurs only for applied fields close to the matching conditions, the convolution of many build-in periods (self-similarity) present in a quasi crystal favors the proliferation of many matching features or an extremely broad peak in $j_c(B)$. In principle, both properties tend to improve the maximum current attainable without dissipation, i.e. the superconducting critical current. These properties were theoretically predicted (Molecular dynamics) and experimentally measured by indirect transport measurements[69, 70, 71, 72, 73, 74]..

By using SHPM we were able to discern and connect vortex properties measured before as a macroscopic response, involving millions of vortices, with the real microscopic vortex distributions. The experimentally observed vortex distributions are contrasted with the theoretical predicted (Molecular dynamics) and experimentally measured (indirect transport measurements) commensurability effects in quasi-periodically nano-structured superconductors. The obtained flux distributions not only show the theoretically and experimentally anticipated vortex configurations for specific matching fields but unveil new and so far unpredicted vortex distributions. The most fascinating result is the collective and synchronized arrangement of both, pinned and interstitial vortices, forming ring-like structures which stabilize a giant vortex

at the center of this "vortex corral". This study illustrates that the ability of observing single vortices by SHPM is a powerful tool to study vortex physics, to check theoretical theories and to reveal new and unexpected behavior, such as the observation of the symmetry induced vortex corral.

As the SHPM allows to observe only static vortex distributions it is difficult to probe dynamical properties of the vortices. In Chapter 4, SHPM is used to probe the critical entry field above which a type-II superconductor is flooded with vortices. To allow the observation of the first vortex entering the sample a carefully sample design is used, being a thin superconducting film with a periodic array of antidots. The periodic antidots assure that the entered vortex is captured in close neighbourhood of the sample border, as in absence of pinning, the entered vortex is driven to the center of the sample by the screening currents at the edge. As such the combination of the single vortex resolution of SHPM and the careful sample design allow to observe the entry of vortices by SHPM, a dynamic property. As the magnetic response of a type-II superconductor is radically different depending on whether the superconductor is in the Meissner state, characterized by a reversible magnetic response, or in the mixed state, where vortices appear, the determination of this field is of fundamental importance. Moreover, the superconducting thin film geometry used here has a remarkable importance as it is used in the vast majority of applications for superconductivity. Despite it's importance it is never investigated at the single vortex level. Through history several contributions are proposed which determine this entry field. These contributions include surface effects, the nucleation process of vortices at the edge, demagnetizing effects, etc. Our results confirm that the mechanism for the first vortex penetration arises as a consequence of the screening Meissner currents reaching values of the depairing current at the edge. The depairing current is the maximum current that can run before superconductivity is locally destroyed and which thus leads to to vortex nucleation. On top of that, we also investigated the vortex entry process for different antidot shapes and distributions. In all cases, the criterium for vortex entry is found to be the same. As in Chapter 3, also here SHPM allows to reveal extraordinary local vortex behavior, unable to be probed by macroscopic measurements. It is shown in Ref.[117] for an identical sample having a triangular array of boomerang shaped antidots and also observed here for a sample with a square array of square antidots, that upon vortex entry, a stepwise flux gradient develops as a consequence of the periodic pinning landscape. This so called 'terraced critical state' was proposed by Cooley and Grishin[116], but up till now it is never directly visualized with single vortex resolution.

While in the two preceding cases the visualisation of a static vortex distribution

by SHPM is used to infer information about the vortex properties, no observations are made during the motion itself. In Chapter 5, we present a novel local imaging technique with unprecedented resolution, termed scanning ac-susceptibility microscopy (SSM), which allows us, for the first time, to directly visualize the microscopic dynamics of an individual flux quantum. The technique combines the ability of scanning Hall probe microscopy to observe a single fluxon and the phase sensitivity of the standard ac-susceptibility technique. The ac-susceptibility technique is a powerful experimental method to gain information about the dynamical properties of these fluxons by detecting their reaction upon shaking them back and forth with a small external ac magnetic field. Whereas in the global ac-susceptibility technique, the recorded signal represents an average over millions of fluxons, each in a different pinning potential and subjected to a different environment, in SSM the ac-response can be probed of a single fluxon. In similar fashion as in a driven damped pendulum, the displacement of the flux quanta will provide us with information about the potential well where the fluxon is trapped into. Whereas the measured phase lag between the oscillatory motion and the driving force reveals the drag a single moving fluxon experiences. In this chapter, the SSM technique will be used to investigate the response of a superconducting Pb ribbon and a nano-structured Pb film to a perpendicular applied ac magnetic field. The results obtained in these two case-studies render new insights on the basic mechanisms of vortex dissipation with unmatched single vortex resolution and provide an essential tool to measure a detailed cartography of the intensity of the pinning landscape. For example, a clear dichotomy between the ac-response of the vortices and the screening currents was observed using the phase sensitive character of the SSM technique. The observed out-of-phase response of the vortices, which was absent for the reversible screening currents, directly shows the local dissipation of the vortex motion. As viscous losses can only account for a small fraction of the measured large phase-lag at the used experimental excitation frequency, the observed large phase-lag, $\Theta = -0.5\text{rad}$, is explained by thermally activated vortex hopping over pinning centers. On top of that, in the second case-study, a clear difference in mobility is observed between pinned and interstitial vortices. This difference arises due to the different pinning potential each vortex species experiences. Whereas, vortices pinned by an antidot are strongly anchored, the interstitial vortices are very mobile as they are weakly caged due to surrounding pinned vortices[46]. Moreover, we made a direct observation of the correlation between the ac-penetration depth and the vortex dynamics used in theoretical models[44, 45, 43] to explain macroscopic ac-susceptibility measurements.

In a last part, the SHPM technique is used to reveal the extraordinary behavior of fluxons in two-gap superconductors. As compared to the conventional

single-gap nano-structured superconductors, where the competition between the repulsive vortex-vortex interactions and the pinning force determines the vortex properties. In two-gap superconductors, the new degrees of freedom, give rise to many more remarkable new possibilities interesting for both fundamental research and applications. An interesting new feature is discussed in Ref.[145, 153, 158] for two uncoupled components having $\xi_2 < \sqrt{2}\lambda < \xi_1$. In this case, where one component is of type-I, while the other is of type-II, it is found within the GL-theory that the vortex-vortex interaction varies non-monotonic. This particular type of interaction results at low fields in a vortex distribution having vortex clusters wherein vortices sit a preferential distance, d_0 , from each other, immersed in domains of Meissner state[145]. Since this peculiar vortex clustering shared reminiscence with both Type-I (Meissner-state) and Type-II superconductors (Vortex-state), it was coined as the ‘semi-Meissner state’[145] or ‘type-1.5 superconductivity’[20]. In Chapter 6, we use SHPM to directly visualize the vortex patterns in clean crystals of the two-gap MgB_2 superconductor, a prototypical two-gap superconductor and a perfect candidate to observe type-1.5 superconductivity. As compared to previous investigations on similar single crystals, SHPM has single-vortex resolution in a broader field range than the measurements described in Ref.[149]. On top of that, SHPM offers in contrast to the Bitter decoration technique the possibility to change the thermodynamic variables, magnetic field and temperature, while simultaneously visualizing the vortex patterns in the same scanarea. We have been able to observe the progressive formation of stripes, in agreement with previous studies. This provides convincing direct experimental evidence that the anomalous vortex distributions observed in MgB_2 result from a non-monotonic VV-interaction and are not caused by inhomogeneous pinning landscapes. One possible explanation for this particular type of interaction reproducing the observed vortex distributions is the type-1.5 superconductivity scenario proposed within the GL-theory. The measured intragroup VV-distance corresponds with the predictions made within this model. The stability of the stripe patterns having a preferential direction when obtained in a FC process at the border is also investigated. No direct correlation is found between the preferential direction of the stripe and the sample boundary. By shaking the distribution with an external ac magnetic field, the orientation of the stripes changes, supporting further that pinning cannot account for the observed inhomogeneous vortex patterns and the existence of a non-conventional VV-interaction is responsible for this behavior. However, the driving mechanism resulting in the preferential nucleation direction of the vortex stripes still remains unsolved.

Outlook

The scanning Hall probe technique and the scanning ac-susceptibility technique have clearly proven their power to investigate the single fluxon world, inaccessible by macroscopic measurements. As the investigation of vortex dynamics is of fundamental importance, SSM is an important new tool. The general principle of operation, namely phase-sensitive detection, can be used in other scanning techniques and extended beyond the superconductivity community. For example, applying the same principle in a scanning tunneling microscopy setup, would allow to check the ac-response at higher magnetic fields, inaccessible by SHPM. Not only within the superconductivity community, the SSM technique could be used, also in magnetic systems it can be a new tool to investigate for example the dynamics of magnetic domain walls. As in this work only the linear low frequency response is considered, this technique is just a first step as a tool to investigate vortex dynamics and will hopefully be extended further or triggers new techniques, to capture locally the vortex motion at higher frequencies and in the non-linear regime.

List of symbols

Constants

Symbol	Name	Value	Unit
e	Electron charge	1.602×10^{-19}	C
h	Planck constant	6.626×10^{-34}	J·s
$\hbar = h/2\pi$	Reduced Planck constant	1.054×10^{-34}	J·s
k_B	Boltzmann constant	1.381×10^{-23}	J/K
Φ_0	Magnetic flux quantum	2.067×10^{-15}	T·m ²

Symbols

Symbol	Object	Unit
T_c	Critical Temperature	K
v_F	Fermi velocity	m/s
k_F	Fermi wavevector	m/s
k_F	Fermi wavevector	m ⁻¹
m^*	effective electron bandmass	kg
ε_k	single particle energy	J
E	Overall energy	J
σ	Spin	\uparrow, \downarrow
Φ	Wavefunction	?
ϑ	Phase of the wavefunction	?
ω_D	Debye angular frequency	rad/s
Δ	Superconducting gap	eV
$N(\varepsilon)$	Density of states at ε	?

Bibliography

- [1] M. Tinkham, *Introduction to superconductivity*. International series in pure and applied physics, McGraw Hill, 1996.
- [2] P. De Gennes, *Superconductivity Of Metals And Alloys*. Westview Press, 1999.
- [3] J. Annett, *Superconductivity, superfluids and condensates*. Oxford Master Series in Condensed Matter Physics Series, OUP Oxford, 2004.
- [4] H. K. Onnes *Leiden Comm.*, vol. 120b,122b,124c, 1911.
- [5] D. van Delft and P. Kes, *100 Years of Superconductivity*. Museum Boerhaave, 2011.
- [6] W. Meissner and R. Ochsenfeld *Naturwissenschaften*, vol. 21, p. 787, 1933.
- [7] J. Bardeen, L. N. Cooper, and J. R. Schrieffer, “Theory of superconductivity,” *Phys. Rev.*, vol. 108, pp. 1175–1204, Dec 1957.
- [8] R. E. Glover and M. Tinkham, “Transmission of superconducting films at millimeter-microwave and far infrared frequencies,” *Phys. Rev.*, vol. 104, pp. 844–845, Nov 1956.
- [9] W. S. Corak, B. B. Goodman, C. B. Satterthwaite, and A. Wexler, “Exponential temperature dependence of the electronic specific heat of superconducting Vanadium,” *Phys. Rev.*, vol. 96, pp. 1442–1444, Dec 1954.
- [10] E. Maxwell, “Isotope effect in the superconductivity of Mercury,” *Phys. Rev.*, vol. 78, pp. 477–477, May 1950.
- [11] C. A. Reynolds, B. Serin, W. H. Wright, and L. B. Nesbitt, “Superconductivity of isotopes of Mercury,” *Phys. Rev.*, vol. 78, pp. 487–487, May 1950.

- [12] B. S. Deaver and W. M. Fairbank, "Experimental evidence for quantized flux in superconducting cylinders," *Phys. Rev. Lett.*, vol. 7, pp. 43–46, Jul 1961.
- [13] H. Fröhlich, "Theory of the superconducting state. I. the ground state at the absolute zero of temperature," *Phys. Rev.*, vol. 79, pp. 845–856, Sep 1950.
- [14] N. Ashcroft and N. Mermin, *Solid state physics*. Saunders College, 1976.
- [15] L. N. Cooper, "Bound electron pairs in a degenerate Fermi gas," *Phys. Rev.*, vol. 104, pp. 1189–1190, Nov 1956.
- [16] L. Landau, "The theory of superfluidity of helium II," *Zh. Eksp. Teor. Fiz.*, vol. 11, p. 592, 1941.
- [17] J. Bednorz and K. Müller, "Possible high T_c superconductivity in the Ba-La-Cu-O system," *Zeitschrift für Physik B Condensed Matter*, vol. 64, pp. 189–193, 1986.
- [18] M. K. Wu, J. R. Ashburn, C. J. Torng, P. H. Hor, R. L. Meng, L. Gao, Z. J. Huang, Y. Q. Wang, and C. W. Chu, "Superconductivity at 93 K in a new mixed-phase Y-Ba-Cu-O compound system at ambient pressure," *Phys. Rev. Lett.*, vol. 58, pp. 908–910, Mar 1987.
- [19] J. Nagamatsu, N. Nakagawa, T. Muranaka, Y. Zenitani, and J. Akimitsu, "Superconductivity at 39 K in magnesium diboride.," *Nature*, vol. 410, no. 6824, p. 63, 2001.
- [20] V. Moshchalkov, M. Menghini, T. Nishio, Q. H. Chen, A. V. Silhanek, V. H. Dao, L. F. Chibotaru, N. D. Zhigadlo, and J. Karpinski, "Type-1.5 superconductivity," *Phys. Rev. Lett.*, vol. 102, p. 117001, Mar 2009.
- [21] E. Babaev, J. Jäykkä, and M. Speight, "Magnetic field delocalization and flux inversion in fractional vortices in two-component superconductors," *Phys. Rev. Lett.*, vol. 103, p. 237002, Dec 2009.
- [22] G. Wu, Y. L. Xie, H. Chen, M. Zhong, R. H. Liu, B. C. Shi, Q. J. Li, X. F. Wang, T. Wu, Y. J. Yan, J. J. Ying, and X. H. Chen, "Superconductivity at 56 K in samarium-doped SrFeAsF," *Journal of Physics: Condensed Matter*, vol. 21, no. 14, p. 142203, 2009.
- [23] V. Ginzburg and L. Landau *Zh. Eksperim. i Teor. Fiz.*, vol. 20, p. 1064, 1950.
- [24] F. London and H. London *Proc. Roy. Soc (London)*, vol. A149, p. 71, 1935.

- [25] L. Gor'kov *Zh. Eksperim. i Theor. Fiz.*, vol. 36, p. 1918, 1959.
- [26] L. Landau, "Second-order phase transitions," *Zh. Eksperim. i Theor. Fiz.*, vol. 7, p. 371, 1937.
- [27] V. Moshchalkov and J. Fritzsche, *Nanostructured superconductors*. World Scientific Publishing Company, Incorporated, 2011.
- [28] J. Pearl, "Current distribution in superconducting films carrying quantized fluxoids," *J. Appl. Phys.*, vol. 37, p. 4139, 1966.
- [29] A. L. Fetter and P. C. Hohenberg, "The mixed state of thin superconducting films in perpendicular fields," *Phys. Rev.*, vol. 159, pp. 330–343, Jul 1967.
- [30] D. Griffiths, *Introduction to electrodynamics*. Prentice Hall, 1999.
- [31] I. Giaever, "Magnetic coupling between two adjacent type-II superconductors," *Phys. Rev. Lett.*, vol. 15, pp. 825–827, Nov 1965.
- [32] G. Blatter, M. V. Feigel'man, V. B. Geshkenbein, A. I. Larkin, and V. M. Vinokur, "Vortices in high-temperature superconductors," *Rev. Mod. Phys.*, vol. 66, pp. 1125–1388, Oct 1994.
- [33] H. Suhl, "Inertial mass of a moving fluxoid," *Phys. Rev. Lett.*, vol. 14, pp. 226–229, Feb 1965.
- [34] N. B. Kopnin and V. M. Vinokur, "Dynamic vortex mass in clean Fermi superfluids and superconductors," *Phys. Rev. Lett.*, vol. 81, pp. 3952–3955, Nov 1998.
- [35] D.-X. Chen, J. J. Moreno, A. Hernando, A. Sanchez, and B.-Z. Li, "Nature of the driving force on an Abrikosov vortex," *Phys. Rev. B*, vol. 57, pp. 5059–5062, Mar 1998.
- [36] M. J. Stephen and J. Bardeen, "Viscosity of type-II superconductors," *Phys. Rev. Lett.*, vol. 14, pp. 112–113, Jan 1965.
- [37] M. Tinkham, "Viscous flow of flux in type-II superconductors," *Phys. Rev. Lett.*, vol. 13, pp. 804–807, Dec 1964.
- [38] J. R. Clem, "Local temperature-gradient contribution to flux-flow viscosity in superconductors," *Phys. Rev. Lett.*, vol. 20, pp. 735–738, Apr 1968.
- [39] G. Mkrtchyan and V. Schmidt, "Interaction between a vortex and a columnar defect in the London approximation," *Sov.Phys.-JETP*, vol. 37, p. 195, 1972.

- [40] V. V. Moshchalkov, M. Baert, V. V. Metlushko, E. Rosseel, M. J. Van Bael, K. Temst, R. Jonckheere, and Y. Bruynseraede, "Magnetization of multiple-quanta vortex lattices," *Phys. Rev. B*, vol. 54, pp. 7385–7393, Sep 1996.
- [41] V. V. Moshchalkov, M. Baert, V. V. Metlushko, E. Rosseel, M. J. Van Bael, K. Temst, Y. Bruynseraede, and R. Jonckheere, "Pinning by an antidot lattice: The problem of the optimum antidot size," *Phys. Rev. B*, vol. 57, pp. 3615–3622, Feb 1998.
- [42] P. Fulde, L. Pietronero, W. R. Schneider, and S. Strässler, "Problem of brownian motion in a periodic potential," *Phys. Rev. Lett.*, vol. 35, pp. 1776–1779, Dec 1975.
- [43] M. W. Coffey and J. R. Clem, "Unified theory of effects of vortex pinning and flux creep upon the rf surface impedance of type-II superconductors," *Phys. Rev. Lett.*, vol. 67, pp. 386–389, Jul 1991.
- [44] C. J. van der Beek, V. B. Geshkenbein, and V. M. Vinokur, "Linear and nonlinear ac response in the superconducting mixed state," *Phys. Rev. B*, vol. 48, pp. 3393–3403, Aug 1993.
- [45] E. H. Brandt, "Penetration of magnetic ac fields into type-II superconductors," *Phys. Rev. Lett.*, vol. 67, pp. 2219–2222, Oct 1991.
- [46] C. C. de Souza Silva, J. A. Aguiar, and V. V. Moshchalkov, "Linear ac dynamics of vortices in a periodic pinning array," *Phys. Rev. B*, vol. 68, p. 134512, Oct 2003.
- [47] J. I. Gittleman and B. Rosenblum, "Radio-frequency resistance in the mixed state for subcritical currents," *Phys. Rev. Lett.*, vol. 16, pp. 734–736, Apr 1966.
- [48] A. M. Campbell, "The response of pinned flux vortices to low-frequency fields," *Journal of Physics C: Solid State Physics*, vol. 2, no. 8, p. 1492, 1969.
- [49] C. P. Bean, "Magnetization of hard superconductors," *Phys. Rev. Lett.*, vol. 8, pp. 250–253, Mar 1962.
- [50] R. N. Goren and J. M. Tinkham, "Patterns of magnetic flux penetration in superconducting films," *Low Temp. Phys.*, vol. 5, p. 465, 1971.
- [51] J. Fritzsche, *Superconductivity controlled by inhomogeneous fields generated by magnetic domains*. PhD Thesis, KU Leuven, 2008.

- [52] E. Hall, "On a new action of the magnet on electric currents," *Am. J. Math.*, vol. 2, p. 287, 1879.
- [53] S. J. Bending, "Local magnetic probes of superconductors," *Advances in Physics*, vol. 48, no. 4, pp. 449–535, 1999.
- [54] K. Vervaeke, *Microscopic Hall sensors for magnetometry and local magnetic imaging*. PhD Thesis, Ku Leuven, Imec, 2007.
- [55] S. Bending and A. Oral, "Hall effect in a highly inhomogeneous magnetic field distribution," *J. Appl. Phys.*, vol. 81, p. 3721, 1987.
- [56] Y. G. Cornelissens and F. M. Peeters, "Response function of a Hall magnetosensor in the diffusive regime," *J. Appl. Phys.*, vol. 92, p. 2006, 2002.
- [57] F. M. Peeters and X. Q. Li, "Hall magnetometer in the ballistic regime," *Appl. Phys. Lett.*, vol. 72, p. 572, 1998.
- [58] A. K. Geim, S. J. Bending, I. V. Grigorieva, and M. G. Blamire, "Ballistic two-dimensional electrons in a random magnetic field," *Phys. Rev. B*, vol. 49, pp. 5749–5752, Feb 1994.
- [59] J. R. Kirtley, "Fundamental studies of superconductors using scanning magnetic imaging," *Reports on Progress in Physics*, vol. 73, no. 12, p. 126501, 2010.
- [60] A. Finkler, Y. Segev, Y. Myasoedov, M. L. Rappaport, L. Neéman, D. Vasyukov, E. Zeldov, M. E. Huber, J. Martin, and A. Yacoby, "Self-aligned nanoscale SQUID on a tip," *Nano Letters*, vol. 10, no. 3, pp. 1046–1049, 2010.
- [61] A. Weldeslassie, *Nucleation of superconductivity and vortex matter in hybrid nanostructures*. PhD Thesis, Ku Leuven, 2011.
- [62] D. Shechtman, I. Blech, D. Gratias, and J. Cahn, "Metallic phase with long-range orientational order and no translational symmetry," *Phys. Rev. Lett.*, vol. 53, p. 1951, 1984.
- [63] R. Penrose, "The role of aesthetics in pure and applied mathematical research," *Bull. Inst. Math. Appl.*, vol. 10, p. 266, 1974.
- [64] F. Nori and J. Rodriguez, "Acoustic and electronic properties of one-dimensional quasicrystals," *Phys. Rev. B*, vol. 34, p. 2207, 1986.
- [65] M. Kohmoto, B. Sutherland, and C. Tang, "Critical wave functions and a cantor-set spectrum of a one-dimensional quasicrystal model," *Phys. Rev. B*, vol. 35, p. 1020, 1987.

- [66] K. Springer and D. Van Harlingen, "Resistive transition and magnetic field response of a Penrose-tile array of weakly coupled superconductor islands," *Phys. Rev. B*, vol. 36, p. 7273, 1987.
- [67] D. Nelson and B. Halperin, "Dislocation-mediated melting in two dimensions," *Phys. Rev. B*, vol. 19, p. 2457, 1979.
- [68] E. Abe, Y. Yan, and S. Pennycook, "Quasicrystals as cluster aggregates," *Nature Mater.*, vol. 3, p. 759, 2004.
- [69] V. Misko, S. Savel'ev, and F. Nori, "Critical currents in quasiperiodic pinning arrays: Chains and penrose lattices," *Phys. Rev. Lett.*, vol. 95, p. 177007, 2005.
- [70] V. Misko, S. Savel'ev, and F. Nori, "Critical currents in superconductors with quasiperiodic pinning arrays: One-dimensional chains and two-dimensional penrose lattices," *Phys. Rev. B*, vol. 74, p. 024522, 2006.
- [71] J. Villegas, M. Montero, C.-P. Li, and I. Schuller, "Correlation length of quasiperiodic vortex lattice," *Phys. Rev. Lett.*, vol. 97, p. 027002, 2006.
- [72] M. Kemmler, C. Grlich, A. Sterck, H. Phler, M. Neuhaus, M. and Siegel, R. Kleiner, and D. Koelle, "Commensurability effects in superconducting Nb films with quasiperiodic pinning arrays," *Phys. Rev. Lett.*, vol. 97, p. 147003, 2006.
- [73] A. Silhanek, W. Gillijns, V. Moshchalkov, B. Zhu, J. Moonens, and L. Leunissen, "Tunable pinning in superconducting films with magnetic microloops," *Appl. Phys. Lett.*, vol. 89, p. 152507, 2006.
- [74] C. Reichhardt and C. O. Reichhardt, "Commensurability effects at nonmatching fields for vortices in diluted periodic pinning arrays," *Phys. Rev. B*, vol. 76, p. 094512, 2007.
- [75] D. Levine and P. J. Steinhardt, "Quasicrystals. I. definition and structure," *Phys. Rev. B*, vol. 34, pp. 596–616, Jul 1986.
- [76] A. Glassner, "Andrew glassner's notebook," *Computer Graphics and Applications, IEEE*, vol. 24, no. 1, pp. 86–91, 2004.
- [77] M. Baert, V. V. Metlushko, R. Jonckheere, V. V. Moshchalkov, and Y. Bruynseraede, "Composite flux-line lattices stabilized in superconducting films by a regular array of artificial defects," *Phys. Rev. Lett.*, vol. 74, pp. 3269–3272, Apr 1995.
- [78] L. F. Chibotaru, A. Ceulemans, V. Bruyndoncx, and V. V. Moshchalkov, "Symmetry-induced antivortices in mesoscopic superconductors," *Nature*, vol. 408, p. 833, 2000.

- [79] A. Silhanek, L. Van Look, S. Raedts, R. Jonckheere, and V. Moshchalkov, "Guided vortex motion in superconductors with a square antidot array," *Phys. Rev. B*, vol. 68, p. 214504, 2003.
- [80] N. Verellen, A. V. Silhanek, W. Gillijns, V. V. Moshchalkov, V. Metlushko, F. Gozzini, and B. Ilic, "Switchable magnetic dipole induced guided vortex motion," *Appl. Phys. Lett.*, vol. 93, p. 022507, 2008.
- [81] D. Niebieskikwiat, A. V. Silhanek, L. Civale, and G. Nieva, "Suppression of matching field effects by splay and pinning energy dispersion in $\text{YBa}_2\text{Cu}_3\text{O}_7$ with columnar defects," *Phys. Rev. B*, vol. 63, p. 144504, 2002.
- [82] R. B. G. Kramer, A. V. Silhanek, J. Van de Vondel, B. Raes, and V. V. Moshchalkov, "Symmetry-induced giant vortex state in a superconducting Pb film with a fivefold penrose array of magnetic pinning centers," *Phys. Rev. Lett.*, vol. 103, p. 067007, Aug 2009.
- [83] E. H. Brandt, "Vortex-vortex interaction in thin superconducting films," *Phys. Rev. B*, vol. 79, p. 134526, Apr 2009.
- [84] V. Moshchalkov, X. Qiu, and V. Bruyndoncx, "Paramagnetic Meissner effect from the self-consistent solution of the Ginzburg-Landau equations," *Phys. Rev. B*, vol. 55, p. 11793, 1997.
- [85] V. Bruyndoncx, J. Rodrigo, T. Puig, L. Van Look, V. Moshchalkov, and R. Jonckheere, "Giant vortex state in perforated Aluminum microsquares," *Phys. Rev. B*, vol. 60, p. 4285, 1999.
- [86] A. Kanda, B. Baelus, F. Peeters, K. Kadowaki, and Y. Ootuka, "Experimental evidence for giant vortex states in a mesoscopic superconducting disk," *Phys. Rev. Lett.*, vol. 93, p. 257002, 2004.
- [87] B. Baelus, L. Cabral, and F. Peeters, "Vortex shells in mesoscopic superconducting disks," *Phys. Rev. B*, vol. 69, p. 064506, 2004.
- [88] G. Berdiyrov, M. Milosevicand, and F. Peeters, "Novel commensurability effects in superconducting films with antidot arrays," *Phys. Rev. Lett.*, vol. 96, p. 207001, 2006.
- [89] A. Bezryadin, Y. Ovchinnikov, and B. Pannetier, "Nucleation of vortices inside open and blind microholes," *Phys. Rev. B*, vol. 53, p. 8553, 1996.
- [90] M. Doria and G. Zebende, "Multiple trapping of vortex lines by a regular array of pinning centers," *Phys. Rev. B*, vol. 66, p. 064519, 2002.

- [91] C. P. Bean and J. D. Livingston, "Surface barrier in type-II superconductors," *Phys. Rev. Lett.*, vol. 12, pp. 14–16, Jan 1964.
- [92] H. J. Fink and A. G. Presson, "Stability limit of the superheated Meissner state due to three-dimensional fluctuations of the order parameter and vector potential," *Phys. Rev.*, vol. 182, pp. 498–503, Jun 1969.
- [93] F. P.-J. Lin and A. Gurevich, "Effect of impurities on the superheating field of type-II superconductors," *Phys. Rev. B*, vol. 85, p. 054513, Feb 2012.
- [94] L. Kramer, "Stability limits of the Meissner state and the mechanism of spontaneous vortex nucleation in superconductors," *Phys. Rev.*, vol. 170, pp. 475–480, Jun 1968.
- [95] R. G. Mints and I. B. Snapiro, "Magnetization relaxation in layered superconductors," *EPL (Europhysics Letters)*, vol. 21, no. 5, p. 611, 1993.
- [96] L. Burlachkov, V. B. Geshkenbein, A. E. Koshelev, A. I. Larkin, and V. M. Vinokur, "Giant flux creep through surface barriers and the irreversibility line in high-temperature superconductors," *Phys. Rev. B*, vol. 50, pp. 16770–16773, Dec 1994.
- [97] P. de Gennes, "Vortex nucleation in type-II superconductors," *Solid State Communications*, vol. 3, no. 6, pp. 127 – 130, 1965.
- [98] L. Aslamazov and S. Lemnitskii, "Resistive state in broad superconducting films," *Zh. Eksp. Teor. Fiz.*, vol. 84, no. 2216, 1983.
- [99] D. Y. Vodolazov, I. L. Maksimov, and E. H. Brandt, "Modulation instability of the order parameter in thin-film superconductors with edge barrier," *EPL (Europhysics Letters)*, vol. 48, no. 3, p. 313, 1999.
- [100] M. Benkraouda and J. R. Clem, "Magnetic hysteresis from the geometrical barrier in type-II superconducting strips," *Phys. Rev. B*, vol. 53, pp. 5716–5726, Mar 1996.
- [101] E. Zeldov, A. I. Larkin, V. B. Geshkenbein, M. Konczykowski, D. Majer, B. Khaykovich, V. M. Vinokur, and H. Shtrikman, "Geometrical barriers in high-temperature superconductors," *Phys. Rev. Lett.*, vol. 73, pp. 1428–1431, Sep 1994.
- [102] B. L. T. Plourde, D. J. Van Harlingen, D. Y. Vodolazov, R. Besseling, M. B. S. Hesselberth, and P. H. Kes, "Influence of edge barriers on vortex dynamics in thin weak-pinning superconducting strips," *Phys. Rev. B*, vol. 64, p. 014503, Jun 2001.

- [103] A. S. Joseph and W. J. Tomasch, "Experimental evidence for delayed entry of flux into a type-II superconductor," *Phys. Rev. Lett.*, vol. 12, pp. 219–222, Mar 1964.
- [104] R. W. De Blois and W. De Sorbo, "Surface barrier in type-II superconductors," *Phys. Rev. Lett.*, vol. 12, pp. 499–501, May 1964.
- [105] A. S. Joseph, W. J. Tomasch, and H. J. Fink, "Intrinsic size effects in type-II superconducting films," *Phys. Rev.*, vol. 157, pp. 315–317, May 1967.
- [106] D. Vodolazov, I. Maksimov, and E. Brandt, "Vortex entry conditions in type-II superconductors.: Effect of surface defects," *Physica C: Superconductivity*, vol. 384, no. 1-2, pp. 211 – 226, 2003.
- [107] D. Cerbu, V. N. Gladilin, J. Cuppens, J. Fritzsche, J. Tempere, J. T. Devreese, V. V. Moshchalkov, A. V. Silhanek, and J. V. de Vondel, "Vortex ratchet induced by controlled edge roughness," *New Journal of Physics*, vol. 15, no. 6, p. 063022, 2013.
- [108] M. Benkraouda and J. R. Clem, "Critical current from surface barriers in type-II superconducting strips," *Phys. Rev. B*, vol. 58, pp. 15103–15107, Dec 1998.
- [109] J. I. Vestgård, D. V. Shantsev, Y. M. Galperin, and T. H. Johansen, "Flux distribution in superconducting films with holes," *Phys. Rev. B*, vol. 77, p. 014521, Jan 2008.
- [110] C. Reichhardt and N. Grønbech-Jensen, "Critical currents and vortex states at fractional matching fields in superconductors with periodic pinning," *Phys. Rev. B*, vol. 63, p. 054510, Jan 2001.
- [111] C. Reichhardt, C. J. Olson, and F. Nori, "Commensurate and incommensurate vortex states in superconductors with periodic pinning arrays," *Phys. Rev. B*, vol. 57, pp. 7937–7943, Apr 1998.
- [112] K. Harada, O. Kamimura, H. Kasai, T. Matsuda, A. Tonomura, and V. V. Moshchalkov, "Direct observation of vortex dynamics in superconducting films with regular arrays of defects," *Science*, vol. 274, no. 5290, pp. 1167–1170, 1996.
- [113] A. N. Grigorenko, G. D. Howells, S. J. Bending, J. Bekaert, M. J. Van Bael, L. Van Look, V. V. Moshchalkov, Y. Bruynseraede, G. Borghs, I. I. Kaya, and R. A. Stradling, "Direct imaging of commensurate vortex structures in ordered antidot arrays," *Phys. Rev. B*, vol. 63, p. 052504, Jan 2001.

- [114] S. B. Field, S. S. James, J. Barentine, V. Metlushko, G. Crabtree, H. Shtrikman, B. Ilic, and S. R. J. Brueck, "Vortex configurations, matching, and domain structure in large arrays of artificial pinning centers," *Phys. Rev. Lett.*, vol. 88, p. 067003, Jan 2002.
- [115] A. N. Grigorenko, S. J. Bending, M. J. Van Bael, M. Lange, V. V. Moshchalkov, H. Fangohr, and P. A. J. de Groot, "Symmetry locking and commensurate vortex domain formation in periodic pinning arrays," *Phys. Rev. Lett.*, vol. 90, p. 237001, Jun 2003.
- [116] L. D. Cooley and A. M. Grishin, "Pinch effect in commensurate vortex-pin lattices," *Phys. Rev. Lett.*, vol. 74, pp. 2788–2791, Apr 1995.
- [117] A. V. Silhanek, J. Gutierrez, R. B. G. Kramer, G. W. Ataklti, J. Van de Vondel, V. V. Moshchalkov, and A. Sanchez, "Microscopic picture of the critical state in a superconductor with a periodic array of antidots," *Phys. Rev. B*, vol. 83, p. 024509, Jan 2011.
- [118] D. Vodolazov and I. Maksimov, "Distribution of the magnetic field and current density in superconducting films of finite thickness," *Physica C: Superconductivity*, vol. 349, no. 1-2, pp. 125 – 138, 2001.
- [119] D. Vodolazov, "Distribution of screening currents in thin superconducting films," *Technical Physics Letters*, vol. 25, no. 10, pp. 838–840, 1999.
- [120] D. L. Decker, D. E. Mapother, and R. W. Shaw, "Critical field measurements on superconducting lead isotopes," *Phys. Rev.*, vol. 112, pp. 1888–1898, Dec 1958.
- [121] M. Tinkham, "Effect of fluxoid quantization on transitions of superconducting films," *Phys. Rev.*, vol. 129, pp. 2413–2422, Mar 1963.
- [122] A. I. Buzdin, "Multiple-quanta vortices at columnar defects," *Phys. Rev. B*, vol. 47, pp. 11416–11419, May 1993.
- [123] A. Wahl, V. Hardy, J. Provost, C. Simon, and A. Buzdin, "Unusual field dependence of the reversible magnetization in heavy ions irradiated thallium-based single crystals," *Physica C: Superconductivity*, vol. 250, no. 1-2, pp. 163 – 169, 1995.
- [124] E. Rosseel, *Critical parameters of superconductors with an antidot lattice*. PhD Thesis. Ku Leuven, 1998.
- [125] A. Fox, *Optical Properties of Solids*. Oxford Master Series in Physics: Condensed Matter Physics, Oxford University Press, 2001.

- [126] R. Feynman, R. Leighton, M. Sands, and M. Gottlieb, *The Feynman lectures on physics*. The Feynman Lectures on Physics, Pearson/Addison-Wesley, 1963.
- [127] F. Gömöry, “Characterization of high-temperature superconductors by ac susceptibility measurements,” *Superconductor Science and Technology*, vol. 10, no. 8, p. 523, 1997.
- [128] F. Gömöry, “Low frequency magnetic measurements on high-Tc superconducting materials,” *Thermochimica Acta*, vol. 174, pp. 299 – 320, 1991.
- [129] S. M. Marchevsky, M.J. Higgins, “Two coexisting vortex phases in the peak effect regime in a superconductor,” *Nature Physics*, vol. 409, pp. 591–594, Feb 2001.
- [130] A. E. Koshelev and V. M. Vinokur, “Dynamic melting of the vortex lattice,” *Phys. Rev. Lett.*, vol. 73, pp. 3580–3583, Dec 1994.
- [131] G. Pasquini, L. Civale, H. Lanza, and G. Nieva, “Dynamic regimes in the ac response of $\text{YBa}_2\text{Cu}_3\text{O}_7$ with columnar defects: Intra- and inter-valley vortex motion,” *Phys. Rev. B*, vol. 59, pp. 9627–9636, Apr 1999.
- [132] N. Morozov, E. Zeldov, D. Majer, and B. Khaykovich, “Negative local permeability in $\text{Bi}_2\text{Sr}_2\text{CaCu}_2\text{O}_8$ crystals,” *Phys. Rev. Lett.*, vol. 76, pp. 138–141, Jan 1996.
- [133] M. Marchevsky, P. Kes, and J. Aarts, “Determination of the quenching temperature for the vortex lattice in field-cooling decoration experiments,” *Physica C: Superconductivity*, vol. 282-287, Part 4, no. 0, pp. 2083 – 2084, 1997.
- [134] E. H. Brandt and M. Indenbom, “Type-II superconductor strip with current in a perpendicular magnetic field,” *Phys. Rev. B*, vol. 48, pp. 12893–12906, Nov 1993.
- [135] Y. B. Kim, C. F. Hempstead, and A. R. Strnad, “Flux-flow resistance in type-II superconductors,” *Phys. Rev.*, vol. 139, pp. A1163–A1172, Aug 1965.
- [136] J. Bardeen and M. J. Stephen, “Theory of the motion of vortices in superconductors,” *Phys. Rev.*, vol. 140, pp. A1197–A1207, Nov 1965.
- [137] R. Labusch *Cryst. Latt. Defects.*, vol. 1, p. 1, 1969.

- [138] D. Golubchik, E. Polturak, and G. Koren, “Mass of a vortex in a superconducting film measured via magneto-optical imaging plus ultrafast heating and cooling,” *Phys. Rev. B*, vol. 85, p. 060504, Feb 2012.
- [139] A. A. Awad, F. G. Aliev, G. W. Ataklti, A. Silhanek, V. V. Moshchalkov, Y. M. Galperin, and V. Vinokur, “Flux avalanches triggered by microwave depinning of magnetic vortices in Pb superconducting films,” *Phys. Rev. B*, vol. 84, p. 224511, Dec 2011.
- [140] P. W. Anderson and Y. B. Kim, “Hard superconductivity: Theory of the motion of Abrikosov flux lines,” *Rev. Mod. Phys.*, vol. 36, pp. 39–43, Jan 1964.
- [141] P. Hänggi, P. Talkner, and M. Borkovec, “Reaction-rate theory: fifty years after Kramers,” *Rev. Mod. Phys.*, vol. 62, pp. 251–341, Apr 1990.
- [142] M. Lange, M. J. Van Bael, A. V. Silhanek, and V. V. Moshchalkov, “Vortex-antivortex dynamics and field-polarity-dependent flux creep in hybrid superconductor/ferromagnet nanostructures,” *Phys. Rev. B*, vol. 72, p. 052507, Aug 2005.
- [143] R. B. G. Kramer, G. W. Ataklti, V. V. Moshchalkov, and A. V. Silhanek, “Direct visualization of the Campbell regime in superconducting stripes,” *Phys. Rev. B*, vol. 81, p. 144508, Apr 2010.
- [144] W. Kleemann, J. Rhensius, O. Petravic, J. Ferré, J. P. Jamet, and H. Bernas, “Modes of periodic domain wall motion in ultrathin ferromagnetic layers,” *Phys. Rev. Lett.*, vol. 99, p. 097203, Aug 2007.
- [145] E. Babaev and M. Speight, “Semi-meissner state and neither type-I nor type-II superconductivity in multicomponent superconductors,” *Phys. Rev. B*, vol. 72, p. 180502, Nov 2005.
- [146] L. F. Chibotaru and V. H. Dao, “Stable fractional flux vortices in mesoscopic superconductors,” *Phys. Rev. B*, vol. 81, p. 020502, Jan 2010.
- [147] L. F. Chibotaru, V. H. Dao, and A. Ceulemans, “Thermodynamically stable noncomposite vortices in mesoscopic two-gap superconductors,” *EPL (Europhysics Letters)*, vol. 78, no. 4, p. 47001, 2007.
- [148] U. Essmann and H. Tr “The direct observation of individual flux lines in type-II superconductors,” *Physics Letters A*, vol. 24, no. 10, pp. 526 – 527, 1967.

- [149] T. Nishio, V. H. Dao, Q. Chen, L. F. Chibotaru, K. Kadowaki, and V. V. Moshchalkov, "Scanning SQUID microscopy of vortex clusters in multiband superconductors," *Phys. Rev. B*, vol. 81, p. 020506, Jan 2010.
- [150] J. Gutierrez, B. Raes, A. V. Silhanek, L. J. Li, N. D. Zhigadlo, J. Karpinski, J. Tempère, and V. V. Moshchalkov, "Scanning hall probe microscopy of unconventional vortex patterns in the two-gap MgB_2 superconductor," *Phys. Rev. B*, vol. 85, p. 094511, Mar 2012.
- [151] E. H. Brandt, "Elastic and plastic properties of the flux-line lattice in type-II superconductors," *Phys. Rev. B*, vol. 34, pp. 6514–6517, Nov 1986.
- [152] L. Kramer, "Thermodynamic behavior of type-II superconductors with small κ near the lower critical field," *Phys. Rev. B*, vol. 3, pp. 3821–3825, Jun 1971.
- [153] V. H. Dao, L. F. Chibotaru, T. Nishio, and V. V. Moshchalkov, "Giant vortices, rings of vortices, and reentrant behavior in type-1.5 superconductors," *Phys. Rev. B*, vol. 83, p. 020503, Jan 2011.
- [154] M. Silaev and E. Babaev, "Microscopic derivation of two-component Ginzburg-Landau model and conditions of its applicability in two-band systems," *Phys. Rev. B*, vol. 85, p. 134514, Apr 2012.
- [155] N. V. Orlova, A. A. Shanenko, M. V. Milošević, F. M. Peeters, A. V. Vagov, and V. M. Axt, "Ginzburg-Landau theory for multiband superconductors: Microscopic derivation," *Phys. Rev. B*, vol. 87, p. 134510, Apr 2013.
- [156] M. E. Zhitomirsky and V.-H. Dao, "Ginzburg-Landau theory of vortices in a multigap superconductor," *Phys. Rev. B*, vol. 69, p. 054508, Feb 2004.
- [157] H. Suhl, B. T. Matthias, and L. R. Walker, "Bardeen-Cooper-Schrieffer theory of superconductivity in the case of overlapping bands," *Phys. Rev. Lett.*, vol. 3, pp. 552–554, Dec 1959.
- [158] A. Chaves, L. Komendová, M. V. Milošević, J. S. Andrade, G. A. Farias, and F. M. Peeters, "Conditions for nonmonotonic vortex interaction in two-band superconductors," *Phys. Rev. B*, vol. 83, p. 214523, Jun 2011.
- [159] R. Prozorov, "Equilibrium topology of the intermediate state in type-I superconductors of different shapes," *Phys. Rev. Lett.*, vol. 98, p. 257001, Jun 2007.

- [160] J. Ge, J. Gutierrez, B. Raes, J. Cuppens, and V. V. Moshchalkov, "Flux pattern transitions in the intermediate state of a type-I superconductor driven by an ac field," *New Journal of Physics*, vol. 15, no. 3, p. 033013, 2013.
- [161] E. Babaev and M. Silaev, "Type-1.5 superconductivity in multiband and other multicomponent systems," *Journal of Superconductivity and Novel Magnetism*, vol. 26, no. 5, pp. 2045–2055, 2013.
- [162] R. Huebener, *Magnetic Flux Structures in Superconductors: Extended Reprint of a Classic Text*. Solid-State Sciences Series, Springer, 2001.
- [163] J. Carlström, J. Garaud, and E. Babaev, "Semi-Meissner state and nonpairwise intervortex interactions in type-1.5 superconductors," *Phys. Rev. B*, vol. 84, p. 134515, Oct 2011.
- [164] E. Babaev, J. Carlström, J. Garaud, M. Silaev, and J. Speight, "Type-1.5 superconductivity in multiband systems: Magnetic response, broken symmetries and microscopic theory-a brief overview," *Physica C: Superconductivity*, vol. 479, no. 0, pp. 2 – 14, 2012.
- [165] J. Karpinski, N. Zhigadlo, S. Katrych, R. Puzniak, K. Rogacki, and R. Gonnelli, "Single crystals of MgB₂: Synthesis, substitutions and properties," *Physica C: Superconductivity*, vol. 456, no. 1, pp. 3 – 13, 2007.
- [166] L. Li, Z. Xu, J. Shen, L. Qiu, and Z. Gan, *J. Phys.: Condens. Matter*, vol. 17, p. 493, 2005.
- [167] I. V. Grigorieva, "Magnetic flux decoration of type-II superconductors," *Superconductor Science and Technology*, vol. 7, no. 4, p. 161, 1994.
- [168] A. Larkin and Y. Ovchinnikov, "Pinning in type-II superconductors," *Journal of Low Temperature Physics*, vol. 34, no. 3-4, pp. 409–428, 1979.
- [169] G. Karapetrov, J. Fedor, M. Iavarone, D. Rosenmann, and W. K. Kwok, "Direct observation of geometrical phase transitions in mesoscopic superconductors by scanning tunneling microscopy," *Phys. Rev. Lett.*, vol. 95, p. 167002, Oct 2005.
- [170] C. Reichhardt, C. J. O. Reichhardt, I. Martin, and A. R. Bishop, "Dynamical ordering of driven stripe phases in quenched disorder," *Phys. Rev. Lett.*, vol. 90, p. 026401, Jan 2003.
- [171] H. Dai, S. Yoon, J. Liu, R. C. Budhani, and C. M. Lieber, "Simultaneous observation of columnar defects and magnetic flux lines in

- high-temperature $\text{Bi}_2\text{Sr}_2\text{CaCu}_2\text{O}_8$ superconductors,” *Science*, vol. 265, no. 5178, pp. 1552–1555, 1994.
- [172] S. O. Valenzuela, “Order and mobility of solid vortex matter in oscillatory driving currents,” *Phys. Rev. Lett.*, vol. 88, p. 247003, Jun 2002.
- [173] P. Seneor, C.-T. Chen, N.-C. Yeh, R. P. Vasquez, L. D. Bell, C. U. Jung, M.-S. Park, H.-J. Kim, W. N. Kang, and S.-I. Lee, “Spectroscopic evidence for anisotropic s-wave pairing symmetry in MgB_2 ,” *Phys. Rev. B*, vol. 65, p. 012505, Nov 2001.
- [174] A. Soibel, Y. Myasoedov, M. L. Rappaport, T. Tamegai, S. S. Banerjee, and E. Zeldov, “Temperature variations of the disorder-induced vortex-lattice-melting landscape,” *Phys. Rev. Lett.*, vol. 87, p. 167001, Sep 2001.
- [175] M. Marchevsky, L. A. Gurevich, P. H. Kes, and J. Aarts, “Flux droplet formation in NbSe_2 single crystals observed by decoration,” *Phys. Rev. Lett.*, vol. 75, pp. 2400–2403, Sep 1995.

Curriculum Vitae



Bart Raes

Date of Birth: October 18, 1985

Place of Birth: Dendermonde, Belgium

09.1998-06.2004: Secondary School, Science and Mathematics at Sjabi, Puurs, Belgium

09.2004-06.2007: University, Bachelor in Physics (Minor: Mathematics), Granted by Katholieke Universiteit Leuven, Leuven, Belgium, June 2007.

09.2007-06.2009: University, Master in Physics (Minor: Solid state physics at the nanometer-scale), Granted by Katholieke Universiteit Leuven, Leuven, Belgium, June 2009 (Magna cum laude)

Thesis Subject: ‘Reversible magnetically controlled superconducting weak links’ (Promotors: Prof.Dr. V.V. Moshchalkov, Prof.Dr. A.Silhanek, Prof.Dr. J. Van de Vondel).

10.2009-current: University, PhD. (Promotors: Prof.Dr. V.V. Moshchalkov, Prof.Dr. J. Tempère), Katholieke Universiteit Leuven, Leuven

Thesis Subject: ‘Scanning Hall probe microscopy of vortex matter in single-and two-gap superconductors’ (Promotors: Prof.Dr. V.V. Moshchalkov, Prof.Dr. J. Tempère)

10.2010: Second price in the poster competition of the ‘Nanoscale superconductivity and Chemistry’ conference in Leuven.

05.2013: Finalist Belgian Physical Society young Researchers Contest for best oral presentations. General Scientific Meeting 2013 in Louvain-la-Neuve, Belgium.

Publications

1. **Magnetically controlled superconducting weak links**
J. Van de Vondel, A. V. Silhanek, B Raes, W. Gillijns, R. B. G. Kramer, V. V. Moshchalkov, J. Sautner, and V. Metlushko
Appl. Phys. Lett. **95**, 032501 (2009)
2. **Symmetry-Induced Giant Vortex State in a Superconducting Pb Film with a Fivefold Penrose Array of Magnetic Pinning Centers**
R. B. G. Kramer, A. V. Silhanek, J. Van de Vondel, B Raes, V. V. Moshchalkov
Phys. Rev. Lett. **103**, 067007 (2009)
3. **Direct visualization of the vortex distributions in a superconducting film with a Penrose array of magnetic pinning centers: Symmetry induced giant vortex state**
R. B. G. Kramer, A. V. Silhanek, J. Van de Vondel, B Raes, V. V. Moshchalkov
Physica C: Superconductivity **470**, 758 - 761 (2010)
4. **Local probing of the vortex-antivortex dynamics in superconductor/ferromagnet hybrid structures**
A. V. Silhanek, V. N. Gladilin, J. Van de Vondel, B. Raes, G. W. Ataklti, W. Gillijns, J. Tempère, J. T. Devreese, V. V. Moshchalkov
Superconductor Science and Technology **24**, 024007 (2011)
5. **Scanning Hall probe microscopy of unconventional vortex patterns in the two-gap MgB₂ superconductor**
J. Gutierrez, B Raes, A. V. Silhanek, L.J. Li, N. D. Zhigadlo, J.Karpinski, J. Tempère, V. V. Moshchalkov
Phys. Rev. B **85**, 094511 (2012)
6. **Two energy gaps in superconducting Lu₂Fe₃Si₅ single crystal derived from the temperature dependence of lower critical field H_{c1}(T)**
J. Ge, J. Gutierrez, B Raes, T. Watanabe, J. Koshio, V. V. Moshchalkov
Physica C: Superconductivity **478**, 5-9 (2012)

7. **Local mapping of dissipative vortex motion**
B Raes, J. Van de Vondel, A. V. Silhanek, C. C. de Souza Silva, J. Gutierrez, R. B. G. Kramer, V. V. Moshchalkov
Phys. Rev. B **86**, 064522 (2012)
8. **Flux pattern transitions in the intermediate state of a type-I superconductor driven by an ac field**
J. Ge, J. Gutierrez, B Raes, J. Cuppens, V. V. Moshchalkov
New Journal of Physics **15**, 033013 (2013)
9. **First vortex entry into a perpendicularly magnetized superconducting thin film**
in preparation, (2013)
10. **Real space visualization of oscillatory vortex dynamics and ordering effects in NbSe₂** *in preparation, (2013)*
11. **Direct observation of the ac-response of a nano-structured superconductor**
in preparation, (2013)

,

Faculty of Science
Department of physics and astronomy
Institute for Nanoscale Physics and Chemistry
Celestijnenlaan 200D
B-3001 Leuven, Belgium
Bart.Raes@fys.kuleuven.be
<http://www.kuleuven.be/INPAC/>

